Dynamics and Control of Tethered Satellite Formations in Low-Earth Orbits

PhD Thesis

Manrico Fedi Casas

Universitat Politècnica de Catalunya

2015

To Flàvia

Contents

1 Introduction 3

1.1 Objectives of the study . . . 3
1.2 Tethers in space and flight formation . . . 3
1.3 State of the Art . . . 5
1.3.1 Space Tether Applications . . . 5
1.3.2 Tether Simulation Analysis . . . 8
1.3.3 Tether Control Approach . . . 9
1.4 Space Tether Missions . . . 9
1.4.1 TSS mission . . . 10
1.4.2 SEDS-1 and SEDS-2 missions . . . 11
1.4.3 TiPS mission . . . 13
1.4.4 YES2 mission . . . 14
1.4.5 SPECS mission . . . 14
1.5 Thesis Outline . . . 14
1.5.1 Objectives of the study . . . 14
1.5.2 Thesis structure . . . 15
1.5.3 Contributions . . . 17

2 Flight Dynamics of Tethered Formations 18

2.1 Review of Orbital Mechanics . . . 18
2.2 Dynamics of Relative Motion . . . 22
2.2.1 Equations of motion relative to a reference orbit . . . 22
2.2.2 Relative equations of Motion based on Orbit Elements . . . 30
2.2.3 Comparison of orbital models . . . 31
2.3 Effects of Orbit Perturbations . . . 32
2.3.1 Perturbations in Equations of Motion . . . 33
2.3.2 Implementation of the J_2 Perturbation . . . 35

2.4 Tether Models . . . 39
2.4.1 Elasticity Model . . . 40
2.4.2 Effects of tether mass . . . 41
2.4.3 Tether Deployment and Retrieval . . . 46
2.4.4 Dynamics of a tether in orbit . . . 47
2.5 Cluster Architectures . . . 55
2.5.1 Planar Formations . . . 55
2.5.2 Three Dimensional Formations . . . 56
2.6 Formation Spin Stabilization . . . 56
2.6.1 Double Pyramid Global Formation Behavior . . . 59
2.7 Agent Control . . . 60

3 Refined dynamical analysis of multi-tethered satellite formations 63
3.1 Tether Model . . . 63
3.2 Initial conditions . . . 64
3.3 Open loop stability analysis . . . 66
3.3.1 In-plane formations . . . 69
3.3.2 Earth-facing formations . . . 75
3.4 Circular formations . . . 84
3.4.1 Closed Hub-And-Spoke in-plane formation . . . 84
3.4.2 Earth-facing formations . . . 88
3.5 Major findings for tethered formation dynamics . . . 89

4 Multi-tethered formation dynamics for non-ideal operating conditions 92
4.1 Effects of eccentricity of the reference orbit on Multi–Tethered Satellite Formations . . . 92
4.1.1 Initial conditions for deputies and beads . . . 94
4.1.2 Formation stability . . . 97
4.1.3 Behavior of the parent body . . . 112
4.1.4 Effects of eccentricity of the reference orbit . . . 114
4.2 Effects of J_2 perturbation on tethered formations . . . 116
4.2.1 Initial conditions for deputies and beads . . . 116
4.2.2 Proposed approach . . . 117
4.2.3 Open–loop dynamics of tethered formation . . . 118
4.2.4 Effect of the J_2 perturbation on the parent body . . . 122
4.2.5 Effects of J_2 perturbation on formation behavior . . . 124

5 Tethered Formation Control 129
5.1 Formation Flying Control . . . 129
5.2 Tethered Formation Flying Control . . . 130
5.3 Virtual Structure Control Approach . . . 131
5.3.1 Centralized Virtual Structure Control Approach . . . 131
5.3.2 Decentralized Virtual Structure Control Approach . . . 133
5.4 VSC model for a spinning Double-Pyramid formation orbiting a central body 135
5.5 Fine positioning control . . . 139
5.5.1 Thruster Control Model . . . 139
5.5.2 Agent dynamics . . . 140
5.5.3 Control Approaches . . . 141
5.5.4 Sliding mode control . . . 143
5.6 Reeling and tether tension control . . . 147
5.7 Vibration control . . . 148
5.7.1 Longitudinal oscillations . . . 148
5.7.2 Transversal oscillations . . . 148
5.8 Control Results . . . 149
5.9 VSC major findings . . . 154

6 Conclusions 156

Nomenclature 160

Acronyms 165

Bibliography 166

Abstract

The thesis is focused on the study of dynamics and control of a multi–tethered satellite formation, where a multi–tethered formation is made up with several satellites (agents) connected by means of cables (tethers).

The interest in tethered formations emerged at the turn of the millennium. The concept of tethered formation would benefit from the availability of a multi–agent system with unique properties: the distribution of the payload over several elements of the formation provides unprecedented mission capabilities, especially in terms of mission flexibility and resilience to failures, while the use of tethers for stabilization and control purposes (and possibly for communication between agents as well) would allow to manoeuvre and reconfigure the formation simply by acting on tether length and tension in order to vary agents' relative position. Mission effectiveness would thus be maximized at a very modest price in terms of energy consumption, as far as no thrust is required for a manoeuvre requiring the variation of tethers length only. Several scientific missions has been envisaged that could benefit from this novel concept, especially in the field of interferometry.

Thesis Information

Thesis Title:

Dynamics and Control of Tethered Satellite Formations in Low-Earth Orbits

Thesis committee information

Thesis Director	Professor Giulio Avanzini Università del Salento giulio.avanzini@unisalento.it
UPC Tutor	Professor Josep Joaquim Masdemont Soler Universitat Politècnica de Catalunya josep.masdemont@upc.edu
Committee President	Professor Gerard Gómez Muntané. Universitat de Barcelona gerard@maia.ub.es
Committee Secretary	Professor Ramon Costa Castelló Universitat Politècnica de Catalunya ramon.costa@upc.edu
Committee Vocal	Professor Camilla Colombo Politecnico di Milano camilla.colombo@polimi.it
Ph.D. Candidate	Manrico Fedi Casas. mfedic@gmail.com

Acknowledgements

Thanks Montse for your constant love and support day after day. You always find the right words for motivation. Thank you also for your patience for so many evenings and weekends spent home because of my studies.

The values my parents taught me since I was a kid have brought me here. The eagerness to pursue new challenges is something I owe them. I want to thank my parents Dolors and Xavier, for their love and for the education they gave me.

Many thanks Giulio for your outstanding scientific guidance during my Ph.D. studies. Living on different countries has not been a problem to perform this work. Your availability, no matter the time of the day, or the day of the week, even during your own holidays, has always been superb.

I would like to thank professors J.J. Masdemont Soler, D. Crespo Artiaga and R. Costa Castelló for their good advice, both technical and administrative received during my Ph.D. studies.

I want to thank Pete Balsells for giving me the opportunity to perform graduate studies at University of California through the Balsells - Generalitat de Catalunya fellowship program. That opportunity was a crucial stepping stone in my career.

Chapter 1

Introduction

1.1 Objectives of the study

This thesis is focused on the study of dynamics and control of a multi-tethered satellite formation, where a multi-tethered formation is made up with several satellites (agents) connected by means of cables (tethers).

The goal of the first part of the study is to evaluate the effect of tether mass on multi-tethered clusters. Due to the complexity of the formations analyzed, the stability of the formation is assessed through a numerical simulation. The behavior is evaluated in the ideal case of circular orbits, but also in non-ideal cases such as that of elliptical reference orbit or perturbed motion.

The second part of the study is focused on deriving a control law for position and attitude control of a multi-tethered cluster. The control problem is decomposed in two levels: A first level to perform position and attitude coarse control of the formation as a whole, and a second level to achieve accurate position and control of each agent of the cluster. This approach benefits from the fact that tethers provide rigidity similar to that of a rigid body, and therefore the cluster exhibits a behavior comparable to that of an orbiting rigid body.

1.2 Tethers in space and flight formation

Tethers are cables that define a physical link between two or more satellites in order to maintain a predefined configuration in space. As shown in [1], the potential applications

of deploying tether systems in space are multiple. The dynamics of tethers under the presence of gravity-gradient, drag and electrodynamic forces, the tether viscoelastic behavior, the momentum transfer capabilities of taut tethers, and other features offer a wide range of possibilities that can be useful for different space missions. A summary of space tether applications and missions is presented in Section 1.4.

The concept of Satellite Formation Flying (SFF) consists of a cluster composed by several satellites cooperating together. The purpose of this cooperation is to perform missions, or achieve a degree of performance not achievable by a single satellite. The characteristics of each mission will introduce requirements regarding the relative position of each satellite and synchronized motion between them. Clearly, the use of tethers as a link among formation constituents can be used to mechanically restrain their relative motion thus providing a constraint for formation keeping purposes.

The concept of Tethered Formation Flying (TFF) benefits from the availability of a multi-agent system with unique properties: the distribution of the payload over several elements of the formation provides unprecedented mission capabilities, especially in terms of mission flexibility and resilience to failures, while the use of tethers for stabilization and control purposes (and possibly for communication between agents as well) would allow to manoeuvre and reconfigure the formation simply by acting on tether length and tension in order to vary agents' relative position. Mission effectiveness would thus be maximized at a very modest price in terms of energy consumption, as far as no thrust is required for a manoeuvre requiring the variation of tethers length only. Several scientific missions has been envisaged that could benefit from this novel concept, especially in the field of interferometry. Some of the TFF applications require high precision formation flying capability.

The purpose to study the effect of massive tethers is motivated by the relatively high mass of tethers compared to that of a typical small satellite. The length of tethers belonging to large formations, combined with the density of suitable tether materials, suggest that the effect of the tether mass on the overall dynamics may not be negligible. Double or triple strand tethers may increase further the effect of the mass on cluster dynamics.

The definition of a suitable tether physical model is fundamental. The model must be rich enough to take into account the effect of the mass and vibration modes, but at the same time its computational cost must be reasonable. The latter feature may be not

a concern for modeling single tethers in the space, but it is an issue for complex multi-tethered structures with several links and equation couplings.

Multi-agent tethered formations are presented as a type of satellite flight formations. Controlling the relative position of the agents is essential in many mission scenarios. For this purpose, it is needed to be able to define accurately an arbitrary relative position and attitude of the members of the cluster. The inclusion of the mass of the tethers in the model complicates the control problem. On the massless case, under the assumption that every agent has full control capability, the tether tension is easy to predict. On the other hand, for the massive case, the force exerted by tethers on the deputies is not easy to model due to the effect of external forces (mainly the gravity force, but also other perturbations) on the mass of the tether. Therefore, the changes in tether tension due to the effect on external forces on tether mass act as a disturbance.

1.3 State of the Art

1.3.1 Space Tether Applications

References [1] and [2] provide a rich and interesting summary of some of the potential applications of space tethers. References [3], [4], [5] and [6] provide an overview of the state of the art of tether research. Most of tether space missions rely on one of the following two fundamental characteristics (or a combination of both): use of tethers with the purpose of momentum exchange, and use of tethers made of materials having electrodynamic properties. The former application uses tethers essentially to transmit forces and/or to distribute momentum to the members of the cluster. The latter takes into account the forces generated in conductive tethers due to Ampere currents related to the Earth's magnetic field, as explained in [7].

Among many others, some of the most significant applications are listed below.

- **Comet rendez-vous and sample retrieval**. The goal of the mission consist in obtaining a sample of a comet. The capsule containing the sample would be retrieved with a tether. This approach requires a penetrator harpoon containing an inner sample capsule container. The penetrator is released, hits the comet, and then the capsule containing the sample is retrieved with a tether attached to the mother spacecraft [2].

- **Spacecraft boosting through electrodynamic tether**. This mission benefits from the fact that Ampere forces along the velocity vector exert a force on the spacecraft. In Ref. [2], Levin considers the mission setup that was intended to extend the life of the Russian Mir space station on orbit. The dynamics involved take into account vehicle attitude dynamics, electrodynamic control, resonant motions, transverse oscillations, torque produced by the Ampere forces and variations on the geomagnetic field. It is shown that the mass-to-current ratio increases with instability. Based on the properties of electrodynamic tethers, Levin proposes the creation of an electrodynamic sail, made of a grid of electrodynamic tethers.

- **Object de-orbiting**. The drag induced by electrodynamic forces can also be used to remove objects from orbit. At the end of the life, a satellite may deploy a tether that generates sufficient drag in order to de-orbit the satellite towards atmosphere in a controlled way. Similarly, some research was performed to investigate the use of tethers with the purpose of capturing orbiting debris through harpoon or throw-nets [8].

- **Momentum exchange electrodynamic reboost system**. In this case, the payload is captured by an end body that rotates at one of the ends of the spinning tether system. This tether works as a skyhook, that releases the payload after half a turn, providing it an additional delta-V that could be on the order of 2 km/s as discussed in [2].

- **Tether space elevator**. The purpose of the tether is to provide a means for a platform to lift payloads into orbit. The elevator (or climber, as called in some references) should have a mean to climb along the tether. The end of the tether should be connected to a ballast mass which acts as a counterweight. The center of mass of the combined system should be above the geostationary orbit, in such a way that the ballast would "pull" the tether anchored to the Earth surface as described in [9].

- **Lunar transportation system**. By using an Earth-Moon space elevator connected through a transfer orbit it should be possible to transport material between Earth and Moon. An additional vehicle or means of transportation would still be necessary to lift material from the lunar surface up to the tether transportation system. This case is analyzed in detail in reference [2]. The same reference also proposes an alternative interplanetary tether transportation system between Martian low orbit, up to escape orbit, by using tethers attached to the orbit of the moons of Mars.

- **Atmospheric probe**. The deployment of a tether from an orbiting spacecraft could be used also with the purpose of a multi-probe for atmospheric studies. A probe released from an orbiting vehicle could be used to acquire relevant measurements at different atmosphere altitudes.

- **Tethered space observatory**. An observation platform can be created by defining a mosaic of several satellites connected through tethers. The measurements of these satellites could be combined in order to achieve high precision interferometry. This could be comparable to using a telescope with a very large aperture that could be used for different kinds of missions, including radio interferometry (as presented in [10], [11] and [12]). Other applications could be multipoint measurement applications, or gravity measurement laboratories (as mentioned in [13]).

As stated before, this thesis focuses on the study of multi-body tethered formations described in the last item of the above list. These formations consist of multi-body tethers performing a coordinated movement.

The main advantages of using tethers for satellite flight formation are:

- **Reduction of fuel consumption of agents**. The natural stabilization of the structure reduces the fuel consumption on devices using actuators to perform position corrections. This is an advantage with respect to free flight formation formations. Considerable fuel consumption limits the operative life of the system.

- **Less actuators needed**. The fact that tethers provide a natural way to prescribe the position of certain constituents, and the wise use of gravitational and/or centrifugal forces, may remove the need to use any actuator to perform position corrections. Less actuators means cheaper satellites, less complexity, more reliability, and less weight.

- **Rigid body behavior**. Under some conditions a tethered cluster behaves like a rigid body. Therefore the equilibrium properties of orbiting rigid bodies are applicable to tethered formations.

- **Potential reduction in computational load**. In a free flight formation, each device shall perform its GNC calculations in order to assess the position at every time. In this case it won't be even necessary that certain orbiting bodies have a CPU with GNC algorithm.

- **Use of tethers for communications**. For these cases when agents need to perform a synchronized control, it is needed to establish a communication link between them. Tethers can be used as a physical communication layer.

On the other hand, potential problems of tethered formation are:

- **Lack of reconfiguration flexibility**. Tethers impose reduced flexibility in terms of formation reconfiguration. Physical links between the orbiting bodies constraint the movements, as opposite to the non-tethered case where there is no limit to any reconfiguration.
- **Potential single point of failure**. In case of failure of one of the constituents of the formation or one of the tethers, it would not be possible to replace it. If the system does not provide redundant components, the whole mission will be lost.
- **Build complexity**. Tethered formations require more complex mechanical construction, as tethers need to link orbiting bodies. In systems with variable length tethers, a reeling mechanism will have to be installed on one or several deputies.
- **Complex deployment**. The complete structure must be launched with tethers already connecting orbiting bodies. Deployment can be complicated specially in these missions where the constellation doesn't have a variable tether mechanism able to extend or retract tethers dynamically in orbit.
- **Effect of tether mass** As shown in this thesis, the effect of the mass of tethers is not negligible. This acts as a perturbation to the position of the agents.
- **Sensitivity to space debris**. In some cases, space debris may hit and break tethers, with the risk of endangering the whole mission.

1.3.2 Tether Simulation Analysis

Reference [13] provides the starting point for the analysis of the effect of tether mass. This paper develops several analytical models for specific tethered formation configurations and orientations. Based on analytical models, it performs a numerical analysis of the stability of the studied formations through the results of simulations for the different formation configurations studied. The model used in the cited paper does not take into account tether mass. The work performed in this thesis defines equivalent massive formations using the lumped mass model [14], [15] with the purpose of comparing the behavior of

massive and massless formations.

Paper [16] defines a model taking into account the effect of the J_2 perturbation due to the Earths oblateness. The advantage of this model is that is formulated in the LVLH (Local Vertical Local Horizontal) reference frame, as it is the case of the HCW equations. This model is used to evaluate the behavior of some of the tethered formations studied in Ref. [13].

The model that incorporates eccentric orbits is presented in Ref. [17]. This paper presents a model for elliptical orbits using true anomaly as independent variable that is formulated also in the LVLH reference frame.

1.3.3 Tether Control Approach

The potential suitability of a double pyramid structure for an Earth-oriented cluster is examined in papers [18] and [15]. The rigidity provided by the tethers provides a behavior similar to that of a rigid body in orbit.

Reference [19] provides the basis for the development of a control law based on the virtual structure principle. This paper defines an approach that allows taking advantage of the rigidity of a tethered structure and the similarity of the behavior of the cluster with that of rigid body. Several other papers [20], [21] and [22] by the same authors provide different variations of the same control law.

For the precision control approach, Refs. [23] and [24] are taken into account. Both papers are valid for the development of a control law for a second order system involving a system of coupled equations.

1.4 Space Tether Missions

The first missions conducted with tethered systems had the purpose of assessing the possibility of deploying tethers over long distances, and to determine the potential stability issues associated to them. Figure 1.1 shows a summary of past and future tethered missions organized by NASA. Table 1.1 lists the most relevant missions of Tethered Satellite Systems (TSS) in LEO based on the information provided in Refs. [7], [25] and [26]. A set of references providing details for each mission is found in [26].

Table 1.1: Flown tether missions in LEO

Name	Year	Organization	Tether Length
Gemini XI	1966	NASA	30 m
Gemini XII	1967	NASA	30 m
TSS-1	1992	ASI/NASA	260 m
SEDS-1	1993	NASA	20 km
PMG	1993	NASA	500 m
SEDS-2	1994	NASA	20 km
Oedipus-C	1995	CRC/CSA/NASA/NRC	1 km
TSS-1R	1996	ASI/NASA	19.6 km
TiPS	1996	NRL/NRO	4 km
ATEx	1999	NRL/NRO	6 km
MAST	2007	NASA/Stanford/TUI	1 km
YES2	2007	ESA	30 km
STARS	2009	Kagawa University	5 m
T-REX	2010	ISAS/JAXA	300 m
TEPCE	2013	NRL/NRO	30 km

The first use of tethers in a space mission took place in 1966 during the Gemini XI mission. The purpose of this mission was to perform a rendezvous between the Gemini capsule and the Agena vehicle which consisted of a docking platform plus a power unit. One of the secondary goals of the mission was to study the stability of the two spacecraft connected through a 30 m tether. The success of this mission assessed the viability of the use of tethers in space missions. Figure 1.1 provides a summary of some of the most significant space missions conducted by NASA.

1.4.1 TSS mission

After the success of the Gemini mission, the TSS-1 (Tethered Satellite System) was the first mission to test the possibilities of tether deployment in space [27]. The purpose of this mission launched on 1992, was to provide the capability of deploying a satellite on a long, gravity-gradient stabilized tether from the Space Shuttle. The (TSS) consisted of three elements: a satellite (Spacelab pallet), an electrodynamic tether, and a tether deployment/retrieval mechanism attached to the Space Shuttle (Fig. 1.2). The objectives of the TSS-1 mission were:

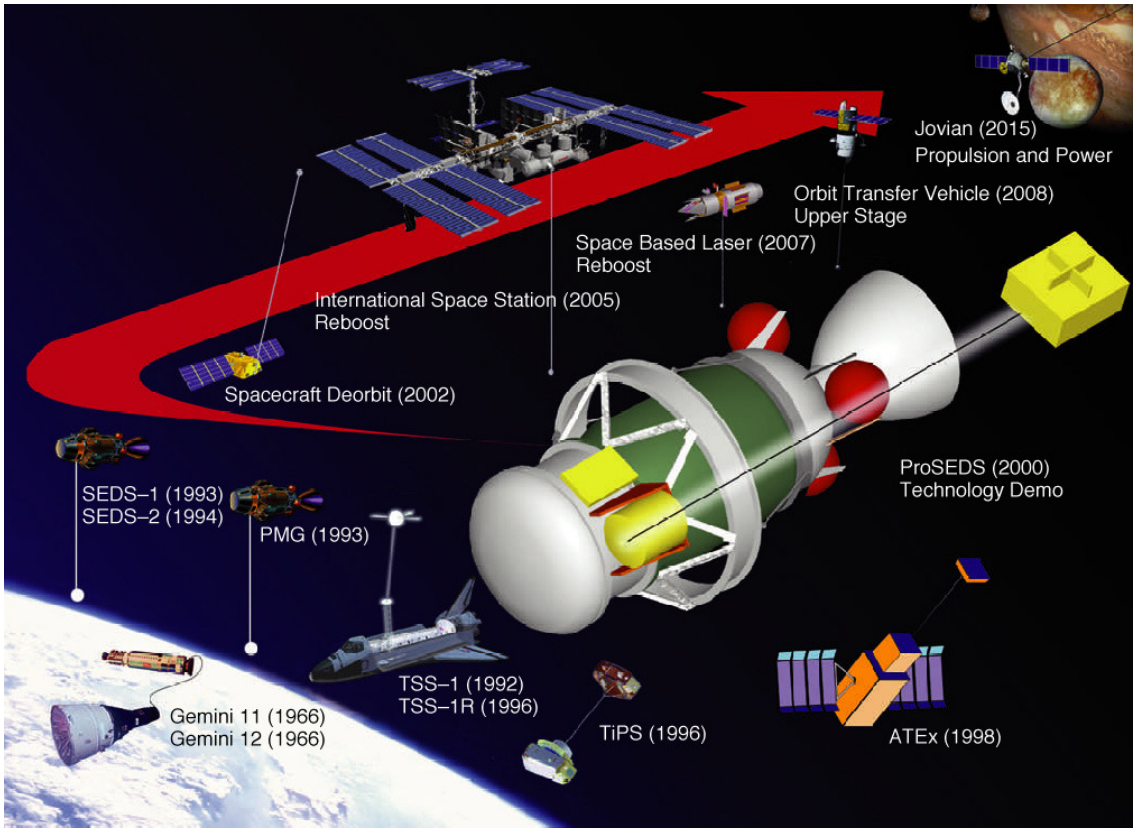

Figure 1.1: **Summary of missions with participation of tethered systems (Credit: NASA)**

- To test the dynamics acting on a variable length tether.
- To determine and understand the electromagnetic interaction between the tether, satellite, orbiter system and space plasma.
- To find potential future tether applications on the Shuttle and Space Station.

The TSS-1 released a satellite while remaining attached to a reel in the Shuttle payload bay. Originally, it was intended to be deployed 20 km above the Shuttle, but due to a malfunction in the reeling system it was deployed only to 268 m. However, this was enough to proof that gravity-gradient stabilized tethers was a valid concept, and the feasibility to deploy satellites to long distances.

1.4.2 SEDS-1 and SEDS-2 missions

The purpose of the Small Expendable Deployment System (SEDS) project was to test the deployment of a 20 km satellite [1], [28], [29], [30].

The SEDS-1 mission demonstrated the capability of deorbiting a 25 kg payload from LEO. The mission objectives were to demonstrate that it was possible to deploy a payload at the end of a 20 km-long tether and to study its reentry after the tether was snapped. The orbit chosen had an inclination of 34 degrees, a perigee altitude of 190 km and an apogee altitude of 720 km.

The second mission SEDS-2, intended to demonstrate the use of a feedback closed loop control law with the purpose of tracking a predetermined trajectory. The main goal of the mission was the deployment of a payload along the local vertical. The mission was intended also to assess the long term evolution of a tethered system. The orbit was circular with an altitude of about 350 km. The SEDS-2 tether was presumably snapped by a micrometeroid or space debris after five days of the mission.

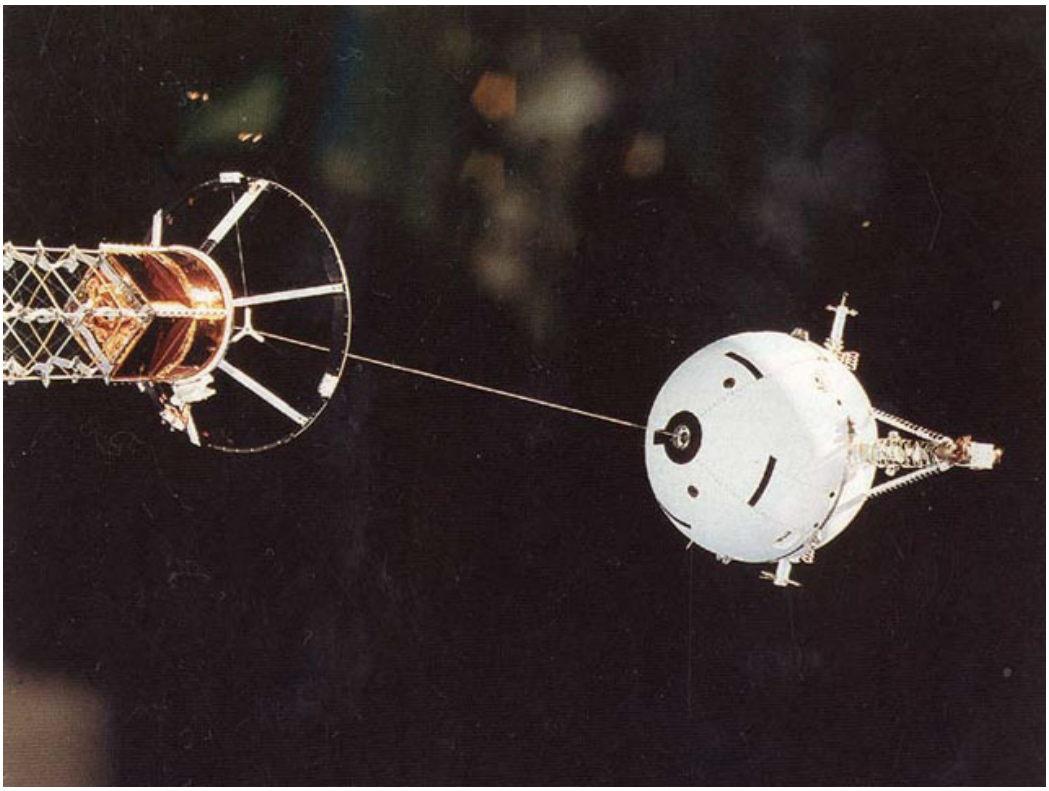

Figure 1.2: **TSS deployment system, tether, and satellite**

1.4.3 TiPS mission

The purpose of the Tether Physics and Survivability (TiPS) mission [31], [32], was to study the long-term behavior and longevity of tethers in space. This mission was motivated by several tether failures in previous missions. Mission TSS-1 was aborted due to a malfunction in the deployment mechanism, the tether of the SEDS-2 mission was cut off by a micrometeorite, and the TSS-1R tether was cut off during deployment. After these results it was needed to assess better the viability of a deployed tether in a long term mission.

Figure 1.3: **TiPS tether deployed as seen from observatory mesurements (Credit: NASA)**

The formation consisted of two bodies (Ralph and Norton) connected by a tether 2 mm diameter. Body Ralph (closest to the Earth) contained the electronics and the actuation system, whereas Norton was a passive satellite. Figure 1.3 shows an image of the tether system as observed from an optical station on ground. The only active mechanism of the mechanism was the deployment device. The formation survived for more than 27 months. Reference [33] provides a summary of the results, showing the evolution of the libration amplitude and libration rate of the formation.

1.4.4 YES2 mission

The YES2 mission aimed at proving the viability of a tether deployment system plus the release of a re-entry capsule. The tether was non-conductive and a had a total length of 31.7 km. The deployer, attached to the Russian Foton platform, had a total mass of 22 kg, and the capsule had a mass of 6 kg. The system was successfully deployed in a very low Earth orbit (around 300 km). Reference [34] provides details on the characteristics of the mission.

1.4.5 SPECS mission

The Submillimeter Probe of the Evolution Cosmic Structure (SPECS) mission is scheduled to be launched around year 2020. This is probably the most ambitious mission involving tethered flight formation. The SPECS formation consist in a 1 km submillimeter interferometer placed in a LEO orbit. The submillimetre band is useful to study the process of star formation and to investigate the processes of constitution and evolution of galaxies. References [35] and [12] describe the mission in detail. Reference [36] provides a detailed analysis on the dynamics of the formation. The main requirements for this mission are:

- Resolution comparable to that of the Hubble Space Telescope.
- Capable of completing a single observation inside a 72 hour frame.

The SPECS formation geometry is based on a central body (the beam collector) having three tethers attached to three mirrors, according to a Tetra-Star configuration [36]. Measurements of mirrors are combined using well known aperture synthesis techniques. Mirrors rotate around the the beam collector and are also able to deploy/retreat thanks to a variable length tether up to a maximum of 595 m. Three ballasts are placed on the opposite side of each mirror, as it is shown in the cited reference. One of the issues to take into account by the feedback law is the change in the inertia tensor during deployment.

1.5 Thesis Outline

1.5.1 Objectives of the study

The thesis goals are the following:

- To develop a dynamic model suitable for the design, simulation and control of a tethered formation of Earth orbiting satellites.

- To analyze the dynamics of the model, by including the effects of of tether mass. Tether masses are modeled as point masses (beads) along the tethers.
- Inclusion of the effects of the so called J_2 perturbation effects in the dynamic model, where J_2 effects are representative of the most significant perturbation induced by Earths oblateness on ideal Keplerian orbits.
- Inclusion of eccentric reference orbits.
- To design a position/trajectory control for a tethered cluster. The control goals include the following possibilities:
  - Development of control laws aimed at maintaining the relative position with respect to an inertially fixed attitude along the orbit (inertial station keeping).
  - Development of control strategies allowing for the reconfiguration of the formation (e.g. expansion of contraction of the whole set of agents).

1.5.2 Thesis structure

This thesis has two main goals. First, it introduces the problem and presents the state of the art of the research on tethered formations. Secondly, and most important, it provides the results of the research activities in accordance with the objectives of the study listed in the previous Section.

The structure of the thesis is the following:

- In Chapter 1, an introduction on tethered space formations is provided, with the presentation of the main applications of tether systems in space. This chapter also provides a short summary of the most representative space tethered formation missions conducted so far. The introduction ends with the description of the works conducted, the results achieved with respect to the original goals and presentation of thesis contributions.
- Chapter 2 briefly recalls major facts on orbital dynamics, as background material for the problem, along with the most suitable alternatives to represent the behavior of formation flight tethered formations. The two main alternatives presented are the representation of the problem in a local reference frame attached to a reference orbit, and the use of differential orbit elements. Both models allow the incorporation of orbital perturbations effects in their equations. This chapter presents also the

model of a single tether based on its visco-elastic properties. Taking into account the related literature, different alternatives are presented, from the rigid massless tether (the simplest scenario), to the most accurate continuous model based on the string equation. The model chosen for this study is a lumped mass model, which presents a good compromise between accurate representation (with a massive tether) and acceptable computational load. In the last part of the chapter, the most representative tethered formation geometries and orientations studied in the literature are introduced. If on one side, the simple dumbbell case is extensively analyzed in many works, there is a variety of more complex tethered systems architectures with different orientations, depending on the purpose of the mission of the cluster.

- Chapter 3 discusses the effect of tether mass on the dynamic behavior of tethered formations. The tethered formation geometries, and the scenarios studied, are identical to those of another paper that studies the behavior of massless tethered formations. This fact allows assessing, on a case by case basis, the difference in behavior when tether mass is incorporated in the model.

- Chapter 4 extends the modeling tools developed in the previous chapter by analyzing the behavior of massive tethered formations on elliptical orbits. The study analyzes the behavior of massive tethered clusters for different eccentricity values. This chapter extends also the work performed in Chapter 2 by studying the effect of the J_2 perturbation on the behavior of tethered formations through the use of a linearized perturbation model. Note that the effect of the Earth oblateness is the most significant perturbation for LEO orbiting satellites.

- Finally, Chapter 5 presents different feedback command laws for formation control. The purpose of an active controller is to achieve high precision pointing accuracy of both the formation as a whole, and for each deputy of the cluster. The alternative chosen consists of a controller that operates at two levels: firstly, it calculates the target position and orientation of each member of the formation (assuming a rigid-body like shape of the formation), and secondly it implements fine position control for each member of the cluster. For the fine position control, two alternatives are presented. At the end of the chapter results of the implementation of the formation controller are presented.

- Chapter 6 summarizes the major findings of the thesis.

1.5.3 Contributions

The following journal publications are published

- G. Avanzini, M. Fedi: *Refined dynamical analysis of multi-tethered satellite formations*, Acta Astronautica, vol. 84, pp. 3648, Mar. 2013. `http://dx.doi.org/10.1016/j.actaastro.2012.10.031`
- G. Avanzini, M. Fedi: *Effects of eccentricity of the reference orbit on Multi-Tethered Satellite Formations*, Acta Astronautica, vol. 94, no. 1, pp. 338350, Jan. 2014. `http://dx.doi.org/10.1016/j.actaastro.2013.03.019`
- M. Fedi, G. Avanzini: *Virtual Structure and Precise Positioning Formation Control for Tethered Satellite Formations*, submitted for possible publication in Journal of Guidance, Control, and Dynamics (AIAA).

The following conference publications are published

- G. Avanzini, M. Fedi: *Effects of J_2 perturbations on multi-tethered satellite formations.* AAS 11-631 AAS/AIAA Astrodynamics Specialist Conference. Alaska, 2011.
- G. Avanzini, M. Fedi: *Effects of Eccentricity of the Parent Body on Multi-Tethered Satellite Formations*, IAA-AAS-DyCoSS1 -06-01
- M. Fedi, G. Avanzini: *Virtual Structure Formation Control for Tethered Satellite Formations*, 7th International Workshop on Satellite Constellations and Formation Flying, 2013

The author attended the second and third conferences and presented both papers.

Chapter 2

Flight Dynamics of Tethered Formations

The goal of this chapter is to briefly describe the orbital mechanics topics related to tethered satellite formations. The models introduced here are focused to single-point objects in order to model the deputies of the formation. The rigid body behavior of the satellites is introduced in Section 2.6.

2.1 Review of Orbital Mechanics

The two–body problem is the starting point for modeling tethered clusters orbiting Earth. From Newton's Second Principle of Dynamics and the Law of Universal Gravitation, it is possible to derive the Equation of Relative Motion for the two-body problem [37]:

$$\ddot{\boldsymbol{R}} = \frac{\mu}{R^2}\frac{\boldsymbol{R}}{|\boldsymbol{R}|} \tag{2.1}$$

where $\boldsymbol{R}$ is the relative position vector from the Earth to the orbiting body, and the Earth gravitational parameter $\mu = GM_e$ is the product of the Universal Constant of Gravitation times the mass of the primary body (the Earth in the present application). Given an initial condition in position and velocity for the three axis (a total of six initial condition values, three for position and three for velocity), it is possible to integrate this equation to determine the position and velocity of the orbiting body at any time.

This equation is derived under the following assumptions:

- The bodies lie in an inertial coordinate system.

- The two bodies can be represented as point masses.
- The only force acting on them is the gravitation attraction between them.

The three laws of planetary motion discovered empirically by Kepler in the 17th century can be derived from the solution of Eq. (2.1). In this respect, one should note that:

- An analytical expression for the trajectory of the mass m with respect to M (the orbit) is available on the basis of simple energy and angular momentum conservation considerations [38];
- When $m << M$, as in the case of satellites orbiting the Earth or planets orbiting the Sun, the largest mass contains most of the mass of the system. In this case the center of mass of the system can be assumed as coincident with the position of M, that can be used as the origin of an inertially fixed reference frame.

Equation (2.1) is the two-body problem equation of motion that will be used as a basis to construct appropriate models for the formation flying problem. It consists of three second order equations, which require six values for initial conditions to determine a specific orbit. As discussed in detail in [39], it is possible to find six values for parameters that depend uniquely on the initial conditions, five of which have a clear geometric interpretation. In the derivation, it is shown that a Keplerian orbit has constants of motion, called constants of integration, that depend from conservation of energy, conservation of angular momentum and the eccentricity vector.

From that equation, it is possible to write the trajectory of motion which turns out to be the equation of a conic section and demonstrate that this solution is consistent with the three laws of Kepler, and actually extends further its application to different non-elliptic conic shapes, namely, parabolic and hyperbolic orbits. The name of the curves called conic sections derives from the fact that they can be obtained as the intersections of a plane with a circular cone.

The six quantities, called classical orbital elements, can be grouped according to their geometrical and physical meaning:

- Two parameters determine the shape of the orbit:
  - e (eccentricity): This parameter defines the shape of the conic orbit. There are three cases depending on the shape of the orbit: $e = 0$ for circular orbits, $0 < e < 1$ for elliptical orbits, $e = 1$ for parabolic orbits and $e > 1$ for hyperbolic orbits.

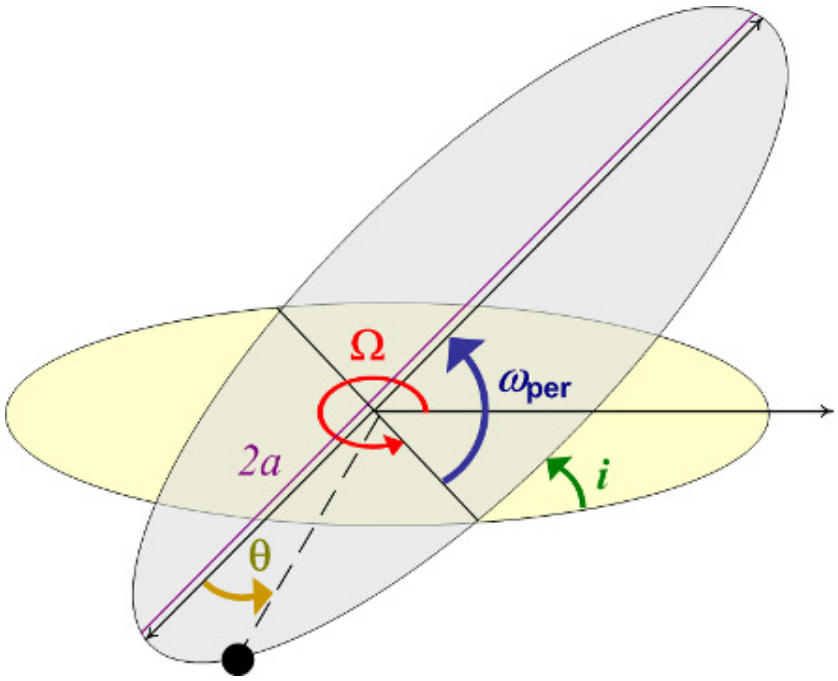

Figure 2.1: **Keplerian Orbit Elements**

  - a (semimajor axis): This parameter describes the size of the elliptical orbit, and is the semi-major axis of the described ellipse. For parabolic orbits, a tends to infinity and has a negative value for hyperbolic orbits. There is a direct relation between the total energy of the orbit and the semi-major axis: $\mathcal{E} = -\mu/2a$.

- Three parameters identify the orientation of the orbit (Euler angles):
  - i (inclination): This parameter defines the angle between the vector normal to the equatorial plane, and the angular momentum vector.
  - Ω (longitude of the ascending node): This is the angle in the equatorial plane, between the reference axis and the point where the satellite crosses the equatorial plane in northerly direction.
  - ω_{per} (argument of periapsis): This is the angle in the plane of the satellite's orbit between the ascending node and the periapsis point, measured in the direction of movement of the satellite.

- The sixth parameter determines the position of the orbiter at a specific time:
  - $t_{\tau 0}$ (time of passage at periapsis): This is the time when the satellite was at periapsis.

The parameter $t_{\tau 0}$ is used to relate a particular time to a particular position. Other parameters can be used for this purpose. This is why, often in the literature, some alternative parameters are used. The most commonly used are θ_0 which is the true anomaly at a given time t_0, or M_0 which is the mean anomaly at a given time t_0. The true anomaly parameter is the angle in the plane of the satellite between the periapsis and the satellite. It can be seen in Fig. 2.1. The mean anomaly is a "scaled" parameter of true anomaly in the sense that the Mean Anomaly evolves at constant rate during a particular period as opposite to the true anomaly that has a non-constant rate. In circular orbits, have the same value and in elliptical orbits, they have the same value at periapsis and apoapsis.

The mean motion is represented with the variable n and measures the average rate of a Keplerian orbit. In the case of a circular orbit n is the constant angular rate in the orbit plane. A Keplerian orbit satisfies the equation:

$$n = \sqrt{\frac{\mu}{a^3}} = \frac{2\pi}{T_O} \tag{2.2}$$

where T_O is the Orbital Period. One of the advantages of using the orbit element approach to model the orbit of a satellite is the lack of need to integrate any differential equation to determine the position of the satellite at a specific time. The position of the satellite can be determined from the mean anomaly,

$$M(t) = M_0 + nt = n(t - t_{\tau 0}) = E_a - e \sin E_a \tag{2.3}$$

where E is the eccentric anomaly and M is the mean anomaly. The conversion between true anomaly θ and mean anomaly parameters is given by

$$\tan \frac{\theta}{2} = \sqrt{\frac{1+e}{1-e}} \cdot \tan \frac{E_a}{2} \tag{2.4}$$

Although the orbital elements are enough to define an orbit, they present singularities. For instance, the longitude of the ascending node is undefined for orbits with zero inclination and the line of apsides is undefined for zero eccentricity (circular orbit). It is possible to formulate differently the orbit elements in order to avoid these singularities. The Equinoctial Lagrange Elements presented in Ref. [40] define six alternative orbital elements to avoid these singularities [41].

An alternative formulation of orbital elements, consist in defining a set of canonical orbital elements. The Delaunay elements are the canonical formulation of the Keplerian

Orbital Elements, and the Poincaré elements are the canonical formulation of the Equinoctial Lagrange Elements. The six Delaunay elements, as found in [42] are expressed as

$$\begin{aligned} l_D &= M \qquad g_D = \omega_{\text{per}} \qquad h_D = \Omega \\ L &= \sqrt{a\mu} \qquad G_D = L\sqrt{1-e^2} \qquad H_D = G\cos i \end{aligned} \tag{2.5}$$

The following identities can be used to relate the true longitude L and mean longitude λ parameters:

$$\begin{aligned} \lambda &= M_D + \omega_{\text{per}} + \Omega \\ L &= \theta + \omega_{\text{per}} + \Omega \end{aligned} \tag{2.6}$$

As stated before, these orbital elements have the property:

$$\begin{aligned} \frac{\mathrm{d}L}{\mathrm{d}t} &= \frac{\partial \mathcal{H}}{\partial l_D} \qquad \frac{\mathrm{d}l_D}{\mathrm{d}t} = -\frac{\partial \mathcal{H}}{\partial L} \qquad \frac{\mathrm{d}G_D}{\mathrm{d}t} = \frac{\partial \mathcal{H}}{\partial g_D} \\ \frac{\mathrm{d}g_D}{\mathrm{d}t} &= -\frac{\partial \mathcal{H}}{\partial G_D} \qquad \frac{\mathrm{d}H_D}{\mathrm{d}t} = \frac{\partial \mathcal{H}}{\partial h_D} \qquad \frac{\mathrm{d}h_D}{\mathrm{d}t} = -\frac{\partial \mathcal{H}}{\partial H_D} \end{aligned} \tag{2.7}$$

where $\mathcal{H}$ is the Hamiltonian as shown in [38] and [43]. The advantage of using canonical elements is that the Lagrange bracket matrix [38] is diagonal.

2.2 Dynamics of Relative Motion

Different alternatives are available to model the problem of formation flight in which there is one or more agents linked through tethers, rotating around the Earth. The two-body approach will be used as a basis to describe the relative equations of motion. On a first approach, the relative motion of two orbiters can be derived by substracting the equation of relative motion of two bodies (or a body and the reference orbit) and thus obtaining the relative dynamics. However, as it will be shown in the sequel, there are other sets of state variables more convenient to model the problem.

2.2.1 Equations of motion relative to a reference orbit

This section presents the derivation of the equations of motion of an orbiting body, expressed in the relative coordinates of a frame attached to a reference orbit. The Euler-Lagrange approach will be used for the derivation. The background behind this approach

is widely explained in mechanics literature [37].

The Euler-Lagrange equations allow one to derive the equations of motion of a mechanical system, based on the expression of its kinetic and potential energy only, if the system is conservative and all constraints are holonomic. Kinetic and potential energy energy must be defined as a function of the so called generalized coordinates. Generalized coordinates is the set of variables that define uniquely the configuration of a system. Generalized velocities are the time derivative of generalized coordinates. Although it is preferable that generalized coordinates are independent, this is not mandatory, but when this happens, the number of generalized coordinates equals that of system degrees of freedom. Euler-Lagrange equations for a conservative system with holonomic constraints and n degrees of freedom are written in the form:

$$\frac{\mathrm{d}}{\mathrm{d}t}\left(\frac{\partial \mathcal{T}}{\partial \dot{q}_j}\right) - \frac{\partial \mathcal{T}}{\partial q_j} + \frac{\partial \mathcal{V}}{\partial q_j} = 0 \tag{2.8}$$

where q_j are generalized coordinates $j = 1, ..., n$. Variable $\mathcal{T}$ is the total kinetical energy of the system and $\mathcal{V}$ its total potential energy. The advantage of this approach over other methods is that the choice of the generalized coordinates is arbitrary. In some problems, writing the equations of motion based on variables having special geometric properties can be much simpler than using, for instance, Cartesian coordinates and/or lead to simpler expressions for the equations of motion. Moreover, for a system with ideal holonomic constraints, writing the equations of motion by means of Euler-Lagrange equations does not require to express explicitly constraint forces.

In the applications considered in the present thesis, the orbital kinetic energy $\mathcal{T}$ is calculated as the sum of kinetic energies of the parent bodies plus that of the agents. The orbital potential energy $\mathcal{V}$ is the sum of the potential energies of the parent body plus that of the agents.

Appropriate extensions of Eq. (2.8) exist for systems affected by non-conservative forces (e.g. the Raleigh dissipation function can be used as a measure of the power dissipated by non-conservative forces), or system with non-holonomic constraints or described by a set of non-independent generalized coordinates (use of Lagrange multipliers). A detailed derivation can be found in [37].

When analyzing formation flight problems, it is often convenient to describe the position of the deputies with respect to the parent body, or with respect to a predefined reference orbit. For this reason it is convenient to describe the motion of the deputy with respect to a non-inertial reference system centered in the parent body or the reference orbit, and not the Earth.

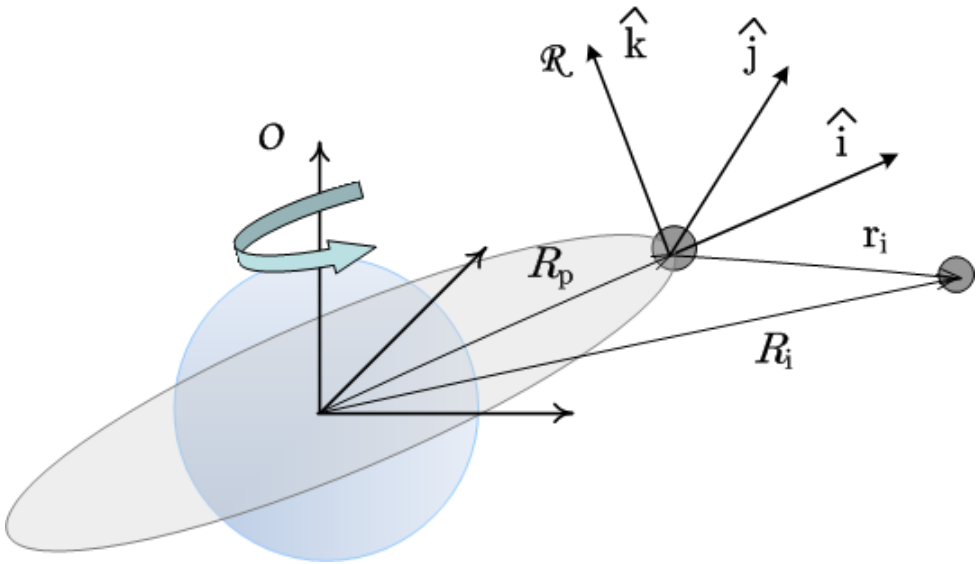

Figure 2.2: **Reference frames $\mathcal{O}$ and $\mathcal{R}$**

This approach is based on two reference systems. The inertial reference system (fixed frame) $\mathcal{O} : \{\hat{\mathbf{I}}, \hat{\mathbf{J}}, \hat{\mathbf{K}}\}$ is Earth-centered with $\hat{\mathbf{K}}$ pointing along the Earth's spin axis, whereas $\hat{\mathbf{I}}$ and $\hat{\mathbf{J}}$ lie on the equatorial plane. The $\hat{\mathbf{I}}$ unit vector lies at the intersection of the (inertially fixed) equatorial and ecliptic planes and $\hat{\mathbf{J}}$ completes a right-handed triad. The rotating or orbital reference frame, also known as Local Vertical Local Horizontal (LVLH) is $\mathcal{R} : \{\hat{\mathbf{i}}_\mathcal{R}, \hat{\mathbf{j}}_\mathcal{R}, \hat{\mathbf{k}}_\mathcal{R}\}$. In this frame, the $\hat{\mathbf{i}}_\mathcal{R}$ axis points outwards in the radial direction from the center of the Earth to the parent body, the $\hat{\mathbf{k}}_\mathcal{R}$ axis is perpendicular to the orbital plane along the angular momentum vector and the $\hat{\mathbf{j}}_\mathcal{R}$ axis completes a right-handed orthogonal triad. When the orbit is circular, $\hat{\mathbf{j}}_\mathcal{R}$ is tangent to the direction of movement. The origin of the LVLH frame coincides with the parent body position following a prescribed reference orbit. In the absence of parent body, the center of the local reference frame is that of the reference orbit.

The expression of the kinetic and potential energy ($\mathcal{T}$ and $\mathcal{V}$ respectively) depends on the orbital parameters of the reference orbit and the position of the agent within the

LVLH frame, that is:

$$\begin{aligned}\mathcal{T} &= \frac{1}{2}\sum_{i=1}^{N+1} m_i(\dot{\boldsymbol{R}}_{\text{ref}}\cdot\dot{\boldsymbol{R}}_{\text{ref}}) + \dot{\boldsymbol{R}}_{\text{ref}}\cdot\sum_{i=1}^{N} m_i(\boldsymbol{v}_i) + \frac{1}{2}\sum_{i=1}^{N} m_i(\boldsymbol{v}_i\cdot\boldsymbol{v}_i)\\ &= \mathcal{T}_{\text{orb}} + \dot{\boldsymbol{R}}_{\text{ref}}\cdot\sum_{i=1}^{N} m_i(\boldsymbol{v}_i) + \frac{1}{2}\sum_{i=1}^{N} m_i(\boldsymbol{v}_i\cdot\boldsymbol{v}_i)\end{aligned} \tag{2.9}$$

and

$$\begin{aligned}\mathcal{V} &= -\mu\sum_{i=1}^{N+1}\frac{m_i}{R_{\text{ref}}} - \frac{\mu}{R_{\text{ref}}^2}\sum_{i=1}^{N} m_i(\hat{\mathbf{i}}_{\mathcal{R}}\cdot\boldsymbol{r}_i) + \frac{\mu}{2R_{\text{ref}}^3}\sum_{i=1}^{N} m_i(\boldsymbol{r}_i\cdot\boldsymbol{r}_i - 3(\hat{\mathbf{i}}_{\mathcal{R}}\cdot\boldsymbol{r}_i)^2)\\ &= \mathcal{V}_{\text{orb}} - \frac{\mu}{R_{\text{ref}}^2}\sum_{i=1}^{N} m_i(\hat{\mathbf{i}}_{\mathcal{R}}\cdot\boldsymbol{r}_i) + \frac{\mu}{2R_{\text{ref}}^3}\sum_{i=1}^{N} m_i(\boldsymbol{r}_i\cdot\boldsymbol{r}_i - 3(\hat{\mathbf{i}}_{\mathcal{R}}\cdot\boldsymbol{r}_i)^2)\end{aligned} \tag{2.10}$$

where the orbital components are grouped in terms $\mathcal{T}_{\text{orb}}$ and $\mathcal{V}_{\text{orb}}$. Vectors $\boldsymbol{r}_i$ and $\boldsymbol{v}_i$ describe the position and velocity of deputy i in the LVLH frame. In these equations N defines the total number of deputies, such that $N+1$ is the total number of agents, including the parent body. The following two sections describe how to derive the equations of motion, taking into account two sets of generalized coordinates. In the first case, a set of cartesian coordinates is used, whereas in the second case it is a set of polar coordinates. The use of this approach requires writing the kinetic and potential energies in terms of the chosen generalized coordinates.

Cartesian coordinates

When the position of the deputies with respect to the parent body is described in the LVLH frame, the most obvious choice for this is to use $\{q_1, q_2, q_3, ..., q_n\} = \{x_j, y_j, z_j, ..., z_N\}$ with $n = 3N$, in the absence of constraints on the position of the N mass elements.

Assuming that the parent body (leader) follows a prescribed reference orbit $\boldsymbol{R}_p = \boldsymbol{R}_{\text{ref}}$, and letting $\boldsymbol{R}_d = \boldsymbol{R}_i$ be the absolute position of a deputy (chaser) in the LVLH frame, these position vectors are expressed in $\mathcal{R}$ as:

$$\begin{aligned}\boldsymbol{R}_p &= R_{\text{ref}}\cdot\hat{\mathbf{i}}\\ \boldsymbol{R}_d &= \boldsymbol{R}_p + \boldsymbol{r}_d = (R_{\text{ref}} + x_d)\cdot\hat{\mathbf{i}}_{\mathcal{R}} + y_d\cdot\hat{\mathbf{j}}_{\mathcal{R}} + z_d\cdot\hat{\mathbf{k}}_{\mathcal{R}}\end{aligned} \tag{2.11}$$

Assuming $\omega_{\mathcal{R}/\mathcal{O}} = \dot{\theta} \cdot \hat{\mathbf{K}}$, the velocities of the leader and the follower(s) are given by:

$$\begin{aligned} \dot{\boldsymbol{R}}_p &= \dot{\boldsymbol{R}}_p|_{\mathcal{R}} + \omega_{\mathcal{R}/\mathcal{O}} \times \boldsymbol{R}_p = \dot{R}_{\text{ref}} \cdot \hat{\mathbf{i}}_{\mathcal{R}} + \dot{\theta} R_{\text{ref}} \cdot \hat{\mathbf{j}}_{\mathcal{R}} \\ \dot{\boldsymbol{R}}_d &= \dot{\boldsymbol{R}}_p + \boldsymbol{v}_d \\ \boldsymbol{v}_d &= \dot{\boldsymbol{r}}_d|_{\mathcal{R}} + \omega_{\mathcal{R}/\mathcal{O}} \times \boldsymbol{r}_d = (\dot{x}_d + \dot{\theta} y_d) \cdot \hat{\mathbf{i}}_{\mathcal{R}} + (\dot{y}_d + \dot{\theta} x_d) \cdot \hat{\mathbf{j}}_{\mathcal{R}} + \dot{z}_d \cdot \hat{\mathbf{k}}_{\mathcal{R}} \end{aligned} \tag{2.12}$$

where $\dot{\theta}$ is the angular rate of the orbiting body, or true anomaly rate. After substituting expressions (2.11) and (2.12) in (2.9) and (2.10) with $\boldsymbol{R}_{\text{ref}} = \boldsymbol{R}_p$, $\boldsymbol{r}_i = \boldsymbol{r}_d$ and $\boldsymbol{v}_i = \boldsymbol{v}_d$, the equations of motion for a particular deputy body d are obtained. Eliminating the subscript d for convenience, the equations of motion for a deputy body, are

$$\begin{aligned} \ddot{x} - 2\dot{\theta}(\dot{y} - y(\dot{R}_{\text{ref}}/R_{\text{ref}})) - x\dot{\theta}^2 &= -\mu(R_{\text{ref}} + x)/R_{\text{ref}}^3 \\ \ddot{y} + 2\dot{\theta}(\dot{x} - x(\dot{R}_{\text{ref}}/R_{\text{ref}})) - y\dot{\theta}^2 &= -\mu y/R_{\text{ref}}^3 \\ \ddot{z} &= -\mu z/R_{\text{ref}}^3 \end{aligned} \tag{2.13}$$

Circular reference orbit

In order to simplify the model, some assumptions can be taken in addition to those associated to Eq. (2.1). When

- $R_{\text{ref}} >> \| \boldsymbol{r}_i \|$
- The parent body of the formation follows a circular orbit, which implies R_{ref} is constant and the eccentricity is zero, $e = 0$.

the so-called *Hill-Clohessy-Wiltshire* (HCW) equations are derived [44]:

$$\begin{aligned} \ddot{x} - 2n\dot{y} - 3n^2 x &= 0 \\ \ddot{y} + 2n\dot{x} &= 0 \\ \ddot{z} + n^2 z &= 0 \end{aligned} \tag{2.14}$$

where, for a circular reference orbit, the true anomaly rate $\dot{\theta}$ is replaced by the constant mean orbital rate n. Notice that the $\hat{\mathbf{k}}_{\mathcal{R}}$ component of the motion is decoupled from displacements in the $\hat{\mathbf{i}}_{\mathcal{R}} - \hat{\mathbf{j}}_{\mathcal{R}}$ plane. When incorporating the presence of external forces,

HCW equations achieve the form:

$$\begin{aligned} \ddot{x} - 2n\dot{y} - 3n^2 x &= f_x/m_i \\ \ddot{y} + 2n\dot{x} &= f_y/m_i \\ \ddot{z} + n^2 z &= f_z/m_i \end{aligned} \tag{2.15}$$

In the absence of external forces, an analytical solution to (2.15) can be found:

$$\begin{aligned} x(t) &= A_0 \cos(nt + k_a) + x_{\mathrm{k0}} \\ y(t) &= -2A_0 \sin(nt + k_a) + y_{\mathrm{k0}} - (3/2)ntx_{\mathrm{k0}} \\ z(t) &= B_0 \cos(nt + k_b) \end{aligned} \tag{2.16}$$

where k_a, k_b, A_0, B_0, x_{k0} and y_{k0} are integration constants. The solution shows a secular term in the second equation. In order to eliminate secular drift, it can be easily shown that x_{k0} must be zero, and therefore the following initial condition must satisfied $\dot{y}_0 = -2nx_0$. Otherwise, the relative orbit will not be bounded and the deputy drifts away from the center of the frame. References [17] and [45] study the effect of incorporating eccentric orbits using the HCW approach.

Elliptical reference orbit

Equation (2.13) is valid for a generic Keplerian orbit. For a Keplerian elliptical orbit, the following equations hold [38]:

$$R = \frac{a(1-e^2)}{\xi} \qquad \dot{\theta} = \xi^2 \sqrt{\frac{\mu}{a^3(1-e^2)^3}} \qquad \xi = (1 + e\cos\theta) \tag{2.17}$$

After linearizing the gravitational term as in [17] and defining the equations of motion in terms of e and θ, the equations of relative motion in R achieve the following form:

$$\begin{aligned} \ddot{x} - 2\dot{\theta}\dot{y} - \dot{\theta}^2 x - \ddot{\theta}y + 2n^2(\xi/(1-e^2))^3 x &= f_x/m_i \\ \ddot{y} + 2\dot{\theta}\dot{x} - \dot{\theta}^2 y + \ddot{\theta}x + n^2(\xi/(1-e^2))^3 y &= f_y/m_i \\ \ddot{z} + n^2 z &= f_z/m_i \end{aligned} \tag{2.18}$$

This equation provides a valid alternative to describe the linearized relative motion with respect to an elliptical reference orbit. Lawden derived a model and obtained an analytical solution for the relative motion in the absence of external forces [46] using

Eq. (2.18), taking true anomaly as independent variable. Unfortunately, the analytical solution derived by Lawden includes an integral which presents singularities for certain values of the eccentric anomaly. Tschauner and Hempel derived a similar set of equations of motion for relative motion with respect to an elliptical orbit, scaling state variables with respect to the radius of the parent body [47]. A significant contribution was provided by Carter [48], who refined Lawden's solution by providing an alternative integral, which is not affected by the above mentioned singularities. A historical perspective on the derivation of this model can be found in Ref. [49].

Reference [50] derives a third-order expression, for both in-plane and out-of-plane dynamics of the solutions of the elliptic HCW non-linear equations. The solutions are in powers of two amplitudes but exact in eccentricity (i.e. accuracy is good also for high eccentricities).

Reference [17] provides a technique for evaluating initial conditions for the elements of the cluster such that deputies do not present secular motion, and the necessary conditions that provide periodic solutions, with deputies returning back to the initial states at the end of each orbit.

Polar coordinates

One of the advantages of using the Lagrangian approach is the freedom of choosing the set of generalized coordinates that better suits each particular problem. The geometry of the system in some cases can make some choice preferable to another. This section focus on the derivation of equations of motion using polar coordinates.

The choice of variables is based on the formation orientations presented in Ref. [13]. The cluster orientations used in this reference are known as In-plane and Earth-facing. Depending on the cluster configuration a different pair of polar coordinates is chosen to represent the motion.

For the In-plane configuration, deputies are nominally in the orbit plane. The orbital plane is defined by axes $\hat{\mathbf{i}}_{\mathcal{R}}$ and $\hat{\mathbf{j}}_{\mathcal{R}}$ of the LVLH reference frame. For this reason, variables l, α and β are used to represent the position as indicated in Fig. 2.3(a), where l defines the distance to the parent body, variable β is used to monitor the out-of-plane elevation from the nominal plane (roll motion), and α will express the in-plane angular

motion of the deputy around the parent body (pitch motion) contained in the orbital plane.

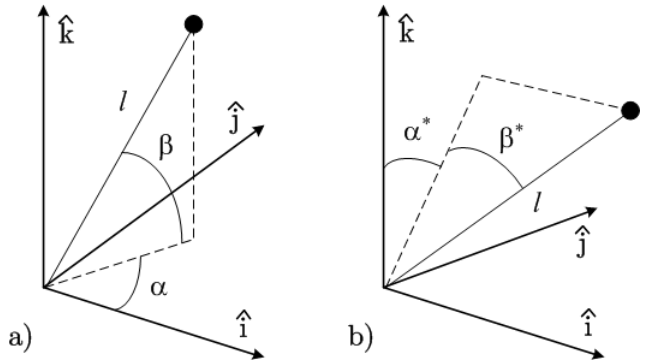

Figure 2.3: **Polar coordinates in LVLH reference: in-plane (a) and Earth-facing (b) cases**

In the Earth-facing configuration, deputies are intended to lie in the plane defined by $\hat{\mathbf{j}}_{\mathcal{R}}$ and $\hat{\mathbf{k}}_{\mathcal{R}}$. Following the same criteria as before, variable l defines the distance to the parent body, variable α^* express the in-plane angular motion contained within the normal plane facing the Earth, and β^* is used to represent the out-of-plane motion with respect to the normal plane facing the Earth as indicated in Fig. 2.3(b).

$$\boldsymbol{r}_i = (l_i \cos\alpha \cos\beta)\hat{\mathbf{i}}_{\mathcal{R}} + (l_i \sin\alpha \cos\beta)\hat{\mathbf{j}}_{\mathcal{R}} + (l_i \sin\beta)\hat{\mathbf{k}}_{\mathcal{R}} \tag{2.19}$$

$$\boldsymbol{r}_i = (l_i \sin\beta^*)\hat{\mathbf{i}}_{\mathcal{R}} + (l_i \sin\alpha^* \cos\beta^*)\hat{\mathbf{j}}_{\mathcal{R}} + (l_i \cos\alpha^* \cos\beta^*)\hat{\mathbf{k}}_{\mathcal{R}} \tag{2.20}$$

For the In-plane case, the relative position vector of the i-th deputy is expressed in terms of l, α and β variables in the form of Eq. (2.19), whereas for the Earth-facing case one gets Eq. (2.20) in terms of l, α^* and β^*. The derivation of the equations of relative motion in terms of the cited variables then follows the procedure used for writing the equations in the Cartesian frame.

In Ref. [13] this is done for different cluster structures. The potential energy due to elasticity and the generalized damping force, depend of the geometry of the links defining the cluster. For this reason it is necessary to perform a complete new derivation of the equations of motion for every formation geometry.

2.2.2 Relative equations of Motion based on Orbit Elements

The orbit elements allow to define the orbit of a single orbiter. For the flight formation problem, it is necessary to define the relative position from a deputy body with respect to a parent body orbiting the Earth. For this reason, it is convenient to define the relative motion of two satellites through the relative orbit element vector:

$$\tilde{\boldsymbol{X}} = \boldsymbol{X}^d - \boldsymbol{X} = (\delta a, \delta e, \delta i, \delta\Omega, \delta\omega_{\text{per}}, \delta\theta) \tag{2.21}$$

The choice of the six orbit elements is not constrained to these shown in Eq. (2.21). As stated before, the derivation of all the $\tilde{\boldsymbol{X}}$ variables does not require the integration of any equation of motion. A further advantage provided by using the formulation in orbit element differences is that in some cases it is possible to have a notion of the relative dynamics directly from the values. For instance, through the difference values of δi and $\delta\Omega$ it is possible to have an idea about the relative out-of plane motion between deputy and chaser.

In the absence of relative drift, vector $\tilde{\boldsymbol{X}}$ should be constant. However, due to external influences such as external perturbations it may be possible that a secular drift is presented between orbiter and chaser, and therefore $\dot{\tilde{\boldsymbol{X}}} \neq 0$. Reference [51] estimates the evolution of the relative motion between deputy and chaser due to different orbital energies, due to atmospheric drag and due the J_2 perturbation.

Reference [52] uses the relative orbit element formulation to define a control law with the purpose of reestablishing a J_2 invariant orbit for a deputy-chief pair. This reference takes into account the results found in [53] where conditions are defined to remove the secular drift between two orbiters. Reference [54] defines a strategy for satellite relative orbital design using least squares methods.

It is possible to define a mapping between the difference among parent and deputy expressed in terms of orbit elements variables and the coordinates in the HCW frame [55], [56]. Reference [57] derives in detail the expression taking into account different

hypotheses. The mapping, assuming chief orbits with small eccentricity is as follows:

$$\begin{aligned} x(\theta) &\approx (1 - e\cos\theta)\delta a + (ae\sin\theta/\sqrt{1-e^2})\delta M - a\cos\theta\delta e \\ y(\theta) &\approx (a/\sqrt{1-e^2})(1 + e\cos\theta)\delta M + a(1 - e\cos\theta)\delta\omega_{\text{per}} \\ &+ a\sin\theta(2 - e\cos\theta)\delta e + a(1 - e\cos\theta)\cos i\delta\Omega \\ z(\theta) &\approx a(1 - e\cos\theta)(\sin\theta\delta i - \cos\theta\sin i\delta\Omega) \end{aligned} \tag{2.22}$$

The mapping is written using the true anomaly θ as independent variable. Using Kepler's equations it is possible to relate θ and time. Reference [58] proposes a positioning hybrid control law that takes into account both the orbit element representation, and the mapping to the Cartesian coordinates shown in Eq. (2.22).

2.2.3 Comparison of orbital models

The main advantage of the Lagrangian approach, using Cartesian coordinates as generalized coordinates, is that the representation of position in the LVLH is straightforward. This property is specially interesting when using elastic tethers when one needs to compute distances to determine elongations. The use of polar coordinates is convenient only for clusters where tethers have a radial geometry with respect to the parent body. In this particular case, defining l_j as a generalized coordinate is very convenient, but in the case of tethers connecting external deputies, the calculation of distances is less straightforward than when using Cartesian coordinates.

One of the most interesting features of using orbital elements to represent the position of an orbiting body is that it is possible to determine its position using algebraic equations only, without the need of integrating differential equations as it is the case in the HCW approach. On the other hand, when incorporating additional forces, like those of spring-dampers or those arising from perturbations, this property vanishes and one still needs to integrate a set of six differential equations as it happens in the HCW case. As it will be explained later, it is possible to use the orbital elements formulation and still define external accelerations in the LVLH frame which is a convenient property. However, the set of differential equations is non-linear as opposite to the linearization used in the HCW case.

2.3 Effects of Orbit Perturbations

As introduced before, Eq. (2.1) does not include effects like the gravity attraction from the Moon or the Sun. It does not include neither solar radiation pressure nor tidal effects. They will be incorporated within the model by defining external perturbations to the motion from the ideal Kepler solution. Table 2.1, taken from [59], presents a list of the most important perturbations affecting a satellite orbiting a Low Earth Orbit, along with an order of magnitude showing their relevance. Earth's gravitational field provides a term of comparison for all the perturbing accelerations. Note that many perturbing terms strongly depend on the orbit and can achieve different importance in different operating conditions, e.g. atmospheric fiction, which is moderate in LEO below 300 km, becomes totally negligible above 500 km of altitude.

Table 2.1: Perturbative accelerations acting on a LEO orbit

Conservative Force	**Acceleration (m/s^2)**
Earth's gravitational field	≈ 10
Earth's oblateness (J2)	$\approx 10^{-2}$
Earth's oblateness (J4)	$\approx 10^{-4}$
Lunar attraction	$\approx 10^{-6}$
Solar attraction	$\approx 10^{-7}$
Planetary attraction	$\approx 10^{-10}$
Tidal Effects	$\approx 10^{-6}$
Relativisitic effects	$\approx 10^{-8}$
Non-Conservative Force	**Acceleration (m/s^2)**
Atmospheric friction	$\approx 10^{-4}$
Solar radiation pressure	$\approx 10^{-7}$
Albedo effect	$\approx 10^{-8}$

Chapter 4 studies the effect of the J_2 perturbation on tethered clusters orbiting in LEO. This is the most significative perturbation in this scenario as shown in Tab. 2.1. The next highest perturbation is atmospheric drag, which is two orders of magnitude smaller. In addition to the fact that is smaller, it is also worth to remark that for Earth-facing clusters the effect on the relative position of the agents should not be noticeable due to the fact that all agents lie approximately at the same altitude. For in-plane clusters, the length of the tethers is small compared with the altitude, and due to the spinning configuration, all cluster members experience the same drag profile on each rotation of the formation. For these reasons it is expected that the effect of atmospheric drag on the relative position of

the agents of the cluster is negligible.

The equations of motion assuming a perturbation causing an acceleration $\boldsymbol{a}_{\text{dist}}$ achieve the form:

$$\ddot{\boldsymbol{R}} = \frac{\mu}{R^2}\frac{\boldsymbol{R}}{|\boldsymbol{R}|} + \boldsymbol{a}_{\text{dist}} \tag{2.23}$$

Reference [55] describes in detail Cowell and Encke's methods to calculate the orbit of a body under perturbation effects. Both methods introduce the concept of osculating orbit and reference orbit. A perturbation acting on an orbiting body affects its position, therefore altering the original keplerian orbital parameters. The osculating orbit is the orbit that at each instant has the orbit parameters determined from the current values of position and velocity vectors.

According to Encke's method, the perturbed orbit is calculated as the sum of the unperturbed orbit trajectory (calculated using the two-body Kepler solution) and the deviation from the reference orbit due to perturbations. This method proposes a way to estimate the deviation with respect to the unperturbed orbit, and therefore allowing to calculate the position of an orbiter as the sum of the deviation plus the nominal unperturbed orbit. This method was used when computing power was limited, and approximative techniques had to be used for orbit computation.

According to Cowell's method, the perturbed orbit is calculated integrating directly Eq. (2.23), that is, the nominal Keplerian model plus the sum of perturbation accelerations.

2.3.1 Perturbations in Equations of Motion

Perturbations in Orbit Element Approach

Some perturbations are conservative, and therefore can be expressed as a disturbance potential that depends only on the distance R. The acceleration $\boldsymbol{a}_{\text{dist}}$ is created as the result of a disturbance potential $\mathcal{V}_R(R)$, where:

$$\boldsymbol{a}_{\text{dist}} = \nabla\mathcal{V}_R(R) \tag{2.24}$$

As reported in [38], is it possible to obtain the variation in the orbit elements as a

function of this potential. This leads to the Lagrange Planetary Equations (LPE):

$$\begin{aligned}
\frac{\mathrm{d}\Omega}{\mathrm{d}t} &= \frac{1}{nab\sin i}\frac{\partial \mathcal{V}_R}{\partial i} \\
\frac{\mathrm{d}i}{\mathrm{d}t} &= -\frac{1}{nab\sin i}\frac{\partial \mathcal{V}_R}{\partial \Omega} + \frac{\cos i}{nab\sin i}\frac{\partial \mathcal{V}_R}{\partial \omega_{\mathrm{per}}} \\
\frac{\mathrm{d}\omega_{\mathrm{per}}}{\mathrm{d}t} &= -\frac{\cos i}{nab\sin i}\frac{\partial \mathcal{V}_R}{\partial i} + \frac{b}{na^3 e}\frac{\partial R}{\partial e} \\
\frac{\mathrm{d}a}{\mathrm{d}t} &= \frac{2}{na}\frac{\partial \mathcal{V}_R}{\partial M_0} \\
\frac{\mathrm{d}e}{\mathrm{d}t} &= -\frac{b}{nea^3}\frac{\partial \mathcal{V}_R}{\partial \omega_{\mathrm{per}}} + \frac{b^2}{nea^4}\frac{\partial \mathcal{V}_R}{\partial M_0} \\
\frac{\mathrm{d}M_0}{\mathrm{d}t} &= -\frac{2}{na}\frac{\partial \mathcal{V}_R}{a} - \frac{b^2}{nea^4}\frac{\partial \mathcal{V}_R}{\partial e}
\end{aligned} \tag{2.25}$$

One of the advantages of using a canonical representation for orbital elements is that the Lagrange matrix is diagonal. The derivation using the Lagrange brackets, however requires that the disturbance can be expressed in the form of a potential, and therefore not admiting disturbances caused by non-conservative forces. In [39] it is shown that this restriction is indeed not necessary, and that it is possible to express the variational equations in a form known as the Gauss Planetary Equations (GPE) which include a general acceleration expressed in the orbital frame coordinates. The definition of the GPE equations in the LVLH frame coordinates leads to the following set of 6 first order differential equations:

$$\begin{aligned}
\frac{\mathrm{d}a}{\mathrm{d}t} &= \frac{2a^2}{h}e\sin\theta a_{\hat{\mathbf{i}}_{\mathcal{R}}} + \frac{p}{R}a_{\hat{\mathbf{j}}_{\mathcal{R}}} \\
\frac{\mathrm{d}e}{\mathrm{d}t} &= \frac{1}{h}(p\sin\theta a_{\hat{\mathbf{i}}_{\mathcal{R}}} + ((p+R)\cos\theta + R\cdot e)a_{\hat{\mathbf{j}}_{\mathcal{R}}}) \\
\frac{\mathrm{d}i}{\mathrm{d}t} &= \frac{r\cos\theta}{h}a_{\hat{\mathbf{k}}_{\mathcal{R}}} \\
\frac{\mathrm{d}\Omega}{\mathrm{d}t} &= \frac{R\sin\theta}{h\sin i}a_{\hat{\mathbf{k}}_{\mathcal{R}}} \\
\frac{\mathrm{d}\omega_{\mathrm{per}}}{\mathrm{d}t} &= -\frac{1}{he}\cos\theta p a_{\hat{\mathbf{i}}_{\mathcal{R}}} + \frac{1}{he}(p+R)\sin\theta a_{\hat{\mathbf{j}}_{\mathcal{R}}} - \frac{R\sin\theta\cos i}{h\sin i}a_{\hat{\mathbf{k}}_{\mathcal{R}}} \\
\frac{\mathrm{d}M}{\mathrm{d}t} &= n + \frac{b}{ahe}(p\cos\theta - 2R\cdot e)a_{\hat{\mathbf{i}}_{\mathcal{R}}} - (p+R)\sin\theta a_{\hat{\mathbf{j}}_{\mathcal{R}}}
\end{aligned} \tag{2.26}$$

where $p = a(1-e^2)$, the modulus of angular momentum is $h = \sqrt{\mu p}$, and R is the distance of the body to the center of the Earth. In this expression, $a_{\hat{\mathbf{i}}_{\mathcal{R}}}$, $a_{\hat{\mathbf{j}}_{\mathcal{R}}}$, $a_{\hat{\mathbf{k}}_{\mathcal{R}}}$ are the accelerations expressed in the local LVLH frame. This representation is convenient since tether forces are easily expressed in a Cartesian coordinate system, and the generic

expression of the acceleration allows incorporating non-conservative forces such as the damping force present in tethers.

Perturbations in the HCW approach

The inclusion of external forces (including perturbations), in the model of relative motion is straightforward as it can be seen in Eq. (2.15). Forces due to a perturbation acting on satellite are directly expressed in terms of components in the LVLH frame on the RHS of the same equation.

2.3.2 Implementation of the J_2 Perturbation

The Earth's gravitational potential $\mathcal{V}_E$, is often represented using spherical harmonics that model the irregularities in the Earth's shape [38]. The potential function $\mathcal{V}_E$ is composed as the sum of terms that describe zonal, sectorial and tesseral spherical harmonics that fit an accurate representation of the gravitational potential. The J_2 harmonic is the lowest-order zonal harmonic Earth's oblateness. It accounts for Earth's bulge around the equator. It's magnitude is by far the most relevant. For this reason, the effect of the so-called J_2 perturbation on tethered formations is analyzed in this study.

In order to simulate the effects of J_2 potential over a cluster of satellites various approaches are available. The first option is to define a model based on Keplerian orbit elements as state variables. In this nonlinear model, the effect of J_2 perturbation can be incorporated as shown in Ref. [38]. The presence of elastic forces due to tether tension between pairs of agents can be included in the model in the form of external forces acting on each agent of the formation, where the tension depends on the distance between the agents connected by the considered tether.

J_2 perturbation in Orbit Element approach

According to [60], the perturbation function $\mathcal{V}_R(R)$ due to the J_2 acceleration is:

$$\mathcal{V}_R = -\frac{J_2}{2}\frac{\mu}{R}\left(\frac{R_e}{R}\right)^2 (3\sin^2\theta \sin^2 i - 1) \tag{2.27}$$

The acceleration component obtained from the gradient of $\mathcal{V}_R$, projected in the LVLH

frame, are given by

$$\begin{aligned} a_{\hat{\mathbf{i}}_{\mathcal{R}}} &= -\frac{3}{2}\frac{\mu J_2 R_e^2}{R^4}\left(1 - 3/2\sin^2 i \cdot (1 - \cos 2\theta)\right) \\ a_{\hat{\mathbf{j}}_{\mathcal{R}}} &= -\frac{3}{2}\frac{\mu J_2 R_e^2}{R^4}\sin^2 i \sin 2\theta \\ a_{\hat{\mathbf{k}}_{\mathcal{R}}} &= -\frac{3}{2}\frac{\mu J_2 R_e^2}{R^4}\sin i \cos i \sin \theta \end{aligned} \tag{2.28}$$

From these equations it can be clearly seen that for a given longitude, the perturbation function vanishes at Earth's poles, and reaches its maximum at the equator.

In order to take into account the J_2 perturbation, Eqs. (2.27) and (2.28) and can be substituted into Eqs. (2.25) and (2.26). It can be shown that the J_2 perturbation does not introduce any secular drift for orbit elements a, e and i. For the purpose of formation control, in order to ensure that the perturbation affects the formation orbiters in the same way, Ref. [53] defines the conditions necessary to avoid secular drift between agents under the action of the J_2 perturbation.

Based on the cited article, Ref. [61] studies the problems associated to near-circular and near-polar orbits of the parent body. Reference [51] by one of the same authors, explores further the incorporation of secular drifts in the formation due to unequal orbit energies and atmospheric drag.

References [62] and [63] evaluates the effect of the J_2 perturbation through a state-transition-matrix. Reference [64] compares different motion models taking into account the J_2 perturbation.

J_2 perturbation in HCW equations

Reference [16] presents the derivation of the linearized equations of motion of an orbiting satellite, under the influence of the J_2 potential, with respect to a reference orbit. This paper analyzes the effect due to the J_2 perturbation for each one of the LVLH axes and derives a set of equations of motion in the LVLH frame. To do this, first one needs to incorporate the effect of the perturbation on the orbiting body acceleration, and then modify the reference orbit accordingly in order to avoid a secular drift between the orbiter and the reference orbit.

The equations of motion are:

$$\ddot{\boldsymbol{r}} + 2\boldsymbol{\omega} \times \dot{\boldsymbol{r}} + \dot{\boldsymbol{\omega}} \times \boldsymbol{r} + \boldsymbol{\omega} \times (\boldsymbol{\omega} \times \boldsymbol{r}) = \ddot{\boldsymbol{R}} - \ddot{\boldsymbol{R}}_{\text{ref}} \tag{2.29}$$

The relative position of the satellite with respect to the reference orbit in the LVLH frame is denoted by $\boldsymbol{r} = \boldsymbol{R} - \boldsymbol{R}_{\text{ref}}$, where $\boldsymbol{R}$ is the position vector of the satellite and $\boldsymbol{R}_{\text{ref}}$ that of the reference orbit. The acceleration for a deputy is:

$$\ddot{\boldsymbol{R}} = g(\boldsymbol{R}_{\text{ref}}) + \nabla g(\boldsymbol{R}_{\text{ref}})\boldsymbol{r} + J_2(\boldsymbol{R}_{\text{ref}}) + \nabla J_2(\boldsymbol{R}_{\text{ref}})\boldsymbol{r} \tag{2.30}$$

This equation is a differential equation with time varying coefficients, because the expression of $\nabla J_2(\boldsymbol{R}_{\text{ref}})$ is a function of latitude. In order to obtain an autonomous (i.e. time-invariant) set of equations, an approximation with constant coefficients is derived, using the average of $\nabla J_2(\mathbf{R}_{\text{ref}})$, over one period, equal to

$$\begin{aligned} \frac{1}{2\pi}\int_0^{2\pi} \nabla J_2(\boldsymbol{R}_{\text{ref}})d\theta &= \frac{\mu}{R_{\text{ref}}^3} + \begin{bmatrix} 4s_J & 0 & 0 \\ 0 & -s_J & 0 \\ 0 & 0 & -3s_J \end{bmatrix} \\ \text{with} \qquad s_J &= (3J_2R_e^2/8R_{\text{ref}}^2)(1+3\cos 2i) \end{aligned} \tag{2.31}$$

instead of its exact value. The modified set of equations poses two problems. On one side, the perturbation terms J_2 and $\nabla J_2(\boldsymbol{R}_{\text{ref}})$ that affect satellite relative position are computed over the reference orbit, $\boldsymbol{R}_{\text{ref}}$, which is also subject to the effects of the J_2 perturbation. This fact needs to be accounted for to prevent the error between the effective orbit and the reference one to grow up unboundedly, thus leaving the small perturbation range necessary for linearization.

The reference orbit $\ddot{\boldsymbol{R}}_{\text{ref}}$ should be redefined in such a way that no secular drift is produced between the orbiting body and the reference orbit. The analysis of the motion within the LVLH frame is as follows:

- For the radial direction, no drift is expected considering that no secular drift is produced on orbit semi-major axis, a, and eccentricity, e [51]. Therefore, taking the time average of the J_2 potential gradient doesn't lead to any secular loss of the accuracy in the predicted motion.

- Changes in the tangential direction due to the J_2 perturbation can be caused by

changes eccentricity or orbital period. Since the first case is not possible, it is sufficient to choose an orbital period for the satellite equal to that of the reference orbit. To avoid secular drift, the initial condition of the satellite will have to be calculated specifically, as it will be shown in the sequel.

- The dynamics in the cross-track direction is more complicated, due to the secular change in the longitude of the ascending node caused by the J_2 perturbation. These dynamics require both a correction of the reference orbit to compensate for the nodal drift and a redefinition of the cross-track dynamics.

After correcting the reference orbit period, and its nodal drift, the acceleration of the corrected reference orbit is calculated as:

$$\ddot{\boldsymbol{R}}_{\text{ref}} = g(\boldsymbol{R}_{\text{ref}}) + \frac{1}{2\pi}\int_0^{2\pi} J_2(\boldsymbol{R}_{\text{ref}})\,\mathrm{d}\theta + [J_2(\boldsymbol{R}_{\text{ref}})\cdot\hat{\mathbf{k}}_{\mathcal{R}}]\hat{\mathbf{k}}_{\mathcal{R}} \tag{2.32}$$

The reference angular velocity is replaced by the value $\boldsymbol{\omega} = nc\,\hat{\boldsymbol{z}}$, where n is the mean motion and $c = \sqrt{(1+s)}$. The following equations are thus derived in [16]:

$$\begin{aligned}
\ddot{x} - 2nc\dot{y} - (5c^2-2)n^2x &= -3n^2J_2(R_e^2/R_{\text{ref}})\cdot \\
&\quad \cdot\{1/2 - [3\sin^2 i_{\text{ref}}\sin^2(kt)/2] - [(1+3\cos(2i_{\text{ref}})/8]\} \\
\ddot{y} + 2nc\dot{x} &= -3n^2J_2(R_e^2/R_{\text{ref}})\sin^2 i_{\text{ref}}\sin kt\cos kt \\
\ddot{z} + (3c^2-2)n^2z &= 0
\end{aligned} \tag{2.33}$$

with $k = nc + \frac{3\sqrt{\mu}J_2R_e^2}{2R^{7/2}}\cos^2 i_{\text{ref}}$ and x, y and z Cartesian coordinates in the LVLH frame.

These equations do not accurately capture the dynamics of the cross-track motion, thus presenting a second problem when $i \neq 0$ due to the averaging of $\nabla J_2(\mathbf{R}_{\text{ref}})$. The approximation makes the effect of the potential symmetric with respect to the normal to the orbit plane, rather than to the vector pointing towards the North pole. In order to solve this issue, it is sufficient to reformulate the cross-track dynamics, that is, the third equation in Eq. (2.33), as

$$\ddot{z} + p_q^2 z = 2p_l p_q\cos(p_q t + p_\phi) \tag{2.34}$$

where the derivation of parameters p_l, p_q and p_ϕ is presented in detail in [16].

As in the Hill-Clohessy-Wilthsire equations, the cross–track and the in-plane dynamics are uncoupled, making it possible to solve the equations separately. In some special cases it is possible to obtain a bounded analytical solution, by imposing restrictions on the initial velocity conditions. Reference [16] also provides the equations that model the orbit of a satellite motion relative to a second satellite, in which case the equations are formulated in terms of Δx, Δy, and Δz variables, that is,

$$\begin{aligned} x &= (x_0 - p_\alpha)\cos(nt\sqrt{1-s}) + \frac{\sqrt{1-s}}{2\sqrt{1+s}} y_0 \sin(nt\sqrt{1-s}) + p_\alpha \cos(2kt) \\ y &= -\frac{2\sqrt{1+s}}{\sqrt{1-s}}(x_0 - p_\alpha)\sin nt\sqrt{1-s} + y_0 \cos(nt\sqrt{1-s}) + p_\beta \sin(2kt) \\ z &= (p_l t + m)\sin(p_q t + p_\phi) \end{aligned} \tag{2.35}$$

$$\begin{aligned} p_\alpha &= -\frac{3J_2 R_e^2 n^2}{4kR_{\text{ref}}} \frac{(3k - 2n\sqrt{1+s})}{n^2(1-s) - 4k^2} \\ p_\beta &= -\frac{3J_2 R_e^2 n^2}{4kR_{\text{ref}}} \frac{2k(2k - 3n\sqrt{1+s}) + n^2(3+5s)}{2k(n^2(1-s) - 4k^2)} \sin^2(i_{\text{ref}}) \end{aligned} \tag{2.36}$$

The initial conditons on the velocity of the deputy that ensure that no secular drift is presented with respect to the reference orbit, are the following:

$$\begin{aligned} \dot{x}_0 &= y_0 n \left(\frac{1-s}{2\sqrt{1+s}} \right) \\ \dot{y}_0 &= -2x_0 n\sqrt{1+s} + \frac{3J_2 R_e^2 n^2}{4kR_{\text{ref}}} \sin^2 i_{\text{ref}} \end{aligned} \tag{2.37}$$

Reference [65] evaluates in detail the results of [16]. Reference [66] derives a model which includes the effect of atmospheric drag, together with J_2 perturbation.

2.4 Tether Models

Several approaches are available in the literature for modeling tether dynamics. When tether elasticity is neglected, the system is rigid and the results for gravity-gradient stabilized rigid bodies derived in [67] can be applied. When elasticity is taken into account, the model may take incorporate different features depending on the degree of fidelity required, and the specific characteristics of the mission scenario. Richer models improve the accuracy of the results, usually at the expense of a higher computational load. There are

different features than can be taken into account for tether modeling:

- **Elasticity:** This property implies that the tether allows longitudinal stretching beyond its natural length.
- **Mass:** The inclusion of tether mass in the model, requires a model for mass distribution, either a continuous model (based on the string equation), or a discrete model based on massless stretches connecting concentrated masses.
- **Extensibility:** The variable unstretched length is needed to represent deployment/retrieval operations.

In the following sections, the implementation of each one of the cited features will be described.

2.4.1 Elasticity Model

A tether elongated beyond the nominal unstretched tether length $l^{(0)}$ exhibits an opposiing restoring force. This force is a combination of an elastic restoring force (such as that of a linear spring) and a damping force that depends on the tether elongation rate (damping effect). Materials showing this behavior are known as visco-elastic materials [68]. There are different variants of visco-elastic models depending on the specific arrangement of the model combining spring and damper: these two can be arranged in series, in parallel or a combination of both.

According to the Kelvin–Voigt visco–elastic model the spring and damper are set up in parallel. In this case the stress-strain relationship is represented as:

$$T = -E_t \cdot \varepsilon - C_t \cdot \dot{\varepsilon} \tag{2.38}$$

where E_t is the material Young's modulus, C_t is the coefficient of internal friction and ε is the strain. For some materials and for some specific applications, accurate modeling of C_t needs to take into account structural (or hysteretic) damping [68]. This approach takes into account an hysteresis cycle in the σ–ε plane, and the effect of the frequency of oscillation. The value of C_t can be calculated as:

$$C_t = \frac{E_t \cdot \eta_t}{\Omega_t} \tag{2.39}$$

where η_t is the loss factor (that depends on the specific characteristics of the material) and on the oscillation frequency Ω_t. Results show that for a space tether, the value of C_t

can be assumed constant and thus independent from frequency.

For a space tether, the visco–elastic properties of the tether material are assumed to be those of a Kelvin–Voigt material model, which consists of a spring and a damper connected in parallel. For a massless tether connecting agents i and j, the force exerted on agent i and agent j can be calculated as:

$$\begin{aligned} \boldsymbol{f}_{i,\text{tens}} &= E_t A_t \cdot \varepsilon_{j,i} \cdot \hat{\mathbf{e}}_{j,i} + C_t \cdot \dot{\varepsilon}_{j,i} \cdot \hat{\mathbf{e}}_{j,i} \quad \text{if} \quad \Delta l_{j,i} > 0 \\ \boldsymbol{f}_{j,\text{tens}} &= -\boldsymbol{f}_{i,\text{tens}} \end{aligned} \tag{2.40}$$

where E_t is the tether material Young's modulus, A_t the area of the section of the tether and C_t the damping constant. Versor $\hat{\mathbf{e}}_{j,i} = (\boldsymbol{r}_j - \boldsymbol{r}_i)/l_{j,i}$ defines the direction connecting agents j and i normalized by the tether length $l_{j,i} = |\boldsymbol{r}_j - \boldsymbol{r}_i|$. Term $\varepsilon_{j,i} = \Delta l_{j,i}/l_{j,i}^{(0)}$ defines the strain between the j–th and i–th bodies, with an elongation $\Delta l_{j,i} = l_{j,i} - l_{j,i}^{(0)}$, being $l_{j,i}^{(0)}$ the tether nominal unstretched length. Expanding Equation (2.40) leads to:

$$\boldsymbol{f}_{i,\text{tens}} = \frac{E_t A_t}{l_{j,i}^{(0)}} \cdot \Delta l_{j,i} \hat{\mathbf{e}}_{j,i} + \frac{C_t}{l_{j,i}^{(0)}} \left[\hat{\mathbf{e}}_{j,i} \cdot (\boldsymbol{v}_j - \boldsymbol{v}_i) - \dot{l}_{j,i}^{(0)} \cdot \frac{l_{j,i}}{l_{j,i}^{(0)}} \right] \hat{\mathbf{e}}_{j,i} \quad \text{if} \quad \Delta l_{j,i} > 0 \tag{2.41}$$

Grouping terms in this equation leads to

$$\boldsymbol{f}_{i,\text{tens}} = k_t \cdot S_{j,i} \cdot \hat{\mathbf{e}}_{j,i} + c_t \cdot D_{j,i} \cdot \hat{\mathbf{e}}_{j,i} \quad \text{if} \quad \Delta l_{j,i} > 0 \tag{2.42}$$

where k_t and c_t are the tether elastic and damping coefficients. Note that if the elongation Δl_j becomes equal or less than zero, the cable does not transmit any force ("slack" condition) and so no action is present between the connected masses and only the gravity gradient force drives their motion.

2.4.2 Effects of tether mass

Modeling transversal deflections requires taking into account the mass of the tether, in order to determine the effect of the gravitational field over the mass distribution of the tether. For this purpose there are two alternatives: A model based on the string equation taking into account a constant density string, or a discretized model composed of massless stretches connecting discrete lump masses.

Continuous Models

References [69], [70] and [71] present a theoretical model that describes tether dynamics based on the string equation. This model determines the governing equations of an arbitrary mass element $\rho\,\mathrm{d}s$ the teher of the tether, as well as the dynamics of the tether ends. The modified string equation takes into account gravitational forces:

$$\rho\frac{\partial^2\boldsymbol{R}}{\partial t^2} = \frac{\partial \boldsymbol{f}_{s,\mathrm{tens}}}{\partial s} - \rho\frac{\mu\boldsymbol{R}}{R^3} + \boldsymbol{f}_{s,\mathrm{grav}} \tag{2.43}$$

where s is a curvilinear abcissa counted along the string. Considering that tension force is always tangent to the thread line, it is

$$\boldsymbol{f}_{s,\mathrm{tens}} = T\cdot\boldsymbol{t}_R \quad \text{with} \quad \boldsymbol{t}_R = \frac{\partial\boldsymbol{R}}{\partial s}\left|\frac{\partial\boldsymbol{R}}{\partial s}\right|^{-1}$$

the magnitude of tension T is defined from the elasticity law considered for each specific tether material, and $\boldsymbol{T}_R$ is the tangent unit vector. The equations of motion at the tether endpoints a and b can be written as:

$$m_a(t)\frac{\mathrm{d}^2\boldsymbol{R}_a}{\mathrm{d}t^2} = \boldsymbol{t}_{R,a}\left[T_a - \rho(s_a)l_a\left(\frac{\mathrm{d}s_a}{dt}\right)^2\right] - m_a(t)\frac{\mu\boldsymbol{R}_a}{R_a^3} + \boldsymbol{f}_{a,\mathrm{grav}} \tag{2.44}$$

$$m_b(t)\frac{\mathrm{d}^2\boldsymbol{R}_b}{\mathrm{d}t^2} = -\boldsymbol{t}_{R,b}\left[T_b - \rho(s_b)l_b\left(\frac{\mathrm{d}s_b}{dt}\right)^2\right] - m_b(t)\frac{\mu\boldsymbol{R}_b}{R_b^3} + \boldsymbol{f}_{b,\mathrm{grav}} \tag{2.45}$$

where l_a and l_b are the extension of the tether at endpoints.

$$t_a = E_t(s_a)(l_a - 1)\ ; \quad l_a = \left|\frac{\partial\boldsymbol{R}}{\partial s}\right|_a \tag{2.46}$$

$$t_b = E_t(s_b)(l_b - 1)\ ; \quad l_b = \left|\frac{\partial\boldsymbol{R}}{\partial s}\right|_b \tag{2.47}$$

Based on the model introduced above, Ref. [69] proposes simplifications that provide different degrees of accuracy in the model. Reference [72] also analyzes tether dynamics by exploiting the fact that tethers usually are very stiff.

Discretized Models

The purpose of discretized models is to address the problem by approximating the behavior of the tether by a series of point-masses connected by straight massless spring–damper

elements. Although the use of continuous models is a valid choice for single tether systems, discretized models alleviate the computational load, when multi-tethered systems are to be dealt with. The first approach presented here consist in a model that defines a single elastic massless elements linking pairs of deputies at the tether ends. For the massive model, an approach is presented that allows discretization of tether by an arbitrary number of stretches.

Massless model The massless model is the simplest one, and in this case the tether is represented as a simplified massless spring–damper system connecting two agents at its ends. For this case, the dynamics of the formation are expressed in the LVLH frame.

Under the assumption that cable mass is assumed zero, as in the analysis reported in Ref. [13], the cables store elastic energy while remaining in a straight position under the action of the tension exchanged between the bodies located at their extremities, induced by gravity–gradient force and formation rotational motion.

The derivation of the equations of motion can be done using Lagrange equations. The effect of the spring is taken into account as a potential energy due to elasticity, and therefore included in the computation of the total potential energy. The damping force shall be included as a dissipation function $Q_{d,qj}$ on the RHS of the equation since the damping force is non-conservative.

$$\frac{d}{dt}\left(\frac{\partial \mathcal{T}}{\partial \dot{q}_j}\right) - \frac{\partial \mathcal{T}}{\partial q_j} + \frac{\partial \mathcal{V}}{\partial q_j} = Q_{d,qj} \tag{2.48}$$

The elastic potential energy, consist of the gravitational term and the elastic term $\mathcal{V} = \mathcal{V}_E + \mathcal{V}_{\text{elast}}$.

$$\mathcal{V}_{\text{elast}} = \sum_{i=1}^{N} \frac{1}{2} k_t \left(l_t - l_t^{(0)}\right)^2 \quad ; \quad \mathcal{V}_E = -GM_e \sum_{i=1}^{N} \frac{m_i}{|\boldsymbol{R}_p + \boldsymbol{r}_i|} \tag{2.49}$$

The Raleigh function for the damping force, can be written as:

$$Q_{d,qj} = -\frac{\partial}{\partial \dot{q}_j}\left(\sum_{i=1}^{N} \frac{1}{2} c_t \dot{l}_t^2\right) \tag{2.50}$$

where k_t and c_t are the elastic and damping constant respectively for the tether, l_t the length of a tether and l_{nom} the nominal lenght of a tether. The expression of the kinetic energy is obtained from Eq. (2.9).

The accelerations exerted by tethers linking pairs of deputies can be incorporated directly in the equations of motion 2.48. Reference [13] uses this approach to study the stability of different satellite cluster morphologies. Through a series of simplifications, and assuming a circular orbit, the only orbital feature present in the equations of motion is the orbital mean motion n. This reference also presents different cluster topologies establishing force links between the deputies. Each deputy will have three equations of motion associated to the three degrees of freedom expressed by the chosen generalized coordinates

Massive model In this model, tether mass is introduced in the model by means of a lumped–mass discretization. This approach was introduced in Ref. [14] and it considers tethers as a sequence of point-masses (beads) and massless springs-dampers. References [73] and [74] also make use of this formulation. It was applied also in Refs. [75] and [76] in order study the behavior of orbiting large tethered structures without active control.

The total mass m_t of a generic tether t is distributed over n_b beads of equal mass, $m_b = m_t/n_b$. Each tether element is considered as a (small) orbiting body integrated in the structure of the cluster. The tether is thus divided into a series of $n_b + 1$ segments, each one connecting two beads in the central portion of the tether, or a bead to either the parent body or one of the deputies at its ends. Fig. 2.4 illustrates the concept.

For each tether segment, values for damping coefficient, c_s, and stiffness, k_s, are assigned considering a massless spring–damper system, where c_s and k_s are obtained by imposing that the series of $s_t = (n_b+1)$ elastic elements provides an assigned value for the equivalent stiffness and damping coefficients k_t and c_t of the whole tether over its length, that is,

$$\begin{aligned} 1/k_t = (n_b+1)/k_s \quad &\Rightarrow \quad k_s = s_t \cdot k_t \\ 1/c_t = (n_b+1)/c_s \quad &\Rightarrow \quad c_s = s_t \cdot c_t \end{aligned} \tag{2.51}$$

where s_t is the number of segments, k_s and c_s are the elastic and damping constant of each segment. The mass m_t, the elastic constant k_t, and the damping constant c_t of the tether are calculated using the following expressions:

$$m_t = \rho A_t l \;\; ; \;\; k_t = E_t A_t / l \;\; ; \;\; c_t = C_t / l \tag{2.52}$$

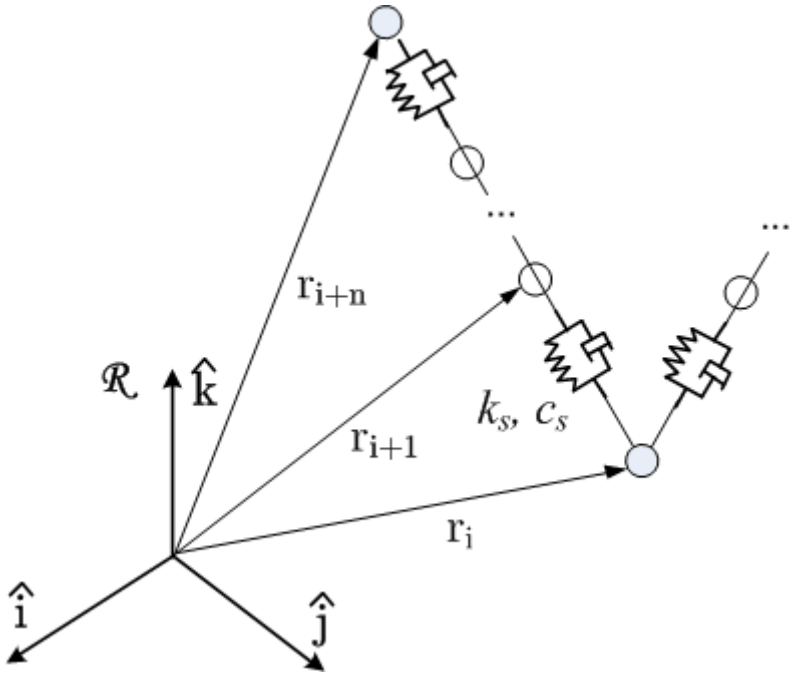

Figure 2.4: **Stretches connecting beads, deputies and parent body**

where ρ_t is the density, E_t is the Young's Modulus, C_t the damping constant of the tether material, and A_t is the cross-section of the tether. Based on these parameters, and the elastic model chosen, it is possible to calculate the force exerted by the tether at its ends.

Coupling of the movement among all the elements of the formation induced by tether tensions is expressed through the components of the tether tension force $\boldsymbol{f}_{i,\text{tens}} = f_{x,i}\hat{\mathbf{i}} + f_{y,i}\hat{\mathbf{j}} + f_{z,i}\hat{\mathbf{k}}$ on the RHS of Equation (2.14). The force exerted by a tether segment s connecting elements a and b (two adjacent beads or a deputy and a bead) can be calculated as:

$$\begin{aligned}
\boldsymbol{f}_{a,\text{tens}} &= \frac{E_t A_t}{l_{b,a}^{(0)}} \cdot \Delta l_{b,a} \hat{\mathbf{e}}_{b,a} + \frac{C_t}{l_{b,a}^{(0)}} \left[\hat{\mathbf{e}}_{b,a} \cdot (\boldsymbol{v}_b - \boldsymbol{v}_a) - \dot{l}_{b,a}^{(0)} \cdot \frac{l_{b,a}}{l_{b,a}^{(0)}} \right] \hat{\mathbf{e}}_{b,a} \quad \text{if} \quad \Delta l_{b,a} > 0 \\
&= k_{s(b,a)} \cdot S_{b,a} \cdot \hat{\mathbf{e}}_{b,a} + c_{s(b,a)} \cdot D_{b,a} \cdot \hat{\mathbf{e}}_{b,a} \\
&= -\boldsymbol{f}_{b,\text{tens}}
\end{aligned}$$

Comparison of Continuous and Discrete Model

Reference [77] analyzes the behavior of N coupled oscillators, which consist of an elastic string attached to N particles of equal mass. The string has fixed ends. This reference shows that as the number of point masses is increased and the length of the elements is reduced, the equations of motion of the discretized model become equivalent to those of the continuous string model. The number of vibration modes represented in the motion will be as high as the number of oscillators N used in the representation of the model. Oscillations of higher frequencies cannot be represented due to aliasing.

Reference [15] performs a modal analysis of the behavior of the tethers for a three-dimensional cluster and presents a simulation showing the different vibration moldes. The paper assesses the suitability of the bead model to represent tether dynamics.

It can be concluded that the discretized lumped-mass model is a valid representation of the tether behavior. The accuracy in the representation of vibration modes wil depend on the number of particles used in the lumped-mass model.

2.4.3 Tether Deployment and Retrieval

Most of the missions involving tethers require tether deployment and retrieval capabilities. From the beginning of the mission it is necessary to unreel tethers in order to deploy the cluster to its intended configuration. During mission operation it might be necessary to be able to reel tethers for tension control purposes. Even if some natural configurations allow keeping tether tension to a minimum level and thrusters play also a role in tether tension, changing the tether natural length also allows modifying tether tension. In missions like SPECS [35] it is necessary to have a formation with variable geometry. The change in the shape is achieved by changing the tether natural lengths. The control of tether tension and the control of tether length is complex problem, as it consist of a system with variable mass due to the variation of the tether natural length. The modification of the tether natural length also involves a change of its natural frequencies as explained before.

References [69], [78], [79], [72] and [80] derive the theoretical equations of motion for deployment assuming a continuous string equations. Reference [70] presents different models of different complexity addressing the deployment/retrieval problem. References [81] and [82] propose an optimal [83] control system for deployment and retrieval based on the continuous model.

There are two main alternatives for reeling control when considering a lumped-mass tether model. The first approach assumes a constant element length. This implies that during deployment/reeling the number of beads will vary. The sudden addition or suppression of a bead into the tether creates a discontinuity in the dynamics of the tether. References [14], [84], [85] and [86] use this approach. In the instant when a new a massive bead (having a certain velocity) leaves the spacecraft and it is incorporated in the tether, momentum conservation needs to be taken into due account in order to determine the state of the beads.

As an alternative, the model proposed in this thesis assumes a constant number of beads and the length of the elements is changed during deployment/retrieval. When deploying or retrieving a tether, the tether unstretched length parameter $l^{(0)}$ must be updated as a consequence of the process of releasing or retrieving the cable. At the same time, a new desired position must be defined for the deputies placed at the ends of that tether, in order to keep the tether taut during the reeling process and at the final configuration state. The change in $l^{(0)}$ and the new desired position for tether ends can be done by tracking a ramp profile, the slope of which is used to regulate the rate of change. The model is explained in more detail in Section 5.6.

2.4.4 Dynamics of a tether in orbit

The models presented so far are useful to define the most basic mechanical dynamics of a tether without incorporating the gravity gradient force, or just by adding it as an external force. The dumbbell model is often used in the literature. The advantage of this model is that it incorporates explicitly the expression of the gravity gradient, and therefore allows to study the dynamics of tethers in space. Different variants of the dumbbell model can be derived, with various degrees of fidelity.

Tether dumbbell model

A first approximation for tether modeling is to consider a massive tether connecting two point masses. A certain number of papers take into account this model, based on the scenario of the TSS mission where a probe is connected to the Space Shuttle [87], [88]. Taking into account the kinetic and potential energy of the tether,

$$\begin{aligned}\mathcal{T} &= \mathcal{T}_{\text{orb}} + \frac{m_e l^2}{2}\left[(\dot{\alpha}+\dot{\theta})^2\cos^2\beta + \dot{\beta}^2\right] + \frac{m_a(m_b+m_t)}{m_T}\dot{l}^2 \\ \mathcal{V} &= \mathcal{V}_{\text{orb}} + \frac{m_e}{2}\frac{\mu}{R^3}l^2\left(1-3\cos^2\alpha\cos^2\beta\right) \qquad (2.53)\\ & \qquad (2.54)\end{aligned}$$

where $\mathcal{T}_{\text{orb}}$, $\mathcal{V}_{\text{orb}}$ are kinetical and potential orbital energy:

$$\mathcal{T}_{\text{orb}} = \frac{m_T}{2}\left(\dot{R}+R^2\dot{\theta}^2\right) \qquad ; \qquad \mathcal{V}_{\text{orb}} = -\frac{\mu m_T}{R}$$

and m_a, m_b are the masses of the tether ends and m_t is the tether mass tether and m_e depends on the three values:

$$\begin{aligned} m_e &= \left(m_a(m_b+m_t/3)+(m_t/3)(m_b+m_t/4)\right)/m_T \\ m_T &= m_a+m_b+m_t \qquad (2.55)\end{aligned}$$

Variable m_a is the mass of the spacecraft containing the tether reeling mechanism, and therefore its value varies with time during tether deployment or retrieval operations. As a consequence the value of m_t also varies during tether reeling. The value of m_b is assumed constant. Variable α is the pitch angle (in-plane libration angle between tether and local vertical), and β is the roll angle (out-of-plane angle with respect to the orbital plane) as represented in Fig. 2.3. The first terms in $\mathcal{T}$ and $\mathcal{V}$ describe the orbital kinetic and potential energy, whereas the remaining terms in each equation describe the energy related to tether attitude and motion.

The equations of motion can be obtained using the Lagrange equations as in Eq. 2.8. Using the generalized variables $\{\alpha, \beta, l\}$:

$$\begin{aligned}\cos^2\beta\left[(\ddot{\alpha}+\ddot{\theta})+\left(\frac{2\dot{l}}{l}m_1^*-2\dot{\beta}\tan\beta\right)(\dot{\alpha}+\dot{\theta})+\frac{3\mu}{R^3}\sin\alpha\cos\alpha\right] &= \frac{f_\alpha}{m_e l^2} \\ \ddot{\beta}+\frac{2\dot{l}}{l}\dot{\beta}\cdot m^*+\left[(\dot{\alpha}+\dot{\theta})^2+\frac{3\mu}{R^3}\cos^2\alpha\right]\sin\beta\cos\beta &= \frac{f_\beta}{m_e l^2} \qquad (2.56)\\ \ddot{l}\cdot m^* - l\cdot m_e\left[\dot{\beta}^2+(\dot{\alpha}+\dot{\theta})^2\cos^2\beta+\frac{\mu}{R^3}(3\cos^2\alpha\cdot\cos^2\beta-1)\right] &= f_l\end{aligned}$$

Where f_i represent the generalized forces. A visco–elastic term modeling the tether elastic behavior can be incorporated in the model through the f_l term in Eq. (2.56), as an

external force.

Variable $m^* = m_a(m_b + m_t/2)/(m_T m_e)$, as shown in [89] and [90]. For non–circular orbits, both R and $\dot{\theta}$ can be written in terms of θ:

$$R = \frac{a(1-e^2)}{\zeta} \qquad \dot{\theta} = \zeta^2 \sqrt{\frac{\mu}{a^3(1-e^2)^3}} \qquad \zeta = (1 + e\cos\theta) \tag{2.57}$$

The model reported in Eq. (2.56) was used in many studies to analyze the behavior of an orbiting tether. References that study the behavior on eccentric orbits, adopt true anomaly θ as the independent variable. In order to study the behavior of an orbiting tether different simplifications can be done to focus on those aspects of the dynamics more relevant for the considered applicative scenario.

In a first approach only roll and pitch dynamics are modeled, and the longitudinal dynamics are eliminated assuming a rigid tether, that is $\dot{l} = 0$. In [94], both in-plane and out-of-plane dynamics of a tether in an elliptic orbit are studied from an analytical and numerical point of view.

To study the planar motion only pitch and longitudinal dynamics are considered, in the absence of roll dynamics. This implies that $\beta = 0$ and $\dot{\beta} = 0$. This scenario is studied in several papers such as [90], [91], and [92].

To further simplify the model, only pitch motion can be studied, eliminating both roll and longitudinal dynamics. This implies that $\dot{l} = 0$, $\beta = 0$ and $\dot{\beta} = 0$. This assumption leads to the well known Beletsky equation, defined with true anomaly as independent variable.

$$(1 + e\cos\theta)\alpha'' - 2\alpha' \cdot e\sin\theta + 3\sin\alpha\cos\alpha = 2e\sin\theta \tag{2.58}$$

This case is studied in Refs. [93], [95], [96], [97] and [94]. Although the behavior of a dumbbell in a circular orbit shows a regular behavior, when the eccentricity of the orbit increases the pitch dynamics of the tether may exhibit a chaotic behavior. The size of the chaotic region between libration and tumbling frequencies increases with eccentricity.

The same dynamics restricted to a circular orbit is studied in [89]. This implies that $\dot{l} = 0$, $\beta = 0$, $\dot{\beta} = 0$ and $n = \dot{\theta}$. Reference [87] proposes a tension control law, based on the

linearization of the equations of motion. Reference [98] proposes an optimal controller for set–point control of $\{\alpha, \beta, l\}$. References [81] and [82] propose, respectively, a controller for deployment and retrieval based on the model presented in Eq. (2.56).

Gravity-gradient stabilization

A single orbiting tether connected by two masses and aligned with the local vertical exhibits a natural stable equilibrium. On the agent placed in the lowest end of the tether (the one closest to the Earth), Gravity force is higher with respect to that exerted over the agent on the furthest end. On the other hand, centrifugal force acting on the furthest agent is higher than that on the lowest one. This fact creates a natural equilibrium state in which the tether remains taut. In the absence of energy dissipation, a slight perturbation leads to a pendulum-like oscillation of the tether with respect to the local vertical. Following Eq. (2.56), the in–plane dynamics, in the absence of external forces is represented by:

$$\ddot{\alpha} + 3n^2 \sin\alpha \cos\alpha = 0 \tag{2.59}$$

In practice, a tether in such condition exhibits low amplitude libration due to external perturbations to the non-uniformity of the gravity field. At the same time, friction and atmospheric drag cause dissipation and thus damp out the oscillations.

Integrating this equation leads to:

$$\dot{\alpha} - 3n^2 \cos^2\alpha = 2\mathcal{H} \tag{2.60}$$

which describes the pitch angular velocity as a function of the pitch angle. This equation allows plotting a phase portrait with different trajectories as a function of the value of $\mathcal{H}$, as shown in Refs. [69] and [88]. The value $\mathcal{H} = 0$ separates the regions of pendulum-like libration ($\mathcal{H} < 0$) and rotation ($\mathcal{H} > 0$). Both references also study the coupled in-plane and out-of-plane dynamics.

For elliptical orbits the Hamiltonian is not constant, and is possible to derive a similar equation to represent the behavior by means of phase portraits. As shown in [88], the tether behavior in elliptical orbits is chaotic.

Electrodynamic tethers

An electrically conductive tether in Low Earth Orbit can be used as a power generator or as a motor generating thrust. The electrodynamic tether principles are described in Ref. [1].

When no external current is applied, an electrical current is induced opposite to the tether's direction of motion. The current is perpendicular to the Earth's magnetic field and to the direction of motion. At the same time, an electromagnetic force is generated opposed to the motion direction and the tether experiences drag. On the other hand, when the current direction is reversed through an internal power source (a satellite battery or a solar panel) thrust is generated along the tether motion and therefore the speed of the tether is increased. The increment of tether energy results into an altitude increase.

References [99] and [100] provide insight and a review of the state of the art about electrodynamic tethers dynamics. Reference [101] studies the effect of energy sources and sinks on the design of an electrodynamic tether mission.

Provided that the scope of this thesis is focused only in non–conductive momentum exchange tethers, electrodynamic forces will not be taken into account in the sequel.

Tether failure modes

One of the main hazards for a space tether mission in Low Earth Orbit is the chances that one or more tethers are severed by micrometeorites or space debris. The main purpose of the TiPS mission was to prove the long-term survivability of a space tether.

Reference [102] presents a collision study based on the failed TSS mission. This paper shows a methodology for estimating the probability of tether failure due to debris, and concludes that while it is likely that the tether collides with several particles less than 0.1 mm, the probability of colliding with large objects is small.

Reference [103] studies the survival of a double–strand tether while performing an active debris removal mission consisting of de-orbiting an artificial satellite. A debris flux is assumed as a function of altitude during the whole mission. The paper concludes that a satisfactory mission success probability is achieved. Reference [104] also studies the debris impact collision probability for a double–strand tether. The study concludes that even

though it is more probable to be hit, the probability of being severed is much lower than that of a single-strand tether.

Tether materials

Space tethers shall made of materials be as light as possible. Some missions require deploying tethers of several kilometers, and the cluster alternatives require often multiple tether links between the agents of the cluster. If the tether material has a density too high, the overall excessive tether mass on each agent will be excessive (having then an impact on satellite fuel consumption), the deployment and retrieval manouvers will require more power, and the bending of the tethers due to the gravitational force will affect the whole cluster dynamics. At the same time, tether materials shall have high tensile stress strength in order to transmit link forces between agents, and in order to support tension peaks during cluster reorientation manouvers.

Table 2.2 provides a list of suitable material candidates for tethered clusters based on the data provided in Refs. [69] and [105]. The first column defines the density ρ, and the second column the tensile strength S^* of the material. The third column shows the tether break length in orbit calculated as,

$$L^* = \frac{1}{n}\sqrt{\frac{2S^*}{3\rho}} \tag{2.61}$$

where the mean orbital period n is taken for a geosynchronous orbit. This is the maximum length that the tether can withstand its own weight in orbit. It is a good metric to assess suitability, since its value increases with the ratio between tensile stress and density. From the presented results, it can be seen how the most common metallic materials clearly fall behind in properties with respect to fibers and crystals. Although crystals present better tensile stress than fibers, they are heavier and their practical use is impeded by to other factors such as cost of manufacturing.

Within the literature the most usual choices for non-conductive tether materials are Kevlar® and Spectra. The former is an aramid fiber of which two variants exist: Kevlar® 29 and Kevlar® 49. According to the manufacturer datasheet [106], both types present the same density and tensile stress. References [107], [106] and [66] provide details on the properties of this material. Several other references [74], [13], [89], [108], [109], [1] and [78] consider Kevlar® a suitable material for tether space applications. According to Ref. [110], Spectra generates less particles during deployment and is more resistant to atomic

Table 2.2: Tether material characteristics

Material	ρ (g/cm^3)	S^* (GPa)	L^* $(10^3$km)
Wires			
Aluminium	2.7	0.6	5.3
Stainless steel	7.9	2.0	5.7
Titanium	4.6	2.25	7.9
Fibers			
Nylon	1.14	0.48	7.3
Glass E	2.55	3.5	13.2
Kevlar® 29/49	1.45	2.8	15.7
Quartz	2.19	6.0	18.7
Spectra 2000	0.97	3.0	19.8
Crystals			
Graphite	2.2	20	34.1
Diamond	3.5	54	44.4

oxygen, but has less heat resistance than Kevlar®.

Reference [111] studies the effect on the mechanical properties of Kevlar® tethers when they are surrounded by a protective layer. The purpose of this protective layer is to provide better resistance to external agents such as atomic oxygen. This paper shows the feasibility of using this protective layer. Furthermore, it also assesses the possibility of covering the tether with a metal layer to provide low conductivity for electrodynamic applications. This could be a valid alternative to aluminium or copper, often considered for such applications.

The use of carbon nanotubes material for tethered missions shows promising results. Reference [105], intended to assess material suitability for a lunar space elevator and cis-lunar transport system, cites carbon nanotubes as a possible choice for an application requiring also material lightness as well extremely high tensile strength. According to this reference laboratory results showed a tensile strength of 50 GPa, nearly that of the diamond. Nonetheless, further research needs to be done in order to confirm the technological maturity of this choice.

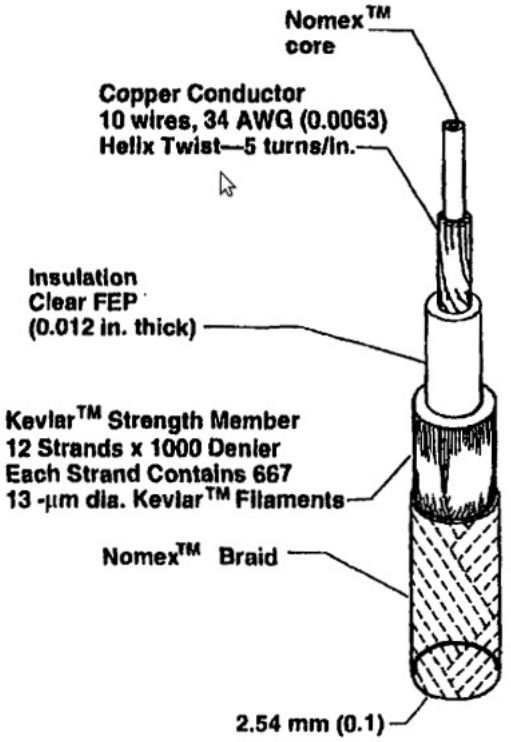

Figure 1.2-6 — Electrically Conductive Tether

Figure 2.5: **TSS jacketed tether layers (Credit: NASA)**

Figure 2.6: **TiPS tether section (Spectra)**

This study will assume that the chosen material is Kevlar®, due to the characteristics of the material presented in this section, and due to the fact that other references also use this material. This is a key reason, in order to be able to compare the results obtained with

other similar studies. There are however, other factors beyond the scope of this thesis, that must be considered when choosing a tether material for a space application. Reference [112] provides a list of criteria to be taken into account when choosing a tether material for a given mission. These criteria are related to tether manufacturing requirements, radiation resistance, presence of atomic oxygen, safe storage, humidity resistance and particulate contamination. This guide also addresses specific requirements concerning electrodynamic tethers and electrical insulation.

2.5 Cluster Architectures

Different architectures have been explored in the literature. In most of the cases, multi-body clusters are spinning around a predefined axis, with the purpose of approximating the dynamics of an orbiting spinning rigid body in equilibrium. Under certain conditions, the results can be achieved. Concerning the geometry of the formation, multi-body tethered formations can be broadly classified in planar and tridimensional. As it is shown in this chapter, each configuration has different stability properties depending on its orientation with respect to the Earth.

2.5.1 Planar Formations

In planar formations all the members of the formation are intended to remain coplanar. In general, planar architectures can be classified as *closed* formations in which the envelope of the formation deputies is closed through perimetral tethers and *open* formations when the formation does not define a closed polygon. The simplest case of an open formation is that of a single tether connecting two deputies at its ends

Reference [13] defines open formations as Hub–And–Spoke (HAS), in which case the formation consist of a parent body (Hub) linked to deputies through radial tethers (Spokes). The same reference defines Closed–Hub–And–Spoke (CHAS) formations, in which case in addition to radial tethers, there are perimetral tethers closing a polygon.

Some references like [113] and [75] define a closed formation without a parent body (ring-shaped formation). In the cited papers the cluster is defined as a ring of three deputies with no parent body, and thus the whole formation always define a plane.

Reference [114] studies the behavior of a cluster consisting of three agents linked with two tether segments defining an open formation.

A different planar configuration geometry is that of the Tetra-Star configuration [115], being used in the SPECS mission [35]. In this case, the three deputies are connected by three tethers defining a triangle. At the same time attached to each pair of deputies there is a countermass defining an outer triangle. Each one of these three triangles have in their vertices two deputies and one counter mass. As defined in the referenced papers, the purpose of the three countermasses is to control spin velocity when changing the aperture of the baseline (as shown in [36]). The Tetra-Star formation is intended to lie in the Lagrangian L2 point, and therefore its dynamics is not influenced by the gravitational field in the same way as a formation placed in the low Earth-Orbit, where gravity gradient plays a more important role.

2.5.2 Three Dimensional Formations

In general three dimensional formations define a structure rigid enough to replicate the behavior of an orbiting rigid body, and thus they can reproduce its equilibrium states.

A typical case of a tridimensional tethered formation is that of a Double–Pyramid, which is based on an inner ring made of four deputies in an Earth-facing orientation with the addition of two anchor masses along the radial direction, each one in one apex: one placed between the formation plane and the Earth, and the second placed beyond the formation plane. This formation is intended to spin with respect to the axis of symmetry. The formation may have a parent body [13] or not [76], [116], [117].

Reference [118] studies the stability and behavior of a space web made of tethers. This web consists of a triangular–shaped thin membrane made of tethers. The web is expected to have daughter satellites on each of its vertices, with robots crawling along the edge of the membrane or towards the interior part of it. References [119] and [120] study the behavior of tethered tetrahedral satellite formations.

2.6 Formation Spin Stabilization

The orientation of tethered formations considered in the literature depend both on the purpose of the mission and on the natural equilibrium of an orbiting body, assuming the formation behaves like a rigid body, as analyzed in more detail in the sequel.

Previous studies [13], [121] demonstrate that relative displacement of agents and parent from the nominal configuration achieved for inextensible tethers remains small with respect to their mutual distance. Consequently, it is possible to approximate the evolution of the attitude of a spinning tethered formation with that of an orbiting rigid body with moments of inertia equal to those of the formation. This simplifying assumption was proposed in Refs. [75] and [76] in order to study the dynamics of spinning tethered formations under gravity gradient torque, starting from the knowledge of equilibria for spinning rigid spacecraft of equal inertia.

Attitude dynamics of rigid spacecraft under gravity gradient on circular and elliptic orbits is analyzed in detail in Refs. [122] and [67]. When spacecraft attitude is referred to the orbit frame, spin conditions such that the spin axis remains fixed in the orbit frame are referred to as relative equilibria [67]. Three classes of relative equilibria can be defined for an axi-symmetric rigid spacecraft on a circular orbit with axial and transverse moments of inertia given by I_a and I_t, respectively: (i) cylindric (or Thomson) equilibria, where the spin axis is perpendicular to the orbit frame; (ii) hyperbolic equilibria, where the spin axis is perpendicular to the local vertical, but tilted away from the normal to the orbit plane by an angle γ_3, measured on the horizontal plane; and (iii) conic equilibria, where the spin axis is perpendicular to the transverse direction, but, again, tilted from the orbit normal by an angle γ_1, measured on a vertical plane normal to the orbit plane. The latter two classes of equilibria are referred to as Likins-Pringle equilibria. In all cases, the name refers to the surface spanned by the spin axis during the orbit (cylinder, hyperboloid and cone, respectively).

As a major difference, in the case of Thomson equilibria the gravity gradient vanishes and rotational angular momentum of the spacecraft, parallel to the orbit normal, is constant along the orbit. Spin rate, in this case, is arbitrary (although stability of the equilibrium may be affected).

As far as the stability of planar formations is concerned, clusters lying in the orbital plane (In-plane formations) are usually stable as they replicate the Thomson equilibria. On the other hand, Earth-facing spinning planar formations do not fulfill the characteristics of the Thomson equilibrium and have a natural precession. The conditions that ensure a Thomson equilibrium are [67]:

$$b_1 > 0, \qquad b_2 > 0, \qquad b_1^2 - 4b_2 > 0 \tag{2.62}$$

$$\begin{aligned} b_1 &= (2+3k_I) + 2(1+k_I)r_s + (1+k_I)^2 r_s^2 \\ b_2 &= (k_I(3-r_s) - 1 - r_s)(-k_I r_s - 1 - r_s) \end{aligned} \tag{2.63}$$

with inertia parameter $k_I = (I_a - I_t)/I_t$ and r_s the relative spin rate with respect to the mean motion n. Conversely, Likins-Pringle conical equilibria exist thanks to the action of the gravity gradient which rotates the angular momentum, but only provided that,

$$\cos\gamma = \frac{\dot{\alpha}/n}{4 \cdot \left(1 - \frac{I_t}{I_a}\right)} \tag{2.64}$$

where $\dot{\alpha}$ is the spin rate and n is the mean motion orbital rate. In particular, this conditions require that the spin rate is in the same order of magnitude of the orbit rate, n. The conditions that ensure a Likins-Pringle conical equilibrium are [67]:

$$\begin{aligned} b_1 &= 1 + 3k_I + 9k_I^2 - 9k_t(1+k_I)\sin^2\gamma \\ b_2 &= -3k_I(1-3k_I)\sin^2\gamma \end{aligned} \tag{2.65}$$

Following the approach proposed in [75] and [76], the formations considered in the present paper can be assimilated to a spinning axi-symmetric oblate rigid body with $I_a = 2I_t \approx 4m_d l_0^2$, where m_d is the mass of the deputies and ℓ_0 is tether length (assuming that tethers are almost inextensible and their contribution to moments of inertia negligible). In the in-plane scenario, roll and yaw components of the gravity gradient vanish and, given the value of $k_I = 1$, it is always possible to find a value of relative spin rate high enough so that directional stability of the spin axis is achieved [67] and formation shape maintained, thanks to centriphugal loads [13].

Hyperbolic relative equilibria are of little practical interest [75], but conical equilibria, where the normal to the formation plane has a non-zero component along the Nadir direction, can be useful. In this respect, the Earth-facing case can be considered as a degenerate conical equilibrium, with $\gamma_1 = 90°$. Unfortunately, the spin rate dictated by the Likins-Pringle equilibrium condition is not sufficient for stiffening the formation by means of centriphugal loads, as spin rates necessary for this task need to be at least one order of magnitude larger than the orbit rate. This means that Likins-Pringle equilibria are not an option for tethered formations, if purely passive stabilization is sought.

2.6.1 Double Pyramid Global Formation Behavior

The purpose of the anchors is to have an stabilizing effect on the orientation of the formation plane, thanks to the gravity gradient torque acting on the anchors placed in the radial direction. The two anchors may consist of ballast bodies (equipped with actuators) or actual satellites having an active role in the mission purpose. The formation is gyroscopically stabilized by means of a spin angular velocity along the direction of the formation pointing axis. The aim is to stabilize the motion of the formation in an Earth–face orientation, so that it points to a fixed point on the Earth surface.

This configuration has been studied extensively in the literature. Reference [116] studied the conditions for stability and the necessary conditions to keep tethers taut for a massless formation. Paper [13], derives the equations of motion of a assuming a predefined orbit of the parent body and explores the stability of different formation configurations (including a double tethraedron) neglecting the mass of the beads. Reference [18] performed a parametric analysis in which the stability was evaluated as a function of different parameters, including the number of elements in the base of the double pyramid. In this regard, the choice of four deputies in the base shows a reasonable trade-off between number of elements and pointing accuracy.

The validity of considering a spinning DP tethered formation as an orbiting rigid body in equilibrium is examined in Ref. [76] where the formation keeps spinning along the major axis which is the axis of stability [67]. References [76] and [15] compare through numerical simulations, the behavior of the DP formation with that of an orbiting rigid body. Paper [15] in addition to perform a modal analysis of the behavior of the tethers, proposes an optimal control approach for a double pyramid formation consisting of a variable inertia model that allows equilibrium at different tilting angles.

For Earth-facing missions, the most advantageous case is that of double–pyramid clusters provide a natural Likins–Pringle equilibrium. For DP formations, it is of special interest the Likins-pringle conic equilibrium, where the spin axis is perpendicular to the transverse direction, but, again, tilted from the orbit normal by an angle γ, measured on a vertical plane normal to the orbit plane. In this configuration, the formation is close to have an Earth-Facing orientation.

For the specific case of a DP cluster with a square base, the relation between the

transverse I_t and axial I_a moments of inertia, can be calculated as:

$$\frac{I_t}{I_a} = \frac{1}{2} + \frac{m_a}{m_s}\frac{L^2}{4D^2} \tag{2.66}$$

Where L is the distance between two anchors, D is the length of diagonal tethers from the base, m_a is the mass of the anchor tether and m_s the mass of a deputy in the base.

Other spinning formations based on lumped mass model have been analyzed in the literature. As it is shown in Ref. [75], it is not possible to achieve a passive conical equilibrium with a planar formation using a model based in massive tethers. The use of control action on deputies to achieve an open Hub–And–Spoke (HAS) planar formation pointing to Earth is excessive as shown in Ref. [123]. The closed HAS configuration was not considered appropriate due to the "bouncing" effects [113] found on external tethers linked to consideration of the massive tethers in the model. Reference [121] shows that this effect constraints the elongation of the radial tethers, leading sometimes to losing tether tension.

2.7 Agent Control

This section describes the different alternatives for position and attitude control of the deputies of the formation. Although the purpose of this thesis is to assess the viability of tethered formation control from an analytical point of view, it is still necessary to define the possible technologies to implement the control action. The approach proposed in Ch. 5 assumes full 6-DOF control capability for every formation member.

Position control can be achieved through thrusters along three axis or a combination of thrusters and attitude control. Among reaction control systems there are essentially two types of propulsion: chemical and electrical propulsion [124], [125] and [126].

Electrical propulsion relies on a power source that may come from nuclear sources, solar panels or internal batteries. That power source is used to expel a propellant in order to generate thrust and gain impulse. There are three variants of electrical propulsion systems: electrothermal, electromagnetic and electrostatic (ion thrusters). In all three cases, the propellant is a gas. In the first two cases, the gas is heated and accelerated either by passing over a hot surface or through an arc discharge. In the third case the gas is ionized and accelerated by an electrical field.

Several industrial projects have incorporated electrical propulsion. The technology is mature enough to be considered for satellites relying exclusively on electrical propulsion [127].

Chemical propulsion requires only a very limited amount of electrical power, needed to command actuators and auxiliary equipment. On the other hand, the amount of propellant mass is much higher than that from the electrical propulsion case. There are two types of chemical propulsion: cold gas and hot gas propulsion.

Cold gas propulsion thrusters are the simplest alternative. Their operation principle consist simply on the release pressurized gas. Their main advantage is simplicity and reliability, at the expense of performance.

Hot gas systems can be classified as solid or liquid propellant system. The liquid propellant thrusters rely on the combustion of one or two propellants plus an oxidizer to generate thrust. On the other hand, solid thrusters are based on an igniter and propellant grain. Liquid propellant thrusters exhibit better controllability and safer operation, for this reason they can be used for accuracy positioning manouvers. Solid propellant thrusters offer better thrust performance but they are far less controllable. Their use is confined to "one shot" operations such as orbit changes.

In general it can be concluded that electrical power systems provide higher performance than chemical power systems in terms of exhaust velocity. On the other hand, the thrust provided is lower. Both chemical and electrical rely on a limited amount of propellant, and therefore this imposes a limitation on the operative life of the satellite. The use of such as solar sails, may be an option in the future.

The current state of the art on optical sensors, laser and Radio-Frequency technologies allow achieving submillimetric navigation accuracy [128], [129].

Attitude control can be achieved through momentum exchange actuators such as reaction wheels, magnetic torquers, control moment gyroscopes or even thrusters. Reaction wheels are flywheels used with the purpose of changing the orientation of the spacecraft with respect to its center of mass, taking advantage of the principle of conservation of angular momentum. Control moment gyroscopes are contain a reaction wheel plus a gimbal.

The gimbal allows to tilt the axis of rotation of the flying wheel. Magnetic torquers allow changing the orientation of the spacecraft by generating a magnetic field that interacts with the Earth's magnetic field.

More detail on attitude control actuators can be found in Ref. [126]. References [130] and [131] provide attitude control laws for this purpose. References [145], [146], and [20] study the attitude control problem for a rigid body, and provide other model independent and model dependent based (including feedback linearization) families of control laws for satellite attitude tracking. Reference [132] compares the performance of these actuators, and that of the attitude sensors: gyroscopes, sun sensors and star trackers.

Chapter 3

Refined dynamical analysis of multi-tethered satellite formations

3.1 Tether Model

A simple, yet effective, model of tethered formation is presented in this chapter, that accounts for the effect of tether mass on formation stability and response to control inputs. Given the overall length of the cables (that in many missions is foreseen in the range of kilometers, as shown in Table 1.1), the total mass of the tethers may be not negligible with respect to that of the satellites attached to them. Cable mass is thus expected to affect system dynamics. As a first, intuitive example, the external tethers in closed formations are expected to bend outwards because of the centrifugal acceleration, when the formation is spinned around the parent body. This effect adds some tension to the cable and it will rotate the direction of the tension, with respect to the radial direction. In this respect, no major differences are expected for the Hub–And–Spoke formations, when the tethers remain in tension because of the centrifugal force acting on the deputies. On the converse, in the closed formation case the behaviour may be significantly different, even for vanishingly small tether mass.

This chapter considers the effects of including a massive cable model in the analysis of the dynamics exhibited by a multi–tethered satellite formation, in order to envisage those situations where the massless cable model captures the most significant aspects of the formation behaviour, identifying at the same time those cases where the cable mass leads to a significantly different response to perturbations and control inputs.

Pizarro–Chong and Misra considered both Hub–And–Spoke (HAS) formations and closed formations (CHAS). Figures 3.1.a and c represent a HAS formation, where each deputy satellite is connected by means of a single tether to the parent body that moves on a prescribed circular orbit. In CHAS formations together with radial cables, deputies are also connected to the nearest ones by means of external cables (Figs. 3.1.b and d). Also a double–pyramid configuration was analyzed (Fig. 3.1.e). The dynamic behavior, including possible instabilities, for the systems listed above was investigated by means of numerical simulation. The same configurations will be considered in the sequel, taking into account the effect of tether mass on system behavior.

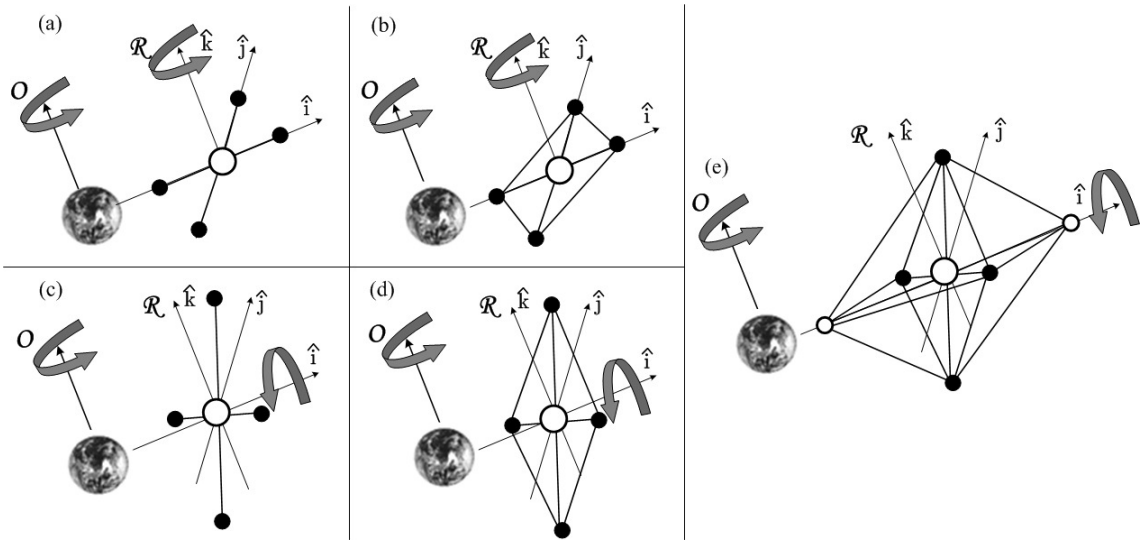

Figure 3.1: **Cluster configurations: (a) HAS in–plane, (b) CHAS in–plane, (c) HAS Earth-facing, (d) CHAS Earth-facing, (e) Double–pyramid.**

3.2 Initial conditions

Equation (2.15) is used to describe the motion of each deputy, bead and the parent body of the formation. An initial condition in terms of position and velocity is needed for each one of these bodies, represented as a mass element. The geometry of the system is determined by the position of deputies $\boldsymbol{r}_i$ in the LVLH frame and on the topology of connecting tethers.

Following this approach, the initial conditions on position and velocity are defined for parent body and deputies first. From these ones the initial conditions for the beads are derived accordingly. It is crucial to define the initial conditions of all members (agents and beads) in a way that the members of the formation follow the spin dynamics of the

tethered unstretched formation.

The initial condition for velocity of the parent body is computed using the expression that ensures that the orbit of the parent does not present secular drift from the solution of HCW equations. This requirement is enforced by choosing

$$\dot{y}_{p_0} \quad = \quad -2nx_{p_0} \tag{3.1}$$

When formations are gyroscopically stabilized, the angular velocity induces a relative motion of each deputy with respect to the parent body. Assuming that the parent is placed (at least initially) in the origin of the LVLH frame, the velocity of a generic deputy d is given by

$$\boldsymbol{v}_{d_0} = \boldsymbol{v}_{p_0} + \boldsymbol{\omega}_0 \times \boldsymbol{r}_{d_0} \tag{3.2}$$

where $\boldsymbol{v}_{p_0} = \dot{x}_{p_0}\hat{\mathbf{i}}_{\mathcal{R}} + \dot{y}_{p_0}\hat{\mathbf{j}}_{\mathcal{R}} + \dot{z}_{p_0}\hat{\mathbf{k}}_{\mathcal{R}}$ is the initial velocity of the parent, defined above, $\boldsymbol{\omega}_0$ is the initial angular velocity of the formation, and $\boldsymbol{r}_{d_0} = x_{d_0}\hat{\mathbf{i}}_{\mathcal{R}} + y_{d_0}\hat{\mathbf{j}}_{\mathcal{R}} + z_{d_0}\hat{\mathbf{k}}_{\mathcal{R}}$ is the initial relative position vector of the deputy, where all the components are expressed in the LVLH frame.

Given the initial position for the deputies, the tether configuration, and the parameter n_b (number of beads in tether t), it is possible to derive the position of the bead labelled b at the initial time assuming that they are equally spaced and tether is at rest:

$$\boldsymbol{r}_{b_0} = \boldsymbol{r}_{d/p_0} + (\boldsymbol{r}_{d_0^\star} - \boldsymbol{r}_{d/p_0})(1 - j_t/n_b)\,,\ j_t = 1, 2, \ldots, n_t \tag{3.3}$$

where the tether is assumed to connect a generic deputy $d^\star$ placed in $\boldsymbol{r}_{d_0^\star}$ to either another deputy d or the parent body p in $\boldsymbol{r}_{d/p_0}$.

The initial velocity for each bead follows the same principle of relative motion used in the case of the deputies and expressed by Eq. 3.2, where

$$\boldsymbol{v}_{b_0} = \boldsymbol{v}_{p_0} + \boldsymbol{\omega}_0 \times \boldsymbol{r}_{b_0} \tag{3.4}$$

The initial value of the angular speed of the formation is expressed in terms of a factor of the orbit rate as

$$\boldsymbol{\omega}_0 = r_s|\boldsymbol{\omega}|\,\hat{\mathbf{h}} = r_s n\,\hat{\mathbf{h}} \tag{3.5}$$

where the direction of the formation angular rate, $\hat{\mathbf{h}}$, is defined for each particular scenario,

e.g. either Earth-facing ($\hat{\mathbf{h}} = \hat{\mathbf{i}}_{\mathcal{R}}$) or in-plane formations (when $\hat{\mathbf{h}} = \hat{\mathbf{k}}_{\mathcal{R}}$).

3.3 Open loop stability analysis

In order to evaluate the effect of tether mass on the dynamics of tethered satellite formations, the behavior of all the configurations represented in Fig. 3.1 is compared with that of the same formations studied in [13], [133] and [134] under the assumption of elastic massless tethers. In the simulations presented in this section, the same data reported in [13] are used for the formation elements (agents and tethers), that is: a mass of the parent body equal to 300 kg; deputy mass equal to 25 kg; spring constant and damping coefficient for a nominal unstretched tether length $l^{(0)} = 1000$ m are 221 N/m and 2.5 kg/s respectively. The fundamental characteristics of the tethers are presented in Table 3.1, assuming they are made of Kevlar 29®.

In what follows, HAS and CHAS formations with 4 deputies will be initially considered. The length of the tethers linking the parent body with the i–th deputy is indicated as l_i, whereas the length of external tethers for CHAS formations linking deputies i and k is $l_{i,k}$ (with $k = i + 1$ for $i < n_d$, $k = 1$ for $i = n_d$), as depicted in Fig. 3.2. In most of the simulation (unless otherwise stated) we have $n_d = 4$ deputies and $n_b = 4$ beads per tether, with $n_t = 8$ tethers, for a total of $N = 37$ orbiting point masses for a CHAS formation. For an open HAS formation, 4 external tether and the corresponding 16 lumped masses removed from the model, so that the formation is represented by one parent, 4 deputies and 4 tethers discretized by means of 16 point masses, for a total of 21 bodies.

A nominal unstretched length $l_i^{(0)} = 1000$ m is adopted for the internal tethers, whereas the external tethers (when present) are assumed to be $l_{i,k}^{(0)} = l_i^{(0)}\sqrt{2} \approx 1414$ m long. Finally, $\gamma_{i,k}$ indicates the angle between tethers connected from the hub to the i–th and k–th deputies (as depicted in Fig. 3.2). The overall elongation of tether i is given by $\Delta l_i = l_i - l_i^{(0)}$ where $l_i^{(0)}$ is tether unstretched length and l_i is obtained by summing the length of the n_b tether segments.

Table 3.2 presents the calculation of the elastic and damping constants of tethers and segments, taking into account the geometry of each formation. The calculation of the constants is performed using Equations (2.51).

The stability of the cluster, analyzed by means of numerical simulation of the dynamic

Table 3.1: Tether characteristics

Parameter	**Symbol**	**Value**	**Units**
Material properties			
Density	ρ	4.51	kg/km
Young Modulus	E	70.5	GPa
Damping constant	D	2500	Ns
Diameter		2	mm

Table 3.2: Tether parameters

Internal tethers (HAS, CHAS). $n_b = 4$				*External tethers* (CHAS, DP). $n_b = 4$			
Parameter	**Symbol**	**Value**	**Units**	**Parameter**	**Symbol**	**Value**	**Units**
Unstretched length	$l_i^{(0)}$	1000	m	Unstretched length	$l_{i,k}^{(0)}$	$1000\sqrt{2}$	m
Elastic constant	k_t	221.00	N/m	Elastic constant	k_t	156.27	N/m
Damping coefficient	c_t	2.50	kg/s	Damping coefficient	c_t	1.77	kg/s
Segment elastic constant	k_s	1105.00	N/m	Segment elastic constant	k_s	781.35	N/m
Segment damping coefficient	c_s	12.50	kg/s	Segment damping coefficient	c_s	8.85	kg/s
Anchor to parent tethers (DP). $n_b = 3$				*Anchor to deputy tethers* (DP). $n_b = 6$			
Parameter	**Symbol**	**Value**	**Units**	**Parameter**	**Symbol**	**Value**	**Units**
Unstretched length	$l_{a,p}^{(0)}$	10000	m	Unstretched length	$l_{a,i}^{(0)}$	10050	m
Elastic constant	k_t	22.10	N/m	Elastic constant	k_t	21.99	N/m
Damping coefficient	c_t	0.25	kg/s	Damping coefficient	c_t	0.25	kg/s
Segment elastic constant	k_s	66.30	N/m	Segment elastic constant	k_s	65.97	N/m
Segment damping coefficient	c_s	0.75	kg/s	Segment damping coefficient	c_s	0.75	kg/s

model derived according to the procedure outlined in the previous section, is assessed by evaluating the evolution of relevant geometrical features of the formation, and in particular:

- Elongation of tethers: The presence of bounds on tether elongation is checked, together with the characteristics of the oscillations in terms of tether length and tension. This applies to internal tethers and external tethers as well.

- Angular difference between adjacent tethers: This is a critical parameter especially for Hub-And-Spoke formations, where no tether directly connects pairs of deputies. The angular separation between tethers can thus easily vary, possibly leading to folding of some of the tethers over other ones. This can happen to CHAS only in the presence of an (unlikely) relevant out-of-plane deformation.

- Orientation: The orientation of the whole cluster in the LVLH frame is determined through the angle between the radial axis $\hat{\mathbf{i}}$ and the vector normal to the plane of

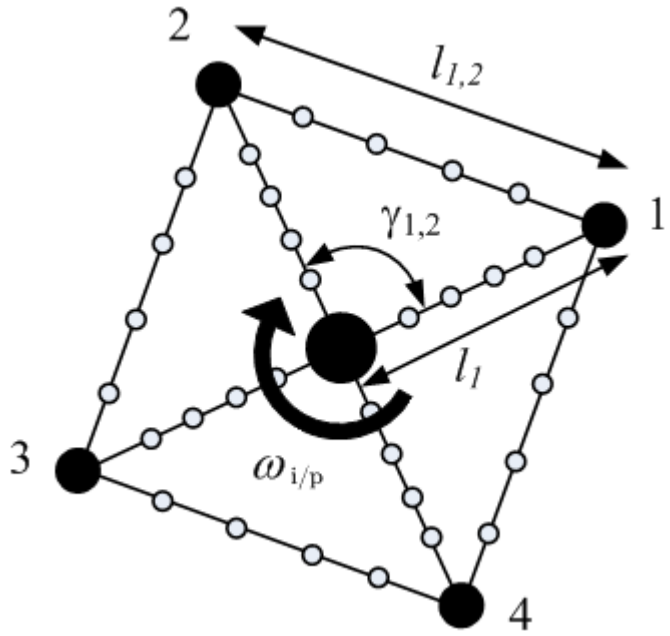

Figure 3.2: **CHAS formation with 4 deputies and 4 discrete point masses (beads) per tether.**

the formation. A least squares fit is used to calculate the unit vector normal to the plane of the formation, as long as in general deputies and parent body may not lie exactly on the same plane. The angle δ as in

$$\cos\delta = \hat{\mathbf{i}}_{\mathcal{R}} \cdot \hat{\mathbf{n}} \tag{3.6}$$

measures the angular distance between the radial axis $\hat{\mathbf{i}}_{\mathcal{R}}$ and the unit vector normal to the plane defined by the formation $\hat{\mathbf{n}}$.

- Coplanarity : A shape factor for the formation as a whole is not available and the qualitative features of formation shape are evaluated on the basis of the results obtained from the simulation. But a necessary condition for preserving the shape is that the agents remain on the same plane. In this latter respect, it is possible to provide a measure for the coplanarity of the agents, that can be evaluated in two cases: coplanarity of deputies and parent body, and coplanarity of deputies alone. A rigorous measure of coplanarity for four (or five) elements (as in the present case) is achieved by evaluating the (sum of the) dot product(s) of the unit vector normal to the plane identified by three of the bodies and the vector(s) linking the remaining

one(s). Coplanarity is measured by the coplanarity parameter C, defined as

$$C = ((\boldsymbol{r}_1 - \boldsymbol{r}_p) \times (\boldsymbol{r}_2 - \boldsymbol{r}_1)) \cdot (\boldsymbol{r}_4 - \boldsymbol{r}_3) \tag{3.7}$$

- Behaviour of the parent body: Regardless of the relative position of deputies and parent body, it is important to check whether the displacement of the parent from the reference orbit remains bounded or if it drifts away because of secular terms induced by the interactions with the deputies.

3.3.1 In-plane formations

The initial condition for the position of the four deputies of the formation is set to:

$$\begin{aligned} \boldsymbol{r}_{1_0} &= [l_i^{(0)}\ l_i^{(0)}\ 0] \cdot \sqrt{2}/2 = -\boldsymbol{r}_{3_0} \\ \boldsymbol{r}_{2_0} &= [-l_i^{(0)}\ l_i^{(0)}\ 0] \cdot \sqrt{2}/2 = -\boldsymbol{r}_{4_0} \end{aligned} \tag{3.8}$$

Initial velocity is computed using Eq. (3.2) with the parent object placed at the origin of the LVLH frame and

$$\boldsymbol{\omega}_0 = [0\ \ 0\ \ r_s n] \tag{3.9}$$

In the case of a HAS in-plane formation, the values of r_s are set to $r_s = 10$ for all deputies. For CHAS in-plane formation, the value of $r_s = 15$ is set for all deputies, for consistency with the examples in [13]. Initial conditions for position and velocity of the beads is computed as outlined at the end of the previous subsection.

Hub–And–Spoke in–plane formation

The HCW equations of motion show that in-plane and out-of-plane dynamics are uncoupled. When using this model, a tether lying initially within the orbital plane with zero initial velocity in the $\hat{\mathbf{k}}_{\mathcal{R}}$ direction remains on the orbit plane. In this particular situation, when using polar coordinates as generalized variables, the in-plane motion can be described by two independent variables: the longitudinal extension of tethers l_i, and the angle of rotation measured with respect to a fixed direction on the plane, α_i. If the longitudinal oscillation of tethers is neglected, the behavior of a particular deputy can be represented in a phase portrait using $\{\alpha, \dot{\alpha}\}$.

Reference [13] shows that the angular velocity $\dot{\alpha}$ oscillates depending on the particular value of α_i. For this reason, the angular displacement between adjacent tethers

$\gamma_{i+1,i} = \alpha_{i+1} - \alpha_i$ remains constant if and only if the trajectories of the deputies in the phase plane are the same. Therefore the definition of the initial condition for α_i for each deputy needs to take into account its initial phase angle, in order to allow all of the agents to follow the same trajectory, thus maintaining a constant angular displacement. Suitable initial conditions can be evaluated through a Hamiltonian approach by computing the total energy of each deputy, as suggested in [13], where an analytic method is proposed to calculate the initial condition of each deputy $\dot{\alpha}_{i_0}$ depending on their initial orientation α_{i_0}.

This approach assumes massless tethers with a prescribed motion of the parent body. Results show that the angular velocity has a period of $\alpha = 180°$, presenting the same instantaneous values at angles $\alpha = \{45°, 135°, 225°, 315°\}$. Choosing these angles as initial condition for each one of the four deputies $\alpha_{1_0} = 45°, \alpha_{2_0} = 135°, \alpha_{3_0} = 225°, \alpha_{4_0} = 315°$ eliminates the need of calculating the initial velocity for each deputy, and it is possible to select $r_s = 10$ in Eq. (3.9) for all four tethers $i = 1,2,3,4$.

Under the assumption of small and almost constant tether elongation and in the absence of significant out-of-plane motion, the phase portrait of the system is represented by the variation of $\dot{\alpha}_i$ vs α_i. As shown in Fig. 3.3(b), the presence of angular velocity variations due to the presence of gravitational field is confirmed. The angular separation between deputies 1 and 2 ($\gamma_{1,2}$) and the phase portrait are practically identical for the massive and the massless tether models (Fig. 3.3).

Results show that for the massive tether model, elongation Δl_i is slightly higher than in the massless case, due to the additional centrifugal force exerted by the beads on the tethers. Figure 3.4 shows the increase of distance of deputy $i = 1$ from the parent body with respect to the nominal unstretched length of the tether $\Delta r_{1/p} = \|\boldsymbol{r}_1 - \boldsymbol{r}_p\| - l_1^{(0)}$ (since the tethers are taut, $\Delta r_{1/p} = \Delta l_1$). The variation with respect to the massless tether model is small, if the 2 mm of increase in tether length is scaled with respect to the unstretched length of 1 km. If the ratio is taken with respect to the 20 mm of elongation, the percentage becomes more significant, being around 10%.

The same simulation also shows that the parent stays within the reference orbit with negligible drift. From a qualitative point of view the behavior of the system can be considered as equivalent to that obtained for the massless tether model, that perfectly suits this kind of application, without the additional complexity of the discretized massive tether. The additional elongation can be easily evaluated a posteriori by means of a static

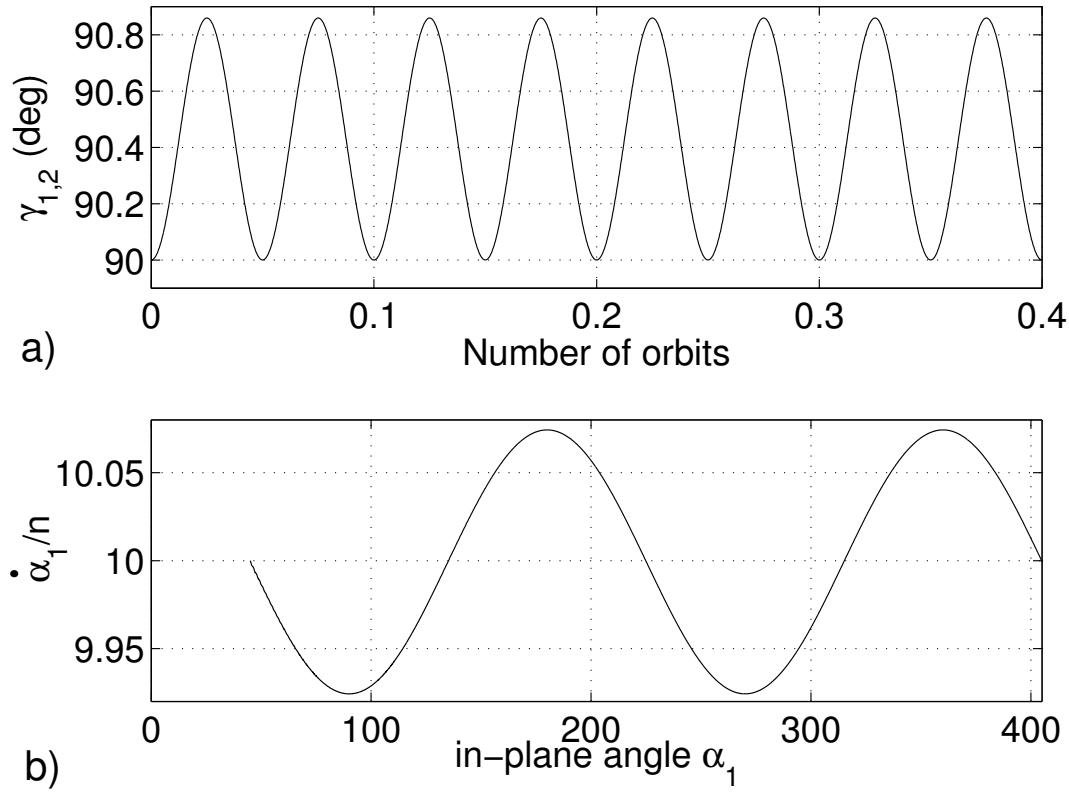

Figure 3.3: **HAS in-plane formation: (a) Angular difference $\gamma_{1,2}$, (b) Phase portrait for deputy $i = 1$.**

analysis for the additional centrifugal load induced by tether mass during the motion.

Closed Hub-And-Spoke in-plane formation

The closed in-plane formation presents the same size and nominal agent relative position of the open case, with the relevant difference represented by the external tethers that directly connect adjacent deputies. In order to properly analyze the shape of the formation, a rotating coordinate reference system is used, as in [15]. The rotating reference $\mathcal{S} : \{\hat{\mathbf{i}}_{\mathcal{S}}, \hat{\mathbf{j}}_{\mathcal{S}}, \hat{\mathbf{k}}_{\mathcal{S}}\}$ spins at the nominal angular velocity, $r_s n$, around the direction $\hat{\mathbf{k}}_{\mathcal{S}} = \hat{\mathbf{k}}_{\mathcal{R}}$, normal to the orbit plane, thus highlighting the relative motion of agents and tethers during the simulation, independently of the overall rotational position of the formation. The initial position and speed of the four deputies is set as for the open HAS formation, following the procedure discussed in the previous section in order to maintain the same angular velocity during the rotation.

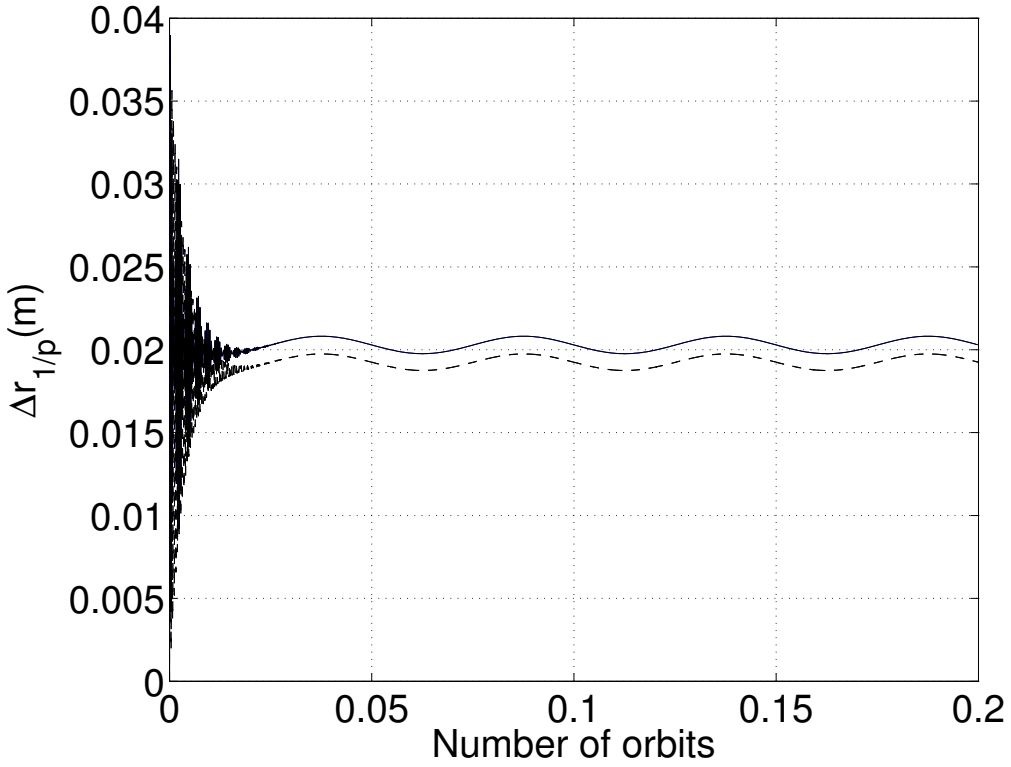

Figure 3.4: **Distance increment between first deputy and parent body $\Delta r_{1/p}$ for HAS in-plane formation (— massive tether; - - - massless tether)**

The evolution of the shape of the formation in the rotating frame for a simulation of four orbital periods is presented in Fig. 3.5, where X and Y are position variables in the $\hat{\mathbf{i}}_{\mathcal{S}} - \hat{\mathbf{j}}_{\mathcal{S}}$ plane, scaled with respect to $l_i^{(0)}$. External tethers are clearly subject to a centrifugal pull which affects their shape, with an influence on the relative position of deputies with respect to the parent body. In particular, the four external tethers achieve a "rounded" shape, with a variation in the direction of external tether tension acting on the deputies. The length of the external tethers does not vary enough, in the considered scenario, under the tension resulting from the centrifugal force in the transverse direction, so that the radial distance between the agents and the parent body becomes smaller than the nominal internal tether length. Increasing the rotation speed to higher values makes things worse, as the external tethers, subject to an increased centrifugal load, move even more pronouncedly outwards, emphasizing the rounding effect and further reducing the distance between agents and parent body.

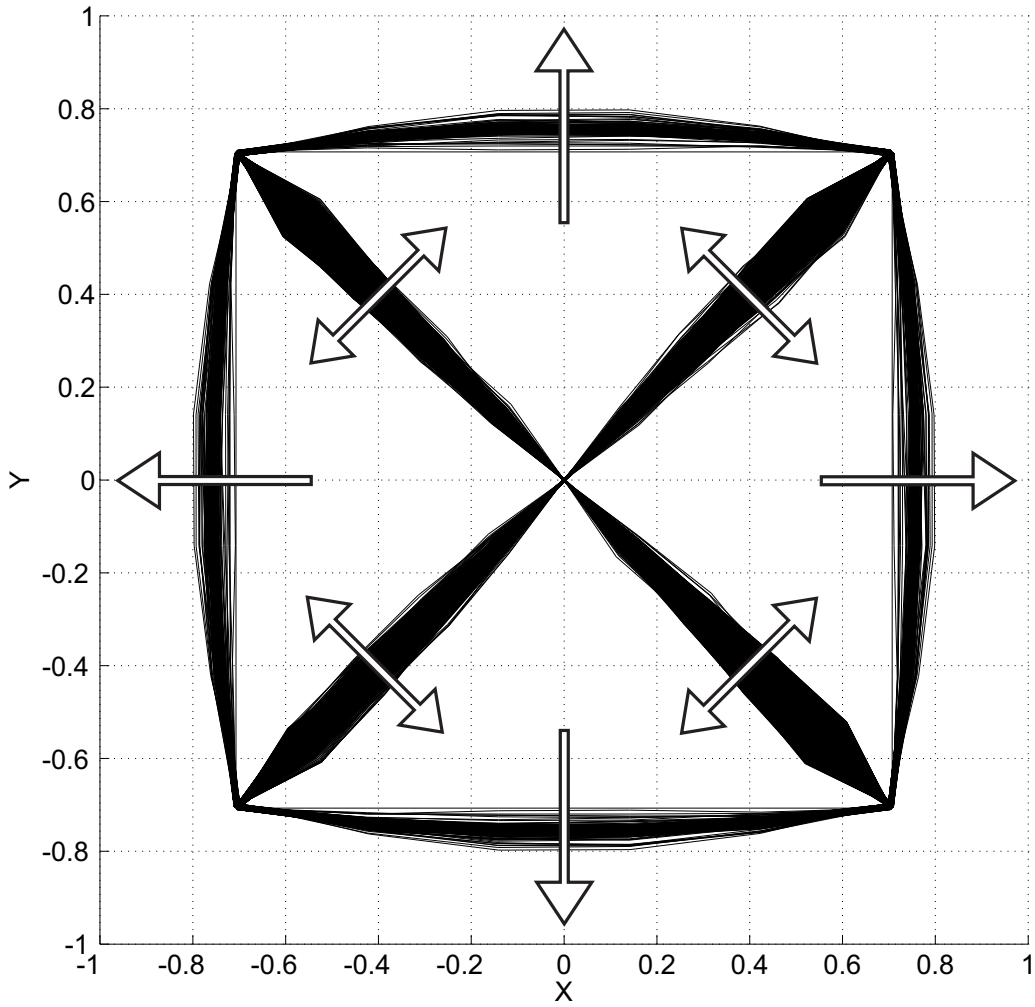

Figure 3.5: **Tether oscillations represented using rotating coordinates. CHAS in-plane formation.**

As a consequence, internal tethers are not in tension, and the elements used for discretizing their mass freely moves in the transverse direction, until a phase shift in the rotational motion puts the tether in tension for a brief moment, making the agent bounce back towards the parent. Figure 3.6(a), where the distance of deputy 1 from the parent body $\Delta r_{1/p}$ during the first two orbits of the simulation is represented, clearly shows this "bouncing" effect, where the distance remains shorter than tether nominal length most of the time and significant deformations of the tether from a straight line connecting the two bodies are thus present. The same behavior can be observed on $\Delta r_{2/p}$, $\Delta r_{3/p}$ and $\Delta r_{4/p}$. This effects cannot be captured by a massless tether model.

Figure 3.6(b) depicts the elongation $\Delta l_{1,2} = l_{1,2} - l_{1,2}^{(0)}$, where $l_{1,2}$ is calculated as the

sum of the 5 elastic elements used for the discretization of the tether. In this case, all external tethers extend beyond their nominal length and almost twice as much as it is predicted by the massless tether model (dashed line). In this scenario, the maximum distance between the parent body and the reference orbit grows to approximately 2.25 m, but the trajectory of the parent does not exhibit a clear drift away from the reference orbit, at least for the considered duration of the simulation. This means that, also in this case, the displacement of the parent from the center of mass of the formation is relatively small, if compared to the size of the formation.

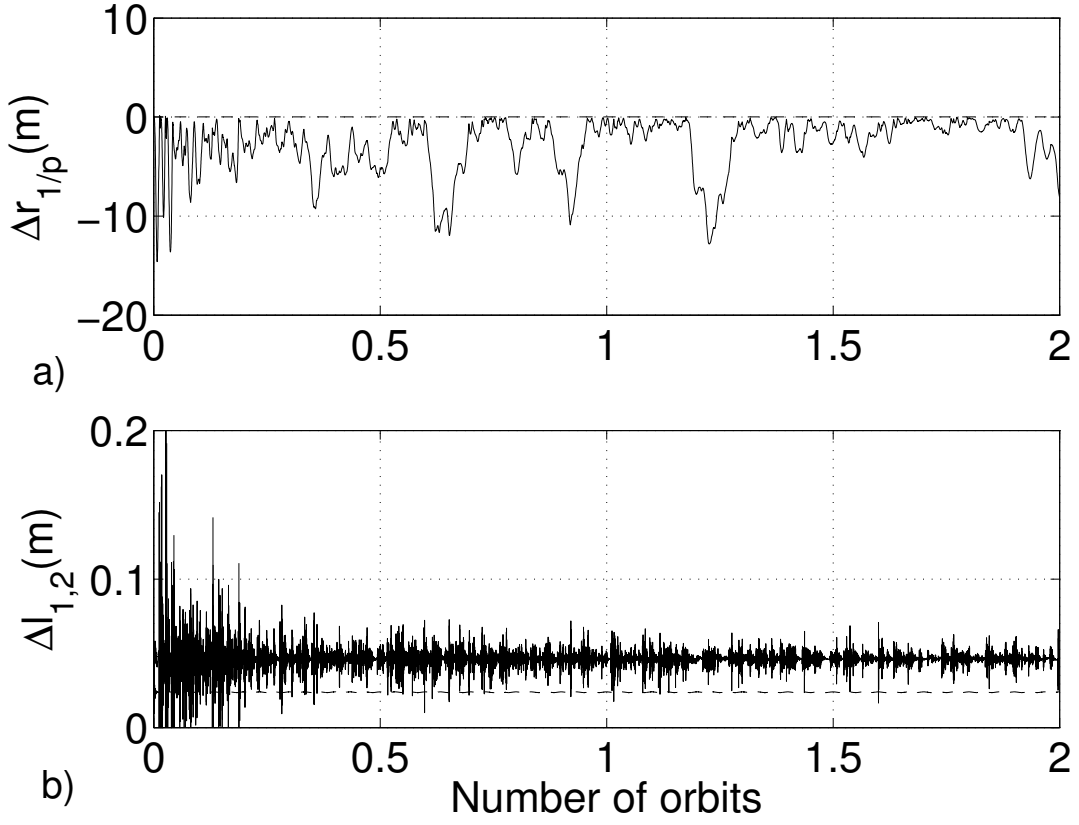

Figure 3.6: **CHAS in-plane formation (solid: massive tether; dashed: massless tether): (a) Distance increment between first deputy and parent body, (b) Length of tether connecting deputies 1 and 2.**

3.3.2 Earth-facing formations

For Earth-facing formations, the initial condition for the position of the four deputies of the formation is given by

$$\begin{aligned} \boldsymbol{r}_{1_0} &= [0\ l_i^{(0)}\ l_i^{(0)}] \cdot \sqrt{2}/2 = -\boldsymbol{r}_{3_0} \\ \boldsymbol{r}_{2_0} &= [0\ -l_i^{(0)}\ l_i^{(0)}] \cdot \sqrt{2}/2 = -\boldsymbol{r}_{4_0} \end{aligned} \tag{3.10}$$

Initial velocities are computed using Eq. (3.2) with the parent object placed at the origin of the LVLH frame and

$$\boldsymbol{\omega}_0 = [-r_s n\ \ 0\ \ 0] \tag{3.11}$$

where a value of $r_s = 10$ is used for the analysis of both open and closed Earth-facing formations, following the value used in [13]. The initial conditions for position and velocity of beads is computed following the procedure outlined at the beginning of this chapter.

In Earth-facing formations, deputies and tethers lie initially on the $\hat{\mathbf{j}}_{\mathcal{R}}$–$\hat{\mathbf{k}}_{\mathcal{R}}$ plane of the LVLH frame. Provided that initial values for z_i and $\dot{z}_i$ are not null, tridimensional trajectories are now expected.

Hub-And-Spoke Earth facing formation

The behavior of HAS Earth-facing formation in terms of distance between external agents and parent body, presented in Fig. 3.7, is similar to that observed for the in-plane formation considered in the previous subsection. Again, tether elongation is slightly higher for the massive model, due to the major centrifugal load, but shape and oscillation amplitude and period exhibit almost identical characteristics with respect to those determined on the basis of a formation model featuring purely elastic massless tethers.

More significant difference between the two models are highlighted in Fig. 3.8, where the angular displacemente $\gamma_{1,2}$ between deputies $i = 1$ and 2 is represented. As already highlighted in [13], the long term behavior is not ascertainable from this simulation, but for a massless tether model an instability is apparent after approximately 20 orbits, which makes the angular separation between tethers slowly drift away from its nominal value of 90°. This effect is not present in the massive model, for which the initial pattern for the initial angular displacement between deputies persists in time even for simulation intervals as long as 30 orbit periods. Tether mass thus plays a stabilizing effect on formation shape, which is not captured by the massless tether model.

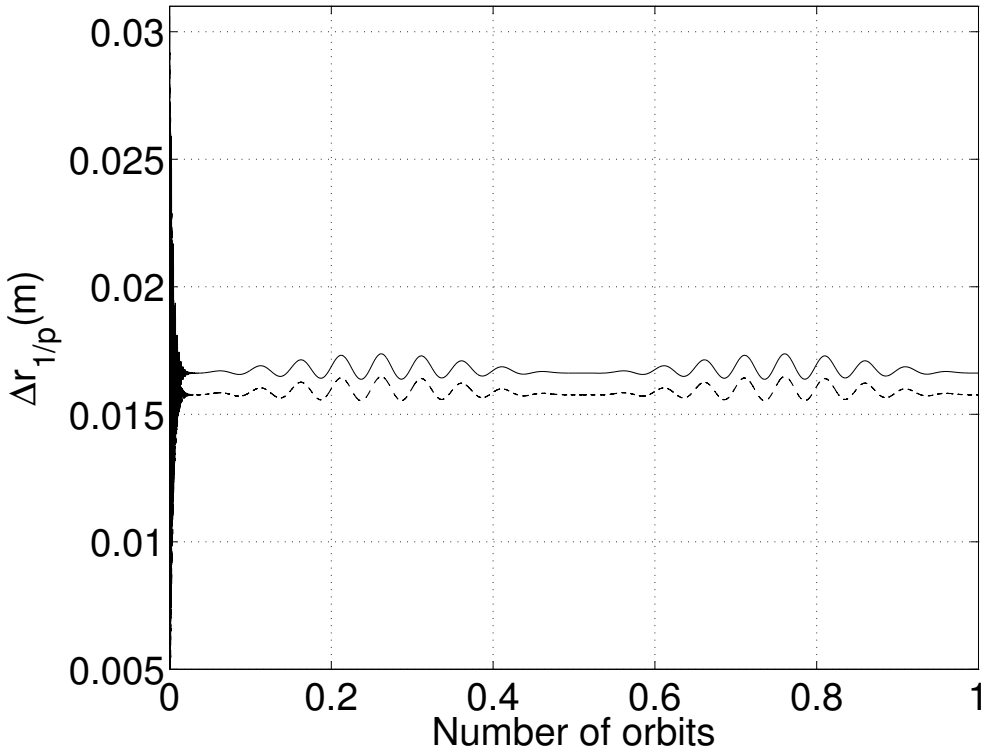

Figure 3.7: **Distance increment between first deputy and parent body $\Delta r_{1/p}$ for HAS earth-facing formation (— massive tether; - - - massless tether).**

The consequence of the coupling between in–plane and out–of–plane dynamics that characterizes this scenario makes the orientation between the formation plane and the radial axis not constant. This means that the formation is not constantly facing the Earth during the orbit. In particular, the variation of angle δ (as in Eq. (3.6)) shown in Fig. 3.9(a) is almost perfectly linear and it goes from -180 to +180° in a period exactly equal to one orbital period. This fact, described in [13] for the massless tether model without a physical explanation, can be interpreted in light of the principle of angular momentum conservation: the formation spins around an inertially fixed direction, $\hat{\mathbf{i}}^{\star}_{\mathcal{R}}$, parallel to $\hat{\mathbf{i}}_{\mathcal{R}}$ at time $t = 0$. The resulting angular momentum, parallel to $\hat{\mathbf{i}}^{\star}_{\mathcal{R}}$, remains almost constant in the absence of significant external torques acting on the formation. As a matter of fact, the angular momentum is not conserved due to the gravity gradient torque. However, it's value is small and it can be shown to have zero average value over one orbit for the spinning formation, so that the (almost) inertially fixed unit vector $\hat{\mathbf{i}}^{\star}_{\mathcal{R}}$ apparently rotates around $\hat{\mathbf{k}}_{\mathcal{R}}$, when seen in the LVLH frame.

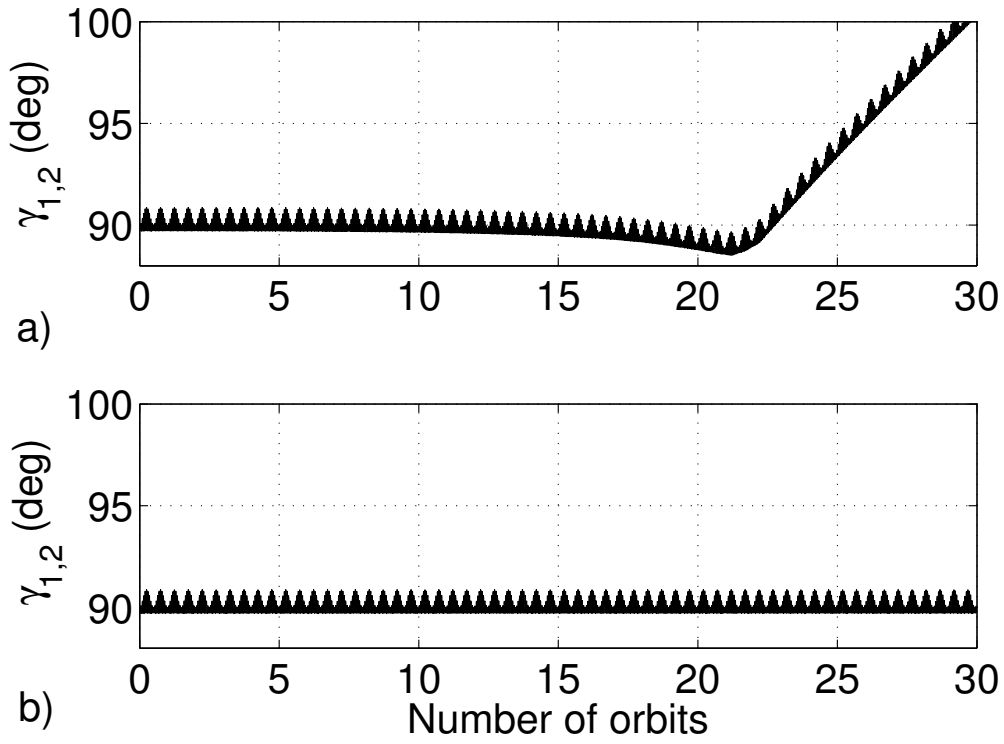

Figure 3.8: **Angular separation between tethers 1 and 2 for HAS Earth-facing formation: (a) Massless tether model, (b) Massive tether models.**

The so called Earth-facing formation is thus not truly facing the Earth during the orbital motion and it appears as an unfeasible solution for Earth-observation missions, at least for this types of configurations for agents and tethers. For in-plane formations the spin axis coincides with the normal to the orbit plane, which is at least approximately an inertially fixed direction (at least for purely Keplerian motion, when orbit perturbations are neglected), so that in-plane formation maintain their initial orientation in the LVLH frame.

In spite of the variation of angular separation between tethers and relative rotation of the formation with respect to the LVLH frame, the agents remain on the same plane for both the massless and massive tether models. This is shown in Fig. 3.9(b), where the coplanarity parameter C, defined as in Eq. (3.7) is represented. Moreover, the parent remains close to the reference orbit with negligible deviations, as for the massless tether model, so that the only, yet significant, difference between the two models is in the long term behavior of the angular separation between tethers.

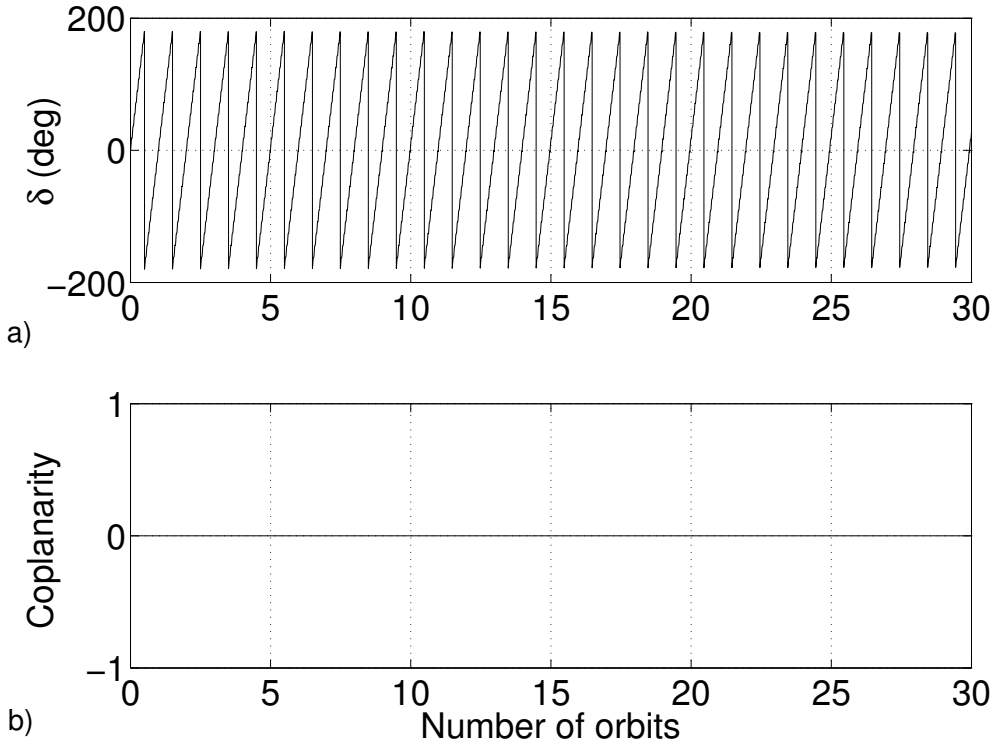

Figure 3.9: **HAS Earth-facing formation: (a) Orientation of the formation plane, (b) Coplanarity measure for deputies and parent body**

Closed Hub-And-Spoke Earth facing formation

The initial condition for the position of agents of the CHAS Earth-facing formation is define as for the corresponding HAS case, with the addition of discretized external tethers, modeled, as usual, with 5 segments and 4 beads. As for the Earth-facing HAS case, the plane of the formation performs a complete rotation around the unit vector normal to the orbit plane, $\hat{\mathbf{k}}_{\mathcal{R}}$, in a time interval equal to the orbit period (see Fig. 3.10(a), where angle δ is shown for a simulation lasting 4 orbits), while the agents remain on the same plane (see the coplanarity measure, C, reported in Fig. 3.10(b)).

The external tethers present the same rounding effect observed for closed in-plane formation, with identical consequences for the internal tethers, that lack tension. The oscillations and variations of distance between formation agents are qualitatively similar to those observed in the CHAS in-plane scenario. As shown in Fig. 3.11(a), internal tethers

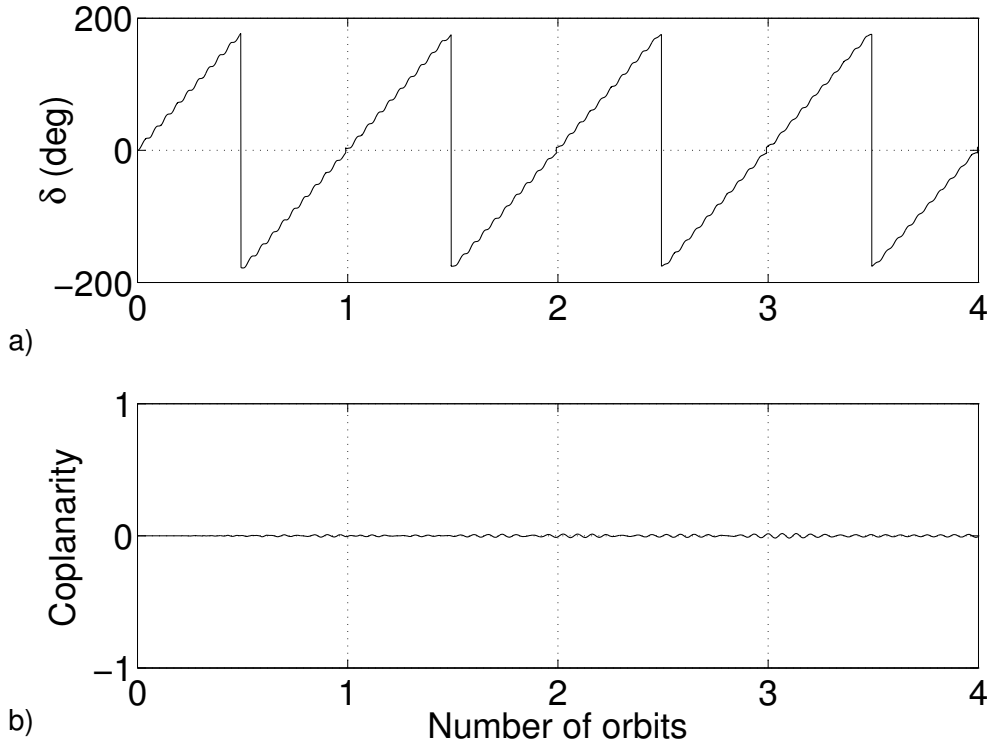

Figure 3.10: **CHAS Earth-facing formation: (a) Orientation of the formation plane, (b) Coplanarity measure for deputies and parent body.**

do not get fully extended, and agents bounce back towards the parent when the corresponding tether becomes taut, as in the CHAS in-plane scenario. At the same time, the external tethers are subject to a higher tension and a correspondingly increased elongation with respect to the massless tether case (Fig. 3.11(b)).

The behavior of the CHAS Earth-facing formation thus adds up features of both the HAS Earth-facing and the CHAS in-plane cases. In this scenario, the maximum distance between the parent body and the reference orbit grows to 7.47 m, but, in spite of this higher deviation, the trajectory does not exhibit a clear drift of the parent body away from the reference orbit, at least for the duration of the simulation here considered, equal to 4 orbital periods.

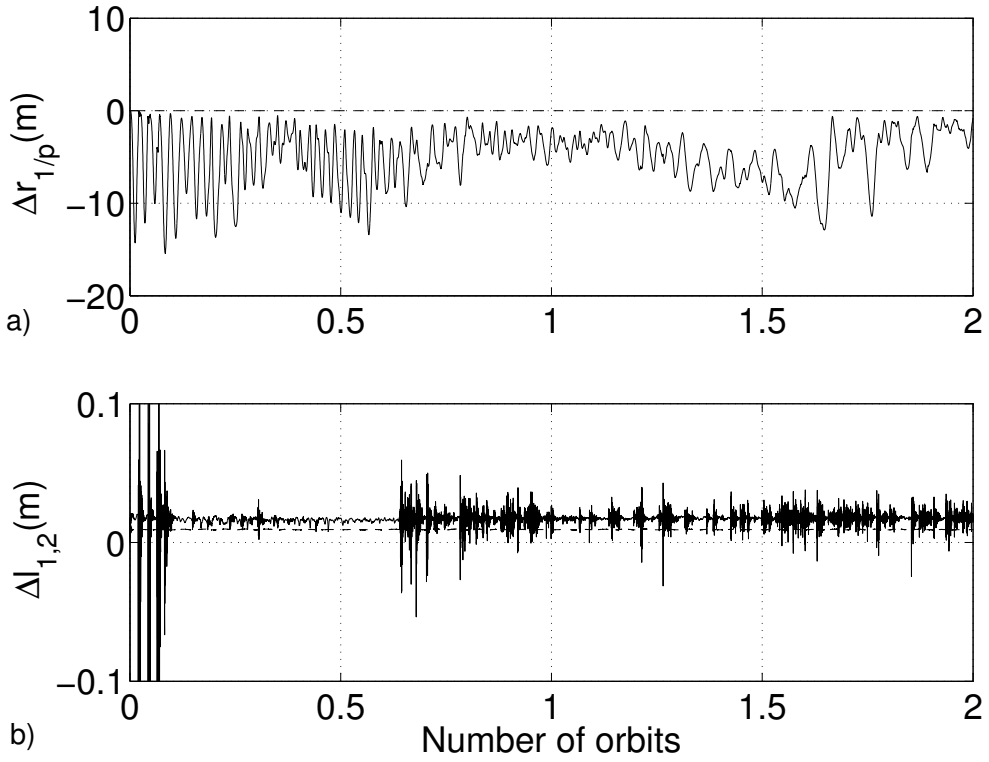

Figure 3.11: **CHAS Earth-facing formation (solid: massive tether; dashed: massless tether): (a) Distance increment between first deputy and parent body, (b) Length of tether connecting deputies 1 and 2.**

Double-pyramid Earth-facing formation

The double-pyramid formation is based on a CHAS Earth-facing formation, with the addition of two anchor masses along the radial direction, one placed between the formation plane and the Earth, and the second placed beyond the formation plane. In the scenario considered here, derived from the data used in [13] for the sake of comparison, anchors have a mass equal to 400 kg. In this case, tethers belonging to the initial CHAS Earth-facing structure are modeled using $n_b = 4$ beads per tether, as before. The tethers connecting anchors with deputies are modeled with $n_b = 6$ beads per tether. Tether connecting anchors with the parent body are discretized by means of $n_b = 3$ beads per tether only, as they remain closer to the formation spin axis and they are thus expected to be less prone to oscillations, because of a reduced centrifugal load.

The initial position for deputies of this formation is defined as in the CHAS Earth-facing formation (see Eq. (3.10)). The rotation rate around $\hat{\mathbf{i}}_{\mathcal{R}}$ is increased to $\omega = 11n$

(that is, $r_s = 11$), for consistency with the values used in [13]. The initial condition for anchors is defined as

$$\boldsymbol{r}_{5_0} = [l_{a,p}^{(0)}\ 0\ 0] = -\boldsymbol{r}_{6_0} \tag{3.12}$$

where $l_{a,p}^{(0)} = 10000$ m. The initial position for beads and the computation of initial velocities for tethers connecting anchors to the remaining bodies of the formation is performed as in section 3.2.

The simulation shows how the bending effect observed in the CHAS formation is amplified here for the case of external tethers connecting anchors with deputies of the CHAS frame. As it happens in external tethers of the CHAS frame, beads belonging to tethers connecting anchors with deputies do not have any radial spoke that limits the outward movement due to centrifugal force. Since tethers connected to anchors are long, they have a considerable mass compared to that of deputies, and therefore the effect of centrifugal force on them is even more noticeable. Figure 3.12(a) clearly shows how deputy 1 is well below the possibility of fully extending the internal tether, and it appears to fluctuate in space, without almost ever reaching a taut condition during the initial portion of the simulation ($t \leq 0.2T_O$, where $T_O = 2\pi/n$ is the orbital period). This is a totally different situation with respect to what is observed for an identical formation featuring a simplified massless tether model, where all tethers appear to be always in tension (see Fig. 3.12(b)).

At the same time, the presence of the anchors has a stabilizing effect on the orientation of the formation plane, thanks to the gravity gradient torque acting on the anchors placed in the radial direction. In this case, the angle δ defined above for Earth-facing scenarios (Eq. (3.6)) exhibits bounded oscillations, as opposed to HAS and CHAS Earth-facing simulations, where an almost constant angular rate around $\hat{\mathbf{k}}_{\mathcal{R}}$ relative to the LVLH frame was present. However, the results shown in Fig. 3.13 indicates a remarkably large deviation from the desired Earth-facing condition for the massive tether model, where pitch rotations up to approximately 15° are reached (solid line in Fig. 3.13(a)), and the deputies are not coplanar (Fig. 3.13(b)). These deviations from the ideal alignment of the formation are again associated to tether mass, as they are not present when a simplified model of the same formation with massless tethers is considered. The oscillation can be explained in virtue of three factors: the bouncing effect exhibit by closed planar formations (as discussed before), the pull exerted by the bending of tethers connecting deputies with anchors, and due to the fact that by the characteristics of the Likins-Pringle conical equilibrium, the formation should be tilted a certain angle (due to the the effect of gravitational torque).

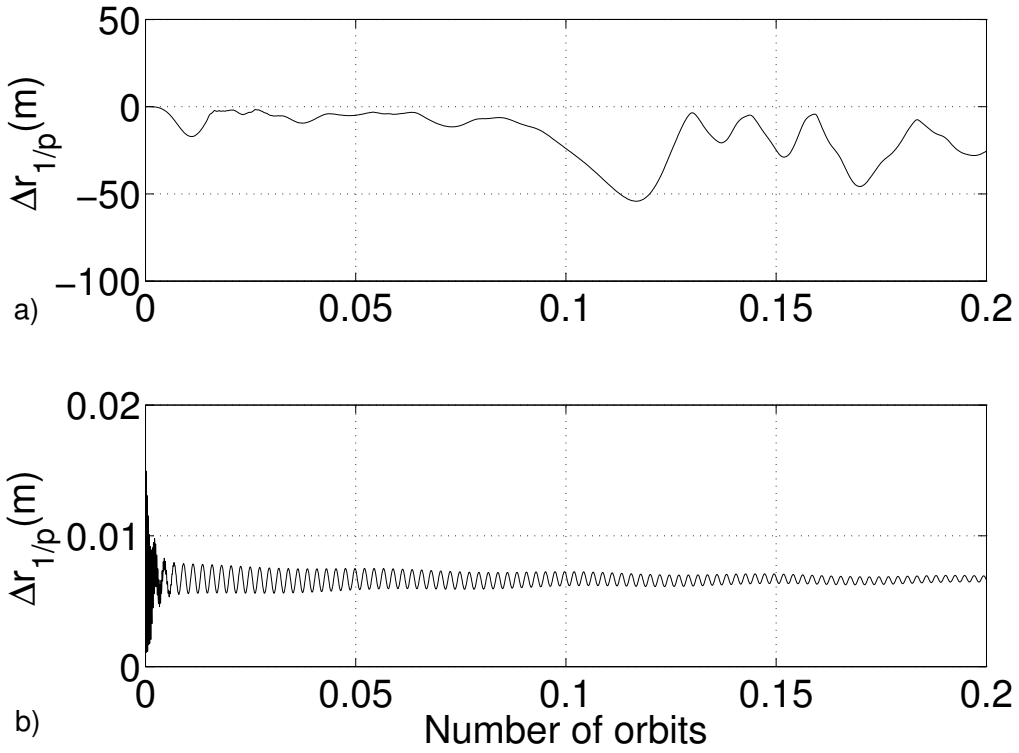

Figure 3.12: **DP formation. Distance increment between first deputy and parent body: (a) Massive tether model, (b) Massless tether model.**

The corresponding results, in this case, show pitch misalignment in the order of a fraction of a degree (dashed lines in Fig. 3.13(a)) and a perfect coplanarity of the agents of the formation.

Figure 3.14 shows the projection in the $\hat{\mathbf{i}}_{\mathcal{R}} - \hat{\mathbf{k}}_{\mathcal{R}}$ plane of the trajectories of the orbiting elements. The deputies oscillate in the $\hat{\mathbf{i}}_{\mathcal{R}}$ direction, thus harming the coplanarity requirement. The most remarkable feature of the formation is the bending of the diagonal tethers between deputies and anchors. When the tether is bended by centrifugal force, the anchors get closer to the parent and the internal tether looses tension. This can be seen by the wide amplitude motion of the 6 beads between the anchors and the parent body, that hardly move along the radial axis, but freely float in the transverse direction.

The plot clearly shows how the distance from the nominal rotation axis $\hat{\mathbf{i}}_{\mathcal{R}}$ becomes

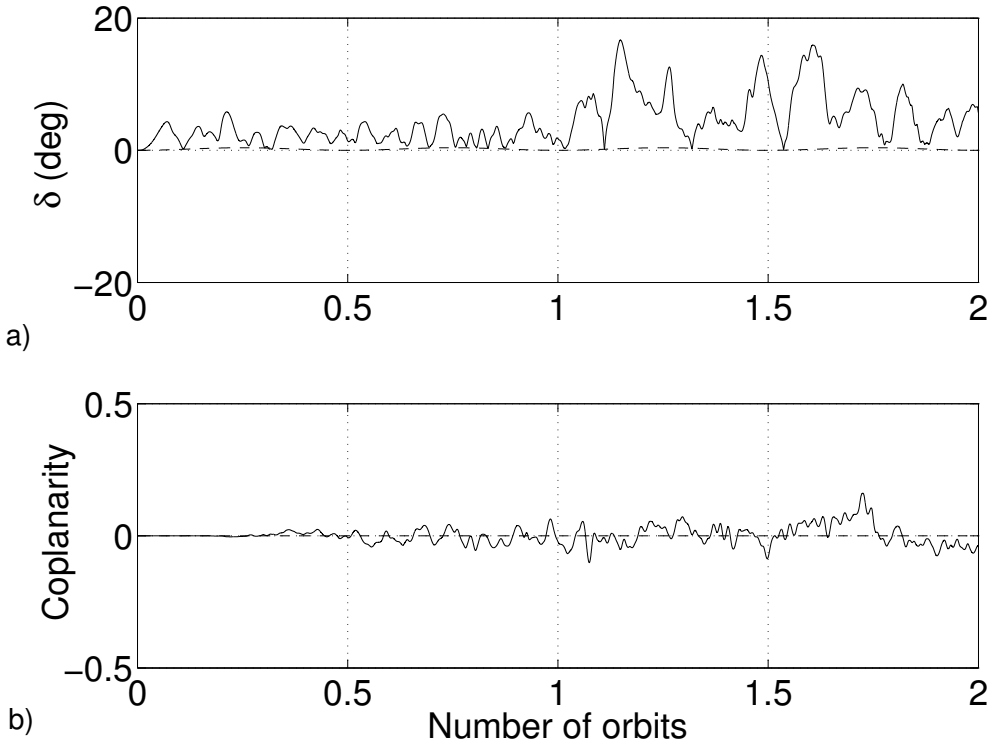

Figure 3.13: **DP formation: (a) Orientation δ, (b) Coplanarity measure for deputies and parent body.**

much larger for beads than for deputies. The same bending effect produced by external tethers in Earth-facing formations is here produced for diagonal tethers, thus adding a sizeable interference with agents coplanarity to the reduction of the distance between deputies and central parent body in the $\hat{\mathbf{j}}_{\mathcal{R}} - \hat{\mathbf{k}}_{\mathcal{R}}$ plane. Only if linear density of tethers is reduced to a (technologically not feasible) value of one tenth of the nominal figure derived for current state-of-the-art tethers, the bending effect is reduced and the results of the simulation (not reported for the sake of conciseness) gets closer to the ideal massless tether model.

Finally, Fig. 3.15 shows the value of the coordinates of the parent body of the formation, which experiences increasingly wider oscillations in all three directions, with amplitudes that become higher than 100 m in less than 2 orbits, that is, of a size comparable with the nominal length of internal tethers (1 km).

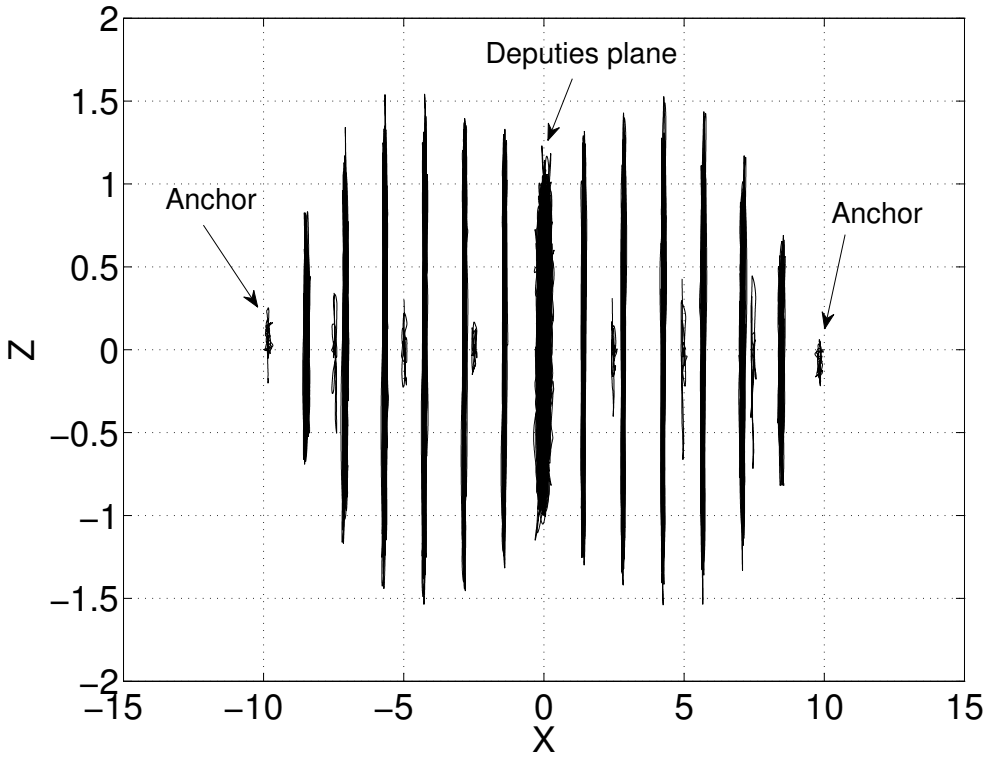

Figure 3.14: **DP formation. Projection of trajectories on $\hat{\mathbf{i}}_{\mathcal{R}} - \hat{\mathbf{k}}_{\mathcal{R}}$ plane for a 2 orbital period simulation.**

3.4 Circular formations

Simulations performed for closed formations show a clear tendency of external tethers to bend outwards under centrifugal loads, thus resulting in an action that reduces the distance between deputies and parent body of the formation. To avoid this problem, a formation with external circular tethers is proposed with a nominal length equal to $l^{(C)} = (\pi/2) \cdot l^{(0)}$. In this way, mass elements that discretize tether mass are placed at the same distance from the center of the formation as deputies, thus experiencing the same centrifugal acceleration. Tension forces exerted by external tethers act along the tangential direction for all deputies and beads and the effect is that internal tethers remain taut.

3.4.1 Closed Hub-And-Spoke in-plane formation

The first simulation for circular external tethers consist of a CHAS in-plane formation in which deputies are connected through four external circular tethers with a nominal length equal to $l^{(C)}$, that allow for a circularization of the external tethers and a uniform

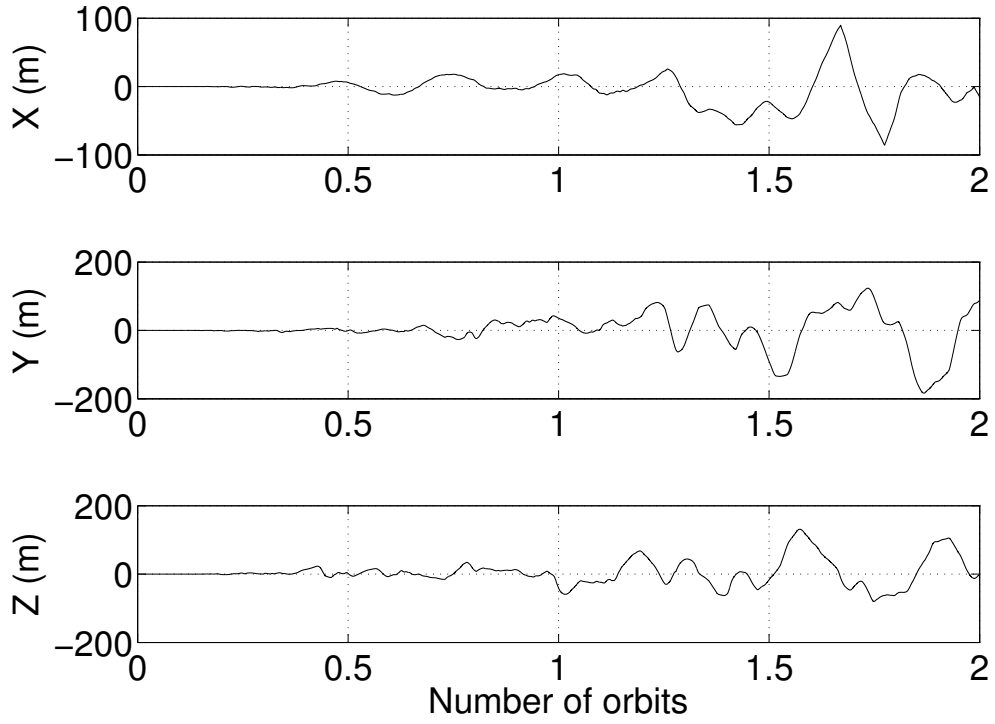

Figure 3.15: **DP formation. Parent body coordinates evolution.**

distribution of centrifugal loads and tangential tension along the external links. In this situation the beads that represent the discretized mass of the external tethers are placed at the same distance from the center of mass, with equal initial tangential velocities. As expected, deputies and beads are constrained by elastic forces from adjacent tether elements along approximately the same tangential direction, and internal tethers remain taut (as shown in Fig. 3.16(a) for deputy 1), thus resulting into a much more regular behavior than internal tethers in formations with rectilinear external tethers. The angular separation between adjacent internal tethers presents bounded oscillations around 90°, as shown in the bottom part of the same figure for tethers 1 and 2.

Figure 3.17 represents the evolution of tether beads and formation agents for the formation featuring circular tethers, as seen in a rotating frame that spins at an angular speed equal to $r_s n$ around $\hat{\mathbf{k}}_{\mathcal{R}}$. The figure was generated by running a simulation for 10 orbital periods. A much more stable behavior can be observed, with oscillations of negligible size for both internal and external tethers, if compared to the results obtained

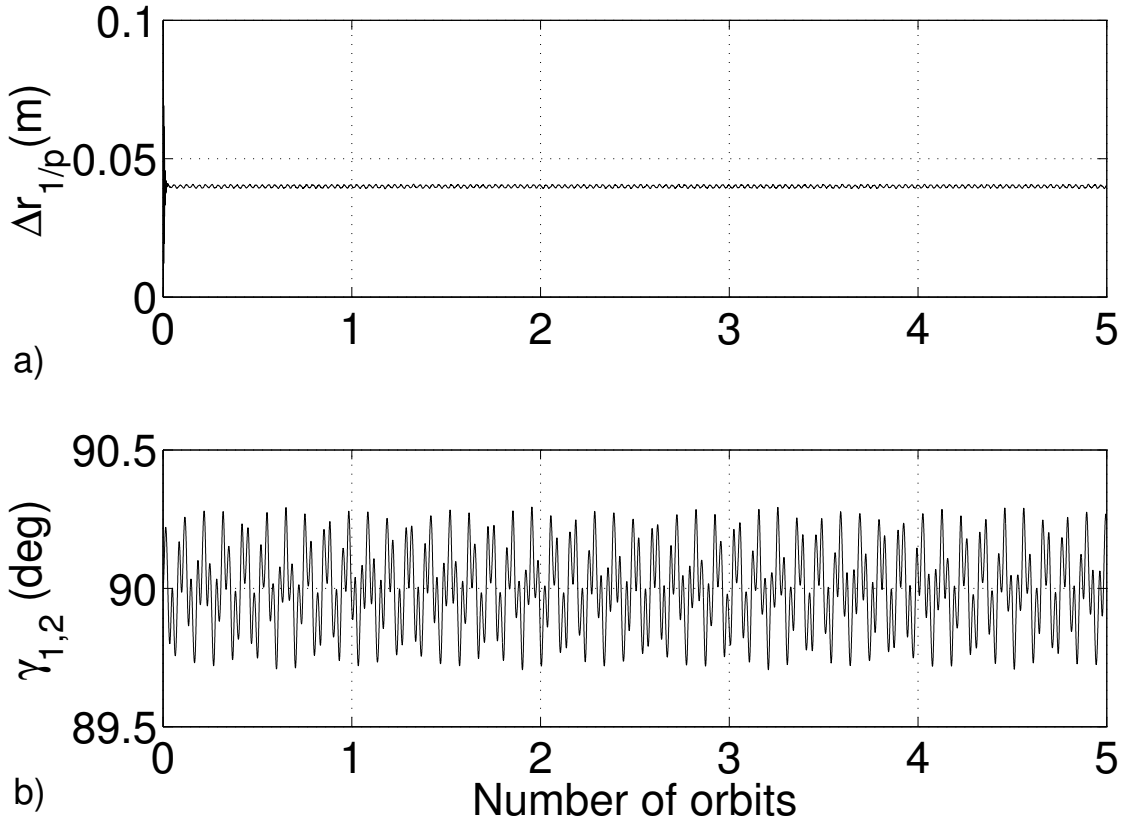

Figure 3.16: **CHAS In-plane formation with circular external tethers: (a) Distance increment between first deputy and parent body $\Delta r_{1/p}$, (b) Angular difference ($\gamma_{1,2}$).**

for straight external tethers, represented in Fig. 3.5.

As discussed in Section 3.3.1 for in-plane formations, when agents are placed at phase angles equal to $\alpha = \{45°, 135°, 225°, 315°\}$, the Hamiltonian of all the deputies has the same value [13], which is a convenient feature for preserving the angular displacement between adjacent tethers. When deputies are placed at $\alpha = \{0°, 90°, 180°, 270°\}$, the values of the individual Hamiltonian for the four deputies are different, unless initial velocity of the deputies is corrected. This issue is crucial for open HAS formation, whereas closed formations with massless external tethers preserve angular distance between internal tether without the need for correcting initial agents velocities. In the equivalent massive tether model, the angular difference remains bounded, but an irregular behavior was highlighted.

As a further advantage for circular tethers, the formation appears to be less sensitive

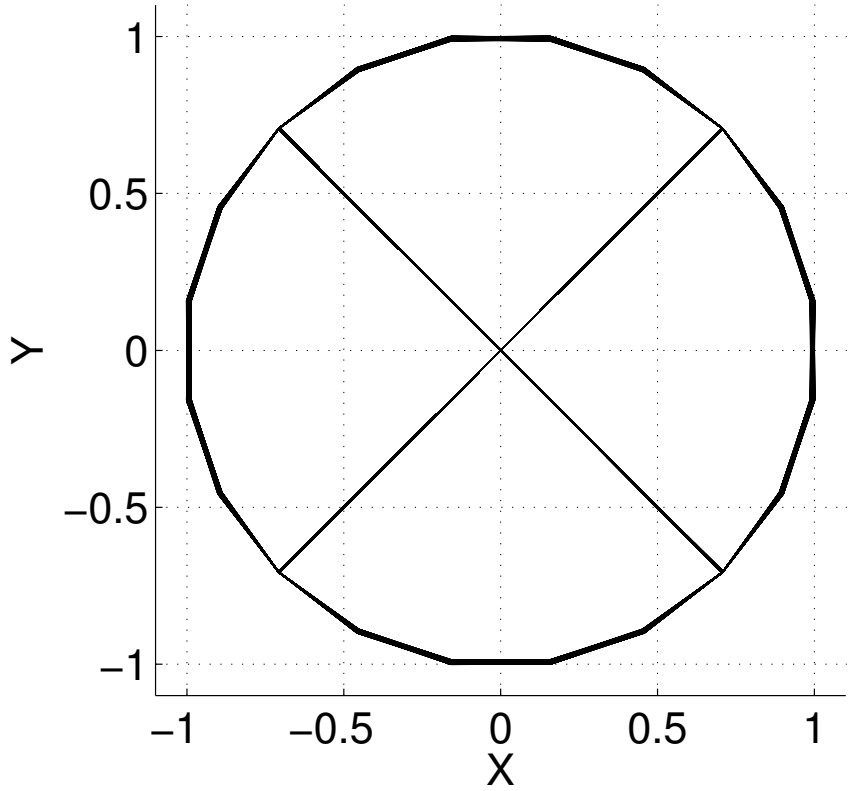

Figure 3.17: **CHAS in-plane formation with round external tethers. Tether oscillations represented using rotating coordinates.**

to the issue of the Hamiltonian for the deputies. In this particular scenario, with deputies initially placed at $\alpha = \{0°, 90°, 180°, \text{and } 270°\}$, the initial position of the four deputies is given by

$$\begin{aligned} \boldsymbol{r}_{1_0} &= [l_i^{(0)}\ 0\ 0] = -\boldsymbol{r}_{3_0} \\ \boldsymbol{r}_{2_0} &= [0\ l_i^{(0)}\ 0] = -\boldsymbol{r}_{4_0} \end{aligned} \tag{3.13}$$

where $l^{(0)} = 1000$ m. Initial velocity is computed using Eq. (3.9) with $r_s = 10$. Results presented in Fig. 3.18 for 10 orbital periods show that angular difference is preserved. Figure 3.19(a) shows that the internal tether associated to deputy 1 remains always taut, whereas Fig. 3.19(b) demonstrates that the angular difference is bounded around 90°.

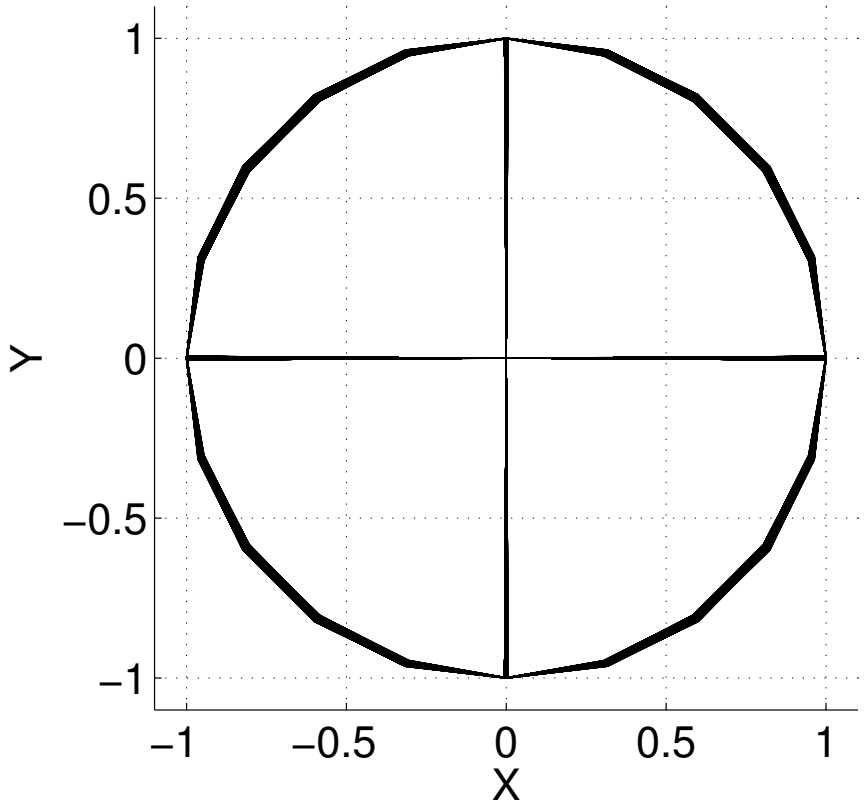

Figure 3.18: **CHAS in-plane formation with round external tethers. Tether oscillations represented using rotating coordinates.**

3.4.2 Earth-facing formations

Using the initial conditions defined in Section 3.3.2, a simulation is performed using circular external tethers also for an Earth-facing formation. The behavior of the pitch angle δ and the coplanarity measure (Fig. 3.20) show results similar to those presented in Fig. 3.10 for the corresponding CHAS Earth-facing formation with straight external tethers. As a major difference, in this case internal tethers remain in tension and a regular behavior for the position of the agents and of the parent body along the nominal orbit is obtained, as shown in Fig. 3.21.

When one tries to stabilize the Earth-facing attitude by introducing anchors along the radial direction, the bending of diagonal tethers connecting anchors to deputies cause the anchors to move inwards, towards the parent body and this condition cannot be corrected simply by making the diagonal tethers longer. The use of circular external tethers and

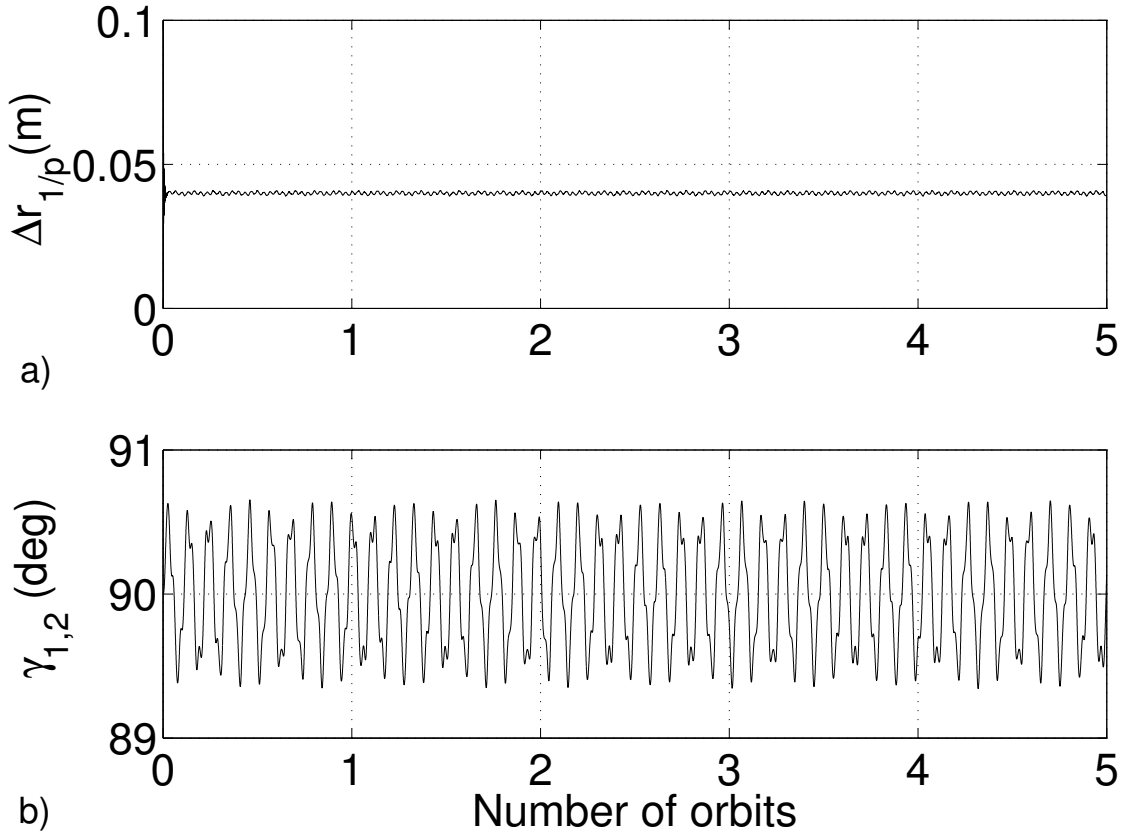

Figure 3.19: **CHAS In-plane formation with circular external tethers: (a) Distance increment between first deputy and parent body $\Delta r_{1/p}$, (b) Angular difference $\gamma_{1,2}$.**

longer diagonal ones apparently does not compensate for the action of centrifugal loads and the motion of the double-pyramid formation remains irregular, as in the previous case analyzed in Section 3.3.2.

3.5 Major findings for tethered formation dynamics

The dynamics of tethered satellite formation was studied, showing that the massless tether model is sufficiently accurate for capturing the most relevant aspects of the behavior of the formation only for open ones, whereas tether mass affects formation dynamics for closed configurations featuring external tethers, inducing significant effects neglected by a more elementary modeling approach. A shape instability for the closed formation is apparent, affecting the position of deputies with respect to the parent body. The fact that tethers linking deputies with the parent body do not remain taut makes the deputies bounce back

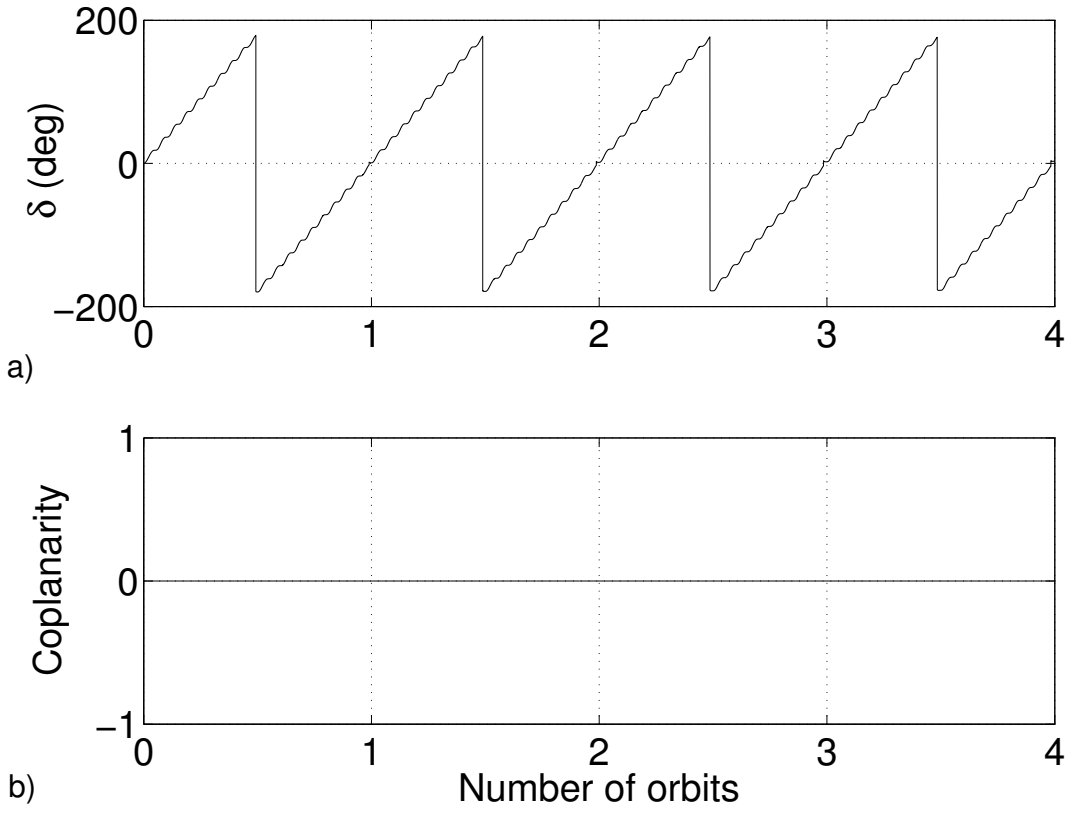

Figure 3.20: **CHAS Earth-facing formation with circular external tethers: (a) Formation orientation δ, (b) Coplanarity measure for deputies and parent body.**

towards the parent body after full extension is reached. This instability is induced by the variation in the shape of the external tethers and it cannot be predicted by means of the simpler massless-cable model. In the case of the double-pyramid formation the instability is even more serious, due to the fact that diagonal tethers connecting anchors to external deputies experience the same centrifugal pull as the external tethers of closed formations, but they are longer and more massive, thus inducing a more pronounced "bulging" effect on the shape of the pyramid.

The behavior of the cluster as a whole, for open formations, is comparable to the one predicted by the massless model with prescribed motion of the parent body. However in closed formations, and more pronouncedly for the double-pyramid case, the parent body of the formation does not remain on the reference orbit, as a consequence of the irregular motion of agents, due to lack of tension in the internal tethers when external ones bend

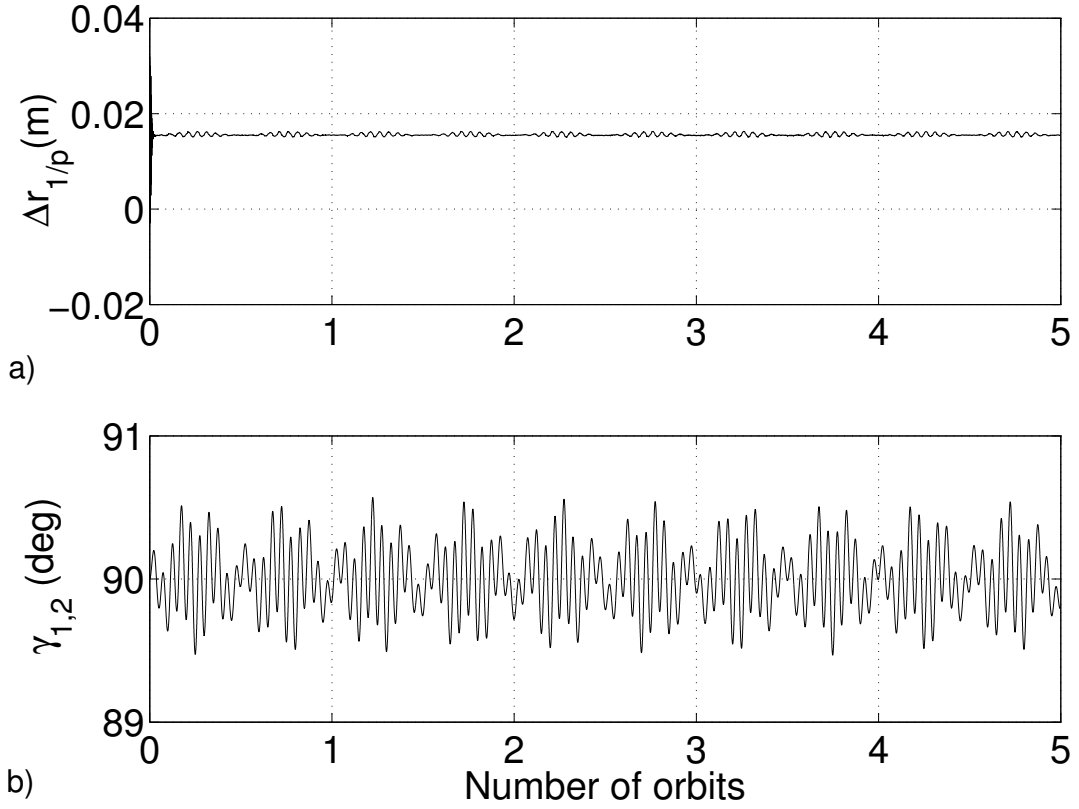

Figure 3.21: **CHAS Earth-facing formation with circular external tethers: (a) Distance increment between first deputy and parent body $\Delta r_{1/p}$, (b) Angular difference between adjacent tethers 1 and 2 ($\gamma_{1,2}$).**

under the action of centrifugal loads. This situation can be corrected for closed planar formations by increasing the length of external tethers, in order to make them circular, but the same strategy does not apply to the Double-Pyramid case.

Chapter 4

Multi-tethered formation dynamics for non-ideal operating conditions

In the previous chapter an ideal condition was assumed, when purely Keplerian motion was considered and a reference circular orbit was selected. Orbit perturbations and a non-zero value of the eccentricity for the whole orbit may lead to significant changes on tethered formation dynamics, either when the formation is considered as a whole, or when the relative position of each agent is considered. As an example, changes in the gravitational force during an orbital period, lead to behavior non-observed in circular orbits as shown in Ch. 2. At the same time, Table 2.1 lists the most significative perturbation in LEO is due to variations in the Earth potential due the Earth oblateness. The present chapter is focused on the effects of reference orbit eccentricity [135] and Earth's oblateness [136] on tethered formation dynamics.

4.1 Effects of eccentricity of the reference orbit on Multi–Tethered Satellite Formations

When a non-circular reference orbit is considered, the dynamics of each agent of the multi-tethered formation can be expressed by means of a model proposed in [17], where the equations of relative motion for two spacecraft on neighboring elliptical orbits are derived using time as independent variable (as shown in Equation 2.13), and then transformed using true anomaly θ as the independent variable, in order to achieve a simpler compact,

periodic formulation. The transformation hinges on the chain rule for derivatives,

$$\dot{(\cdot)} = (\cdot)'\,\dot{\theta}\ ; \quad \ddot{(\cdot)} = (\cdot)''\,\dot{\theta}^2 + \dot{\theta}\,\dot{\theta}'(\cdot)' \tag{4.1}$$

where a dot and a double dot indicate first and second derivatives with respect to time t, respectively, whereas a prime and a double prime sign indicate first and second derivatives with respect to θ.

For an object describing an elliptical orbit, the angular velocity depends on the true anomaly. Letting e be the eccentricity of the orbit of the parent body and n the mean motion, the local angular velocity of the orbiter along the reference orbit is given by [55]

$$\dot{\theta} = \frac{n(1+e\cos\theta)^2}{(1-e^2)^{3/2}} \tag{4.2}$$

When the distance between the orbiting bodies remains small compared to the distance of the origin O of the orbit frame from the center of the Earth, gravitational field can be linearized around the current position of the centre of mass of the formation along the reference orbit. The state vector for the i-th agent is given by its position and relative position rates in the LVLH frame, that is, $\boldsymbol{X}_i = (x_i', x_i, y_i', y_i, z_i', z_i)^T$. Note that position rates with respect to true anomaly θ of the center of mass (indicated by primes) are used instead of velocity components. The equations of motion for the i-th agent are expressed by means of a periodic linear system in the form

$$\frac{d\boldsymbol{X}_i}{d\theta} = [\boldsymbol{A}(e,\theta)]\ \boldsymbol{X}_i + [\boldsymbol{B}(n,e,\theta)]\ \boldsymbol{f}_i/m_i \tag{4.3}$$

where the periodic matrices $\boldsymbol{A}$ and $\boldsymbol{B}$ are defined, respectively, as [17]

$$\boldsymbol{A} = \begin{bmatrix} \frac{2e\sin\theta}{\zeta} & \frac{3+e\cos\theta}{\zeta} & 2 & \frac{-2e\sin\theta}{\zeta} & 0 & 0 \\ 1 & 0 & 0 & 0 & 0 & 0 \\ -2 & \frac{2e\sin\theta}{\zeta} & \frac{2e\sin\theta}{\gamma} & \frac{e\cos\theta}{\zeta} & 0 & 0 \\ 0 & 0 & 1 & 0 & 0 & 0 \\ 0 & 0 & 0 & 0 & \frac{2e\sin\theta}{\zeta} & \frac{-1}{\zeta} \\ 0 & 0 & 0 & 0 & 1 & 0 \end{bmatrix}$$

and

$$\boldsymbol{B} = \frac{(1-e^2)^3}{\zeta^4 n^2} \begin{bmatrix} 1 & 0 & 0 \\ 0 & 0 & 0 \\ 0 & 1 & 0 \\ 0 & 0 & 0 \\ 0 & 0 & 1 \\ 0 & 0 & 0 \end{bmatrix}$$

with $\zeta = (1 + e\cos\theta)$. External forces and disturbances $\boldsymbol{f}_i$ acting on the generic i-th agent of the formation are also expressed in the LVLH frame, $\boldsymbol{f}_i = f_{x,i}\hat{\mathbf{i}}_{\mathcal{R}} + f_{y,i}\hat{\mathbf{j}}_{\mathcal{R}} + f_{z,i}\hat{\mathbf{k}}_{\mathcal{R}}$, where $\boldsymbol{f}_i$ is the sum of external forces minus gravity (which is already accounted for) acting on the i-th body of mass equal to m_i.

4.1.1 Initial conditions for deputies and beads

Equation (4.3) is used to describe the motion of each deputy, bead and the parent body of the formation. A set of initial conditions expressed in terms of position and velocity is required for each one of these bodies, represented as a mass element. As mentioned above, the independent variable is the true anomaly instead of time. For this reason, equations are defined in terms of position rates and angular rates (with respect to θ) instead of velocities. The geometry of the system is determined by the position of deputies $\boldsymbol{r}_i$ in the LVLH frame and how connecting tethers are arranged. First of all, the initial conditions on position and position rates need to be defined for parent body and deputies. The initial conditions for the beads are then derived from the former ones.

The initial condition for the velocity components of the parent body is computed using the expression that ensures that the orbit of the parent does not present any secular drift with respect to the center of mass of the formation. This constraint is enforced by assuming that when the cluster is initialized at perigee ($\theta = 0$) the following relation holds [17]

$$\frac{y'_{p_0}}{x_{p_0}} = -\left[\frac{2+e}{1+e}\right] \tag{4.4}$$

Following the approach described in [13], the formation spins around an axis perpendicular to the formation plane, in the attempt of gyroscopically stabilizing them. This angular rate induces a relative motion of each deputy with respect to the parent body.

Assuming that (i) the parent is placed in the origin of the LVLH frame, and (ii) the velocity of formation elements at the initial time $t = 0$ follows that of a rigid body, with an angular velocity equal to $\boldsymbol{\omega}_0$, the position rate of deputy d is given by

$$\boldsymbol{r}'_{d_0} = \boldsymbol{r}'_{p_0} + \hat{\boldsymbol{\omega}}_0 \times \boldsymbol{r}_{d_0} \tag{4.5}$$

where $\boldsymbol{r}'_{p_0} = x'_{p_0}\hat{\mathbf{i}}_{\mathcal{R}} + y'_{p_0}\hat{\mathbf{j}}_{\mathcal{R}} + z'_{p_0}\hat{\mathbf{k}}_{\mathcal{R}}$ is the initial position rate of the parent, defined above, $\hat{\boldsymbol{\omega}}_0 = \boldsymbol{\omega}_0/\dot{\theta}$ is the angular rate of the formation relative to the orbit frame, and $\mathbf{r}_{d_0}$ is the initial relative position vector of the deputy, where all the vectors are expressed in terms of components in the LVLH frame.

For in-plane formations, it is possible to define a local non dimensional spin rate,

$$\hat{\omega}_{d/p} = \omega_{d/p}/\dot{\theta} \tag{4.6}$$

that provides a measure of the spin speed of deputy d around the parent, scaled with respect to the time derivative of the true anomaly. This scalar parameter is equal to

$$\hat{\omega}_{d/p} = \|(\boldsymbol{r}'_d - \boldsymbol{r}'_p) - (\boldsymbol{r}'_d - \boldsymbol{r}'_p) \cdot \hat{\mathbf{i}}_{d/p}\|/\|\boldsymbol{r}_d - \boldsymbol{r}_p\| \tag{4.7}$$

where $\hat{\mathbf{i}}_{d/p} = (\boldsymbol{r}_d - \boldsymbol{r}_p)/\|\boldsymbol{r}_d - \boldsymbol{r}_p\|$ is the unit vector parallel to the relative position of the deputy with respect to the parent body. The initial angular position for the deputies is chosen such that a constant angular separation is maintained when $\hat{\omega}_{d/p} = \|\hat{\boldsymbol{\omega}}_0\|$ is assumed at the initial time, $t = 0$ [13]. Equation (4.7) requires that agents and parent body constantly lie on the same plane. When the initial spin plane of the formation is not maintained during the evolution, as it happens with Earth-facing formations, Equation (4.7) does not hold.

Given the initial position for the deputies, tether configuration, and number n_t of beads in tether t, it is possible to derive the position of the bead labelled b at the initial time assuming that they are equally spaced,

$$\boldsymbol{r}_{b_0} = \boldsymbol{r}_{d/p_0} + (\boldsymbol{r}_{d_0^\star} - \boldsymbol{r}_{d/p_0})(1 - j_t/n_t)\,,\ j_t = 1, 2, \ldots, n_t \tag{4.8}$$

where the tether is assumed to connect a generic deputy $d^\star$ placed in $\boldsymbol{r}_{d_0^\star}$ to either another deputy d or the parent body p in $\boldsymbol{r}_{d/p_0}$. The initial position rate for each bead follows the same assumption of relative motion used in the case of the deputies, that is, a rigid-body

velocity distribution expressed by Eq. (4.5), such that

$$\boldsymbol{r'}_{b_0} = \boldsymbol{r'}_{p_0} + \hat{\boldsymbol{\omega}}_0 \times \boldsymbol{r}_{b_0} \tag{4.9}$$

The approach used to define the characteristics of the orbit scenarios considered in this study takes into account that the cluster is initialized at the perigee. Therefore, when defining the initial conditions of the agents, it is necessary to define the value of $\hat{\boldsymbol{\omega}}_0$ at $\theta = 0$. There are different possible criteria to define the size and shape of the orbits of the cluster through the semimajor axis a and eccentricity e. In this study a constant perigee radius is assumed equal to $R_p = 6578$ km for all the reference orbits, which corresponds to an approximate altitude of 200 km over the Earth surface and it is equal to the radius of the circular reference orbit considered in Ref. [13].

The distance R between the primary body (the Earth, in the present case) and the center of mass of the formation is expressed in polar coordinates as [55]

$$R(\theta) = \frac{a(1-e^2)}{1 + e\cos\theta} \tag{4.10}$$

For given values of eccentricity e and perigee altitude R_p, the semimajor axis a is given by $a = R_c/(1-e)$. The mean motion for the considered orbit is $n = \sqrt{\mu/a^3}$, where μ is Earth's gravitational parameter. Note that it is not possible to consider orbits with the same mean motion n (that is, the same semi-major axis), because perigee altitude would go below Earth's radius for small values of the eccentricity, resulting into unfeasible orbits crossing the Earth's surface. The semi-major axis for the reference orbit needs thus to be increased when cases with $e > 0$ are to be dealt with and perigee altitude is prescribed.

Defining the same value of $\hat{\boldsymbol{\omega}}_0$ for all the scenarios considered having different eccentricities is not considered a viable option, as the approach used to define the reference orbit for each value of e leads to orbits with different mean motion and orbital periods. Sizeable differences in the dimensional values of formation angular speed would be obtained for different cases, that in turn cause different tensions in the tether system and centrifugal loads. Considering that all the scenarios have the same perigee altitude, which is equal to the altitude of reference circular orbit, the value of $\hat{\boldsymbol{\omega}}_0$ is chosen such that the clusters flying different orbits are characterizes by the same dimensional angular velocity at perigee pass, a value which will be indicated as

$$\boldsymbol{\omega}_{0_P} = r_s \cdot n_c \, \hat{\mathbf{h}} \tag{4.11}$$

Table 4.1: Orbit and agents characteristics

Parameter	Symbol	Value	Units
Perigee altitude	R_p	6578	km
Eccentricity values	e	0.0, 0.3, 0.5	
Mass of parent body		300	kg
Mass of deputies body		25	kg

The initial angular velocity of the formation is thus defined as a factor r_s of the circular orbit mean motion n_c having a perigee radius $R_c = R_p = 6578$ km. The direction of the initial formation angular rate, $\hat{\mathbf{h}}$, depends on the particular scenario (either Earth-facing, with $\hat{\mathbf{h}} = \hat{\mathbf{i}}_{\mathcal{R}}$, or in-plane formations, with $\hat{\mathbf{h}} = \hat{\mathbf{k}}_{\mathcal{R}}$). Using the transformation defined in Eq. (4.1), the initial value of the angular rate $\hat{\boldsymbol{\omega}}_0$ at perigee is equal to

$$\hat{\boldsymbol{\omega}}_0 = \frac{\boldsymbol{\omega}_{0_P}}{\dot{\theta}_{(\theta=0)}} = \left(\frac{r_s}{\sqrt{1+e}}\right) \hat{\mathbf{h}} \tag{4.12}$$

4.1.2 Formation stability

Provided that the major objective of this work is to evaluate the effect of eccentricity and tether mass on the dynamics of tethered satellite formations, the behavior of each configuration considered in this study is compared with the behavior of the same formations when tethers are modeled as massless elastic cables, for different values of the eccentricity of the cluster orbit. The tether characteristics is the same as the one defined in Chapter 3, in Table 3.2, and also in accordance with [13].

The stability of the cluster is analyzed performing a numerical simulation of the dynamic model. Similar to the work performed in Chapter 3, in order to assess stability of the formation the following features are observed in the simulations.

In-plane formations

The initial condition for the position of the four deputies of the formation is set to

$$\begin{aligned} \boldsymbol{r}_{1_0} &= [l_i^{(0)}\ l_i^{(0)}\ 0] \cdot \sqrt{2}/2 = -\boldsymbol{r}_{3_0} \\ \boldsymbol{r}_{2_0} &= [-l_i^{(0)}\ l_i^{(0)}\ 0] \cdot \sqrt{2}/2 = -\boldsymbol{r}_{4_0} \end{aligned} \tag{4.13}$$

where $l^{(0)} = 1000$ m. In Ref. [13], a method for calculating initial velocities of the deputies is proposed, which is based on the calculation of the Hamiltonian for each tether initial orientation, in order to ensure that tethers exhibit the same trajectory without presenting any drift in their relative position. This approach is specific for circular reference orbits, but when used for formations of four deputies on elliptical orbits, it provides again an initial relative position such that the angular separation between deputies remains constant.

It can be shown that, in order to ensure a constant angular difference, it is sufficient to initially place the four deputies at angles $\alpha_1 = 45°$, $\alpha_2 = 135°$, $\alpha_3 = 225°$ and $\alpha_4 = 315°$ with respect to the $\hat{\mathbf{i}}_{\mathcal{R}}$ axis, and use the same initial value of spin rate $\boldsymbol{\omega}_{i/p} = \|\boldsymbol{\omega}_0\|$ for all four deputies.

Initial position rate at perigee is computed using Eq. (4.5), with the parent body placed in the origin of the orbit frame and

$$\hat{\boldsymbol{\omega}}_0 = \begin{bmatrix} 0 & 0 & r_s/\sqrt{1+e} \end{bmatrix} \tag{4.14}$$

In the case of a HAS in-plane formation, a value of $r_s = 10$ is selected for all deputies. For the CHAS in-plane formation, it is $r_s = 15$, for consistency with Ref. [13]. Simulations are run considering three different values of eccentricity: $e = 0.0$ (circular orbits), $e = 0.3$ and $e = 0.5$.

For in-plane formations, due to the fact that there is no net gravity gradient torque on the satellite, it is possible to invoke conservation of angular momentum. The dissipation caused by damping in the tethers is assumed negligible. In addition to the considerations relative to Thomson equilibria for rigid bodies, outlined in 2, the model considered in this paper, based on discrete point masses, clearly shows that in-plane and transverse dynamics are uncoupled, when initial position and velocities lie on the orbit plane. This means, again, that a planar spinning formation lying initially on the orbital plane will evolve on this plane.

Hub-and-spoke in-plane formation

In this section, the results for deputies 1 and 2, of a HAS in-plane formation are discussed. The behavior of deputies 3 and 4 is perfectly equivalent, and it will not be presented. Figures 4.1 to 4.3 show the dynamic behavior in terms of deputy position, local spin rate

and formation angular displacement between adjacent tethers for different values of eccentricity.

Figure 4.1 represent the evolution of the distance between deputy 1 and the parent body, $\Delta r_{1/p} = \|\boldsymbol{r}_1 - \boldsymbol{r}_p\| - l_1^{(0)}$, for a circular orbit ($e = 0$, plot (a)), $e = 0.3$ and 0.5 (plots (b) and (c), respectively). For elliptical cases, the formation is initialized at perigee and the number of orbits reported on the horizontal axis is increased at every perigee pass of the cluster. One easily notice that the size of the elongation for elliptical cases matches that for the circular reference orbit, but in the former cases oscillations in tether length grow when the formation is close to the perigee (Figure 4.1).

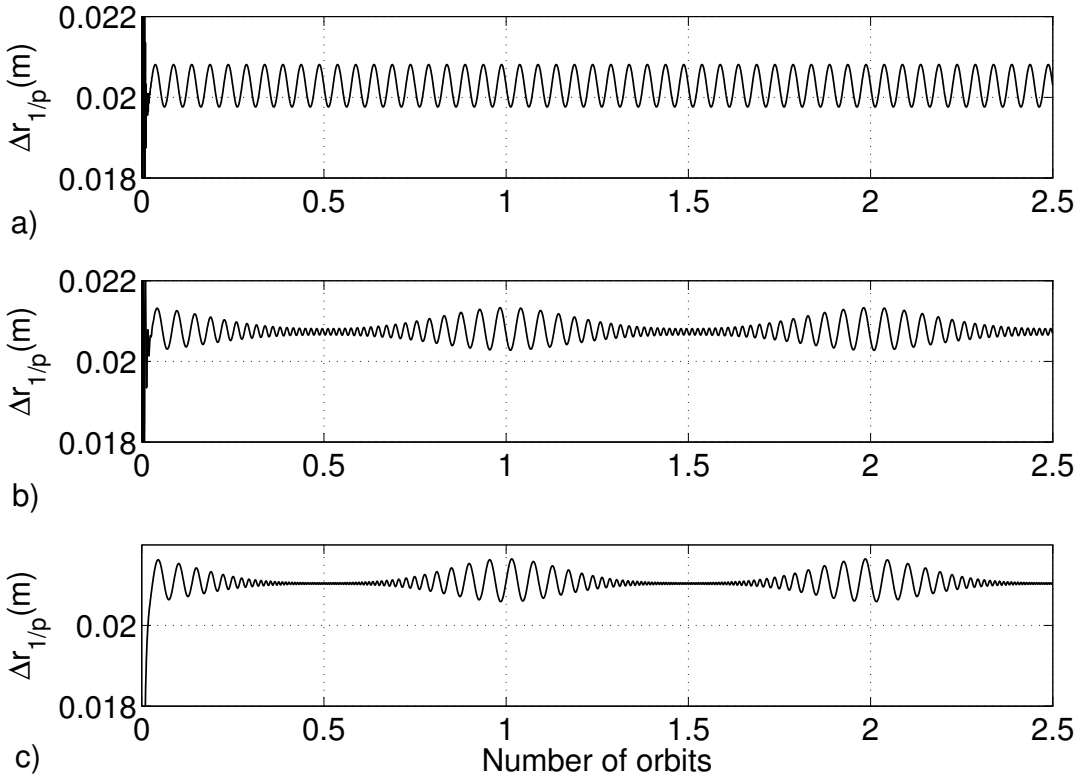

Figure 4.1: **HAS In-plane formation. Distance from deputy 1 to parent body: (a)** $e = 0.0$**, (b)** $e = 0.3$**, (c)** $e = 0.5$**.**

This is a combined effect of several factors: the variation of the local orbital angular rate causes a fluctuation in the relative spin speed of the tethers, $\|\boldsymbol{\omega}_{i/p}\|$, induced by

conservation of absolute angular momentum, such that if the formation spins at an approximately constant angular speed with respect to the inertial frame (as in the present case), its angular speed relative to the LVLH orbit frame becomes smaller at perigee, when orbit rate is higher, and vice-versa it is higher at apogee, when the orbit rate is lower (Figure 4.2, upper plot). This effect is amplified when θ is used as the independent variable. In this case the non-dimensional relative angular rate, $\hat{\boldsymbol{\omega}}_{1/p} = \boldsymbol{\omega}_{1/p}/\dot{\theta}$, is obtained by dividing the dimensional value by the local orbit rate which is higher at the perigee.

At the same time, the gravity gradient forcing term is more intense closer to the Earth and this causes a stronger periodic action on tethers while the formation spins at a slower rate at perigee pass, relative to the orbit frame. On the other hand, when the formation moves away from perigee and the influence of the gravity field becomes weaker, oscillations almost vanish in amplitude, but they are characterized by a higher frequency, related to the more frequent passage of each deputy along the local vertical, when the formation angular speed relative to the LVLH frame grows. This effect increases with orbit eccentricity, when the distance from the cluster to the Earth at apogee is higher, if a constant perigee altitude is assumed, as in the present case.

When transforming the nondimensional spin rate of deputy 1, $\hat{\omega}_{1/p}$, defined according to Eq. (4.7), into its dimensional counterpart, $\omega_{1/p} = \hat{\omega}_{1/p}\dot{\theta}$ (shown in Fig. 4.2(b)), an increase in the spin rate close to apogee is still visible, which is due to conservation of angular momentum around the orbit normal, but this effect is clearly less relevant in quantitative terms, with variations in the order of 5 up to 7% of the initial formation angular rate. This means that variations in amplitude of the oscillations is mostly related to variations of orbit rate $\dot{\theta}$ and intensity of gravity gradient between their maximum and minimum values at perigee and apogee, respectively.

Higher frequency terms in the variation of angular velocity shown in the bottom plot of Fig. 4.2(b) are related to the exchange between kinetic and potential energy due to the orientation of the deputy (deputy 1 in the considered example) in the LVLH frame. This can be proven taking into account the expressions of kinetic and potential energy derived in [13] and the fact that the total energy is conserved. In this respect dissipative damping forces in the tethers can be neglected, as they depend on elongation rate only, which is small, thus producing only a negligible effect on the short term evolution of total energy.

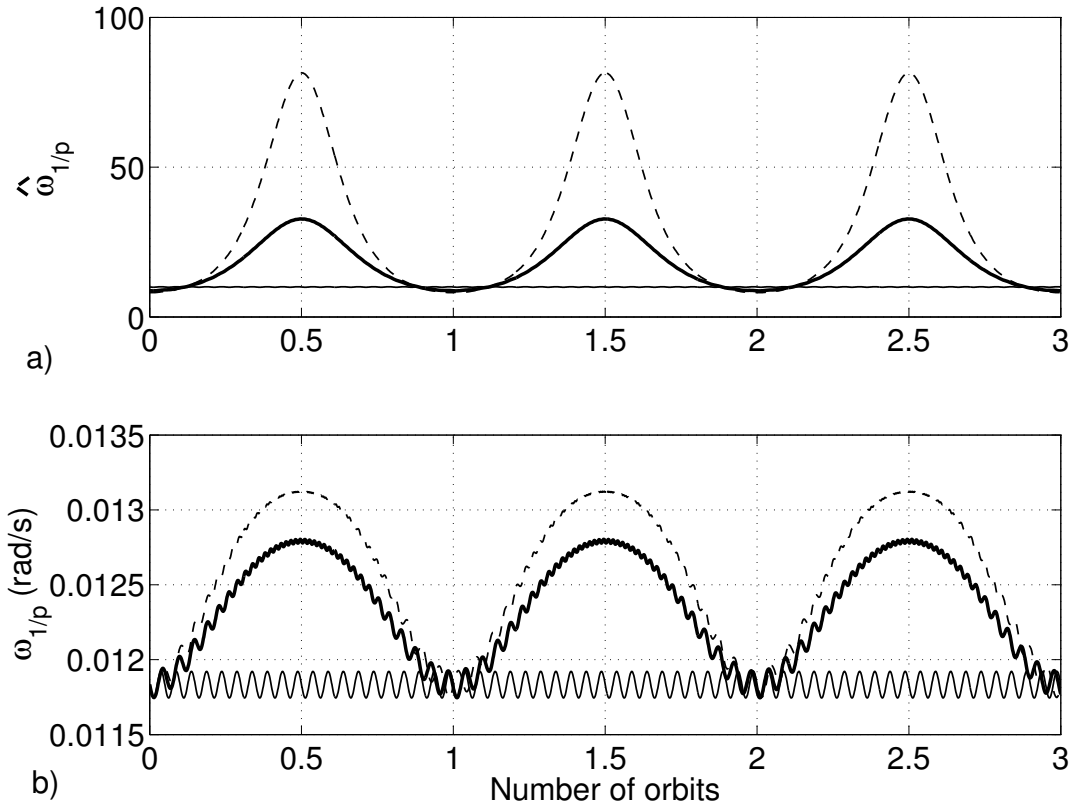

Figure 4.2: **HAS In-plane formation (solid:** $e = 0.0$**; bold:** $e = 0.3$**; dashed:** $e = 0.5$**): (a) Local spin rate of deputy 1, (b) Local spin speed of deputy 1.**

In this scenario, eccentricity plays a significant role in system dynamics, whereas incorporating tether mass in the model produces only a marginal increase in the elongation of tethers with respect to that obtained when a simplified massless tether model is used. In particular, Figure 4.3 shows the angular displacement between tethers connected to deputies 1 and 2. The results for circular orbits (plot (a)) are equivalent to those found for the massless tether case (not reported here, for the sake of conciseness, but analyzed in detail by Pizarro-Chong and Misra in [13]). For eccentricities e equal to 0.3 and 0.5, the magnitude of the angular difference decreases at apogee passage, but it is hardly affected by the use of a massive tether model. As in the circular orbit case [121], the simpler purely elastic tether model appears adequate for describing this type of formations, also when the reference orbit is elliptical.

One should note that a deputy belonging to the cluster is affected by gravity-gradient

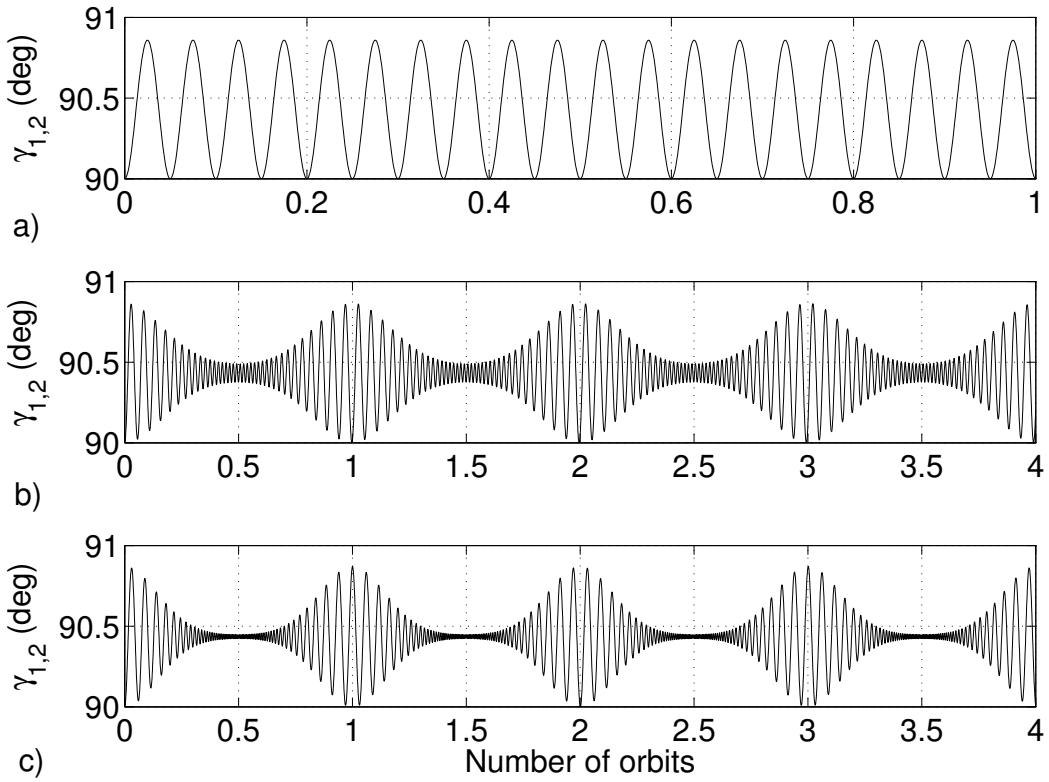

Figure 4.3: **HAS In-plane formation. Angular distance between deputies 2 and 1: (a)** $e = 0.0$**, (b)** $e = 0.3$**, (c)** $e = 0.5$**.**

force on two different timescales. On one side, the spin rate of a deputy derived from Eq. (4.7), is not constant, and it oscillates with its angular position, as already demonstrated in Ref. [13], where a Hamiltonian for the system is formulated that allows for computing initial conditions of different deputies with equal energy values for avoiding secular variations in their relative angular position. On the other hand, the angular rate of the whole cluster varies with true anomaly for elliptical orbits, as discussed above and shown in Figure 4.2. The superposition of these two motions is highlighted in Figure 4.4(a), shows the spin rates relative to the parent body, $\hat{\omega}_{1/p}$ and $\hat{\omega}_{2/p}$, of deputies 1 and 2, respectively. The enlargement highlights the difference in agent spin rates associated to different orientations within the cluster at perigee pass, where this effect is more significant. Plot (b) shows the evolution of $\hat{\omega}_{2/p} - \hat{\omega}_{1/p}$ over two orbits, which explains the variation in the angular displacement $\gamma_{1,2}$ between tethers connected to the considered deputies shown in Figure 4.3.

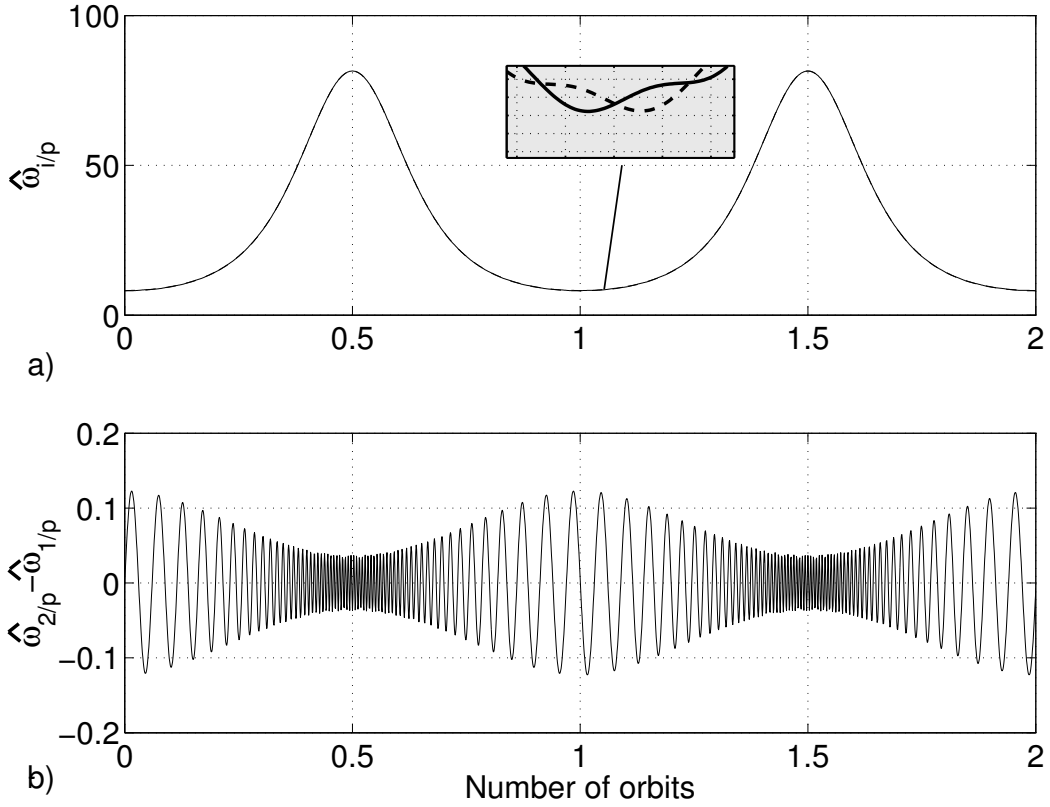

Figure 4.4: **HAS In-plane formation: (a) Spin rate for agents 1 (solid) and 2 (dashed), (b) Spin rate difference between agents 1 and 2.**

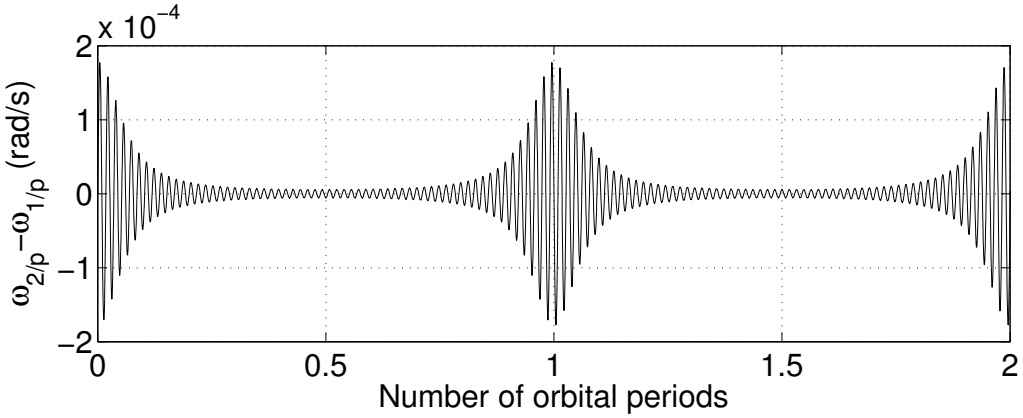

Figure 4.5: **HAS In-plane formation: Dimensional spin rate difference between agents 1 and 2 as a function of time, t/T_O.**

The increase in frequency of the oscillations at apogee visible in the lower plot of Figure 4.4 is only apparent, as it is mostly related to the use of true anomaly as independent variable, as in [17]. The actual frequency of the oscillations in the time domain can be

easily recovered by plotting $\omega_{2/p} - \omega_{1/p}$ as a function of time, where $t = t(\theta, e)$ is obtained from Kepler's time equation [55]. The frequency of the oscillations of $\omega_{2/p} - \omega_{1/p}$ as a function of time is almost constant (Figure 4.5), whereas the amplitude of the oscillations of this dimensional variable undergoes more severe variations over one orbit, when compared to its non-dimensional counterpart.

Closed hub-and-spoke in-plane formation

The closed in-plane formation presents the same initial relative position of deputies with respect to the parent adopted for the open formation, with the relevant difference represented by the presence of external tethers connecting deputies (as shown in Fig. 3.1). In order to properly analyze the shape of the formation, a rotating coordinate reference system is introduced. The rotating reference, formed by unit vectors $\hat{\mathbf{i}}_{\mathcal{S}}$, $\hat{\mathbf{j}}_{\mathcal{S}}$, and $\hat{\mathbf{k}}_{\mathcal{R}}$, is chosen such that its angular velocity around the normal to the orbit plane $\hat{\mathbf{k}}_{\mathcal{R}}$ is equal to the average spin rate of internal tethers relative to the orbit frame. This allows for removing the overall formation rotation dynamics and to highlight deviations from a nominal, ideal behavior of uniform spin speed for all the agents. The behavior of deputies, beads and tethers and their relative oscillations from the ideal in-plane rotation can thus be determined. Initial position and velocity for the four deputies is set following the procedure already summarized in the previous section for the HAS in-plane case, so that all the agents and tethers have the same spin rate at initial time.

The results for a simulation of 4 orbital periods are presented in Figs. 4.6 and 4.7 for $e = 0.0$ and $e = 0.3$ respectively. Variables X and Y are the position variables in the $\hat{\mathbf{i}}_{\mathcal{S}} - \hat{\mathbf{j}}_{\mathcal{S}}$ plane scaled with respect to $l^{(0)}$. The shape of the formation is characterized by two effects. First of all, external tethers are subject to a centrifugal pull that bends them, transforming the initial square into a "rounded" quadrangle. This fact, in turn, affects the relative position of deputies with respect to the parent body as the direction of external tether tension acting on the deputies is varied with respect to the nominal square shape and the tension force on the internal tethers vanishes, as long as they do not reach full extension. This represents a major difference with respect to the massless tether model, already discussed in Ch. 3.

The effects of eccentricity on formation geometry is only apparently marginal, as there are at least two significant differences between the cases of circular and elliptical reference

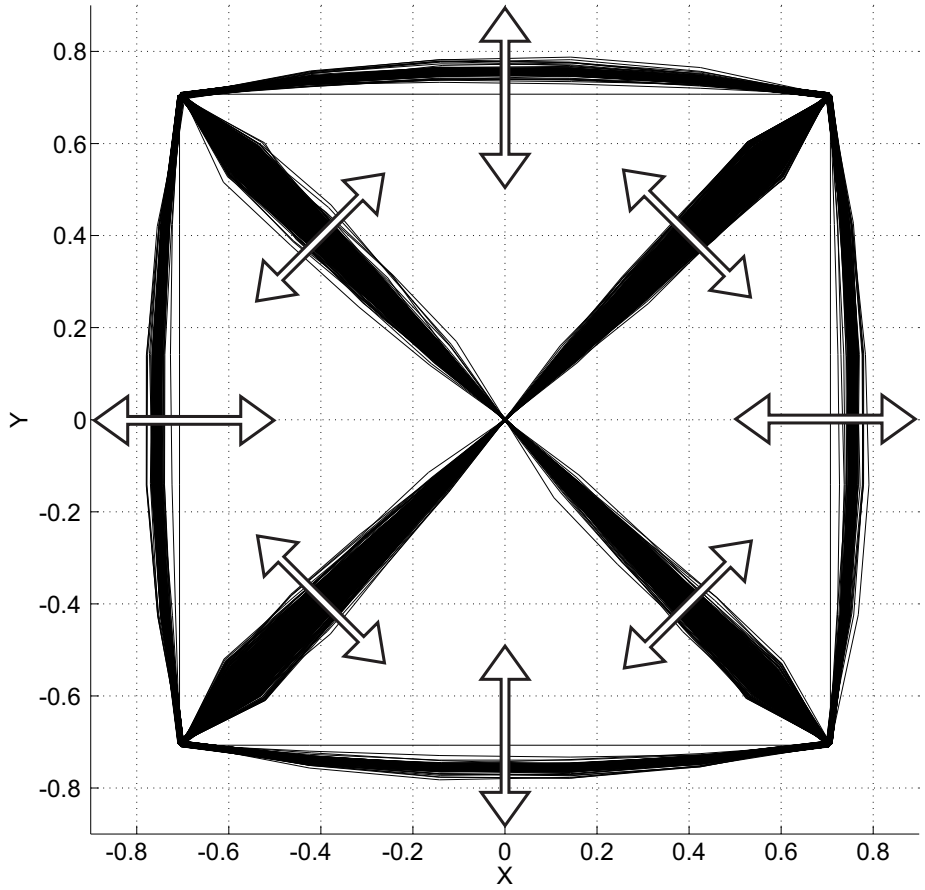

Figure 4.6: **CHAS In-plane formation. Shape of formation (6-orbit run),** $e = 0.0$

orbits. For $e = 0$ the external tethers approach the bulged configuration almost monotonically, residual vibrations being present which are related only to the loads transmitted by internal tethers during the rotation when one or more of them reaches full extension. On the converse, the oscillations in formation rotation rate induced by the periodic variation of orbit rate coupled with differences in gravity gradient intensity at perigee and apogee (as discussed above) force vibrations in the external tethers during the whole time-history. At the same time, the behaviour of the oscillations for internal tethers appears to be less regular for $e = 0.3$, with oscillations that are characterized by different amplitude and frequency between different tethers and for the same tethers during different orbits.

This latter fact is confirmed by the analysis of Figs. 4.8 and 4.9, where the evolution of $\Delta r_{i/p} = \|\boldsymbol{r}_i - \boldsymbol{r}_p\| - l_i^{(0)}$ (when tethers are taut $\Delta r_{i/p} = \Delta l_i$) is presented for $e = 0.0$ and $e = 0.3$ respectively. In both cases, three out of four deputies are close to full extension at the same time, whereas the fourth one, connected to an agent that reduces its distance

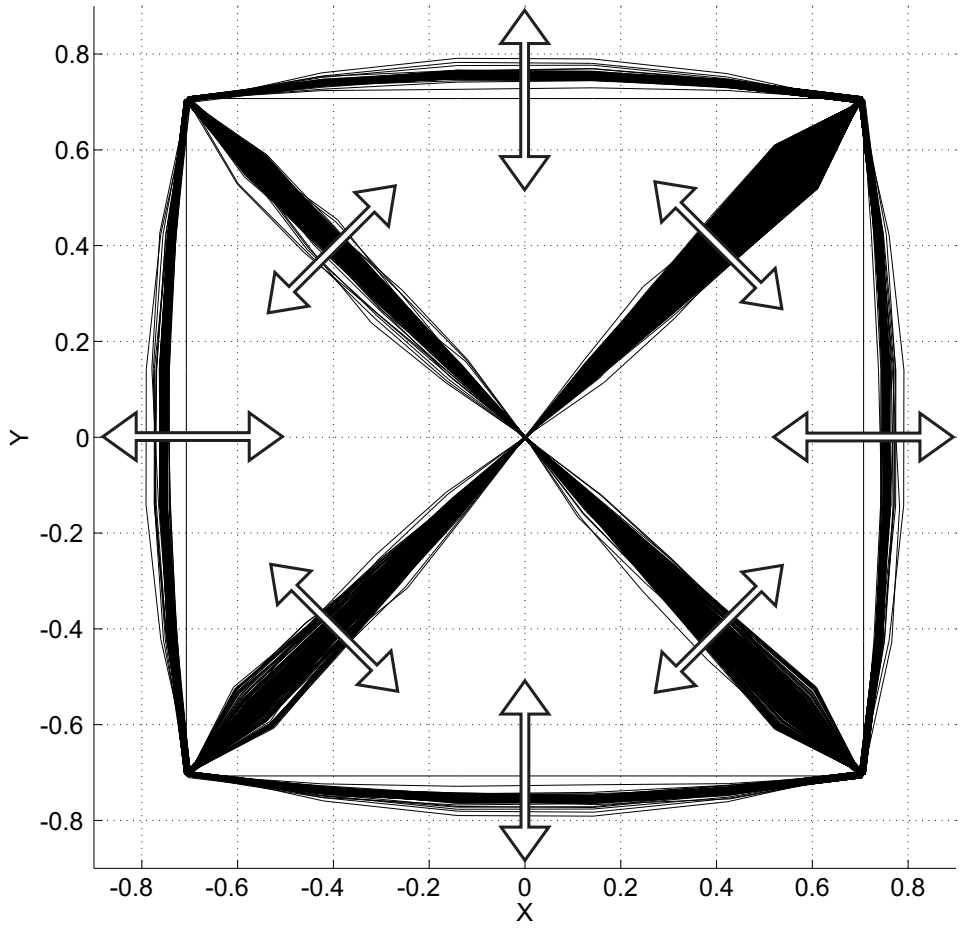

Figure 4.7: **CHAS In-plane formation. Shape of formation (10-orbit run),** $e = 0.3$**.**

from the parent body by approximately 16 m, remains loose. In the circular case the slack tether changes constantly, whereas, in the elliptical orbit case, one of the tethers remains loose for long time intervals (up to several revolutions). Changes between loose and (almost) taut conditions usually take place at or close to perigee pass, where the effect of the gravity gradient is stronger and differences on the gravity pull acting on different deputies get higher.

The result is that for the circular case, short-term fluctuations of $\Delta r_{i/p}$ are highly irregular for all the agents of the formation, but they are characterized by high-frequency variations of the distance between each deputy and parent body with similar characteristics. On the converse, high-frequency variations of $\Delta r_{i/p}$ almost disappear in the elliptic case, when one of the tethers remains loose for long time intervals, allowing for wider fluctuations of beads under the action of gravity gradient only, with no tension acting between

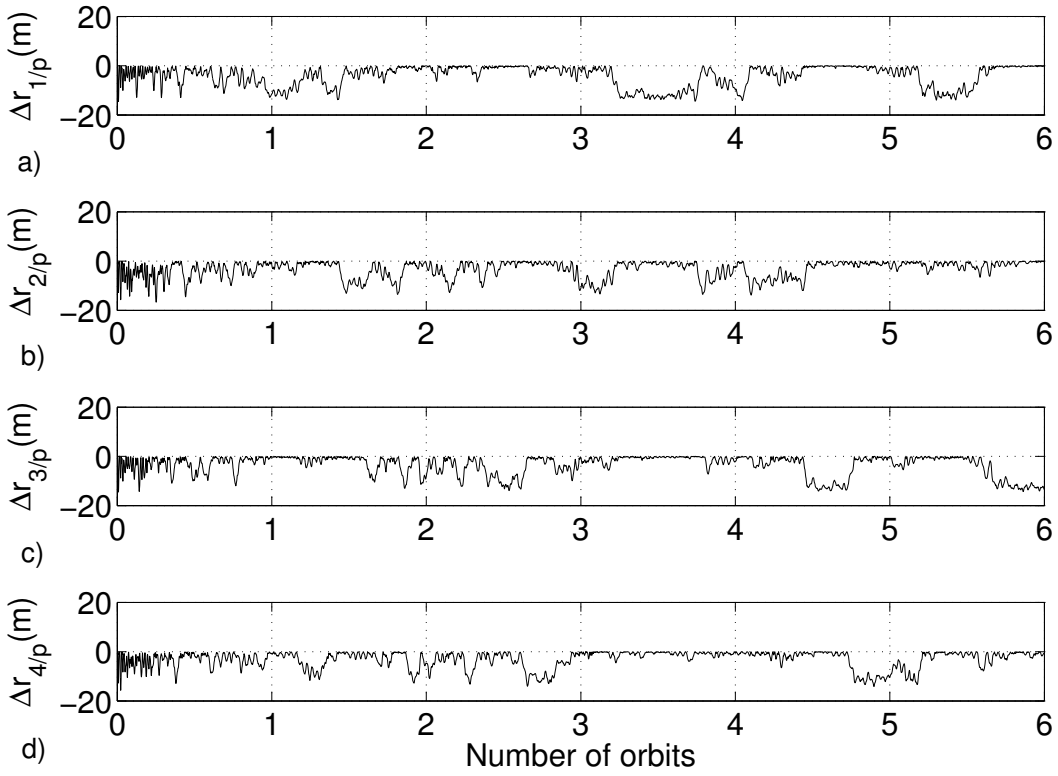

Figure 4.8: **CHAS In-plane formation. Distance $\Delta r_{i/p}$ time evolution,** $e = 0.0$**.**

them in the loose tether. This can also be seen in Figure 4.9, where the internal tether linking deputy 2 shows smaller oscillations, after an initial transient, due to the fact that it never becomes slack. When eccentricity is increased, this behavior is more pronounced, and for $e = 0.7$ the same tether remains slack for a simulation of 10 orbits.

When compared to the open formation in-plane case, external tethers in closed formations provide a stabilizing effect for the angular displacement of adjacent tethers. Even at high values of eccentricity ($e = 0.7$), the angular displacement between adjacent tethers remains close to 90°. As discussed in Paragraph 4.1.2 the rounded shape induced by the centrifugal pull can be compensated either by making external tethers l_{ext} longer, or reducing the internal tether length, l_{int}, such that the ratio between their lengths becomes $l_{ext}/l_{int} < \sqrt{2}$. This avoids or at least limits the irregular fluctuations in the distance between deputies and parent body.

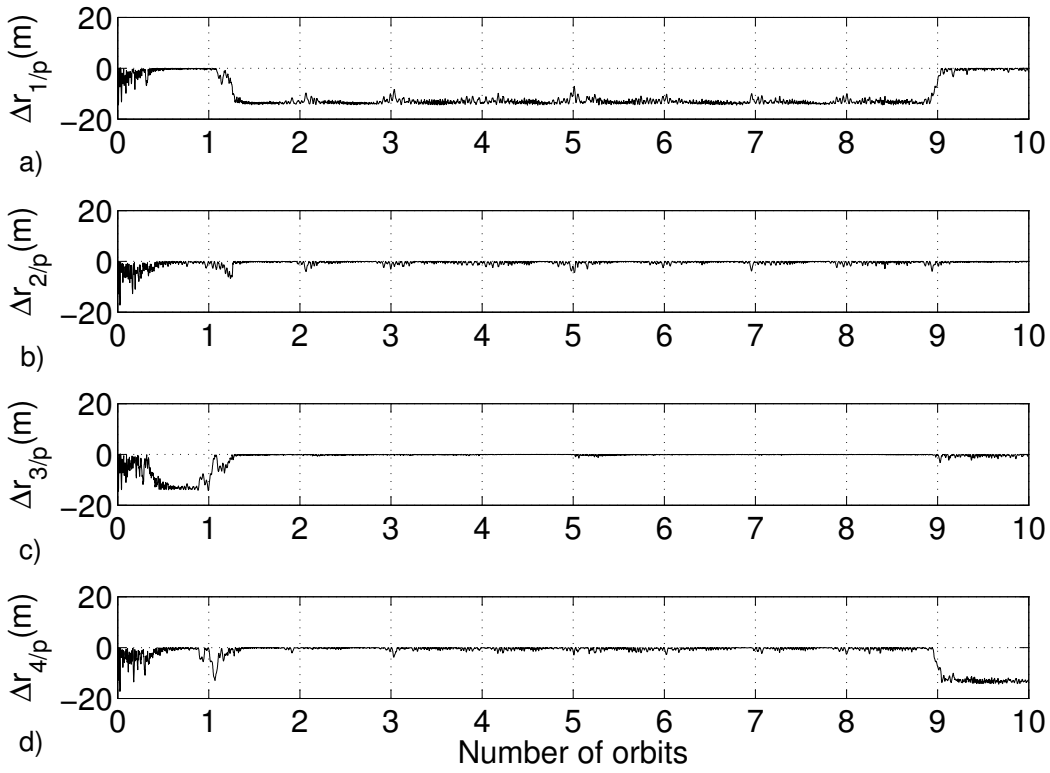

Figure 4.9: **CHAS In-plane formation. Distance $\Delta r_{i/p}$ time evolution,** $e = 0.3$**.**

Earth-facing formations

The initial condition for the position of the four deputies of the formation for the Earth-facing case is set to

$$\begin{aligned} \boldsymbol{r}_{1_0} &= [0\ l_i^{(0)}\ l_i^{(0)}] \cdot \sqrt{2}/2 = -\boldsymbol{r}_{3_0} \\ \boldsymbol{r}_{2_0} &= [0\ -l_i^{(0)}\ l_i^{(0)}] \cdot \sqrt{2}/2 = -\boldsymbol{r}_{4_0} \end{aligned} \tag{4.15}$$

Initial velocity is computed using Equation (4.5) with the parent body placed at the origin of the LVLH frame and

$$\hat{\boldsymbol{\omega}}_{i/p} = \left[-\frac{r_s}{\sqrt{1+e}} \ \ 0 \ \ 0 \right] \tag{4.16}$$

where $l^{(0)} = 1000$ m. The value of r_s is set to $r_s = 10$ for both open HAS and CHAS Earth-facing formations, as in [13]. The initial condition of beads is computed following the same procedure as for the in-plane formation.

For an Earth-facing formation, deputies and tethers initially lie on the horizontal $\hat{\mathbf{j}}_{\mathcal{R}}$-$\hat{\mathbf{k}}_{\mathcal{R}}$ plane of the LVLH orbital reference frame. The fact that initial values of z_i and corresponding velocity components are non-zero leads to tridimensional trajectories, in contrast to what happens for the in-plane case, where initial conditions and resulting trajectories remain constrained on the $\hat{\mathbf{i}}_{\mathcal{R}}$-$\hat{\mathbf{j}}_{\mathcal{R}}$ orbit plane.

In the Earth-facing scenario, it is no longer possible to establish an analogy with the attitude behavior of a spinning rigid body, as transverse dynamics becomes relevant and deputies no longer lie on the same plane, normal to the formation spin axis, especially when spin rates are in the same order of magnitude as the orbit mean motion. For the specific case of a spin axis pointing along the Nadir direction, a null spin rate relative to the orbit frame is required. Such a situation is clearly not realistic for a tethered formation, as in this case tethers loose tension, the formation does not maintain its shape, and the analogy with a rigid body is not valid anymore.

Therefore, for a circular orbit it is not possible to achieve a relative equilibrium state in which the spin axis of the formation points along the radial axis $\hat{\mathbf{i}}_{\mathcal{R}}$ in the LVLH frame. For elliptical orbits, Likins-Pringle equilibria do not exist at all, and it is not possible to achieve any relative equilibrium state in which the formation constantly faces the Earth.

As opposite to the in-plane case, the net torque exerted by the gravity gradient on an Earth-facing formation is not null in general, and therefore it is no longer possible to invoke conservation of angular momentum. Reference [122] provides a detailed study on the variation of the angular momentum vector of a spinning satellite under the gravitational field. But in all the cases here considered formations are provided with a spin rate sufficient for gyroscopically stiffening the tethers. Thanks to this rotation rate, angular momentum is high, and fluctuations of angular momentum induced by gravity gradient over one orbit remain sufficiently small.

Hub-and-spoke Earth-facing formation

Coupling between orbital plane dynamics and crossrange dynamics peculiar to this scenario makes the orientation between the formation plane and the radial axis not constant. Provided that gravity torque affects only marginally the direction of angular momentum, the spin axis of the formation and the direction of angular momentum point approximately

along an inertially fixed direction. Therefore, the component of angular momentum in the radial direction at initial time remains almost constant, and agents of the formation rotate (approximately) on an inertially fixed plane that spins around the orbit normal with respect to the orbit frame. This means that the formation is not constantly facing the Earth.

This fact is confirmed by the angle δ, measured between the radial axis $\hat{\mathbf{i}}_{\mathcal{R}}$ and the vector $\hat{\mathbf{n}}$ normal to the plane defined by the deputies and parent body. The angle δ, shown in Figure 4.10, grows monotonically between $-180°$ and $180°$. The angle is assumed 0 at perigee and it switches from -180° and 180° at apogee, making the formation unstable from the point of view of the desired Earth-pointing attitude of the formation. The same figure also shows that in this respect the effect of eccentricity on δ is not relevant. As it can be observed, the variation of the pitch angle for $e = 0.5$ (plot (b)) follows almost exactly the same pattern of the circular case (plot (a)). Only small amplitude higher frequency fluctuations of δ are affected by e, as oscillations become less frequent when the formation gets closer to perigee pass. This effect is similar to that observed for angular displacement in open in-plane formations (Figure 4.3), and it is related to the same causes, but it is less relevant from the point of view of the application.

The pattern of the elongation of tethers for open formations differs significantly from that observed for the in-plane configuration. Again, highly eccentric reference orbits cause the gravity gradient to become weaker when the cluster moves away from perigee, but this time a reduction of the amplitude of oscillations is observed for higher values of e and the amplitude of oscillations almost vanish at both apogee and perigee passes (that is $N = 0.5$, 1.0, 1.5 and 2 orbits), when the formation lies on a plane perpendicular to the radial direction. This is shown in Figure 4.11, where oscillations in tether length are represented. This figure also shows that massless and massive tether models result into a dynamic behaviour qualitatively very similar, where the only (and hardly noticeable) effect is a slightly higher elongation Δl_i for the massive tether case.

Also the angular distance between adjacent tethers oscillates according to a pattern that depends on eccentricity in all cases, as shown in Figure 4.12. This represents a behavior peculiar of this type of configuration that could not be found for the in-plane formation case, when oscillations in the angular displacement almost disappear at apogee. Again, no significant differences can be observed when comparing the massive and massless models, which is a characteristic already found for in-plane open formations.

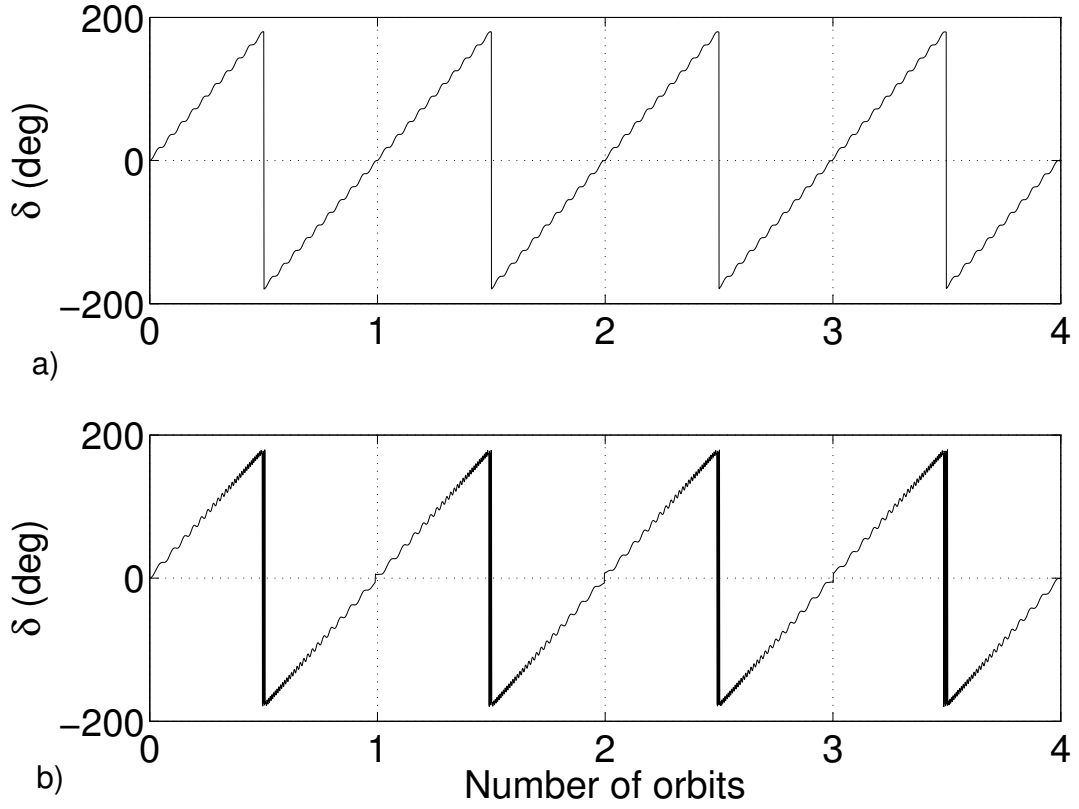

Figure 4.10: **HAS Earth-facing formation pitch angle δ. (a) $e = 0.0$, (b) $e = 0.5$.**

Closed hub-and-spoke Earth-facing formation

The initial condition for agents and beads belonging to internal and external tethers are defined as for the in-plane case, but placed in an Earth-facing orientation in this scenario. As for the HAS case, the deputies approximately lie on a plane that performs a complete rotation around the axis $\hat{\mathbf{k}}_{\mathcal{R}}$ during each orbit around the primary body (Figure 4.13). In addition to this, external tethers present the same deformation induced by the centrifugal load that can be observed for closed in-plane formations. Consequences for internal tethers are similar, with at least one internal tether loosing tension, all of them vibrating in the transverse direction. Oscillations and variations of distance between formation agents are qualitatively similar to those observed in the CHAS in-plane scenario and are not reported for the sake of conciseness.

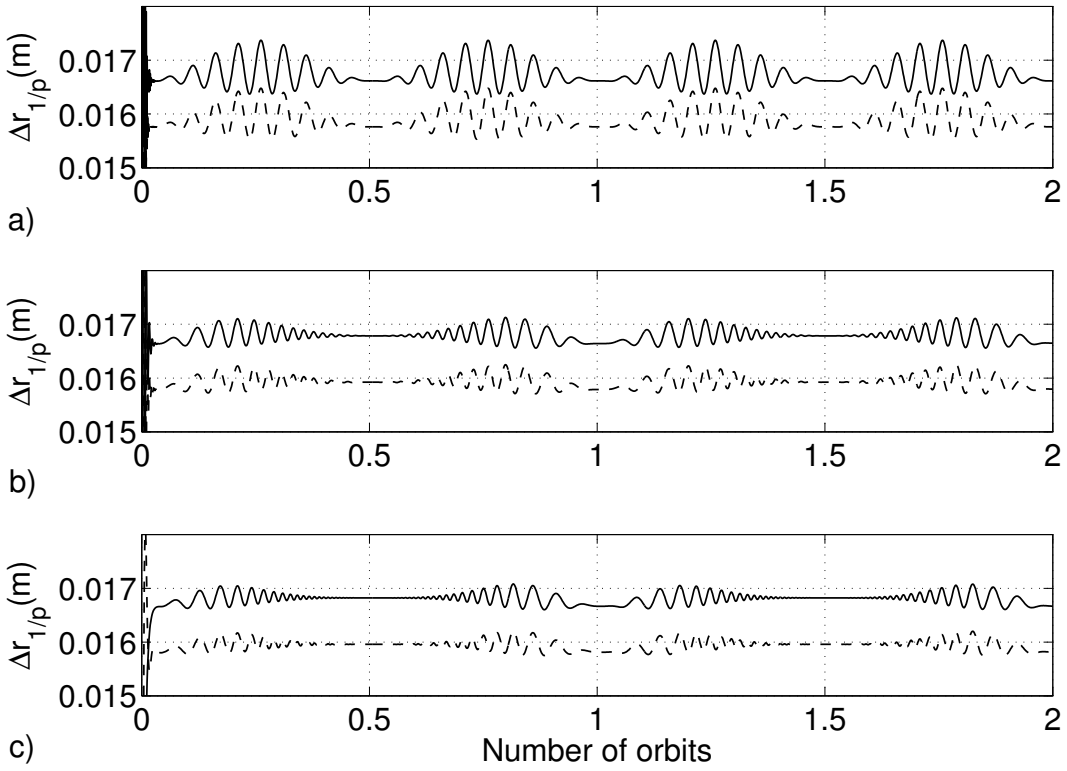

Figure 4.11: **HAS Earth-facing formation distance $\Delta r_{1/p}$. Solid: massive model, dashed: massless model. (a) $e = 0.0$, (b) $e = 0.3$, (c) $e = 0.5$.**

4.1.3 Behavior of the parent body

The analysis of the dynamic behavior of the formation is completed by inspecting the trajectory followed by the parent body of the formation. In all the configurations presented in this paper, the position of the parent body at initial time coincides with that of the center of mass of the formation, which is the origin of the LVLH reference frame. For this reason, as discussed previously (see in particular Eq. (4.4)), the initial condition of the parent is determined in order to avoid secular drift of the cluster away from the reference orbit. Consequently, the initial velocity of the parent is set to zero along the axes $\hat{\mathbf{i}}_{\mathcal{R}}$, $\hat{\mathbf{j}}_{\mathcal{R}}$, and $\hat{\mathbf{k}}_{\mathcal{R}}$ of the LVLH frame. Figure 4.14 shows the distance between the reference elliptical orbit and the parent body for different configurations and eccentricity e equal to 0 (solid lines) and 0.5 (dashed ones). The distance $D_p = \|\mathbf{r}_p\|$ is given by the norm of the position of the parent body in the LVLH frame.

In the case of open formations, the position of the parent body remains almost exactly

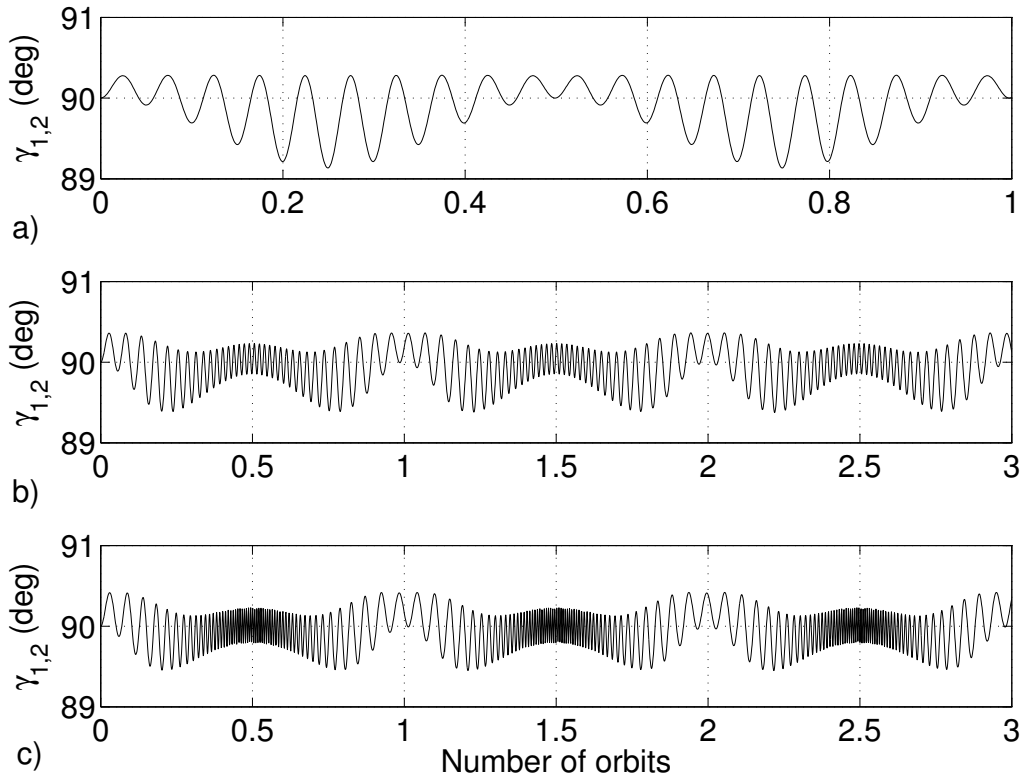

Figure 4.12: **HAS Earth-facing formation, angle $\gamma_{1,2}$. (a)** $e = 0.0$**, (b)** $e = 0.3$**, (c)** $e = 0.5$**.**

on the reference orbit. D_p grows in time, but in the order of 10^{-9} m, clearly related more to numerical errors when integrating the equations of motion then to some physical effects. In these two cases the position of the center of mass coincides with that of the parent body for the whole simulation.

On the other hand, for closed formations the evolution of the position of the parent body exhibits a different behavior. For both in-plane and Earth-facing cases, the center of mass remains on the reference orbit as in open formations, which demonstrates how numerical errors in the integration do not cause violation of this important physical fact. However, the position of the parent body does not remain on the reference elliptical orbit described by the center of mass of the formation. The distance D_p remains bounded, but it presents considerable aperiodic fluctuation. In the case of in-plane formations, the parent body shows a motion that can be approximately confined to a circle with a 2 m radius around the reference orbit, as presented in Figure 4.15, so that stability of the formation is not compromised. Wider deviations are present for the Earth-facing case, with peak

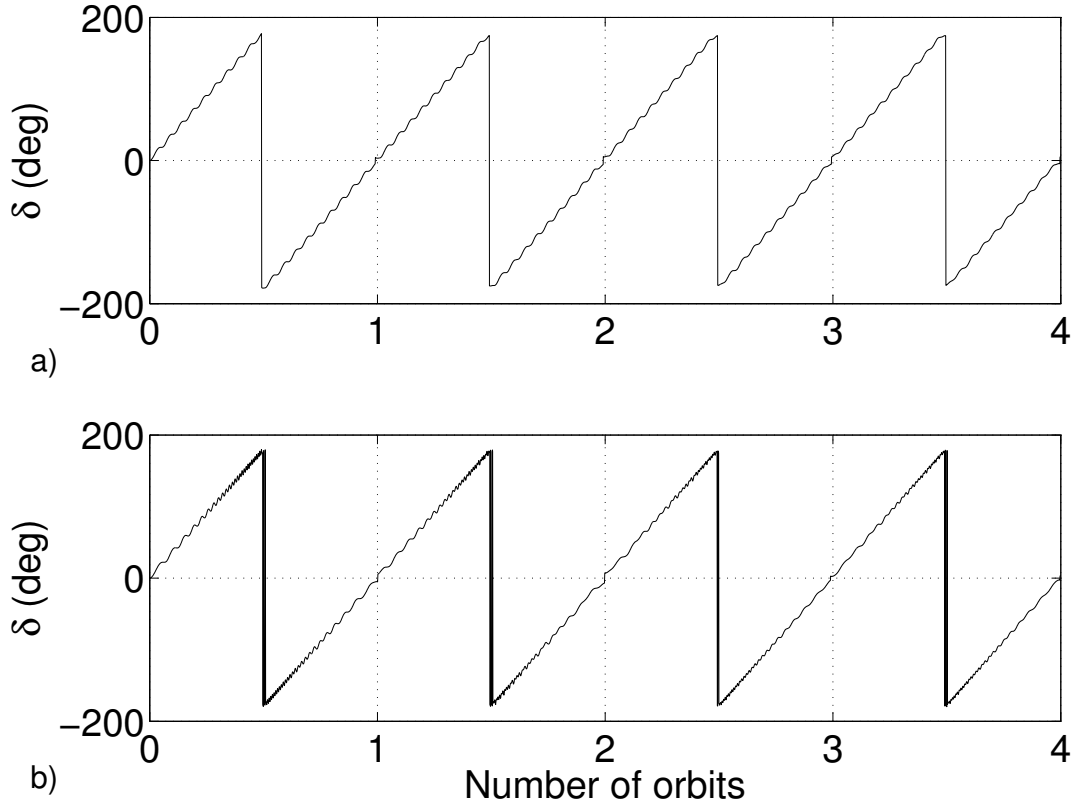

Figure 4.13: **CHAS Earth-facing formation pitch angle δ. (a) $e = 0.0$, (b) $e = 0.5$.**

values as high as 10 m for $e = 0.5$.

4.1.4 Effects of eccentricity of the reference orbit

When combined effect of orbit eccentricity and tether mass on tethered formations is analyzed, the most noticeable effect due to eccentricity is the increase in the variation of the local spin rate of the cluster between perigee and apogee passes of the reference elliptical orbit.

This effect has consequences over the elongation of tethers, shape of tether oscillations and angular separation between adjacent tethers especially for open formations. The amplitude of oscillations for both tether length and separation between neighboring tethers is reduced at apogee passes, where gravity gradient is weaker, for in-plane formation, whereas for open Earth-facing formations that rotate around the orbit normal oscillations are smaller at apogee and perigee passes, when the normal to the formation plane is

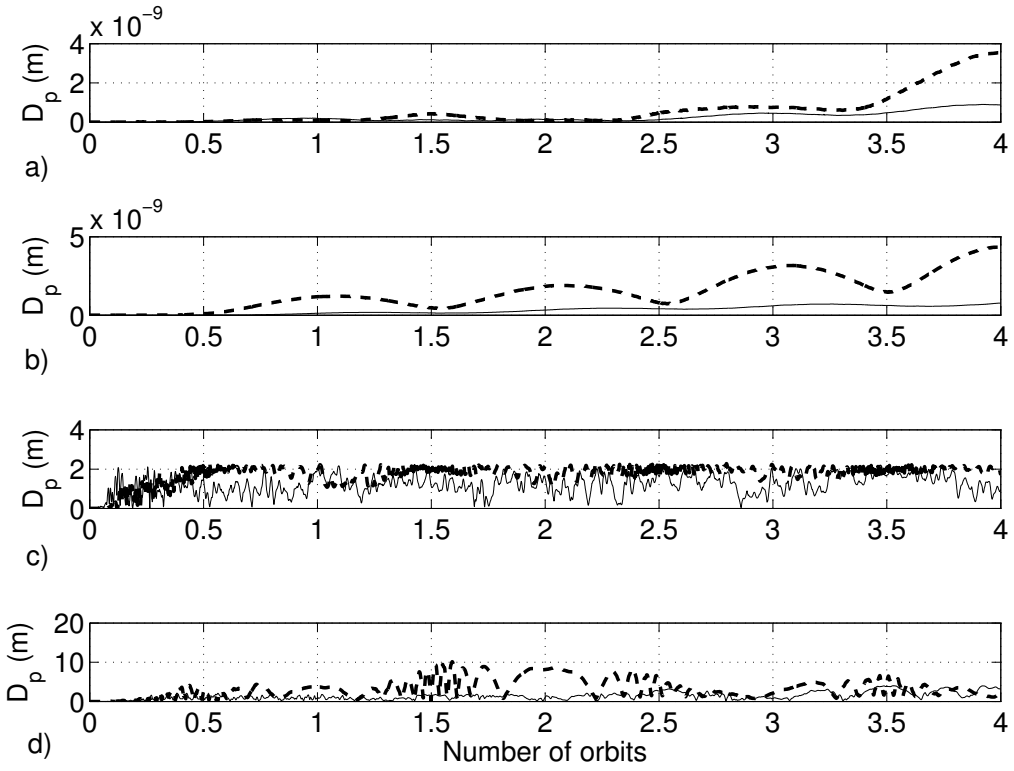

Figure 4.14: **Distance D_p. (a) HAS In-plane, (b) HAS Earth-facing, (c) CHAS In-plane, (d) CHAS Earth-facing. Solid, $e = 0.0$, dashed, $e = 0.5$**

aligned with the radial direction (with maxima when the formation is in quadrature with the primary body). These effects are more noticeable as eccentricity of the reference orbit is increased.

For closed formations external tethers provide a stabilizing effect on angular separation between adjacent tethers. On the other hand, centriphugal loads bend external tethers, preventing deputies from achieving a stable position because the tethers that connect them with the parent body are not in tension. For eccentric orbits, as the cluster moves away from perigee and the gravity gradient becomes weaker, the formation shows a more stable behavior, where a single tether remains loose for long time intervals, in contrast with the circular orbit case, when the slack tether changes continuously. These effects cannot be observed when the simulation model does not feature a massive tether model, as tether mass plays a crucial role in the dynamics of the system.

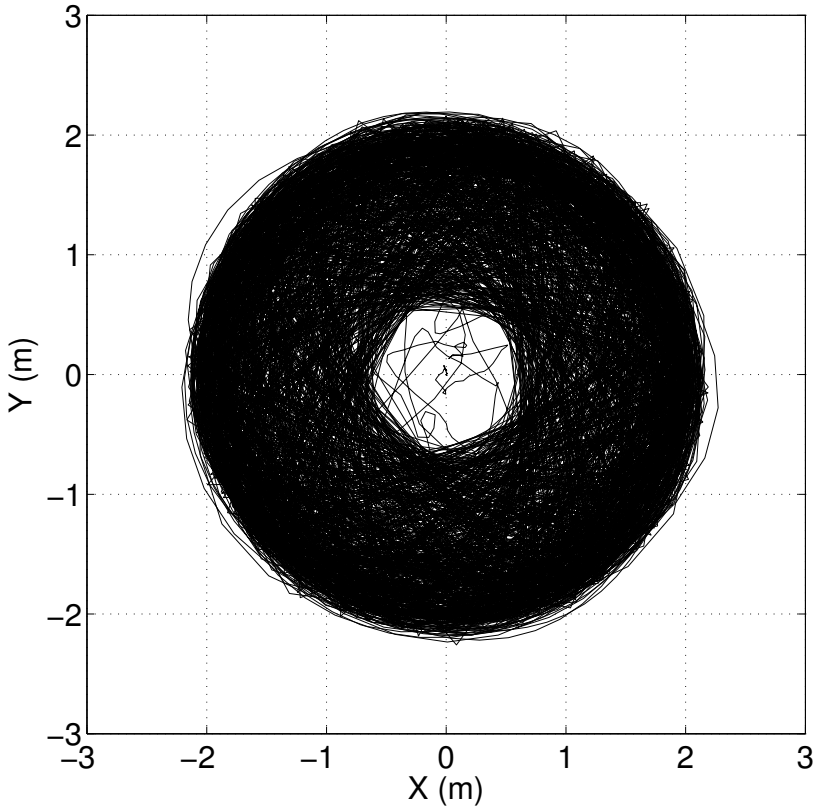

Figure 4.15: **Trajectory of parent body of CHAS In-plane formation for** $e = 0.7$ **(6 orbits).**

4.2 Effects of J_2 perturbation on tethered formations

The combined effects of tether mass (simulated by means of a discrete bead model [14]) and J_2 perturbation on the dynamics of various tethered formations is now analyzed taking into account the dynamics modeled in Eqs. 2.33 and 2.34.

4.2.1 Initial conditions for deputies and beads

Equations 2.33 and 2.34 are used to describe the motion of each deputy, bead and the parent body of the formation. An initial condition in terms of position and velocity is needed for each one of these bodies, represented as a mass element. The initial condition for velocity of the parent body is computed using the expressions presented in Ref. [16] that ensures that the orbit of the parent does not present any secular drift. These initial conditions are on $\dot{x}_{p_0}$ and $\dot{y}_{p_0}$, and depend on the initial values, x_{p_0} and y_{p_0}, for the same

mass element:

$$\dot{x}_{p_0} = y_{p_0}\, n\frac{1-s}{\sqrt{1+s}} \tag{4.17}$$

$$\dot{y}_{p_0} = -2x_{p_0}\, n\sqrt{1+s} + \frac{3J_2R_e^2n^2}{4kr_{\text{ref}}}\sin^2 i_{\text{ref}} \tag{4.18}$$

There is no particular requirement on the initial condition z_{p_0} and $\dot{z}_{p_0}$ in the $\hat{\mathbf{z}}$ axis direction for the parent body. The calculation of the initial position and velocity for each deputy and bead, follows the same principle described in chapter 3 for the simplified case of circular unperturbed reference orbit.

The mechanical properties of the tethers is equivalent to that defined in Ch. 3. The undesirable "rounding" effect on closed formations shown in Ch. 2, does not allow to precisely determine the effect of the J_2 perturbation on formation dynamics, for this reason only open (HAS) planar formations are analyzed in detail. The mission characteristics are different since in this case the reference orbit is elliptical, and it presents a non-zeroinclination.

4.2.2 Proposed approach

The J_2 terms along the $\hat{\mathbf{i}}_{\mathcal{R}}$ and $\hat{\mathbf{j}}_{\mathcal{R}}$ direction in the LVLH frame reported in Eqs. (2.33) have the same value for elements of the same formation since the inclination of the reference orbit is the same for all elements of the same formation. This means that when studying the relative dynamics of elements in the same formation these terms cancel out one another. In this case, and only for in-plane dynamics ($\hat{\mathbf{i}}_{\mathcal{R}}$-$\hat{\mathbf{j}}_{\mathcal{R}}$), the only difference with respect to the HCW equations is the change in the reference orbit angular rate. On the converse, the J_2 perturbation along the $\hat{\mathbf{k}}_{\mathcal{R}}$ axis may affect differently elements belonging to the same formation. In the absence of external forces, the analytical solution for the cross track dynamics is

$$z(t) = (p_l t + p_m)\sin(p_q t + p_\phi) \tag{4.19}$$

Variables p_q, p_l, p_m and p_ϕ, depend on the initial condition on position and velocity in the $\hat{\mathbf{k}}_{\mathcal{R}}$ direction. A value of $p_l \neq 0$ determines the presence of a secular drift term growing with time t in the $\hat{k}_{\mathcal{R}}$ direction. The procedure to calculate p_l is described in detail in Reference [16], where the necessary corrections for the cross–track motion are provided. The value of p_l is zero if one of these two conditions holds:

- The initial inclination of the satellite i_{sat} is the same as the one of the reference

orbit;

- The initial separation in the longitude of the ascending node between the satellite and the reference orbit $\Delta\Omega_0$ is zero.

Values for i_{sat} and $\Delta\Omega_0$ can be calculated from the following equations:

$$\begin{aligned} i_{\text{sat}} &= \dot{z}_0/(kr_{\text{ref}}) + i_{\text{ref}} \\ \Delta\Omega_0 &= \arcsin\left[\frac{\sin(z_0/r_{\text{ref}})}{\sin(i_{\text{ref}})}\right] \approx \frac{z_0}{r_{ref}\sin(i_{\text{ref}})} \end{aligned} \tag{4.20}$$

In conclusion, the presence of secular motion for a particular body in the formation is determined by the initial condition on z_0 and $\dot{z}_0$. Depending on the structure and orientation of the formation, it is possible to fulfill at least one of these two conditions. For in–plane formations deputies and tethers lie on the same reference orbit plane, such that both conditions, $z_0 = \dot{z}_0 = 0$ are satisfied. Therefore the absence of any secular drifting motion is guaranteed.

The case of Earth–facing configurations is more complex. For the elements lying on the $\hat{\mathbf{i}}_{\mathcal{R}}$-$\hat{\mathbf{j}}_{\mathcal{R}}$ plane at initial time, the $z_0 = 0$ condition is satisfied, whereas for elements with $z_0 \neq 0$, the requirement for the absence of secular behaviour is satisfied only if the relative motion at initial time provides a zero value for the initial speed component normal to the orbit plane, that is, $\dot{z}_0 = 0$. In the most general case a secular term is present, that affects the resulting behaviour of the formation.

As anticipated above, the behaviour of Hub–And–Spoke (HAS) and Closed–Hub–And–Spoke (CHAS) formations for in–Plane and Earth–Facing configurations is analysed in the sequel.

4.2.3 Open–loop dynamics of tethered formation

The purpose of this chapter is to evaluate the effect of the J_2 perturbation on tethered satellite formations. For this reason, the behaviour of a HAS formation will be compared with the behaviour of the same formation in the absence of the perturbation. The scenario incorporating the perturbation is that of a non–equatorial orbit, since it is the case where the perturbation effect is more significant. The inclination of the orbit is $i_{\text{ref}} = 45°$ and the altitude of the parent body is 200 Km above the surface of the Earth. The effects of the perturbation on formations flying in equatorial orbits are much less significative than

in non-equatorial orbits and are not considered in the sequel. The stability of the cluster is analyzed by performing a numerical simulation of the dynamic model as in Ch. 2.

In-plane formations

For the HAS in–plane formation, all the deputies plus the parent body lie in the orbital plane. Since equations for orbital dynamics and cross–track dynamics are uncoupled, the fact that $z_0 = 0$ and $\dot{z}_0 = 0$ eliminates any cross–track trajectory. This configuration simplifies considerably the equations, since $i_{\text{sat}} = i_{\text{ref}}$ and $\Delta\Omega_0 = 0$. The absence of cross-track motion in the in–plane formation, makes the correction in the reference orbital rate the only change in the equations of motion with respect to the unperturbed equation model, because as outlined above the J_2 term in the $\hat{\mathbf{i}}_{\mathcal{R}}$ and $\hat{\mathbf{j}}_{\mathcal{R}}$ direction is the same for all elements of the cluster.

The position initial condition for the four deputies of the formation is set to:

$$\begin{aligned} \boldsymbol{r}_{1_0} &= [l_i^{(0)}\ l_i^{(0)}\ 0] \cdot \sqrt{2}/2 = -\boldsymbol{r}_{3_0} \\ \boldsymbol{r}_{2_0} &= [-l_i^{(0)}\ l_i^{(0)}\ 0] \cdot \sqrt{2}/2 = -\boldsymbol{r}_{4_0} \end{aligned} \tag{4.21}$$

Initial velocity is computed using Equation (3.2) with the parent object placed at the origin of the LVLH frame and

$$\boldsymbol{\omega}_0 = [0\ \ 0\ \ r_s\omega] \tag{4.22}$$

where $l^{(0)} = 1000$ m and $\omega = nc$. In the case of the HAS in–plane formation, the value of r_s is set to $r_s = 10$. The initial condition of beads is computed in the same way, with the local angular velocity equal to that of the deputy belonging to each tether.

The results shown in Fig. 4.16 demonstrate that values for tether elongation are very close, when comparing the unperturbed case with that in the presence of J_2 effects. The figure represents the increment of the distance between the first deputy and the parent body, but the behaviour is rather similar also for the other three deputies. Only a slight phase shift in the oscillations and a minimal change in distance increment can be noticed. These minor variations are due to the fact that the orbital rate with the J_2 model is slightly faster, and this has an impact over the initial velocity of deputies that are computed as a factor of ω. The orbital angular velocity n is increased by a factor $c = 1.00019$.

As far as the angular distance between tethers is concerned, in the absence of the J_2

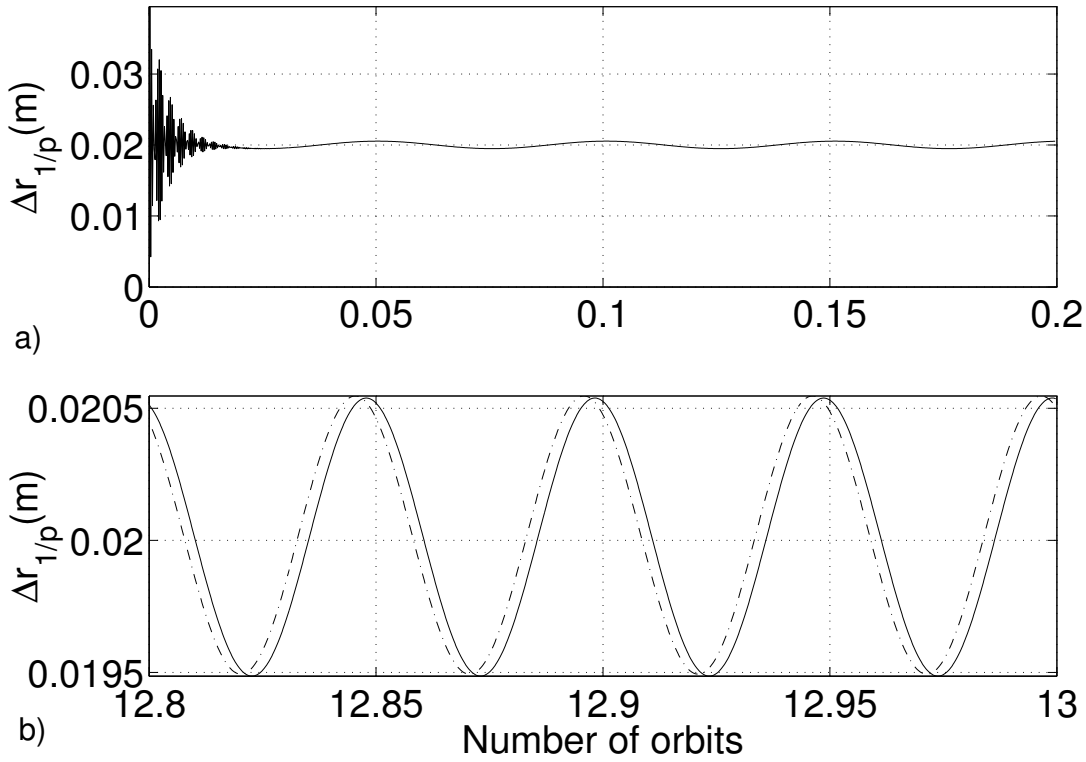

Figure 4.16: **HAS in–plane formation. Distance increment between first deputy and parent body Δl_1, (solid line, with J_2 effects; dotted one, without J_2).**

perturbation the angle between tethers connecting adjacent deputies oscillates around 90° with an amplitude of less than 0.5° and a mean value slowly increasing with time. In Fig. 4.17 it can be appreciated how in the perturbed scenario (plot (b)), the increase of mean value of the oscillations grows faster than in the non–perturbed case (plot (a)). This fact affects formation stability, where in spite of the elongation of the tethers being fairly stable, with the formation keeping its orientation within the orbital plane, the angular displacement between pairs of tethers slowly grows, thus making in the long run two of the tethers fold onto the neighbouring ones.

Earth-facing formations

Earth–facing configurations exhibit a more complex behaviour than in–plane formations due to the presence of cross–track dynamics. First of all, even though the deputies of an Earth–facing formation initially lie on the $\hat{\mathbf{j}}_{\mathcal{R}} - \hat{\mathbf{k}}_{\mathcal{R}}$ plane and have an initial velocity with non–zero components along one or both these axes, with initial values in the $\hat{\mathbf{i}}_{\mathcal{R}}$ direction $x_0 = 0$ and $\dot{x}_0 = 0$, the dynamic equations clearly show that values of $y_0 \neq 0$ or $\dot{y}_0 \neq 0$

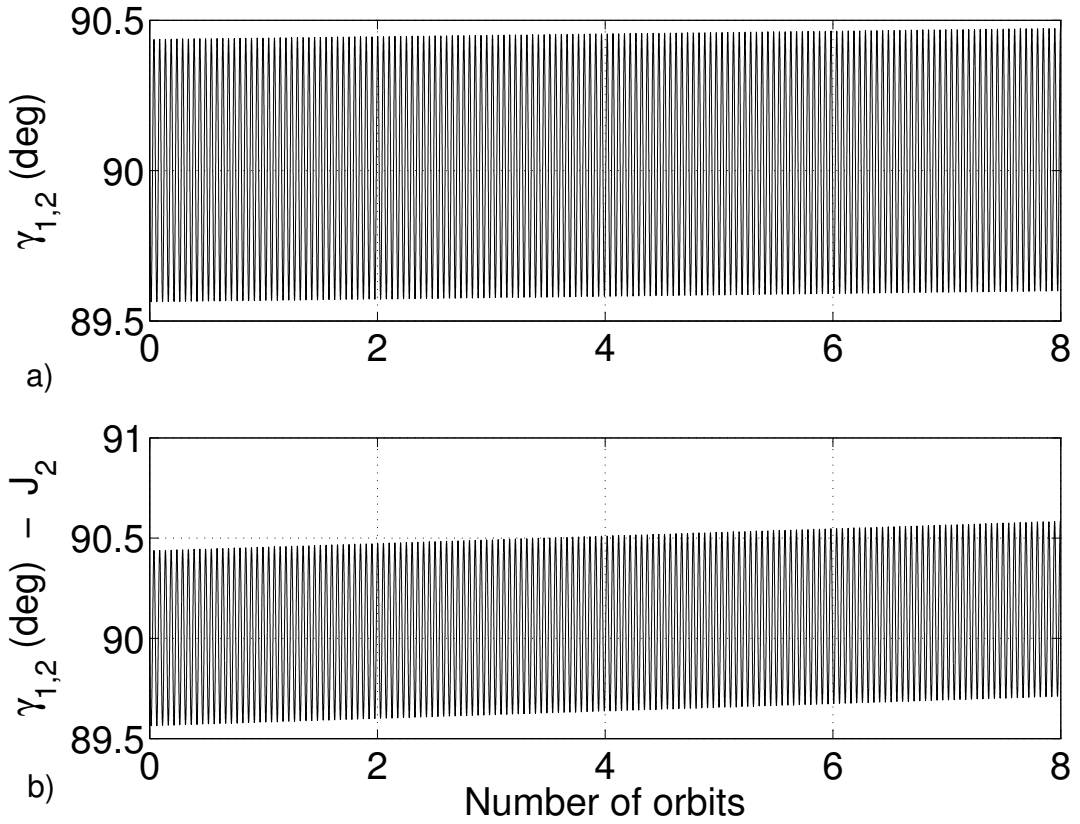

Figure 4.17: **HAS in–plane formation. Angular separation between tethers 1 and 2, $\gamma_{1,2}$ without J_2 effects (a) and with J_2 (b).**

affect the dynamics in the $\hat{\mathbf{i}}_{\mathcal{R}}$ direction as well, thus creating a three-dimensional trajectory. Incorporating tethers creates an additional coupling due to the constraint imposed by tether length: tension forces exchanged between pairs of bodies directly connected by a tether couple cross–track and and in–plane dynamics.

The initial condition for the position of the four deputies of the formation is set to

$$\begin{aligned} \boldsymbol{r}_{1_0} &= [0\ l^{(0)}\ l^{(0)}] \cdot \sqrt{2}/2 = -\boldsymbol{r}_{3_0} \\ \boldsymbol{r}_{2_0} &= [0\ -l^{(0)}\ l^{(0)}] \cdot \sqrt{2}/2 = -\boldsymbol{r}_{4_0} \end{aligned} \tag{4.23}$$

whereas initial velocity is computed according to Eq. (3.2) with the parent object placed at the origin of the LVLH frame and

$$\boldsymbol{\omega}_{i/p} = [-r_s\omega\ \ 0\ \ 0] \tag{4.24}$$

A value of $l^{(0)} = 1000$ m is again chosen for the nominal length of tethers connecting the parent body to the deputies. As for the angular speed, it is $\omega = nc$ with values of r_s set to $r_s = 10$ for all deputies and tethers, as indicated in Ref. [13] for the massless tether case. The value of r_s is the same for the HAS and CHAS formation scenarios.

Note that the considered initial condition provides for a situation where none of the deputies satisfy one of the conditions necessary for making the secular drift term to vanish, that is, either $z_0 = 0$ or $\dot{z}_0 = 0$. The l term of the cross–track dynamics affects all the deputies (and most of the beads), and therefore, all these masses should present a secular drift, which is counteracted upon by the presence of tether tension.

In terms of distance between external agents and parent body, the behaviour (presented in Fig. 4.18) is similar to that observed for the in–plane formation considered in the previous subsection. As for the angular displacement, in this case, there is almost no difference between the perturbed and unperturbed scenarios, as demonstrated by the plots in Fig. 4.19. As for the elongation, minor differences are present, due to the different orbital rate used to compute the velocity initial condition of deputies, as required in Eq. (3.2).

The overall behaviour of the formation is the same observed for the unperturbed scenario in a way similar to what happens for the massless tether case). Figure 4.20 shows how the normal vector to the formation, tilts around the $\hat{\mathbf{x}}$ axis, and that the four deputies plus the parent body are coplanar most of the time. The coplanarity parameter C, as defined in Eq. (3.7) is reported in Fig. 4.20(b).

4.2.4 Effect of the J_2 perturbation on the parent body

As described previously, the equations of motion take into consideration the fact that the parent body is not attached to the reference orbit. In an unperturbed scenario, the centre of mass of the formation always remains on the reference orbit, with small oscillations of the parent body around the reference due to internal forces exerted by tethers. However, when J_2 perturbation affects deputies and beads in a different way, small variations of tether tension may results that are not perfectly balanced on the parent body, thus pulling it away, in the long run, from the reference orbit. As a consequence, the whole formation slowly drifts away from the reference orbit.

In Fig. 4.21, the distance D_p between the parent and the reference orbit is computed for the different scenarios studied in this study. As it can be seen, in–plane orbits are less

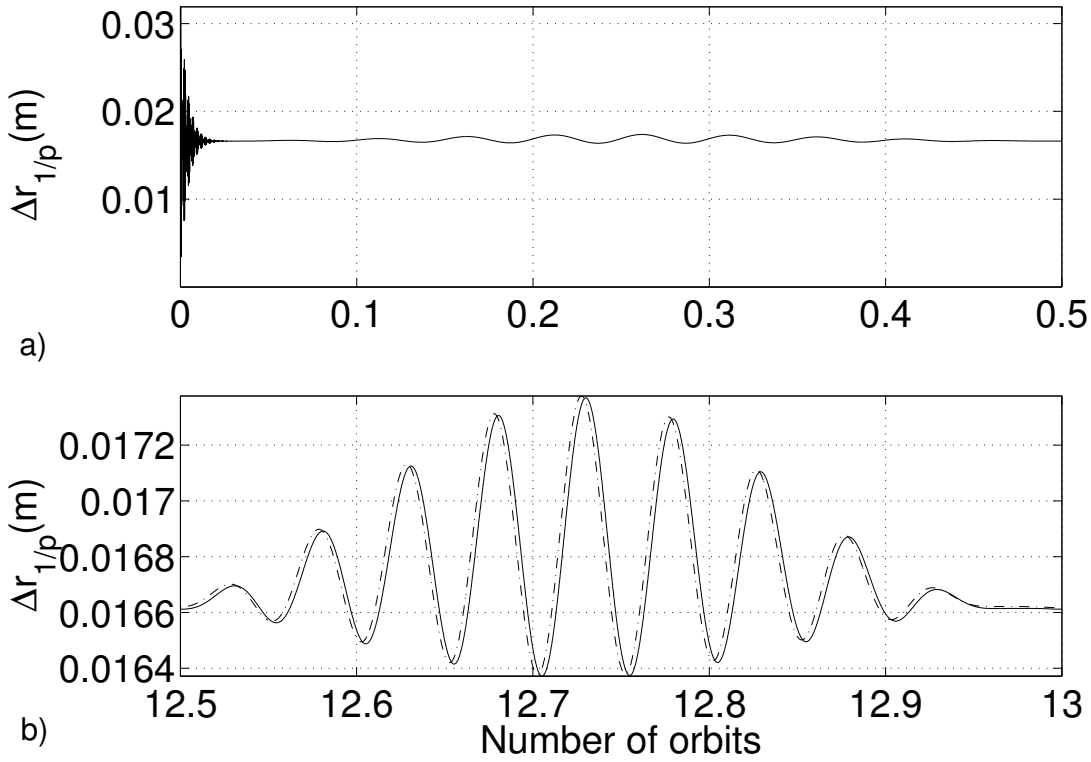

Figure 4.18: **Elongation of 1–st tether, Δl_1, for HAS Earth–facing formation (solid line, with J_2 effects; dotted one, without J_2).**

affected by the dynamics of the tethers than Earth-facing ones.

For the in-plane case, all the elements are affected in the same way by the J_2 perturbation. On the other hand, the Earth–facing case provides the most interesting scenario, where the elements are affected differently by Earth's oblateness. Since the orbiting elements (deputies and beads) have different parameter values in Eq. 4.19 at the initial time, all of them are characterized by a secular term p_l different from zero.

Figure 4.22 shows the separation from the reference orbit in the $\hat{\mathbf{k}}_{\mathcal{R}}$ direction. It can be noted how the parent body presents an oscillatory movement of increasing amplitude in the cross-track direction. This is very evident in the HAS Earth–facing scenario. It turns out that the period of the oscillation approximately matches that of the orbit rotation, and also that of the variable p_q in Eq. (4.19).

It is important to highlight that the parent body in all cases is placed at the origin

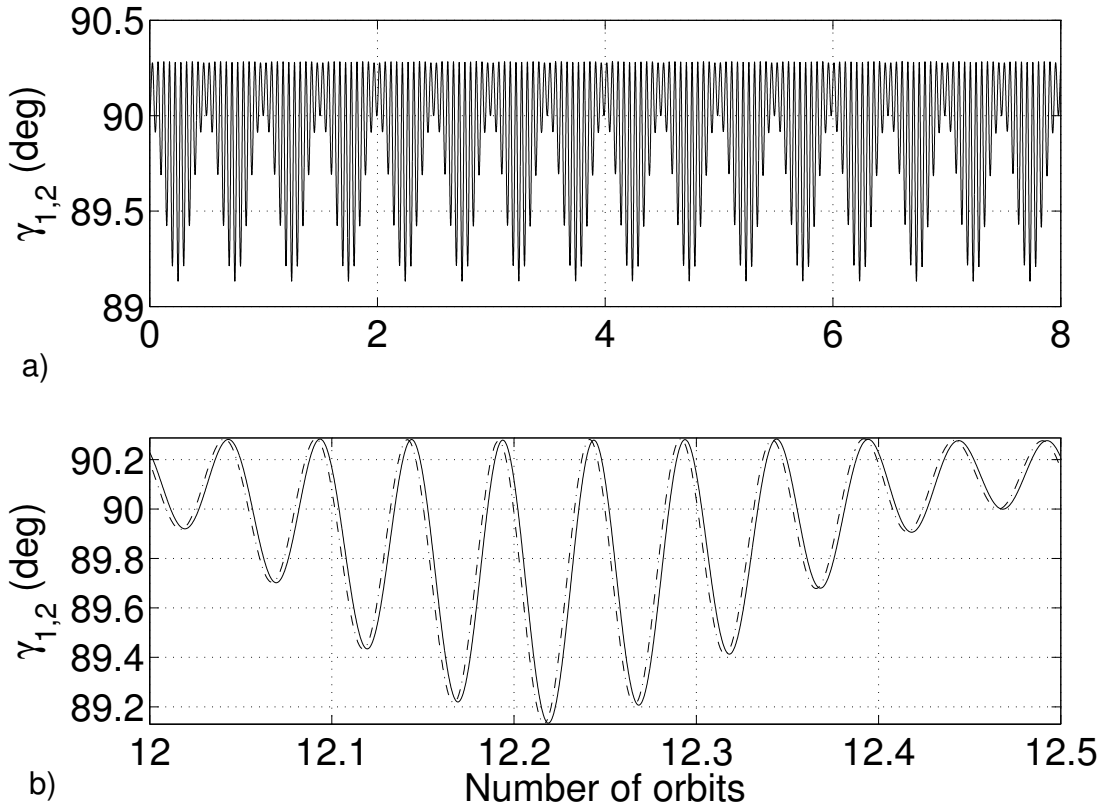

Figure 4.19: **Angular separation between tethers 1 and 2, $\gamma_{1,2}$ (solid line, with J_2 effects; dotted one, without J_2).**

with zero velocity. This initial condition should make the parent body to lie on the orbit plane. However, the forces exerted by tethers with non-zero secular terms (Earth-facing scenarios) move it apart from the reference orbit with oscillations of growing amplitude. The same Earth-facing configurations without the J_2 perturbation show the behaviour presented in Fig. 4.23, where it can be clearly seen that a bounded oscillation in the $\hat{\mathbf{k}}_{\mathcal{R}}$ direction is present with respect to the reference orbit.

4.2.5 Effects of J_2 perturbation on formation behavior

This study has presented the effects of incorporating the J_2 effect on massive tethered satellite formations modelled following a HCW approach. No significant differences were found in terms of elongation of tethers and angular separation for the HAS and CHAS configurations in the in-plane and Earth-facing orientations. In the Earth–facing scenario,

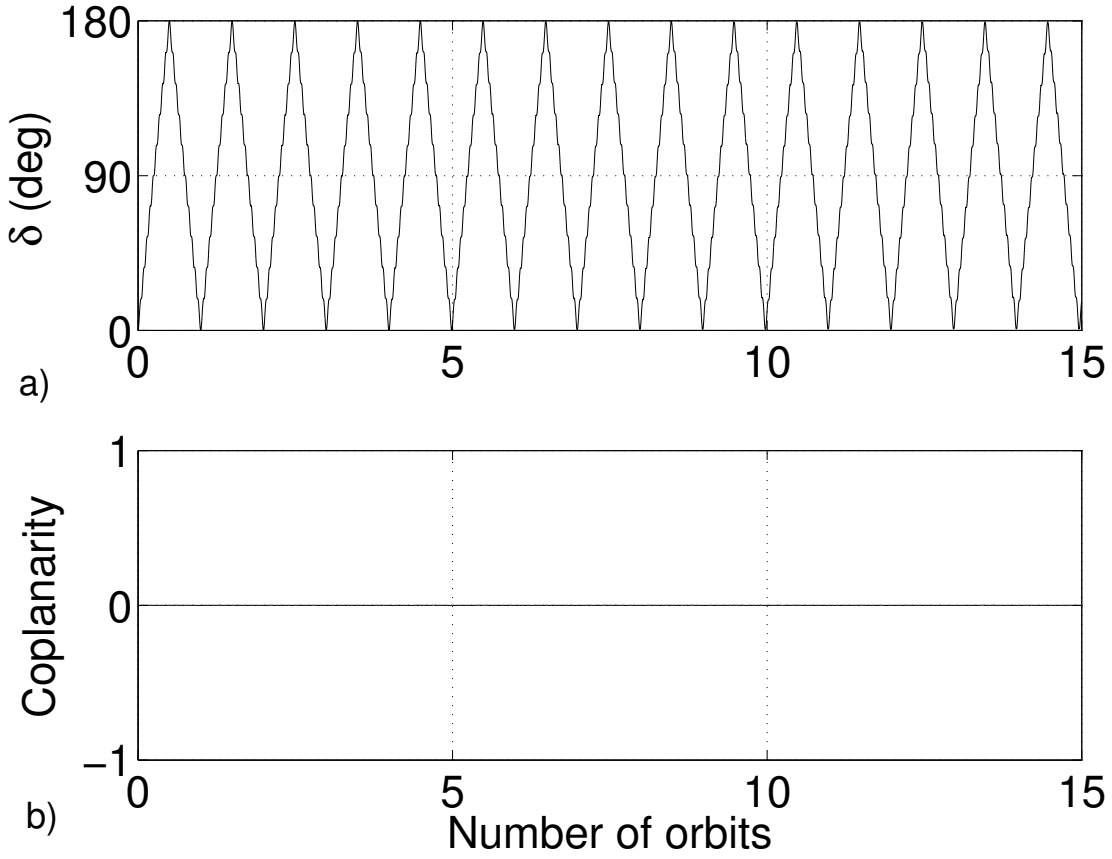

Figure 4.20: **Orientation and coplanarity parameters for the HAS Earth–facing formation.**

objects of the formation are affected differently by the perturbation, some of them potentially having secular drifts. It is interesting to observe that the trajectory of the parent body in the Earth–facing cases presents oscillations of increasing amplitude in the $\hat{\mathbf{k}}_{\mathcal{R}}$ (cross–track) direction. As it was pointed before, in this case, all the elements of the formation are affected differently by the perturbation in their cross–track dynamics.

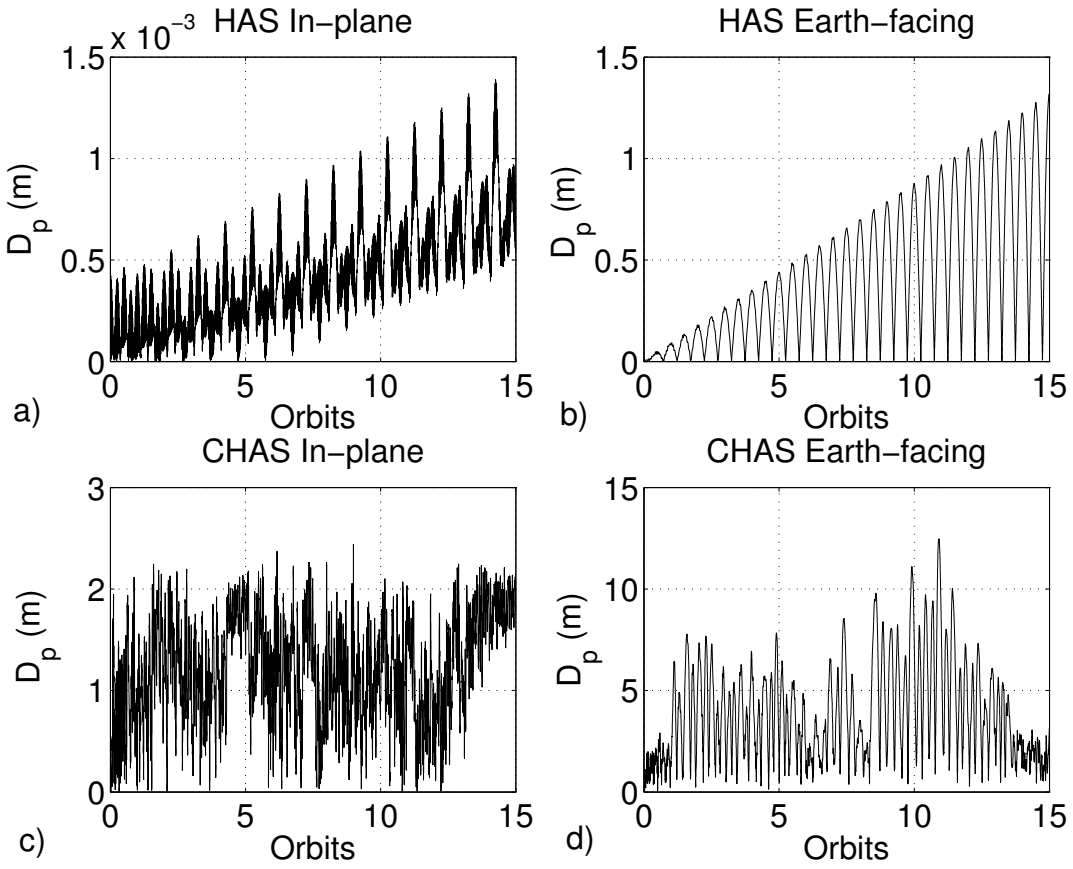

Figure 4.21: **Distance of parent body from reference orbit.**

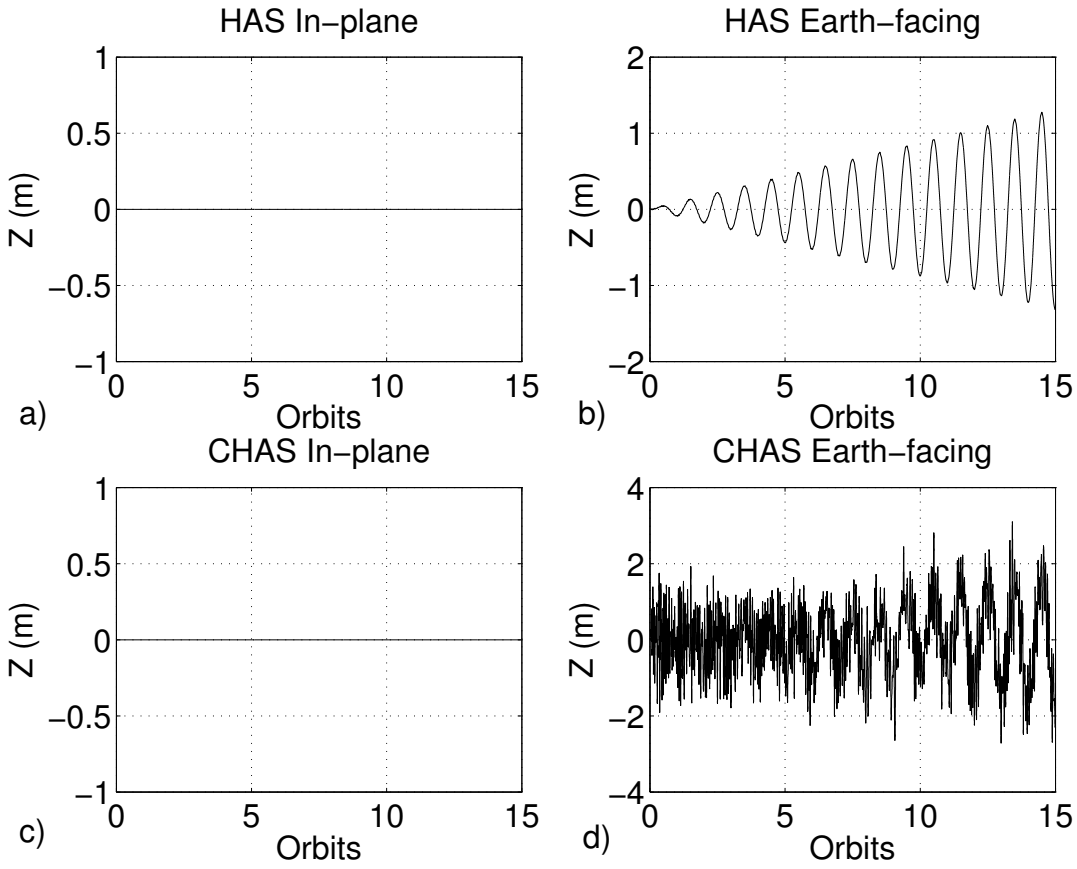

Figure 4.22: **Elevation along the Z axis of parent body.**

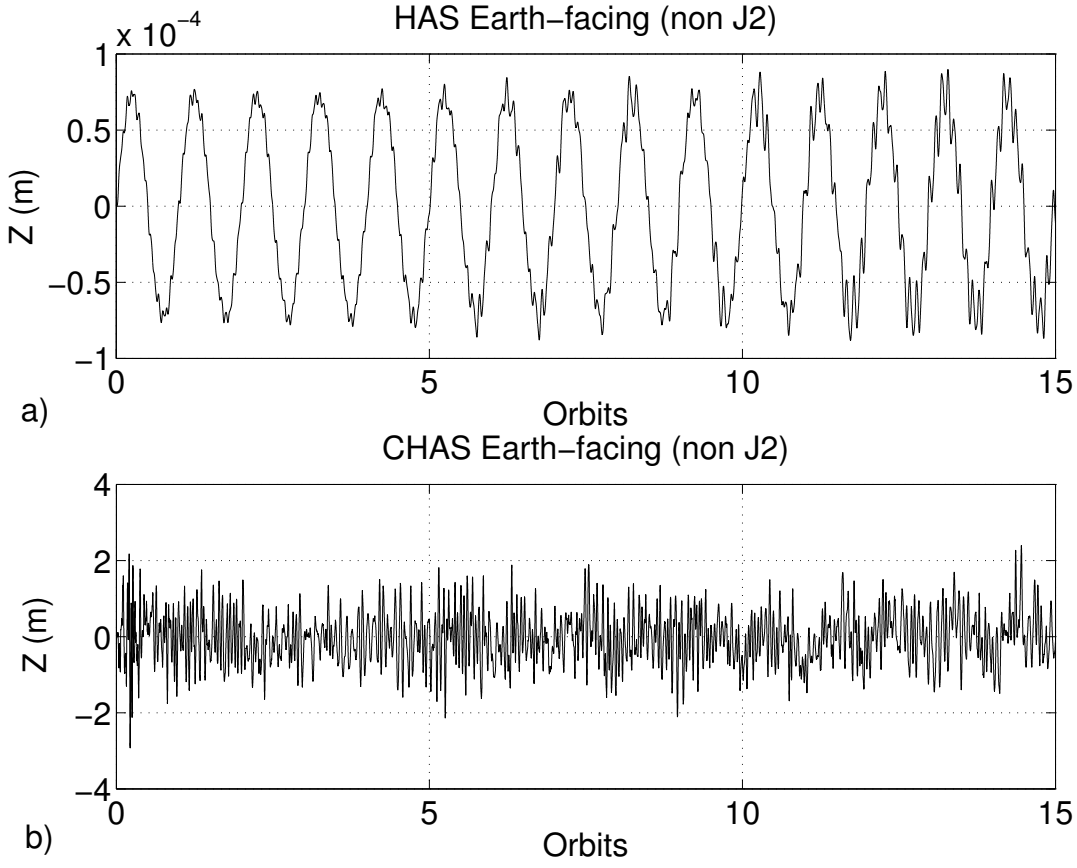

Figure 4.23: **Elevation in Z axis of parent (no J_2)**

Chapter 5

Tethered Formation Control

The behavior of tethered formations in Low Earth Orbit was analyzed in Ch. 3 and 4 proving that there is no formation configuration that guarantees a stable natural equilibrium of a spinning tethered cluster. Only formations lying in the orbital plane present a certain degree of stability, but still a controller is needed to ensure that deputies maintain the desired position. This chapter presents a control strategy for a tethered formation cluster that provides position and attitude control.

Taking into account the arguments presented in Ch. 2, the Thomson and the conical Likins–Pringle equilibrium orientations appear as the most appropriate for practical purposes. The latter, in particular, allows for an almost Earth–facing orientation when a small tilt angle γ is achieved. The cluster geometry chosen for this study is the Double–Pyramid without parent body, since according to [76] exhibits a behavior similar to that of a spinning rigid body.

5.1 Formation Flying Control

One of the reasons to study the behavior and control tethered formations is to address ultimately the formation flying problem. Reference [137] provides a deep insight into spacecraft formation flying topics. As cited in this book, formation flying is about *"The tracking or maintentance of a desired spacecraft separation, orientation or position between or among spacecrafts"*. References [138] and [139] summarize a state of the art of Spacecraft Formation Flying. The first paper addresses the guidance problem, which consist in defining the appropriate relative orbits, whereas the second is focused on active

control strategies. Reference [140] studies the stability of the relative motion dynamics of two spacecraft in the phase plane taking into account the J_2 perturbation. Decentralized control techniques applied to satellite flight formation are explored in references [22] and [141]. Other modern control techniques like optimal control, adaptive control and μ control are studied in references [108], [142], [143] and [144] respectively.

5.2 Tethered Formation Flying Control

Figure 5.1 shows a diagram of the most common mission profiles related to tether formations. The nomenclature follows that used in references [1] and [138]. Relative orbits can be passive (PRO) or active (ARO). In the first case, no active control is needed, whereas in the second case a control loop needs to be implemented to maintain the relative configuration of formation members. In Deep Space (DS) applications, relative spacecraft dynamics in general is not subject to orbital dynamics or external perturbations, which is the case of Planet Orbital Environment (POE) missions. The POE literature is focused mainly on finding Passive Relative Orbits (PRO). The case of Active Relative Orbits (ARO) is that case requiring closed loop control to maintain the structure within the required configuration shape.

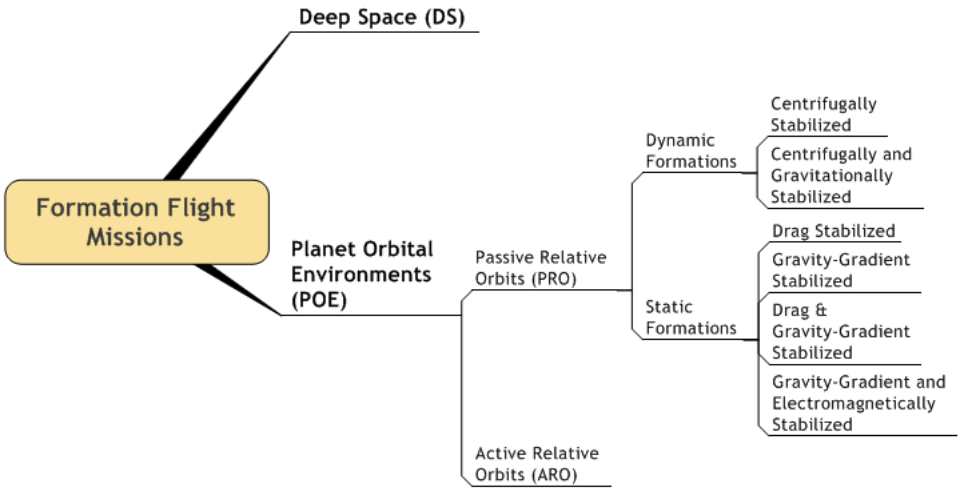

Figure 5.1: **Mission Profiles (taken from [1] and [138])**

Among Tethered (PRO) formations there are dynamic formations where the structure is stabilized through centrifugal and in some cases gravitational forces. Gravitational

forces have a stabilizing role for Earth-pointing dumbell tethers as described in detail in Ch. 2, due to differential gravity effect on tether ends.

The static formations PROs, can be stabilized through drag, by the gravitational potential, or electromagnetically. On a tethered system moving through the Earth's magnetic field, electric potential is created along conductive tethers. This fact can be used to generate electrical power/thrust as presented in [1].

When implementing an active controller, solving the spacecraft formation flying control problem can be further decomposed in two different problems, or a combination of both:

- Development of control strategies allowing for the reconfiguration of the formation (e.g. expansion, contraction or change of orientation of the whole set of agents). This involves developing techniques to avoid spacecraft interference and collision. This is a coarse control strategy with the purpose of orientating the overall formation along an specific direction. This kind of control is specially suited for missions in which the overall cluster must point to a specific direction.
- Development of control laws aimed at maintaining the relative position with respect to an inertially fixed attitude along the orbit (inertial station keeping). Accurate precision control requires compensating perturbations. This level consist of a fine control approach in order that each agent achieves the desired location and orientation with respect to a formation-fixed reference frame, assuming 6-DOF agent control capability.

5.3 Virtual Structure Control Approach

This section introduces the virtual structure control approach, both in the centralized and decentralized versions. This technique will be adapted for formation control of a tethered formation.

5.3.1 Centralized Virtual Structure Control Approach

In addition to frames $\mathcal{O}$ (inertial) and $\mathcal{R}$ (LVLH) introduced in Chapter 2, two additional reference frames are needed to define the virtual structure approach. Frame $\mathcal{F}$ is fixed at the center of the formation (or equivalently the center of the virtual structure); frame $\mathcal{I}$ is a reference frame fixed at agent i. Following the same approach proposed in Reference [20], the equations of motion for the translational and rotational dynamics of the

virtual structure are given by

$$\begin{pmatrix} \dot{\boldsymbol{r}}_F \\ M_F\dot{\boldsymbol{v}}_F \\ \dot{\hat{\boldsymbol{q}}}_F \\ \dot{\bar{q}}_F \\ \boldsymbol{J}_F\dot{\boldsymbol{\omega}}_F \\ \dot{\boldsymbol{\lambda}}_F \\ \ddot{\boldsymbol{\lambda}}_F \end{pmatrix} = \begin{pmatrix} \boldsymbol{v}_F \\ \boldsymbol{f}_F \\ -\frac{1}{2}\boldsymbol{\omega}_F \times \hat{\boldsymbol{q}}_F + \frac{1}{2}\bar{q}_F\boldsymbol{\omega}_F \\ -\frac{1}{2}\boldsymbol{\omega}_F \cdot \hat{\boldsymbol{q}}_F \\ -\boldsymbol{\omega}_F \times \boldsymbol{J}_F\boldsymbol{\omega}_F + \boldsymbol{\tau}_F \\ \dot{\boldsymbol{\lambda}}_F \\ \boldsymbol{\sigma}_F \end{pmatrix} \tag{5.1}$$

The state variables of this equation are the rigid body position vector $\boldsymbol{r}_F$, the velocity vector, $\boldsymbol{v}_F$, the rigid body attitude quaternion $\boldsymbol{q}_F = (\hat{\boldsymbol{q}}_F, \bar{q}_F)$, the body angular velocity $\boldsymbol{\omega}_F$, and the two vectors of parameters $\boldsymbol{\lambda}_F$ and $\boldsymbol{\mu}_F$. Parameters $\boldsymbol{\lambda}_F$ and $\boldsymbol{\mu}_F$ are used to express the expansion ratio and expansion rate of the formation along the axes of $\mathcal{F}$. The position and orientation of the virtual structure F is controlled through the main controls of force $\boldsymbol{f}_F$, torque $\boldsymbol{\tau}_F$, and straint $\boldsymbol{\sigma}_F$ for controlling position, attitude and expansion ratio respectively. Constants M_F and $\boldsymbol{J}_F$ are the virtual mass and inertia tensors of the virtual structure F. Reference [20] presents a control law that stabilizes the virtual structure to a given position, attitude and expansion ratio.

The state of the formation is defined by the coordination vector,

$$\boldsymbol{\xi}_F = [\boldsymbol{r}_F^T, \boldsymbol{v}_F^T, \boldsymbol{q}_F^T, \boldsymbol{\omega}_F^T, \boldsymbol{\lambda}_F^T, \dot{\boldsymbol{\lambda}}_F^T]^T \tag{5.2}$$

which provides the state of the virtual structure F, and consequently the overall shape of the formation. In the centralized approach, this vector is broadcasted to all the agents of the formation and each agent derives its own desired state to be tracked in order to maintain the formation shape.

The desired position and orientation of the i–th agent with respect to the virtual structure is defined through vector $\boldsymbol{X}_{iF}^d = [\boldsymbol{r}_{iF}^d, \boldsymbol{v}_{iF}^d, \boldsymbol{q}_{iF}^d, \boldsymbol{\omega}_{iF}^d]$ which expresses the desired state of the agent i in the $\mathcal{F}$ reference frame. If the shape of formation must remain fixed, the components of $\boldsymbol{X}_{iF}$ will be constant.

Letting the direction cosine matrix $\boldsymbol{C}_{RF}$ be the transformation from the virtual structure based reference frame $\mathcal{F}$ to the orbit frame $\mathcal{R}$, the following equations transform

vector components to the orbital reference coordinate system:

$$\begin{aligned} \boldsymbol{r}_i^d(t) &= \boldsymbol{r}_F(t) + \boldsymbol{C}_{RF}(t) \cdot \boldsymbol{\Lambda}(t) \cdot \boldsymbol{r}_{iF}^d(t) \\ \boldsymbol{v}_i^d(t) &= \boldsymbol{v}_F(t) + \boldsymbol{C}_{RF}(t) \cdot \dot{\boldsymbol{\Lambda}}(t) \cdot \boldsymbol{r}_{iF}^d(t) + \boldsymbol{\omega}_F(t) \times \boldsymbol{C}_{RF}(t) \cdot \boldsymbol{\Lambda}(t) \cdot \boldsymbol{r}_{iF}^d(t) \\ \boldsymbol{q}_i^d(t) &= \boldsymbol{q}_F(t) + \boldsymbol{q}_{iF}^d(t) \\ \boldsymbol{\omega}_i^d(t) &= \boldsymbol{\omega}_F(t) \end{aligned} \tag{5.3}$$

Matrix $\boldsymbol{\Lambda}(t) = \mathrm{diag}(\boldsymbol{\mu}_F(t))$ with $\boldsymbol{\mu}_F(t) = [\mu_1(t), \mu_2(t), \mu_3(t)]^T$ expresses the expansion rate of the formation. Vector $\boldsymbol{X}_i^d = [\boldsymbol{r}_i^d, \boldsymbol{v}_i^d, \boldsymbol{q}_i^d, \boldsymbol{\omega}_i^d]$ defines the desired state for agent i in orbital reference coordinates. The direction cosine matrix $\boldsymbol{C}_{RF}$ can be calculated as

$$\boldsymbol{C}_{RF} = (2\bar{q}_F^2 - 1)I + 2\hat{\boldsymbol{q}}_F\hat{\boldsymbol{q}}_F^T + 2\bar{q}_F\hat{\boldsymbol{q}}_F^{\times} \tag{5.4}$$

The equations of motion of the i–th agent (assumed as rigid body) are

$$\begin{pmatrix} \dot{\boldsymbol{r}}_i \\ M_F\dot{\boldsymbol{v}}_i \\ \dot{\hat{\boldsymbol{q}}}_i \\ \dot{\bar{q}}_i \\ \boldsymbol{J}_F\dot{\boldsymbol{\omega}}_i \end{pmatrix} = \begin{pmatrix} \boldsymbol{v}_i \\ \boldsymbol{f}_i \\ -\frac{1}{2}\boldsymbol{\omega}_i \times \boldsymbol{q}_i + \frac{1}{2}\bar{q}_i\boldsymbol{\omega}_i \\ -\frac{1}{2}\boldsymbol{\omega}_i \cdot \boldsymbol{q}_i \\ -\boldsymbol{\omega}_i \times \boldsymbol{J}_F\boldsymbol{\omega}_i + \boldsymbol{\tau}_i \end{pmatrix} \tag{5.5}$$

Once the desired values $\boldsymbol{X}_i^d$ are derived, they will be used as the input for a feedback control law in order to ensure asymptotic stability. References [145], [146] and [20] study the attitude control problem for a rigid body, and provide other model independent and model dependent based (including feedback linearization) families of control laws for attitude tracking of a rigid body in the following form:

$$\begin{aligned} \boldsymbol{f}_i &= m_i[\dot{\boldsymbol{v}}_i^d - K_{ri}(\boldsymbol{r}_i - \boldsymbol{r}_i^d) - K_{vi}(\boldsymbol{v}_i - \boldsymbol{v}_i^d)] \\ \boldsymbol{\tau}_i &= \boldsymbol{J}_i\dot{\boldsymbol{\omega}}_i^d + \frac{1}{2}\boldsymbol{\omega}_i \times \boldsymbol{J}_i(\boldsymbol{\omega}_i + \boldsymbol{\omega}_i^d) - k_{qi}\boldsymbol{q}_i^e + \boldsymbol{K}_{\omega i}(\boldsymbol{\omega}_i - \boldsymbol{\omega}_i^d) \end{aligned} \tag{5.6}$$

It can be proven [19] that Eq. (5.6) successfully stabilizes the formation to its desired state.

5.3.2 Decentralized Virtual Structure Control Approach

Reference [19] shows an evolution of the virtual structure control, in which the control is decentralized. In this case, a copy of the virtual structure dynamics is implemented

on each satellite, producing a local coordination vector i that evolves under the feedback obtained from the adjacent neighbors in the formation. In this approach, an instance of the virtual structure is integrated on each deputy. Differences between the state of adjacent virtual structure instances are corrected by using appropriate control terms. The equations of motion of each virtual structure F_i are

$$\begin{pmatrix} \dot{\boldsymbol{r}}_{Fi} \\ M_F \dot{\boldsymbol{v}}_{Fi} \\ \dot{\hat{\boldsymbol{q}}}_{Fi} \\ \dot{\bar{q}}_{Fi} \\ \boldsymbol{J}_{Fi} \dot{\boldsymbol{\omega}}_{Fi} \\ \dot{\boldsymbol{\lambda}}_{Fi} \\ \ddot{\boldsymbol{\lambda}}_{Fi} \end{pmatrix} = \begin{pmatrix} \boldsymbol{v}_{Fi} \\ \boldsymbol{f}_{Fi} \\ -\frac{1}{2}\boldsymbol{\omega}_{Fi} \times \hat{\boldsymbol{q}}_{Fi} + \frac{1}{2}\bar{q}_{Fi}\boldsymbol{\omega}_{Fi} \\ -\frac{1}{2}\boldsymbol{\omega}_{Fi} \cdot \hat{\boldsymbol{q}}_{Fi} \\ -\boldsymbol{\omega}_{Fi} \times \boldsymbol{J}_F \boldsymbol{\omega}_{Fi} + \boldsymbol{\tau}_{Fi} \\ \dot{\boldsymbol{\lambda}}_{Fi} \\ \boldsymbol{\sigma}_{Fi} \end{pmatrix} \tag{5.7}$$

The transformation to the desired values is performed using again Eq. (5.3), but in this case, the calculation of $\boldsymbol{C}_{RFi}$ is based on the individual instantiation of the orientation quaternion $\boldsymbol{q}_{Fi}$ rather than $\boldsymbol{q}_F$ used in the centralized case. Position, orientation and expansion ratio of each virtual structure F_i are controlled through the main controls of force $\boldsymbol{f}_{Fi}$, torque $\boldsymbol{\tau}_{Fi}$, and straint $\boldsymbol{\sigma}_{Fi}$ for changing position, attitude and expansion ratio respectively. The coordination vector in this case is specific for each instance $\boldsymbol{\xi}_{Fi}$ instead of a global coordination vector $\boldsymbol{\xi}_{Fi}$. Reference [19] proposes the control law

$$\begin{aligned}
\boldsymbol{f}_{Fi} =& M_F\{-K_G(\boldsymbol{r}_{Fi} - \boldsymbol{r}_F^d) - \boldsymbol{\Gamma}_{Gi}\boldsymbol{v}_{Fi} + \\
&- \boldsymbol{K}_S(\boldsymbol{r}_{Fi} - \boldsymbol{r}_{F(i+1)}) - \boldsymbol{D}_S(\boldsymbol{v}_{Fi} - \boldsymbol{v}_{F(i+1)}) + \\
&- \boldsymbol{K}_S(\boldsymbol{r}_{Fi} - \boldsymbol{r}_{F(i-1)}) - \boldsymbol{D}_S(\boldsymbol{v}_{Fi} - \boldsymbol{v}_{F(i-1)})\} \\
\boldsymbol{\tau}_{Fi} =& - k_G \widehat{\boldsymbol{q}_F^{d*} \boldsymbol{q}_{Fi}} - \boldsymbol{\Gamma}_{Gi}\boldsymbol{\omega}_{Fi} + \\
&- k_S \widehat{\boldsymbol{q}^*_{F(i+1)} \boldsymbol{q}^*_{F(i)}} - \boldsymbol{D}_S[\boldsymbol{\omega}_{Fi} - \boldsymbol{\omega}_{F(i+1)}] + \\
&- k_S \widehat{\boldsymbol{q}^*_{F(i-1)} \boldsymbol{q}^*_{F(i)}} - \boldsymbol{D}_S[\boldsymbol{\omega}_{Fi} - \boldsymbol{\omega}_{F(i-1)}] \\
\boldsymbol{\sigma}_{Fi} =& - \boldsymbol{K}_G \widehat{\boldsymbol{q}_F^{d*} \boldsymbol{q}_{Fi}} - \boldsymbol{\Gamma}_{Gi}\boldsymbol{\omega}_{Fi} + \\
&- \boldsymbol{\Gamma}_S[\boldsymbol{\lambda}_{Fi} - \boldsymbol{\lambda}_{F(i+1)}] - \boldsymbol{D}_S[\boldsymbol{\mu}_{Fi} - \boldsymbol{\mu}_{F(i+1)}] + \\
&- \boldsymbol{\Gamma}_S[\boldsymbol{\lambda}_{Fi} - \boldsymbol{\lambda}_{F(i-1)}] - \boldsymbol{D}_S[\boldsymbol{\mu}_{Fi} - \boldsymbol{\mu}_{F(i-1)}] \\
\boldsymbol{\Gamma}_{Gi} =& \boldsymbol{D}_G + \boldsymbol{K}_F \cdot e_{Ti} = \boldsymbol{D}_G + \boldsymbol{K}_F \|\tilde{\boldsymbol{X}}_i\|^2
\end{aligned} \tag{5.8}$$

The term $\boldsymbol{\Gamma}_{Gi}$ provides the formation feedback [21] from low level (agent level) control

error to the virtual structure control. The value of constant $\boldsymbol{K}_F$ determines the amount of formation feedback in the model. The error $\tilde{\boldsymbol{X}}_i$ can be calculated as $\tilde{\boldsymbol{X}}_i = \boldsymbol{X}_i - \boldsymbol{X}_i^d$, where $\boldsymbol{X}_i = [\boldsymbol{r}_i^T, \boldsymbol{v}_i^T, \boldsymbol{q}_i^T, \boldsymbol{\omega}_i^T]$ and $\boldsymbol{X}_i^d = [\boldsymbol{r}_i^{dT}, \boldsymbol{v}_i^{dT}, \boldsymbol{q}_i^{dT}, \boldsymbol{\omega}_i^{dT}]$. Variables $k_G > 0$ and $k_S \geq 0$ are constant scalars, and $\boldsymbol{D}_G$, $\boldsymbol{D}_S$ and $\boldsymbol{K}_F$ are symmetric positive definite constant matrices. Terms k_G, $\boldsymbol{K}_G$ and $\boldsymbol{D}_G$ define a typical PD control action, whereas, matrices $\boldsymbol{K}_S$ and $\boldsymbol{D}_S$ are used to define the amount of synchronization of neighboring virtual structures.

5.4 VSC model for a spinning Double-Pyramid formation orbiting a central body

This section defines the adaptation of the decentralized VSC to a spinning DP tethered formation placed on a Keplerian circular orbit, using a control method similar to that found in Ref. [147]. In addition to the frames already presented, an additional reference frame $\mathcal{S}$ is also introduced to define the rotational motion of the spinning cluster as shown in Figure 5.2. One of the axis of this frame coincides with the axis of rotation of frame $\mathcal{F}$, but it is fixed in the orbit frame, in order to provide a reference to the spin motion of the cluster.

The decentralized model is of special interest in the case of tethered formation over the centralized approach, as the tether could provide physical support for communication between adjacent agents.

The motion of the virtual structure with respect to the inertial frame evolves according to the following dynamics

$$\begin{pmatrix} \dot{\boldsymbol{r}}_{Fi} \\ M_F \dot{\boldsymbol{v}}_{Fi} \\ \dot{\hat{\boldsymbol{q}}}_{Fi} \\ \dot{\bar{q}}_{Fi} \\ \mathbf{J}_F \dot{\boldsymbol{\omega}}_{Fi} \\ \dot{\boldsymbol{\nu}}_{Fi} \\ \dot{\boldsymbol{\lambda}}_{Fi} \\ \ddot{\boldsymbol{\lambda}}_{Fi} \end{pmatrix} = \begin{pmatrix} \boldsymbol{v}_{Fi} \\ \boldsymbol{f}_{Fi} \\ -\frac{1}{2}\boldsymbol{\omega}_{Fi} \times \hat{\boldsymbol{q}}_{Fi} + \frac{1}{2}\bar{q}_{Fi}\boldsymbol{\omega}_{Fi} \\ -\frac{1}{2}\boldsymbol{\omega}_{Fi} \cdot \hat{\boldsymbol{q}}_{Fi} \\ -\boldsymbol{\omega}_{Fi} \times \mathbf{J}_{Fi}\boldsymbol{\omega}_{Fi} + \boldsymbol{\tau}_{Fi} \\ \dot{\boldsymbol{\nu}}_{Fi} \\ \dot{\boldsymbol{\lambda}}_{Fi} \\ \boldsymbol{\sigma}_{Fi} \end{pmatrix} \tag{5.9}$$

The equations of motion of the Virtual Structure don't take into account the orbital motion, nor the presence of external (gravitational) forces and torques, since they express

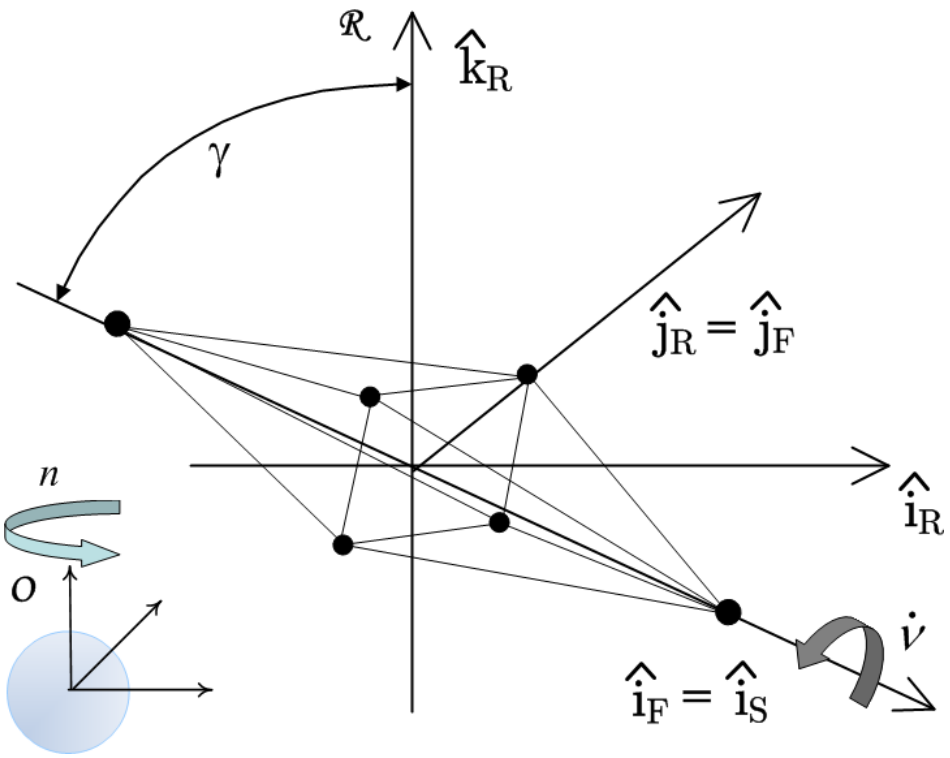

Figure 5.2: **Orbiting spinning double pyramid cluster. Reference frames**

the ideal motion of an spinning rigid body to be matched by the cluster. If the virtual structure is required to remain fixed on the circular orbit, then $\boldsymbol{r} = 0$ and $\boldsymbol{v} = 0$. The expansion dynamics defined by variable $\boldsymbol{\lambda}$ is used to model tether extension through a deployment/retrieval mechanism. Variable $\dot{\boldsymbol{\nu}}_{Fi}$ defines the spin velocity of the formation, and $\boldsymbol{\nu}_{Fi}$ the angle between frames $\mathcal{S}$ and $\mathcal{F}$.

The simple translational agent dynamics of Equation (5.5) for $\boldsymbol{r}_i$ is now substituted by HCW equations

$$\begin{pmatrix} \ddot{x}_i - 2n\dot{y}_i - 3n^2 x_i \\ \ddot{y}_i + 2n\dot{x}_i \\ \ddot{z}_i + n^2 z_i \end{pmatrix} = \frac{\boldsymbol{f}_i}{m_i} \tag{5.10}$$

which model the dynamics of agents in the $\mathcal{R}$ frame coordinates, taking into account the effect of the gravity gradient. The angular rate $n = (\mu/R^3)^{1/2}$ describes the rotation rate of reference frame $\mathcal{R}$ with respect to the inertial frame $\mathcal{O}$, where $\mu = GM_{\oplus}$ is Earth's gravitational parameter and R is the radius of the considered circular orbit.

In Equation (5.10), force $\boldsymbol{f}_i = \{f_{i,x}, f_{i,y}, f_{i,z}\}$ is the resultant of external forces acting on agent i. It is the sum of the control force and forces exerted by tethers $\boldsymbol{f}_i = \boldsymbol{u}_{i,\text{control}} + \boldsymbol{f}_{i,\text{tens}}$. The approach to calculate elastic force is presented in Eq.(2.41) in the tether elasticity model section 2.4.1. The control force is supposed to track a desired position $\boldsymbol{X}_i^d$ and velocity $\dot{\boldsymbol{X}}_i^d$ profiles.

The rotational dynamics of i–th agent,

$$\begin{pmatrix} \dot{\hat{\boldsymbol{q}}}_i \\ \dot{\bar{q}}_i \\ \boldsymbol{J}_F \dot{\boldsymbol{\omega}}_i \end{pmatrix} = \begin{pmatrix} -\frac{1}{2}\boldsymbol{\omega}_i \times \boldsymbol{q}_i + \frac{1}{2}\bar{q}_i \boldsymbol{\omega}_i \\ -\frac{1}{2}\boldsymbol{\omega}_i \cdot \boldsymbol{q}_i \\ -\boldsymbol{\omega}_{Fai} \times \boldsymbol{J}_F \boldsymbol{\omega}_i + \boldsymbol{\tau}_{g,i} + \boldsymbol{\tau}_{c,i} \end{pmatrix} \tag{5.11}$$

where $\boldsymbol{\tau}_{g,i} = -3n^2 \cdot (\hat{\mathbf{k}}_O \times \boldsymbol{J}_F \cdot \hat{\mathbf{k}}_O)$ is the gravity gradient torque (defined as in [67]) and $\boldsymbol{\tau}_{c,i}$ is the control torque. The rotation rate of frame $\mathcal{F}$ with respect to the inertial frame $\mathcal{O}$, is expressed as $\boldsymbol{\omega}_{Fai} = \boldsymbol{\omega}_F + n \cdot \hat{\mathbf{k}}_O$.

The calculation of the desired state $\boldsymbol{X}_i^d = [\boldsymbol{r}_i^d, \boldsymbol{v}_i^d, \boldsymbol{q}_i^d, \boldsymbol{\omega}_i^d]$ for each deputy, follows a similar principle to the one defined in the section describing the general virtual structure approach. As shown in Reference [20], the virtual structure approach allows to set the orientation of the whole cluster and define a quaternion feedback control law to successfully point the structure along a required direction. However, in the case of a spinning formation it is not only needed to control the orientation of the formation, but it is also needed to keep it spinning along the commanded axis. For this purpose, an additional rotation matrix $\boldsymbol{C}_{FiSi}$ that relates frames $\mathcal{F}$ and $\mathcal{S}$, is introduced in the calculation of the agent desired position and velocity. This rotation matrix will depend on the angle $\boldsymbol{\nu}_{Fi}$ and the vector $\boldsymbol{\phi}$ that defines the direction of $\boldsymbol{\nu}_{Fi}$ (the spinning motion of the rigid body), which will be typically one of the axis of the reference frame $\mathcal{F}$.

The expansion parameter $\boldsymbol{\Lambda}$ typically used to stretch the formation is included in this case to control the reeling of the tethers attached to the two anchors. This allows to change the inertia properties of the cluster.

The desired position and velocity of each agent is expressed as

$$\begin{aligned}
\boldsymbol{r}_i^d(t) &= \boldsymbol{r}_{Fi}(t) + \boldsymbol{C}_{RFi}(t) \cdot \boldsymbol{C}_{FiSi}(t) \cdot \boldsymbol{\Lambda}(t) \cdot \boldsymbol{r}_{iF}^d(t) \\
\boldsymbol{v}_i^d(t) &= \boldsymbol{v}_{Fi}(t) + (\boldsymbol{C}_{RFi}(t) \cdot \boldsymbol{C}_{FiSi}(t) \cdot \dot{\boldsymbol{\Lambda}}(t) + \\
&\quad \boldsymbol{\omega}_{Fi}(t) \times \boldsymbol{C}_{RFi}(t) \cdot \boldsymbol{C}_{FiSi}(t) \cdot \boldsymbol{\Lambda}(t) + \\
&\quad \boldsymbol{C}_{RFi}(t) \cdot (\dot{\boldsymbol{\nu}}_{Fi} \cdot \boldsymbol{\phi} \times \boldsymbol{C}_{FiSi}(t)) \cdot \boldsymbol{\Lambda}(t)) \cdot \boldsymbol{r}_{iF}^d(t) \\
\boldsymbol{q}_i^d(t) &= \boldsymbol{q}_{Fi}(t) + \boldsymbol{q}_{iF}^d(t) \\
\boldsymbol{\omega}_i^d(t) &= \boldsymbol{\omega}_{Fi}(t)
\end{aligned} \tag{5.12}$$

where the term

$$\boldsymbol{C}_{RFi} = (2\bar{q}_{Fi}^2 - 1)I + 2\hat{\boldsymbol{q}}_{Fi}\hat{\boldsymbol{q}}_{Fi}^T + 2\bar{q}_{Fi}\hat{\boldsymbol{q}}_{Fi}^{\times} \tag{5.13}$$

represents the direction cosine matrix used to transform vector components from the frame $\mathcal{F}$ which defines the axis of the pointing vector of the virtual structure, to the desired to the LVLH frame coordinates. In this equation, the position $\boldsymbol{r}_{iF}^d$ defines indeed the position of a deputy in frame $\mathcal{S}$. Therefore, a constant value of $\boldsymbol{r}_{iF}^d$ means that in fact the deputy will be spinning with frame $\mathcal{S}$ with respect to frame $\mathcal{F}$.

Reference [19] includes a convergence analysis that proves position and velocity Lyapunov asymptotic stability. The proof is based on the construction of Lyapunov function based on four terms:

$$V = V_{sp} + V_{Ft} + V_{Fr} + V_{Fe} \tag{5.14}$$

where the term $V_{sp} = V_{sp}(\tilde{\boldsymbol{r}}_i, \tilde{\boldsymbol{v}}_i, \tilde{\boldsymbol{q}}_i, \tilde{\boldsymbol{\omega}}_i)$ includes the state variables related to the position and orientation of each agent, and the rest of the terms $V_{Ft} = V_{Ft}(\tilde{\boldsymbol{r}}_{Fi}, \boldsymbol{v}_{Fi})$, $V_{Fr} = V_{Ft}(\tilde{\boldsymbol{q}}_{Fi}, \boldsymbol{\omega}_{Fi})$, and $V_{Fe} = V_{Fe}(\tilde{\boldsymbol{\lambda}}_{Fi}, \dot{\boldsymbol{\lambda}}_{Fi})$ include the state variables related to the decentralized virtual structure dynamics. The reference first proves that $\dot{V} \leq 0$ and subsequently by using LaSalle's invariance principle the stability proof is extended to prove asymptotic stability. For the tethered formation equations of motion terms describing the virtual structure coordination remain the same in this approach, and therefore the same logic can be applied to ensure that the decentralized coordination approach is asymptotically stable. On the other hand, the term V_{sp} that includes the i-th agent state variables has a different expression as the agent state is affected by tether tension and gravitational forces. The following section proposes a control approach to ensure stability of $\tilde{\boldsymbol{X}}_i = [\tilde{\boldsymbol{r}}_i^T, \tilde{\boldsymbol{v}}_i^T, \tilde{\boldsymbol{q}}_i^T, \tilde{\boldsymbol{\omega}}_i^T]$.

5.5 Fine positioning control

The Virtual Structure Control approach defines formation control at two levels. At the outer level, the overall formation control sets attitude and position of the overall formation (the virtual structure). At the inner one, the fine precision control regulates position and attitude of the formation members with respect to the virtual structure fixed reference frame. Provided that a satisfactory solution for the outer level has been provided, a novel feedback command law for the inner level is now introduced, that addresses the peculiarities of its application to the tethered formation case.

5.5.1 Thruster Control Model

In this study it is assumed to have thrusters and reaction wheels on each agent capable of full 6–axis control. References [20], [22], and [19], assume full 6–DOF axis control through thrusters and torque actuators for position and orientation control respectively. Additionally, Ref. [148] proposes an implementation of the virtual structure control approach, based on adaptive and sliding surface control techniques always assuming full control capability. References [149], [150], and [151] study tether control strategies for underactuated tethered formations.

Although the effect of gravity gradient force is cancelled for each deputy, their behavior is still affected by the force exerted by the tethers linked to them, which in turn is affected by the action of gravity gradient on tether mass, discretized by means of beads. Obviously no direct control action can be performed on the beads in order to cancel the gravitational force on them. As a consequence, gravitational force on tethers affects the motion of deputies, acting as an external disturbance.

The goal of this part of the study is to present a control approach that allows to arbitrarily orient the formation and to perform accurate deputy positioning. When the formation does not require accurate positioning, the Likins-Pringle conical natural equilibrium would keep the formation stable in a station-keeping equilibrium. In the presence of perturbations, or whenever accurate positioning requirements arise, the formation would activate the fine positioning control loop to achieve accurate formation pointing and stabilization.

The findings of Ref. [152] will be revisited here, showing that control forces on agents

need to be based on low gains and slow dynamics. Therefore, step commands shall be avoided because they induce oscillations in tethers that require long time to damp out, in the absence of dissipative terms. For this reason the control law, even if with very small control gains is permanently acting on deputies.

5.5.2 Agent dynamics

In order to track the position $\boldsymbol{r}_i^d(t)$, velocity $\boldsymbol{v}_i^d(t)$, attitude $\boldsymbol{q}_i^d(t)$ and angular rate $\boldsymbol{\omega}_i^d(t)$ desired profiles obtained through the virtual structure transformation matrices, as in Eq. (5.12).

$$\begin{aligned} \dot{\boldsymbol{v}}_i &= \sum_{j=1}^{T_i} \boldsymbol{f}_{j,i,\text{tens}} + \boldsymbol{f}_{i,\text{grav}} + \boldsymbol{u}_i \\ \boldsymbol{f}_{j,i,\text{tens}} &= c_t(\hat{\mathbf{e}}_{j,i}^T \cdot \hat{\mathbf{e}}_{j,i}) \cdot \boldsymbol{v}_{j,i} + k_t \Delta l_{j,i} \hat{\mathbf{e}}_{j,i} \\ \boldsymbol{f}_{i,\text{grav}} &= m_i[(-2n\dot{y}_i - 3n^2 x_i) \cdot \hat{\mathbf{i}}_{\mathcal{R}} + 2n\dot{x}_i \cdot \hat{\mathbf{j}}_{\mathcal{R}} + n^2 z_i \cdot \hat{\mathbf{k}}_{\mathcal{R}}] \end{aligned} \tag{5.15}$$

The equations of motion for agent i presented in Equation (5.12) assume massless tethers. For massive tethers the elastic and damping terms should be replaced by the forces exerted by adjacent beads. The external forces acting on the tether are gravity, and both elastic and damping forces exerted by tethers. The goal of the low-level controller is to track the state vector $\boldsymbol{X}_i^d = [\boldsymbol{r}_i^d, \boldsymbol{v}_i^d, \boldsymbol{q}_i^d, \boldsymbol{\omega}_i^d]$.

The equations defining the position of an agent are thuse of a second order mechanical system under the requirement or assumption that tethers remain always taut. Rearranging terms in Equation (5.15), it is possible to describe the dynamics of the whole cluster in compact form as

$$\boldsymbol{M} \cdot \dot{\boldsymbol{v}} + (\boldsymbol{N} + \boldsymbol{P}(\boldsymbol{r})) \cdot \boldsymbol{v} + \boldsymbol{Q}(\boldsymbol{r}) = \boldsymbol{u} \tag{5.16}$$

The equations of motion for an agent i cannot be written independently, as there is a coupling betweein pairs of agents i and j in the elastic and damping forces terms as it can be appreciated in Eq. (5.15). This coupling is related to relative position $\boldsymbol{r}_{i,j}$ and velocity $\boldsymbol{v}_{i,j}$.

Equations (5.16) defines the motion of the whole cluster. Vectors $\boldsymbol{r} \in \Re^{3n_d}$ and $\boldsymbol{v} \in \Re^{3n_d}$ contain the position and velocity, respectively, in Cartesian coordinates of the n members of the cluster. The inertia matrix $\boldsymbol{M} \in \Re^{3n_d \times 3n_d}$ is a diagonal matrix containing the masses of the agents. Matrix $\boldsymbol{N} \in \Re^{3n_d \times 3n_d}$ is a skew-symmetric matrix that contains

the Coriolis/centrifugal acceleration terms $[(-2n\dot{y}_i)\cdot\hat{\mathbf{i}}_{\mathcal{R}}+2n\dot{x}_i\cdot\hat{\mathbf{j}}_{\mathcal{R}}]$ of each agent according to the Hill model. Vector $\boldsymbol{Q}(\boldsymbol{r})=\boldsymbol{G}\cdot\boldsymbol{r}+\boldsymbol{T}(\boldsymbol{r})$ incorporates all the the conservative forces acting on each agent: gravity gradient and elastic forces respectively. Matrix $\boldsymbol{G}\in\Re^{3n_d\times 3n_d}$ contains the terms $[(-3n^2x_i)\cdot\hat{\mathbf{i}}_{\mathcal{R}}+n^2z_i\cdot\hat{\mathbf{k}}_{\mathcal{R}}]$ of the Hill model for each agent. Matrix $\boldsymbol{P}(\boldsymbol{r})\in\Re^{3n_d\times 3n_d}$ and vector $\boldsymbol{T}(\boldsymbol{r})\in\Re^{3n_d}$ define the damping and coupled elastic forces respectively, between each tether–linked pair of agents i and j. Dissipative damping forces are included in the term $\boldsymbol{P}(\boldsymbol{r})$, which can be expressed as the sum of damping terms for each tether T:

$$\boldsymbol{P}(\boldsymbol{r})=\sum_{T}\boldsymbol{P}_T(\boldsymbol{r}) \tag{5.17}$$

Elements I,J represent the index of the 3-by-3 submatrix within matrix $\boldsymbol{P}(\boldsymbol{r})$. These submatrices describe the $\{\hat{\boldsymbol{i}}_{\mathcal{R}},\hat{\boldsymbol{j}}_{\mathcal{R}},\hat{\boldsymbol{k}}_{\mathcal{R}}\}$ Cartesian coordinates for the i and j deputies.

$$\begin{aligned}\boldsymbol{P}_T(\boldsymbol{r})|_{I,I} &= \boldsymbol{P}_T(\boldsymbol{r})|_{J,J}=c_t(\hat{\mathbf{e}}_{i,j}^T\hat{\mathbf{e}}_{i,j})\\ \boldsymbol{P}_T(\boldsymbol{r})|_{I,J} &= \boldsymbol{P}_T(\boldsymbol{r})|_{J,I}=-c_t(\hat{\mathbf{e}}_{i,j}^T\hat{\mathbf{e}}_{i,j})\end{aligned} \tag{5.18}$$

The matrices introduced above have the following properties:

$$\begin{aligned}\|\boldsymbol{M}\| &\leq \lambda_M(\boldsymbol{M})=m_+>0\\ \|\boldsymbol{N}\| &\leq \lambda_M(\boldsymbol{N})=2n &(5.19)\\ \|\boldsymbol{G}\| &\leq \lambda_M(\boldsymbol{G})=3n^2 &(5.20)\\ \|\boldsymbol{P}(\boldsymbol{r})\| &\leq \beta_P &(5.21)\\ \|\boldsymbol{T}(\boldsymbol{r})\| &\leq \beta_T &(5.22)\end{aligned}$$

where $\lambda_M(\boldsymbol{A})$ stands for the maximum eigenvalue of matrix $\boldsymbol{A}\in\Re^{n\times n}$. Values β_P and β_T are bounded and positive scalars. Matrix $\boldsymbol{P}(\boldsymbol{r})$ is symmetric, and its norm is bounded as it is composed of combinations of versors $\hat{\mathbf{e}}_{i,j}$. The rank of each matrix $\boldsymbol{P}_T(\boldsymbol{r})$ is 1 by construction, according to Equation (5.18). The only non-zero eigenvalue must be positive because trace$(\boldsymbol{P}_T(\boldsymbol{r}))>0$. Since all eigenvalues are non-negative, $\boldsymbol{P}_T(\boldsymbol{r})$ is positive semi–definite, and therefore $\boldsymbol{P}(\boldsymbol{r})$ is positive semi-definite too. Vector $\boldsymbol{T}(\boldsymbol{r})$ is bounded since the elastic constant, elongation and versor $\hat{\mathbf{e}}_{i,j}$ are bounded. Matrix $\boldsymbol{N}$ is positive semi-definite by construction.

5.5.3 Control Approaches

Two different classes of approaches will be considered fro the inner level control of the virtual structure, namely model-based control or model independent control strategies.

Typically the first strategy provides better results at the expense of requiring accurate model information. This would be the case of feedback linearization controllers for instance. Robust control strategies relieve the need of model knowledge, by allowing some uncertainty in model structure and parameters [153]. Model independent control laws, require less information on the model, but they often lead to worse performance as they do not take advantadge of model-specific features.

Reference [154] provides a good insight about control strategies applicable to second order mechanical systems with a structure similar to that of Eq. (5.16). Among the model dependent strategies there are the ones that depend on an accurate definition of the model, and the ones that only require knowledge of the model structure because model parameters are estimated. Reference [155] shows an overview of stability of second order systems, and Refs. [156], [157] introduce the terminology for different types of stability definitions.

Under the premise that tethers remain taut, the equations of motion of an agent i consist essentially of a set of second order spring-mass-damper that relate its position and velocity to other deputies. Although the structure of the model is rather simple, the incorporation of massive tethers and the inability to estimate the state of the beads makes a model-based controller not a viable option. As a first attempt, the control action can be computed on the basis of a model assuming massless tethers as an approximation and then apply this controller to the complete model, including tether mass (e.g. the lumped mass tethered formation model). In order to provide a robust controller, parameters k_t and c_t of the modelled massless tether could be estimated by using an adaptive controller inspired by that presented in Ref. [158], which presents a controller based on a PD control action plus an adaptive feedforward term. This approach works indeed very well for open Hub-And-Spoke formations in which each agent is connected uniquely to one tether that is assumed to be taut, but for closed formations such those analyzed in this thesis, the bouncing (curvature) of the tethers makes impossible to estimate the length of the tether as $\hat{l}_{j,i} = |\boldsymbol{r}_j - \boldsymbol{r}_i|$. The length of the tether is a crucial parameter that defines the behavior of the system. An error in the tether measurement length leads not only to a quantitative deviation of the tension, but it may be unable to properly represent the difference between a taut tether and a "slack" tether not exerting any force at all. For this reason, a model-based controller is discarded. Although it could be possible to estimate the gravity-gradient force, it is not possible to obtain a reliable estimate of the tether elastic forces model structure.

For a system like that of Eq. (5.16) a Proportional-Derivative (PD) feedback controller is not capable of providing perfect set-point regulation [154]. It is only *strictly stable* from a Lyapunov point of view), and the steady-state error for ramp tracking is not bounded. In the absence of dissipative forces, a well-known solution to achieve asymptotic stability of set-point regulation is to use a PD controller plus a feedforward term for gravity gradient cancellation [159], [160], [161]. Although this approach is good, and could be extended to incorporate the elastic force as an additional conservative force in $\boldsymbol{Q}(\boldsymbol{r})$, it doesn't incorporate the dissipative damping forces $\boldsymbol{P}(\boldsymbol{r})$ in the model. In addition to this the performance of the controller depends on the accuracy of the model of $\boldsymbol{Q}(\boldsymbol{r})$ for gravity gradient and elastic forces (which is not trivial to estimate, as explained before).

A valid candidate to eliminate steady-state error could be a PID controller. This controller applied to a second order spring-mass-damper linear system leads to a system type 1 in the open-loop transfer function, which results in a closed loop system with zero steady-state error response to a step input (setpoint) and a constant steady-state error to a ramp input. The stability analysis of PID control applied to the system defined in Equation (5.16) has received considerable attention in the literature. The use of a linear PID controller only allows to prove *semi-global asymptotic* stability for set-point regulation [162].

The use of nonlinear PID controllers consisting of a linear PD control plus a nonlinear Integral term, provides better results. Reference [161] defines a $\mathrm{PI}_d\mathrm{D}$ controller in which the integral action is delayed after initial time. This strategy provides *semi-global asymptotic* stability for set-point regulation.

According to Ref. [163], for a given inertia matrix $\boldsymbol{M}$, if the constants of a linear PID controller are chosen adequately and the desired tracking trajectory is sufficiently slow, the system is *locally asymptotically stable* for a tracking application.

5.5.4 Sliding mode control

Reference [23] proposes a PID controller in which the integral action is not linear and is calculated using the sliding mode technique. This controller provides *semi-global exponential* tracking stability for a system such as that in Eq. (5.16) avoiding the need of any knowledge about the plant model. This approach relies on a dynamical change of variables. For a given desired trajectory $\boldsymbol{r}^d$, using the change of variables $\boldsymbol{S}_r = \boldsymbol{v} - \boldsymbol{v}^r$,

and using the control law defined by $\boldsymbol{u} = -\boldsymbol{K}_d \cdot \boldsymbol{S}_r$, Eq. (5.16) can be rewritten as:

$$\boldsymbol{M}\ \dot{\boldsymbol{S}}_r + (\boldsymbol{N} + \boldsymbol{K}_d + \boldsymbol{P}(\boldsymbol{r}))\ \boldsymbol{S}_r = -\boldsymbol{Y}_r\boldsymbol{\Theta} \tag{5.23}$$

where $\boldsymbol{Y}_r = \boldsymbol{Y}_r(\boldsymbol{r}, \boldsymbol{v}^r, \dot{\boldsymbol{v}}^r)$ is the *regressor* term, and $\boldsymbol{\Theta}$ is a parametrization vector of known constant parameters.

$$\boldsymbol{Y}_r\Theta = \boldsymbol{M}\ \dot{\boldsymbol{v}}^r + (\boldsymbol{N} + \boldsymbol{P}(\boldsymbol{r}))\ \boldsymbol{v}^r + \boldsymbol{Q}(\boldsymbol{r}) \tag{5.24}$$

A nominal reference trajectory dependent on $\tilde{\boldsymbol{r}}$ and $\tilde{\boldsymbol{v}}$, is defined for convenience as:

$$\begin{aligned} \boldsymbol{v}^r &= \boldsymbol{v}^d - k_\alpha\tilde{\boldsymbol{r}} + \boldsymbol{S}_d - k_\gamma\boldsymbol{\sigma}_\gamma \\ \boldsymbol{\sigma}_\gamma &= \mathrm{sgn}(\boldsymbol{S}_q) \end{aligned} \tag{5.25}$$

where function $\mathrm{sgn}(\cdot)$ is the signum function. Variable $\boldsymbol{S}_q$ is defined as

$$\begin{aligned} \boldsymbol{S}_q &= \boldsymbol{S} - \boldsymbol{S}_d \\ \boldsymbol{S} &= \tilde{\boldsymbol{v}} + k_\alpha\tilde{\boldsymbol{r}} \\ \boldsymbol{S}_d &= \boldsymbol{S}(t_0)\exp(-\kappa(t - t_0)) \end{aligned} \tag{5.26}$$

The proof of stability [23] will be performed in two steps. First it will be proven the boundness of tracking errors by showing that $\boldsymbol{S}_r$ (which depends on $\tilde{\boldsymbol{r}}$ and $\tilde{\boldsymbol{v}}$) is upper bounded by a given constant ϵ. In a second step it will be shown that a sliding mode is induced on $\boldsymbol{S}_q$ and tracking is achieved: $\tilde{\boldsymbol{r}} \to 0$ and $\tilde{\boldsymbol{v}} \to 0$.

For the first part of the proof, taking the kinetic energy of the system as a Lyapunov function

$$V = \frac{1}{2}\boldsymbol{S}_r^T \cdot \boldsymbol{M} \cdot \boldsymbol{S}_r \tag{5.27}$$

and using Eq. (5.24), the derivative of the Lyapunov function is equal to:

$$\begin{aligned} \dot{V} &= -\boldsymbol{S}_r^T \cdot (\boldsymbol{N} + \boldsymbol{K}_d + \boldsymbol{P}(\boldsymbol{r})) \cdot \boldsymbol{S}_r - \boldsymbol{S}_r^T \cdot \boldsymbol{Y}_r\boldsymbol{\Theta} \\ &\leq -\|\boldsymbol{K}_1\boldsymbol{S}_r\|^2 + \|\boldsymbol{S}_r\|\eta(t) \end{aligned} \tag{5.28}$$

where $\boldsymbol{K}_1^T\boldsymbol{K}_1 = \boldsymbol{N} + \boldsymbol{K}_d + \boldsymbol{P}(\boldsymbol{r})$. The matrix $\boldsymbol{N} + \boldsymbol{K}_d + \boldsymbol{P}(\boldsymbol{r})$ is positive definite, since the first term is positive semi-definite by definition, the second one is positive definite by construction, and the second one is semi-positive definite as discussed before. From this equation it can be concluded that it exist a large enough gain $\boldsymbol{K}_d$ such that $\boldsymbol{K}_1 > \|\eta(t)\|$,

and thus $\boldsymbol{S}_r$ converges to a bounded set ϵ as $t \to \infty$.

The proof of exponential convergence for tracking errors is analogous to that shown in Ref. [23]. It takes into consideration the following equation:

$$\dot{\boldsymbol{S}}_q = -k_\gamma \mathrm{sgn}(S_q) + \dot{\boldsymbol{S}}_r \tag{5.29}$$

with the Lyapunov function

$$V = (1/2)\boldsymbol{S}_q^T \boldsymbol{S}_q \tag{5.30}$$

Taking the derivative of the former equation, and using Eq. (5.29) the derivative of the Lyapunov function is equal to

$$\dot{V} \leq -k_\gamma \|\boldsymbol{S}_q\| + \varsigma_{\sup} \|\boldsymbol{S}_q\| \tag{5.31}$$

where $\varsigma_{\sup}$ is the supremum of $\dot{\boldsymbol{S}}_r$. The latter value can be estimated by using the bounds calculated in Eq. (5.19), as shown in Ref. [23]. It is sufficient to choose $k_\gamma > \varsigma_{\sup}$ to ensure exponential stability. The details of the proof are presented in Ref. [23]. The controller that provides semi-global exponential stability is

$$\boldsymbol{u} = -\boldsymbol{K}_p \tilde{\boldsymbol{r}} - \boldsymbol{K}_v \tilde{\boldsymbol{v}} + \boldsymbol{K}_d \cdot \boldsymbol{S}_d - \boldsymbol{K}_i \int_{t_0}^{t} \mathrm{sgn}(\boldsymbol{S}_q(\varsigma))\, \mathrm{d}\varsigma \tag{5.32}$$

Where $\boldsymbol{K}_p = \boldsymbol{K}_d \cdot k_\alpha$, $\boldsymbol{K}_v = \boldsymbol{K}_d$ and $\boldsymbol{K}_i = \boldsymbol{K}_d \cdot k_\gamma$. Reference [23] proposes a tuning procedure for scenarios with slow tracking reference trajectories. The controller parameters are essentially $\boldsymbol{K}_d, k_\alpha$, k_γ and κ. The first two parameters are chosen in accordance with the proportional and derivative constants of a typical PD controller. According to the same reference, parameter k_γ must be bounded as,

$$k_\gamma \geq \lambda_M(\boldsymbol{M}^{-1}) \left[(\lambda_M(\boldsymbol{K}_d + \boldsymbol{P}(\boldsymbol{r}) + \lambda_M(\boldsymbol{N} + \boldsymbol{P}(\boldsymbol{r})) \cdot ||\boldsymbol{v} - \boldsymbol{v}^r|| + ||\boldsymbol{Y}_r \Theta|| \right] \tag{5.33}$$

Typically, sliding-mode based controllers are prone to induce the "chattering" effect related to a switching in the control command. Although the derivation of this controller is based on sliding-mode, the switching term is within the integral term in Equation (5.32). Therefore, the control command $\boldsymbol{u}_i$ is a continuous function. This is of special importance in this application, since abrupt changes in the control action could induce undesired tether oscillations.

Nonlinear PID Control

Reference [164] studies the use of PID control for tracking applications of mechanical systems. One of the solutions proposed takes into account the concept of *input-to-state stability (ISS)* [157] which means that the behavior of the system remains bounded under external bounded perturbations, and that the system tends to the equilibrium point when the disturbance vanishes. System (5.16) can be written as:

$$\boldsymbol{M}\ \dot{\boldsymbol{S}} + \boldsymbol{N}\ \boldsymbol{S} = \boldsymbol{w}\left(t, \tilde{\boldsymbol{r}}, \tilde{\boldsymbol{v}}, \int \tilde{\boldsymbol{r}}\right) + \boldsymbol{u} \tag{5.34}$$

Where $\boldsymbol{S}$ is defined as $\boldsymbol{S} = \tilde{\boldsymbol{v}} + \boldsymbol{K}_P\tilde{\boldsymbol{r}} + \boldsymbol{K}_I \int \tilde{\boldsymbol{r}}$. The approach presented above defines the extended disturbance term $\boldsymbol{w}$ that includes the desired tracking trajectory, the gravity gradient effect and a generic external disturbance $\boldsymbol{d}(t)$. In this case, the external disturbance $\boldsymbol{d}(t)$ is replaced by the elastic and damping forces exerted by tethers:

$$\boldsymbol{w}\left(t, \tilde{\boldsymbol{r}}, \tilde{\boldsymbol{v}}, \int \tilde{\boldsymbol{r}}\right) = \boldsymbol{M}\ (\dot{\boldsymbol{v}}^d + \boldsymbol{K}_P\ \tilde{\boldsymbol{v}} + \boldsymbol{K}_I\ \tilde{\boldsymbol{r}}) + \boldsymbol{N}\ \left(\boldsymbol{v}^d + \boldsymbol{K}_P\ \tilde{\boldsymbol{r}} + \boldsymbol{K}_I\ \int \tilde{\boldsymbol{r}}\right) + \boldsymbol{P}(\boldsymbol{r}) + \boldsymbol{Q}(\boldsymbol{r}) \tag{5.35}$$

The controller will make the system ISS if there exist a class $\mathcal{KL}$ function $\boldsymbol{\Psi}_1$ and a class $\mathcal{K}$ function $\boldsymbol{\Psi}_2$ such that the state $\boldsymbol{x} = [\int \tilde{\boldsymbol{r}}^T, \tilde{\boldsymbol{r}}^T, \tilde{\boldsymbol{v}}^T]^T$ satisfies:

$$\|\boldsymbol{x}(t)\| \leq \boldsymbol{\Psi}_1(\|\boldsymbol{x}(0)\|, t) + \boldsymbol{\Psi}_2\left(\|\boldsymbol{w}(t)\|_\infty\right) \tag{5.36}$$

If $\boldsymbol{x}$ is stabilized, then the system in Ref. 5.34 is also stable. Using $\boldsymbol{x}$ as state variable, Eq. 5.34 can be written as

$$\dot{\boldsymbol{x}} = [\boldsymbol{A}(\boldsymbol{x}, t)]\ \boldsymbol{x} + [\boldsymbol{B}(\boldsymbol{x}, t)]\ \boldsymbol{w} + [\boldsymbol{B}(\boldsymbol{x}, t)]\ \boldsymbol{u} \tag{5.37}$$

with

$$\boldsymbol{A} = \begin{bmatrix} 0 & \boldsymbol{I} & 0 \\ 0 & 0 & \boldsymbol{I} \\ -\boldsymbol{M}^{-1}\boldsymbol{C}\boldsymbol{K}_I & -\boldsymbol{M}^{-1}\boldsymbol{C}\boldsymbol{K}_P - \boldsymbol{K}_I & -\boldsymbol{M}^{-1}\boldsymbol{C} - \boldsymbol{K}_P \end{bmatrix} \quad ; \quad \boldsymbol{B} = \begin{bmatrix} 0 \\ 0 \\ \boldsymbol{M}^{-1} \end{bmatrix}$$

Reference [164] proves that the controller:

$$\boldsymbol{u}_i = \left(\boldsymbol{K} - \frac{1}{\gamma_P^2}\boldsymbol{I}_3\right)\left(-\boldsymbol{K}_{Pi}\tilde{\boldsymbol{r}}_i - \tilde{\boldsymbol{v}}_i - \boldsymbol{K}_{Ii}\int_{t0}^{t} \tilde{\boldsymbol{r}}_i\, \mathrm{d}t\right) \tag{5.38}$$

makes system (5.34) extended disturbance ISS under the condition that $\boldsymbol{K}, \boldsymbol{K}_P, \boldsymbol{K}_I > 0$

are constant diagonal matrices, and $\boldsymbol{K}_P^2 > 2\boldsymbol{K}_I$. Furthermore, the controller is optimal according to an $\mathcal{H}_\infty$ performance index. Still, *global asymptotic* stability (GAS) cannot be ensured for the trajectory tracking problem. The varying reference trajectory and the presence of the gravity term, lead to a positive term in the derivative of the Lyapunov function that doesn't vanish in the origin $\boldsymbol{x} = 0$. However, it is shown an stable equilibrium point exist in the neighborhood of the origin $\boldsymbol{x}_p$. The bound on performance limitation $\|\boldsymbol{x}_p\|$ depends on the bound of the extended disturbance $\|\boldsymbol{w}\|$. However, as stated in Ref. [164], estimation of $\boldsymbol{K}$ shall be done empirically, by trial and error, until the closed-loop performance are satisfactory. Therefore, parameter $\boldsymbol{K}_T = \left(\boldsymbol{K} - \frac{1}{\gamma_P^2}\boldsymbol{I}_3\right)$ cannot be tuned through analysis.

5.6 Reeling and tether tension control

When deploying or retrieving a tether, the tether unstretched length parameter must be updated as a consequence of the process of releasing or retrieving the cable. At the same time, a new desired position must be defined for the deputies placed at the ends of that tether, in order to keep the tether taut during the reeling process and at the final configuration state.

Position control of deputies will be performed in the frame of the Virtual Structure approach. Since the goal is to stretch the formation shape (in order to alter its moments of inertia), position control will be used taking into account the extension parameter $\boldsymbol{\Lambda}(t)$ presented in Eq. (5.12). Using this parameter, the new desired position of the agent will be calculated based on the change of shape of the Virtual Structure.

For the specific Double-Pyramid cluster geometry, only anchors will be used to alter the moment of inertia of the cluster. Therefore, only the tethers connecting anchors with deputies will be reeled. Since the structure is symmetric, the unstretched length of all the tethers connected to the each anchor shall be the same at all times.

At the same time the unstretched tether length $l_{j,i}^{(0)}$ and the tether length rate must be updated when releasing or retrieving tethers. Based on the updated unstretched tether length and rate, variables k_s c_s $l_{b,a}^{(0)}$ in Eq. (2.51) will also be updated. Finally, mass of tether beads will be updated based on the new tether length.

Two different techniques were considered for reeling control that suit the analysis of the system with a lumped-mass tether model. The first approach assumes a constant segment length. This implies that during deployment/reeling the number of beads will vary. The sudden addition or suppression of a bead into the tether creates a discontinuity in the dynamics of the tether [86], [15], [84]. In the instant when a new massive bead (having a certain velocity) is incorporated in the tether, requires taking into account the momentum conservation laws in order to on the deputy.

As an alternative, the proposed model assumes a constant number of beads and only the length of the segments is changed during deployment/retrieval. In order to minimize abrupt changes in setpoint, the deployment of tethers is performed by tracking a ramp setpoint. As already introduced before, after a change in segment length $l_{i,j}^{(0)}$, variables k_s, c_s shall be updated accordingly.

5.7 Vibration control

There are different alternatives for controlling the amplitude and frequency of orbiting tether vibrations. In general, one can distinguish between longitudinal vibrations (along the the direction of a taut tether) and transversal vibrations.

5.7.1 Longitudinal oscillations

Reference [74] proposes a method to control longitudinal oscillations of a tether. This paper uses a lumped mass model, and derives an active damping optimal control law, using energy as cost function. The control is achieved through force control by an actuator at the end of the tether, and the measured variables are tether elongation and tether length rate.

5.7.2 Transversal oscillations

References [165] and [166] propose a method for vibration control of transversal oscillations. The first reference proposes a mission consisting of a satellite anchored to a mother satellite (ISS) and tether length is assumed constant. In the second case, the approach is defined for a triangular spinning tethered formation. In both cases, it is assumed that it is possible to actuate over a moveable tether boom that allows modifying the separation of the tether from the anchoring point. Reference [167] proposes an impedance matching

procedure for transverse oscillation control.

The proposed control law relates the slope of the tether boom with the velocity of separation:

$$\frac{\partial v(0,T)}{\partial t} = K\frac{\partial v(0,T)}{\partial s} \tag{5.39}$$

The relationship between the outcoming and incoming waves is determined by:

$$B/A = [K-c]/[K+c] \tag{5.40}$$

Where $c = \sqrt{T/\rho}$ is the speed of the traveling wave, assuming a constant tension along the tether. The optimum control gain to minimize the amplitude of the outcoming waves can be set to $K = c$. From a practical point of view, the controller can be implemented by integrating Eq. (5.39), and deriving the value $v(0,t)$ which should be the displacement of the boom at the attachment point. The displacement of the system will be limited by the maximum boom extension, so a limitation on the control gains is required, in order to avoid saturation issues.

Reference [168] proposes also a similar method based on an active damping mechanism, relying also on moving the tether ends attachment points. In this case, the derivation of the control law is done in the frequency domain.

5.8 Control Results

Reference [76] shows that satisfaction of the rigid solid Likins-Pringle conical equilibrium condition, does not guarantee stability of tethered formations with equivalent moment of inertia. As a general rule, stability of a passive spinning double-pyramid cluster is increased for high m_a/m_s ratios, low spin relative rates $\dot{\boldsymbol{\nu}}/n$, high γ angles (low pitch), and high L/D ratios.

The goal of the presented mission consist in reorienting a cluster between two conical equilibrium states. To achieve this, the spinning rate and moment of inertia of the formation will be modified using agents actuators, in order to adapt to the end equilibrium conditions as defined by Eq. (2.64). The moment of inertia will be changed by varying the unstretched tether length of tethers connecting anchors with deputies.

The purpose of this scenario is to define a formation in a stable station-keeping equilibrium without requiring any fuel consumption. Only in the presence of perturbations, or whenever accurate positioning requirements arise the formation would activate the VSC and accurate positioning control loops for stabilization purposes. Performing positioning control around a natural equilibrium state such as the conical equilibrium, minimizes thrusting control and therefore fuel consumption.

Table 5.1 shows the initial and final formation geometry for the proposed mission scenario, that were calculated taking into account the formation geometry, and the equilibrium condition defined by Eq. (2.64).

Table 5.1: Initial and final equlibrium states

Initial State Equilibrium Condition			
Parameter	**Symbol**	**Value**	**Units**
Unstretched diagonal tether length (D)	$l_{i,k}^{(0)}$	$1000\sqrt{2}$	m
Unstretched anchor tether length	$l_{i,k}^{(0)}$	10050	m
Cluster length (L)	L	20000	m
Transversal and axial MOI ratio	I_t/I_a	75.5	
Spin rate / Orbital rate	$\dot{\boldsymbol{\nu}}/n$	-2	
Likins–Pringle equilibrium angle	γ	89.72	deg
Final State Equilibrium condition			
Parameter	**Symbol**	**Value**	**Units**
Unstretched diagonal tether length (D)	$l_{i,k}^{(0)}$	$1000\sqrt{2}$	m
Unstretched anchor tether length	$l_{i,k}^{(0)}$	7071	m
Cluster length (L)	L	14000	m
Transversal and axial MOI ratio	I_t/I_a	37.5	
Spin rate / Orbital rate	$\dot{\boldsymbol{\nu}}/n$	-4	
Likins–Pringle equilibrium angle	γ	88.42	deg

Table 5.2 summarizes the characteristics of the orbit and the agents. They correspond to a Low Earth Orbit (LEO) satellite following a circular keplerian orbit.

Table 5.3 presents the characteristics of the tether material as defined in Refs. [13], [74]. The material used for the tethers is assumed to be Kevlar 29®. Since it is crucial to keep the tethers taut to ensure the rigidity of the formation, the position of the agents within the

Table 5.2: Orbit and agents characteristics

Parameter	**Symbol**	**Value**	**Units**
Perigee altitude	R_p	6578	km
Orbital period	T	5310	s
Mass of anchor body		1500	kg
Mass of deputies body		1000	kg

virtual structure is commanded slightly beyond the unstretched position (approximately 0.01%) in order to ensure tension in tethers.

Table 5.3: Tether characteristics

Parameter	**Symbol**	**Value**	**Units**
Density	ρ	4.51	kg/km
Young Modulus	E	70.5	GPa
Diameter		2	mm
$E \cdot A$		221482	Nm^2
Damping constant	C	2500	N·s
Break elongation		3.6	%

Table 5.4 presents the controller parameters for both the high level VSC and the precision control laws. The constants of the virtual structure model are chosen in order to avoid overshoot in the time response and a dynamic slow enough that guarantees the absence of undesired tether oscillations. On the other hand, the constants of the control of the agents have been selected to provide a quick response in order to track accurately the state of the virtual structure.

For the classical PID controller, the requirements of $\boldsymbol{K}, \boldsymbol{K}_P, \boldsymbol{K}_I > 0$ being constant diagonal matrices, and $\boldsymbol{K}_P^2 > 2\boldsymbol{K}_I$ were fulfilled. For the sliding mode control, parameters $\boldsymbol{K}_d$ and α_S were defined as in the PID controller case. Parameter γ_S was defined in such a way that the effect of the integral part in the control command in Equation (5.32) avoids excessive oscillations around the equilibrium setpoint. Increasing the value of γ_S increases the integral action at the expense of higher amplitude oscillations around the setpoint belonging to the sliding manifold. In order to smooth the transition to the desired manifold, the transition term is chosen as follows: $\boldsymbol{S}_d = \boldsymbol{S}(t)\exp(-\kappa \cdot (t - t_0))$, instead of using a term based only on the measurement of $\boldsymbol{S}$ at t_0. This choice is compatible with the

requirements of the aforementioned reference paper. In both cases, controller constants were chosen with the goal of achieving submillimetric positioning accuracy.

Table 5.4: Control parameters

Virtual Structure parameters		
PD Control	**Neighbor sync.**	**Form. feedback**
$k_G = 5 \cdot 10^{-3} \cdot I_3$	$k_S = I_3$	$K_F = 0.2 \cdot I_3$
$K_G = 5 \cdot 10^{-3} \cdot I_3$	$K_S = I_3$	
$D_G = 0.4 \cdot I_3$	$D_S = I_3$	
Deputy control parameters		
PID Control	**Sliding PID**	
$\boldsymbol{K}_P = 20 \cdot I_3$	$\boldsymbol{K}_d = 3 \cdot I_3$	$\kappa = 0.1$
$\boldsymbol{K}_I = \frac{5}{3} \cdot I_3$	$\alpha_S = 20$	
$\boldsymbol{K}_T = 3 \cdot I_3$	$\gamma_S = 0.02$	

Control forces on agents shall be based on low gains and slow dynamics [84]. Step commands shall be avoided because they induce oscillations in the tethers that take a long time to dissipate. For this reason the control law, even if with very small control gains is permanently acting on deputies during the reorientation manouver. The desired spin rate $\dot{\boldsymbol{\nu}}$ and the unstretched tether length for deployed tethers $l^{(0)}$ are commanded through ramp setpoints.

The mission is scheduled in three steps. Initially formation is spinning at the initial equilibrium point with both the VSC and low-level controller activated. At $t = 2000$s, the reorientation manouver starts, until $t = 3000$s. From this time onwards, the formation spins until the end of the orbital period at $t = 5310$s.

Figure 5.3 shows the behavior of the deputies and beads during the manouver. It can be seen how the shape of the formation is shrinked along $\hat{i}_R$ axis, in order to reduce the transversal moment of inertia I_t required in the end state conditions of the mission.

Figure 5.4 displays the magnitude of the error of an agent in the plane of the formation $\tilde{\boldsymbol{r}}_1$. The upper plot shows the error when using the PID controller, and the lower plot the error when applying the sliding mode control. In both cases the formation achieves submillimetric precision. However, in the second case, the error is more bounded than in

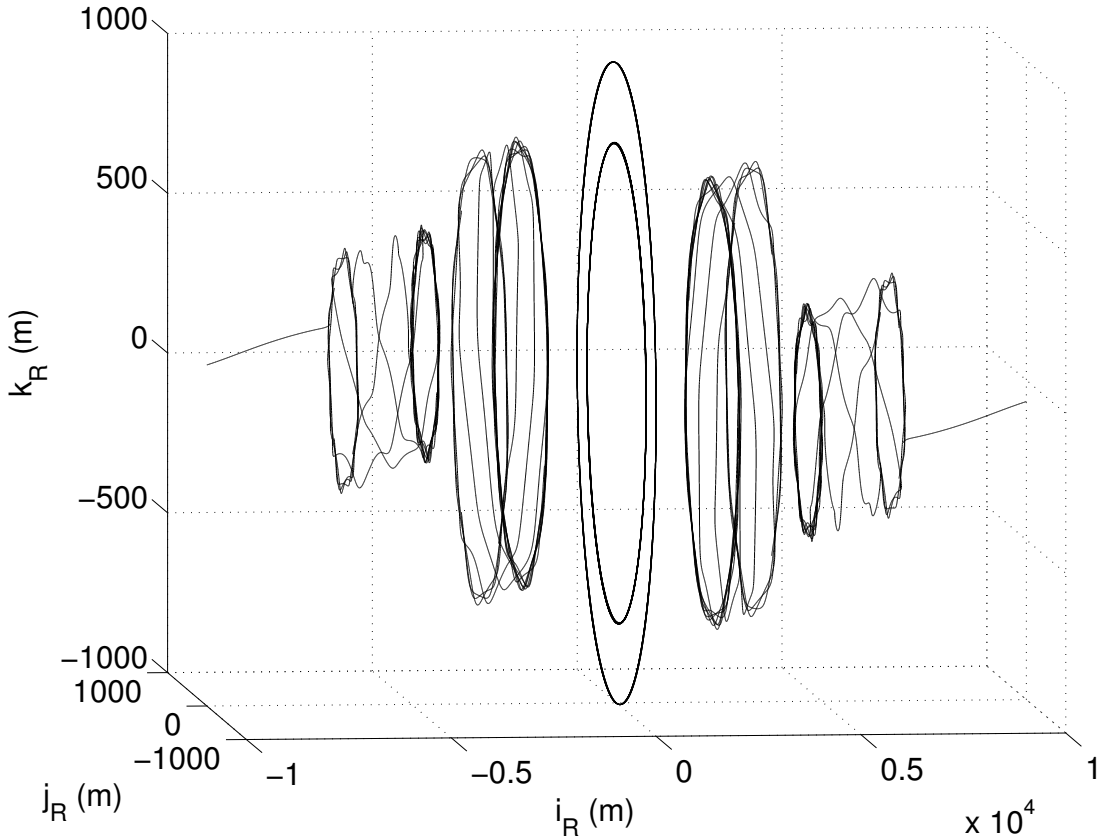

Figure 5.3: **Evolution of the formation elements during manouver**

the first case. This figure shows the norm of the error, however the final extension of the tether slightly oscillates around the setpoint in both cases. This means that in both cases the controller allows to achieve better performance than just Lyapunov stability.

Figure 5.4 displays the control accelerations $\boldsymbol{a}_1 = \boldsymbol{f}_1/m_1$ of an agent belonging to the formation plane during the mission. The upper plot shows the acceleration when using the PID controller, and the lower plot the error when applying the sliding mode control. Although the second case shows a value that tends to be more constant than in the first case, the second cases suggests a much higher fuel consumption since the integral of the force over time will be much higher.

When comparing the results achieved by both controllers, it can be concluded that the PID controller provides better accuracy and less high frequency oscillations with less force (and thus less control effort) than the sliding mode controller. However, the sliding mode controller allows to achieve less variability around the setpoint, keeping the envelope of

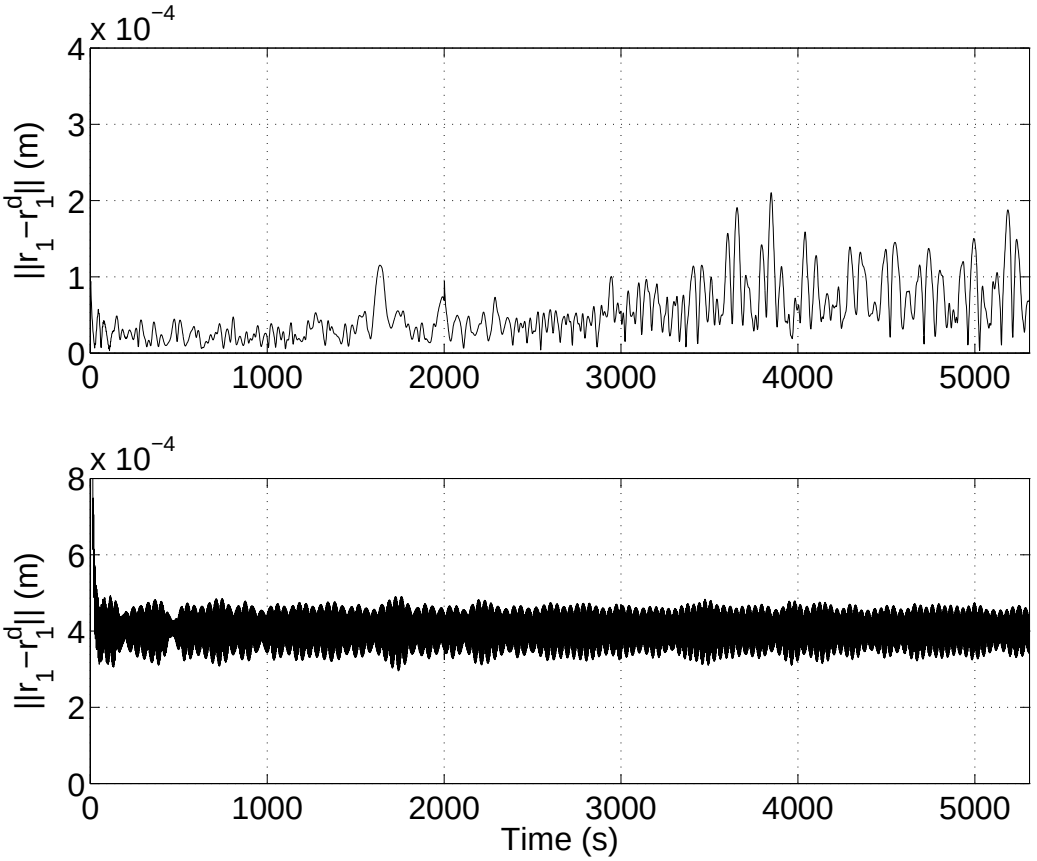

Figure 5.4: **Positioning error of deputy 1. Upper: PID control. Lower: Sliding mode control**

the oscillations much more contained than when using the PID control.

5.9 VSC major findings

This chapter presents an extension of the application of the virtual structure control technique to double–pyramid tethered formations with an evaluation of the effect of internal forces exerted by tethers when the attitude and spin velocity of the formation is modified through virtual structure control.

It t the VSC approach by adding the spinning dynamics of the formation in the model. The presented controller allows controlling the formation spin rate and supports variable

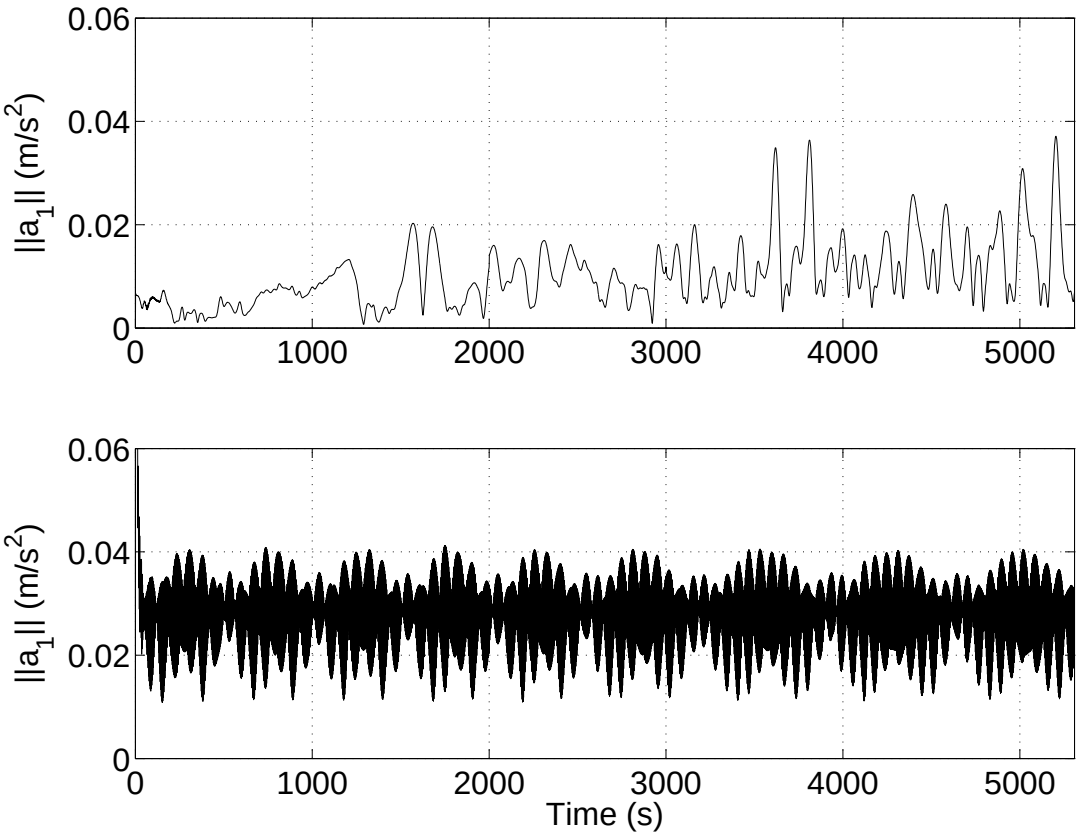

Figure 5.5: **Control acceleration of deputy 1. Upper: PID control. Lower: Sliding mode control**

moment of inertia through a deployment/retrieval mechanism. Two alternatives are presented for accurate control of deputies in the presence of gravity gradient perturbation. An scenario assesses the performance of the controller by showing successful submillimetric positioning capability.

Chapter 6

Conclusions

The first part of this work introduces the topic, and shows the maturity of the state of the art techniques for modeling the problem and the viability of the space tether applications, including tethered cluster missions.

As part of the analysis of the effect of massive tethers in cluster dynamics, this work shows that the effect of tether mass is almost negligible for open (HAS) formations, in which case the massless model captures the dynamics of the cluster. It has a minimal effect on the elongation and the angular separation of the tethers compared to the behavior of the massless model. Thus, a simplified model featuring purely elastic massless tethers is sufficient for the purposes of preliminary mission analysis and possibly design of formation control laws. Conversely, for closed formations, Closed-Hub-And-Spoke and Double-Pyramid (CHAS and DP respectively), there are substantial differences in the behavior of the formation between the two models, which means that the simplified one may miss relevant effects. The most noticeable effect is the monotonical bending of the external tethers towards the exterior of the formation due mainly to the centriphugal force, and in a lesser degree due to the effect of the gravitational force. This deformation of the external tethers prevents the internal tethers from being fully extended, which is specially noticeable in a DP cluster. The oscillation of internal tethers due to the to their intermittent extension and loss of tension has a significant negative effect on the positioning of the deputies, making closed formations with a parent body not suitable for accurate agent positioning. Both in the CHAS and DP cases, the parent body drifts away from the reference orbit due to the irregular motion of the agents.

As a novelty, the thesis proposes the use of circular shaped closed formations as an

alternative to planar square shaped formations in order to eliminate the bouncing effect on inner tethers, highlighted by the refined tethered formation model featuring massive tethers. This type of formations provide improved rigidity that allows adjacent agents to preserve their separation angle. At the same time, this configuration avoids the bouncing problem and formation center of mass drift from the reference orbit.

One of the purposes of tethered formations is to establish a link between agents, such that when the tethers remain taut, the formation replicates the behavior of an orbiting spinning body exhibiting a natural equilibrium state. Three equilibrium conditions exist for an spinning axisymmetrical rigid body. For practical reasons, this thesis is focused on two scenarios: the Thomson equilibrium (for spinning formations lying in the orbital plane), and the conical Likins-Pringle equilibrium (for formations facing the Earth). The third possible equilibrium state, the hyperbolic Likins-Pringle, is not considered adequate for most practical applications.

For tethered clusters with the spinning axis perpendicular to the orbital plane, the Thomson equilibrium conditions define the constraints that ensure the equilibrium of the formation. Furthermore, the HCW model used uncouples the planar of the the cross range dynamics, therefore if the members of the formation lie in the orbital plane with null cross track initial velocity, it can be guaranteed that the motion will be planar. This kind of stability is shown in all the planar formations lying in the orbital plane analyzed in this study.

For Earth-facing applications, the conical Likins-Pringle equilibrium is the most suitable state as it considers a spinning formation facing the Earth with a slight tilt angle with respect of the local vertical. The elevation angle equilibrium condition depends essentially on the moment of inertia of the formation and its spinning rate. For this purpose, and due to its prolate axisymmetric characteristics, the DP formation is chosen as a suitable candidate. An Earth-facing planar (oblate) formation does not maintain its axis pointing to the Earth, as it tends to have the direction angular momentum pointing approximately to an inertially fixed direction. This effect can be appreciated in all the Earth-facing planar formations analyzed in this study.

In order to evaluate the feasibility of tethered formations for missions in LEO, deviations from the ideal cases of purely Keplerian motion in the neighborhood of a circular reference orbit were analyzed, focusing on the effects of eccentricity of the reference orbit and Earth's oblateness. In particular, variation of orbital angular rate and distance from

the Earth associated to an eccentric orbit cause a periodic variation of the gravity gradient and inertial loads, whereas J_2 effects represents the most relevant perturbation in LEO, such that its effect needs to be accounted for even at a preliminary mission design stage.

For formations lying in the orbital plane, the spin rate of the formation with respect to the orbital frame varies along the orbit, being higher at apogee (where orbit frame angular speed is slower) and lower at perigee, due to the principle of conservation of angular momentum. The effect of the gravitational gradient can also be observed in the dynamics, being higher at perigee and lower at apogee. This affects the amplitude of the elongation of tethers in open formations, and also in the oscillations of the bouncing of external tethers in closed formations.

The J_2 perturbation does not have a significant effect on the relative motion of the deputies. However, in this study it can be clearly seen that it affects the trajectory of the formation as a whole through a secular drift of the parent body. Due to tether tensions on the initial instant of the simulation, the parent body is slightly shifted from the LVLH origin, which leads subsequently to the parent body and the cluster drifting away in a more noticeable way than in the unperturbed scenario case.

In order to address the control of tethered formations, a controller to stabilize an Earth-facing double pyramid tethered cluster is proposed. The control strategy has a double purpose: attitude control of the cluster and accurate position control of its agents. For the purpose of attitude control, and taking advantage again of the similarities between a tethered cluster and a rigid body, the virtual structure approach is chosen as the most suitable option. The formulation shown in this thesis augments the general virtual structure equations valid for a static formation by adding the kinematics of a spinning formation, since the original formulation is valid only to achieve a static final state. The controller is designed to modify the spin rate and the moment of inertia of the formation through a reeling mechanism, and therefore to be able to control the Likins-Pringle tilting angle of the cluster.

For the derivation of the accurate positioning control law, the study initially discusses different alternatives based on the state of the art of the robotics control literature. After evaluating other alternatives, two control laws are chosen for this application: One based on a PID controller and one based on the sliding mode control technique. For the sliding mode based control, a proof of semi-global exponential stability is provided. Results of a

representative simulation assess the viability of the control approach proposed leading to a submillimetric positioning accuracy.

The work performed in this thesis could be extended by redesigning the fine position control with the purpose of optimizing fuel consumption. The effect of electrodynamic tethers is not within the scope of this work, although it could be studied in order to identify potential advantages related to the use of electrodynamic forces. An additional field of investigation for future work on the subject stemming from the results presented in this thesis is represented by the design of an active vibration control system that damps oscillations originated by abrupt manouvers. The study of the potential effect of orbit debris on a tethered structure and the possible reconfiguration options after a tether failure could also complement the present study.

Nomenclature

Orbit Symbols

G	=	Gravitational constant
M_e	=	Earth's mass
R_e	=	Radius of the Earth
μ	=	Earth's standard gravitational parameter
T_O	=	Orbital period
n	=	Orbital rate mean motion
a	=	Semimajor axis
i	=	Inclination
e	=	Eccentricity
E_a	=	Eccentric anomaly
θ	=	True anomaly
L	=	True longitude
M	=	Mean anomaly
λ	=	Mean longitude
Ω	=	Longitude of the ascending node
ω_{per}	=	Argument of periapsis
$t_{\tau 0}$	=	Time when the satellite was at periapsis
$\boldsymbol{R}$	=	Vector from center of the Earth to a given point
$\boldsymbol{R}_{\text{ref}}$	=	Vector from center of the Earth to a reference orbit.
$\boldsymbol{r}_i$	=	Position vector of a body i in the LVLH reference frame $\mathcal{R}$
$\boldsymbol{v}_i$	=	Velocity vector of a body i in the LVLH reference frame $\mathcal{R}$

Tether Symbols

k_t	=	Elastic constant of a tether
k_s	=	Elastic constant of a stratch
$S_{j,i}$	=	Tether elastic factor between objects j and i
c_t	=	Damping constant a tether.
c_s	=	Damping constant of a stratch
$D_{j,i}$	=	Tether damping factor between objects j and i
T	=	Tether tension
$\varepsilon_{i,j}$	=	Tether strain between objects i and j
A_t	=	Cross section area of a tether
C_t	=	Tether coefficient of internal friction
E_t	=	Tether Young's modulus
ρ	=	tether linear density
η_t	=	Tether's loss factor
Ω_t	=	Tether oscillation frequency

Tethered Cluster Symbols

$\hat{\mathbf{e}}_{i,j}$	=	Unit vector in the local reference frame
$\boldsymbol{f}_i$	=	Force exerted over body i
$\boldsymbol{f}_{i,\text{tens}}$	=	Tether elastical force exerted over body i
$\boldsymbol{f}_{i,\text{grav}}$	=	Gravitational force exerted over body i
$l_{i,j}^{(0)}$	=	Nominal tether length between bodies i and j
$l_{i,j}$	=	Length of stratch between bodies j and i
l_i	=	Length of tether i
$(\cdot)_d$	=	Value related to deputy d
$(\cdot)_p$	=	Value related to parent body p
$(\cdot)_{i/p}$	=	Value related to body i with respect to parent body p

m_i	=	Mass of body i
m_t	=	Mass of tether t
n_b	=	Number beads on each tether
n_d	=	Number of deputies in the formation
n_p	=	Number of parents in the formation
n_t	=	Number of tethers in the formation
s_t	=	Number of stretches in tether t
q_j	=	Generalized coordinate for object j
Q_d	=	Raleigh function for damping force.
m_i	=	Mass of object i
α	=	Pitch angle (in-plane angle for orbital motion)
β	=	Roll angle (out-of-plane angle for orbital motion)
α^*	=	In-plane angle for normal plane motion
β^*	=	Out-of-plane angle for normal plane motion
D_p	=	Distance of center of mass to parent body
r_s	=	Factor of spin velocity
δ_j	=	In–plane angular orientation of deputy j with respect to axis $\hat{\mathbf{i}}$
$\gamma_{i,j}$	=	Angular separation between tether i and j
$\boldsymbol{\omega}_0$	=	Formation initial spin angular velocity
$\boldsymbol{\omega}_{i/p}$	=	Local angular rotation velocity of object i with respect to parent body
$\hat{\boldsymbol{\omega}}_{i/p}$	=	Local angular rotation rate of object i with respect to parent body
$\boldsymbol{h}$	=	Angular momentum vector
$\dot{\theta}$	=	Angular velocity of the LVLH reference frame
$\boldsymbol{\tau}$	=	Torque
k_I	=	Inertia parameter
γ	=	Likins-Pringle tilting angle

Virtual Structure Control Symbols

R_d	=	Distance of parent body to center of the Earth

q_j	=	Generalized coordinate for object j
m_i	=	Mass of object i
$\tilde{\boldsymbol{r}}_i$	=	Position error of body i
$\tilde{\boldsymbol{v}}_i$	=	Velocity error of body i
$\boldsymbol{q}_i$	=	Quaternion defining the orientation of body i
$\hat{\boldsymbol{q}}_i$	=	Vector part of quaternion $\boldsymbol{q}_i$
$\bar{q}_i$	=	Scalar part of quaternion $\boldsymbol{q}_i$.
$\boldsymbol{\omega}_i$	=	Spin velocity of agent i.
$(\cdot)_i^d$	=	Desired coordinate for agent i
$(\cdot)_F$	=	Coordinate related to Virtual Structure F
$(\cdot)_{Fi}$	=	Coordinate related to ith instance of Virtual Structure F.
$(\cdot)_{iF}$	=	Coordinate related to agent i relative to Virtual Structure F.
$\boldsymbol{C}_{RF}$	=	Direction cosine matrix between reference frame $\mathcal{R}$ and $\mathcal{F}$
$\boldsymbol{C}_{FS}$	=	Direction cosine matrix between reference frame $\mathcal{F}$ and $\mathcal{S}$
$\dot{\alpha}$	=	Spin rate
$\boldsymbol{\phi}$	=	Axis of spin motion
$\boldsymbol{\lambda}$	=	Formation expansion ratio.
$\dot{\boldsymbol{\lambda}}$	=	Formation expansion rate.
$\boldsymbol{\nu}$	=	Formation expansion straint.
$\boldsymbol{k}_S$, $\boldsymbol{K}_S$, $\boldsymbol{D}_S$	=	Agent synchronization constants.
$\boldsymbol{k}_G$, $\boldsymbol{K}_G$, $\boldsymbol{\Gamma}_G$	=	Proportional-Deriviative constants.
$\boldsymbol{K}_F$, $\boldsymbol{D}_G$	=	Formation feedback constants.
k_α, k_γ	=	Sliding mode control constants.
$\boldsymbol{K}_P$,$\boldsymbol{K}_I$,$\boldsymbol{K}_D$	=	Proportional, Integral and Derivative constant matrices.
$\boldsymbol{S}$	=	Sliding surface.
$\boldsymbol{S}_r$	=	Reference sliding surface.
$\boldsymbol{Y}_r\Theta$	=	Regressor.
$\boldsymbol{d}(t)$	=	External disturbance.
$\boldsymbol{M}$	=	Inertia matrix
$\boldsymbol{N}$	=	Coriolis/centrifugal terms matrix
$\boldsymbol{P}$	=	Coupled elastic forces terms matrix
$\boldsymbol{Q}$	=	Gravity gradient term matrix.

Other Symbols

$\mathcal{H}$	=	Hamiltonian
$\mathcal{I}$	=	Agent i fixed reference frame.
$\mathcal{O} : \{\hat{\mathbf{I}}, \hat{\mathbf{J}}, \hat{\mathbf{K}}\}$	=	Inertial Earth-fixed reference frame.
$\mathcal{R} : \{\hat{\mathbf{i}}, \hat{\mathbf{j}}, \hat{\mathbf{k}}\}$	=	Orbital Local Vertical Local Horizontal (LVLH) reference frame.
$\mathcal{F} : \{\hat{\mathbf{i}}_F, \hat{\mathbf{j}}_F, \hat{\mathbf{k}}_F\}$	=	Reference frame attached to the virtual structure.
$\mathcal{S} : \{\hat{\mathbf{i}}_S, \hat{\mathbf{j}}_S, \hat{\mathbf{k}}_S\}$	=	Cluster spinning reference frame.
$\mathcal{T}$	=	Kinetic energy
$\mathcal{T}_{\text{orb}}$	=	Orbital kinetic energy
$\mathcal{V}$	=	Potential energy
$\mathcal{V}_{\text{orb}}$	=	Orbital potential energy
$\mathcal{V}_R$	=	Disturbance potential
$\mathcal{V}_E$	=	Earth gravitational potential
$\mathcal{V}_{\text{elast}}$	=	Elastic potential

Acronyms

CHAS	=	Closed Hub-And-Spoke
DOF	=	Degree Of Freedom
DP	=	Double Pyramid
GAS	=	Global Asymptotic Stability
GPE	=	Gauss Planetary Equations
HAS	=	Hub-And-Spoke
HCW	=	Hill Clohessy Wiltshire
ISS	=	Input-to-State Stability
LEO	=	Low Earth Orbit
LVLH	=	Local Vertical Local Horizontal
PID	=	Proportional Integral Derivative
SEDS	=	Small Expendable Deployment System
SFF	=	Satellite Flight Formation
SPECS	=	Submillimeter Probe of the Evolution Cosmic Structure
TSS	=	Tethered Satellite System
VSC	=	Virtual Structure Control

Bibliography

[1] M.L. Cosmo, E.C. Lorenzini: *Tethers in Space Handbook*, Smithsonian Astrophysical Observatory for NASA Marshall Space Flight Center, December 1997.

[2] E.M. Levin.: *Dynamic Analysis of Space Tether Missions*, Advances in Astronautical Sciences, Volume 126, 2007.

[3] K.D. Kumar: *Review of Dynamics and Control of Nonelectrodynamic Tethered Satellite Systems*, Journal of Spacecraft and Rockets, vol. 43, no. 4, pp. 705720, Jul. 2006. http://dx.doi.org/10.2514/1.5479

[4] M.P. Cartmell, D.J. McKenzie: *A review of space tether research*, Progress in Aerospace Sciences, vol. 44, no. 1, pp. 121, Jan. 2008. http://dx.doi.org/10.1016/j.paerosci.2007.08.002

[5] H. Wen, D.P.Jin, H.Y. Hu: *Advances in dynamics and control of tethered satellite systems*, Acta Mech Sin, vol. 24, no. 4, pp. 473473, Jul. 2008. http://dx.doi.org/10.1007/s10409-008-0178-6

[6] Y. Chen, R. Huang, L. He, X. Ren, B. Zheng: *A review of dynamical modelling and control for space tethers*, Nonlinear Dyn, vol. 77, no. 4, pp. 10771099, Apr. 2014. http://dx.doi.org/10.1007/s11071-014-1390-5

[7] E.C. Lorenzini, J.R. Sanmartin, *Electrodynamic Tethers in Space*, Scientific American, vol. 291, no. 2, pp. 5057, Aug. 2004. http://dx.doi.org/10.1038/scientificamerican0804-50

[8] K. Wormnes, R. Le Letty, L.Summerer, R. Schonenbor, O. Dubois-Matra, E. Luraschi, A. Cropp, H. Krag and J. Delaval: *ESA technologies for space debris remediation.* 6th European Conference on Space Debris, Darmstadt, 2013.

[9] P. K. Aravind: *The Physics of the Space Elevator*, Am. J. Phys., vol. 75, no. 2, p. 125, 2007. http://dx.doi.org/10.1119/1.2404957

[10] M. Quadrelli: *Modeling and Dynamics Analysis of Tethered Formations for Space Interferometry*, AAS/AIAA Spaceflight Mechanics Meeting, Santa Barbara, CA, February 11-14, 2001.

[11] M. Quadrelli, F.Y. Hadaegh, E.C. Lorenzini, C. Bombardelli: *Precision Tethered Formations for LEO and Space Interferometry Applications*, 16th International Symposium on Spaceflight Dynamics, Pasadena, CA, December 3-7, 2001.

[12] R. Farley, D. Quinn: *Tethered formation configurations: meeting the scientific objectives of large aperture and interferometric science*, AIAA Space 2001 Conference and Exposition, Aug. 2001. http://dx.doi.org/10.2514/6.2001-4770

[13] A. Pizarro-Chong, A. K. Misra: *Dynamics of multi-tethered satellite formations containing a parent body*, Acta Astronautica, vol. 63, no. 1112, pp. 11881202, Dec. 2008. http://dx.doi.org/10.1016/j.actaastro.2008.06.021

[14] E. Kim, S.R. Vadali: *Modeling Issues Related to Retrieval of Flexible Tethered Satellite Systems*, Journal of Guidance, Control, and Dynamics, vol. 18, no. 5, pp. 11691176, Sep. 1995. http://dx.doi.org/10.2514/3.21521

[15] P. Williams: *Optimal control of a spinning double-pyramid Earth-pointing tethered formation*, Acta Astronautica, vol. 64, no. 1112, pp. 11911223, Jun. 2009. http://dx.doi.org/10.1016/j.actaastro.2009.01.014

[16] S.A. Schweighart, R.S. Sedwick: *High-Fidelity Linearized J2 Model for Satellite Formation Flight*, Journal of Guidance, Control, and Dynamics, vol. 25, no. 6, pp. 10731080, Nov. 2002. http://dx.doi.org/10.2514/2.4986

[17] G. Inalhan, M. Tillerson, J.P. How: *Relative Dynamics and Control of Spacecraft Formations in Eccentric Orbits*, Journal of Guidance, Control, and Dynamics, vol. 25, no. 1, pp. 4859, Jan. 2002. http://dx.doi.org/10.2514/2.4874

[18] M. Sabatini, G.B. Palmerini: *Linearized Formation-Flying Dynamics in a Perturbed Orbital Environment*, 2008 IEEE Aerospace Conference, Mar. 2008. http://dx.doi.org/10.1109/aero.2008.4526271

[19] W. Ren, R. Beard: *Decentralized Scheme for Spacecraft Formation Flying via the Virtual Structure Approach*, Journal of Guidance, Control,

and Dynamics, vol. 27, no. 1, pp. 7382, Jan. 2004. http://dx.doi.org/10.2514/1.9287

[20] R.W. Beard, J. Lawton, F.Y. Hadaegh: *A Coordination Architecture for Spacecraft Formation Control*, IEEE Trans. Contr. Syst. Technol., vol. 9, no. 6, pp. 777790, 2001. http://dx.doi.org/10.1109/87.960341

[21] W. Ren, R. Beard: *Virtual Structure Based Spacecraft Formation Control with Formation Feedback*, AIAA Guidance, Navigation, and Control Conference and Exhibit, Aug. 2002. http://dx.doi.org/10.2514/6.2002-4963

[22] R. Beard, W. Ren: *Formation feedback control for multiple spacecraft via virtual structures*, IEE Proceedings - Control Theory and Applications, vol. 151, no. 3, pp. 357368, May 2004. http://dx.doi.org/10.1049/ip-cta:20040484

[23] V. Parra-Vega, S. Arimoto, G. Hirzinger, P. Akella: *Dynamic Sliding PID Control for Tracking of Robot Manipulators: Theory and Experiments*, IEEE Transactions on Robotics and Automation, vol. 19, no. 6, pp. 967976, Dec. 2003. http://dx.doi.org/10.1109/tra.2003.819600

[24] Y. Choi, W.K. Chung, I.H. Suh: *Performance and H-inf Optimality of PID Trajectory Tracking Controller for Lagrangian Systems*, IEEE Transactions on Robotics and Automation, vol. 17, no. 6, pp. 857869, 2001. http://dx.doi.org/10.1109/70.976011

[25] Earth Observation Portal: https://directory.eoportal.org/web/eoportal/satellite-missions/s/space-tethers

[26] Y. Chen, R. Huang, X. Ren, L. He, Y. He: *History of the Tether Concept and Tether Missions: A Review*, ISRN Astronomy and Astrophysics, vol. 2013, pp. 17, 2013. http://dx.doi.org/10.1155/2013/502973

[27] N. H. Stone, W. J. Raitt, K. H.Wright, Jr.: *The TSS-1R Electrodynamic Tether Experiment: Scientific and Technological Results*. Advances in Space Research, vol. 24, no. 8, pp. 10371045, Jan. 1999. http://dx.doi.org/10.1016/s0273-1177(99)00551-7

[28] J.A. Carroll: *SEDS Deployer Design and Flight Performance*, Space Programs and Technologies Conference and Exhibit, Sep. 1993. http://dx.doi.org/10.2514/6.1993-4764

[29] J. Glaese, R. Issa, and P. Lakshmanan: *Comparison of SEDS-1 Pre-Flight Simulations and Flight Data*. Space Programs and Technologies

Conference and Exhibit, Sep. 1993. http://dx.doi.org/10.2514/6.1993-4766

[30] M. Grassi, M.L. Cosmo: *Attitude Dynamics of the Small Expendable-Tether Deployment System.* Acta Astronautica, vol. 36, no. 3, pp. 141148, Aug. 1995. http://dx.doi.org/10.1016/0094-5765(95)00093-f

[31] W. Barnds, S. Coffey, M. Davis, B. Kelm, W. Purdy: *TiPS: Results of a Tethered Satellite Experiment*, Advances in the Astronautical Sciences, AAS paper 97-600, 1997.

[32] K.T. Alfriend, W.J. Barnds, S.L. Coffey, L.M. Stuhrenberg: *Attitude and Orbit Determination of a Tethered Satellite System*, Advances in the Astronautical Sciences, AAS paper 95-351, 1995.

[33] http://www.thelivingmoon.com/41pegasus/02files/Electrodynamic_01.html

[34] M. Kruijff, E. J. van der Heide: *Qualification and in-flight demonstration of a European tether deployment system on YES2.* Acta Astronautica, vol. 64, no. 910, pp. 882905, May 2009. http://dx.doi.org/10.1016/j.actaastro.2008.10.014

[35] D.A. Quinn, D.C. Folta: *A Tethered Formation Flying Concept for the SPECS Mission*, 23rd Annual AAS Guidance and Control Conference, February 2-6, 2000.

[36] C.D. Hall, M. Kim: *Dynamics and Control of Rotating Tethered Satellite Systems*, Journal of Spacecraft and Rockets, vol. 44, no. 3, pp. 649659, May 2007. http://dx.doi.org/10.2514/1.17065

[37] H. Goldstein, C. Poole, J. Safko, S.R. Addison, *Classical Mechanics*, Addison Wesley, 2000. http://dx.doi.org/10.1119/1.1484149

[38] H. Schaub, J.L. Junkins: *Analytical Mechanics of Space Systems*, AIAA Education Series, 2003. http://dx.doi.org/10.2514/4.861550.

[39] R. Battin: *An Introduction to the Mathematics and Methods of Astrodynamics*, AIAA Education Series, New York, 1987. http://dx.doi.org/10.2514/4.861543.

[40] R.A. Broucke, P.J. Cefola: *On The Equinoctial Orbit Elements*, Celestial Mechanics, vol. 5, no. 3, pp. 303310, May 1972. http://dx.doi.org/10.1007/bf01228432

[41] M.J.H. Walker, B. Ireland, and J. Owens: *A set of modified equinoctial orbit elements*, Celestial Mechanics, vol. 36, no. 4, pp. 409419, Aug.

1985. http://dx.doi.org/10.1007/bf01227493

[42] O. Stone: *On the solution of Delaunay's canonical system of equations*, The Astronomical Journal, vol. 20, no.2, 1899. http://dx.doi.org/10.1086/103072

[43] F.T. Geyling, H.R. Westerman: *Introduction to Orbital Mechanics*, Addison-Wesley Aerospace Series, 1971.

[44] W.H. Clohessy, R.S. Wiltshire: *Terminal guidance system for satellite rendezvous*, Journal of the Aerospace Sciences, vol. 27, no. 9, pp. 653658, Sep. 1960. http://dx.doi.org/10.2514/8.8704

[45] S.S. Vaddi, S.R. Vadali, K. T. Alfriend: *Formation Flying: Accommodating Nonlinearity and Eccentricity Perturbations*, Journal of Guidance, Control, and Dynamics, vol. 26, no. 2, pp. 214223, Mar. 2003. http://dx.doi.org/10.2514/2.5054

[46] D.F. Lawden: *Optimal Trajectories for Space Navigation*, Butterworths, London, pp. 79–86, 1963. http://dx.doi.org/10.2307/3611765

[47] J.F. Tschauner, P.R. Hempel: *Rendezvous zu einemin elliptischer Bahn umlaufenden Ziel*, Astronautica Acta, Vol. 11, No. 2, pp. 104109, 1965.

[48] T.E. Carter: *New Form for the Optimal Rendezvous Equations near a Keplerian Orbit*, Journal of Guidance, Control, and Dynamics, vol. 13, no. 1, pp. 183186, Jan. 1990. http://dx.doi.org/10.2514/3.20533

[49] T.E. Carter, M. Humi: *Fuel-Optimal Rendezvous near a Point in General Keplerian Orbit*. Journal of Guidance, Control, and Dynamics, vol. 10, no. 6, pp. 567573, Nov. 1987. http://dx.doi.org/10.2514/3.20257

[50] Y. Ren, J. J. Masdemont, M. Marcote, and G. Gómez: *Computation of analytical solutions of the relative motion about a Keplerian elliptic orbit*, Acta Astronautica, vol. 81, no. 1, pp. 186199, Dec. 2012. http://dx.doi.org/10.1016/j.actaastro.2012.07.026

[51] H. Schaub: *Incorporating Secular Drifts into the Orbit Element Difference Description of Relative Orbits*, 13th AAS/AIAA Space Flight Mechanics Meeting, February 9-13, 2003.

[52] H. Schaub, S. R. Vadali, J. L. Junkins, and K. T. Alfriend: *Spacecraft formation flying control using mean orbital elements*, Journal of the Astronautical Sciences, vol. 48, No. 1, pp. 69-87, Jan-March, 2000.

[53] H. Schaub and T. Alfriend: *J_2 invariant relative orbits for spacecraft formations*, Flight Mechanics Symposium, (NASA Goddard Space Flight

Center, Greenbelt, MD), pp. 125-139, 1999.

[54] H. Yan, K.T. Alfriend, S.R. Vadali, P. Sengupta: *Optimal Design of Satellite Formation Relative Motion Orbits Using Least-Squares Methods*, Journal of Guidance, Control, and Dynamics, vol. 32, no. 2, pp. 599604, Mar. 2009. http://dx.doi.org/10.2514/1.35044

[55] R.R. Bate, D.D. Mueller, J.E. White: *Fundamentals of Astrodynamics*, Dover, New York, 1971.

[56] S.R.Vadali, K.T.Alfriend, S.Vaddi: *Hill's equation, Mean Orbital Elements, and Formation Flying of Satellites*, Advances in the Astronautical Sciences, AAS 00–258, 2000.

[57] H. Schaub: *Relative Orbit Geometry Through Classical Orbit Element Differences*, Journal of Guidance, Control, and Dynamics, vol. 27, no. 5, pp. 839848, Sep. 2004. http://dx.doi.org/10.2514/1.12595

[58] H. Schaub and K. T. Alfriend: *Hybrid Cartesian and Orbit Element Feedback Law for Formation Flying Spacecraft*, Journal of Guidance, Control, and Dynamics, vol. 25, no. 2, pp. 387393, Mar. 2002.

[59] M. Capderou: *Satellites: orbits and missions, Volume 1*, Springer, 2005.

[60] V.A. Chobotov: *Orbital Mechanics*, AIAA Education Series, 2002. http://dx.doi.org/10.2514/4.862250

[61] K.T. Alfriend, H. Schaub: *Dynamics and Control of Spacecraft Formations: Challenges and Some Solutions*, Journal of the Astronautical Sciences, vo.l 48, no. 2, pp. 249-267, April-September 2000.

[62] K. Yamada, T. Shima, S. Yoshikawa: *Effect of the J_2 Perturbation on Relative Spacecraft Position in Near-Circular Orbits*, Journal of Guidance, Control, and Dynamics, vol. 33, no. 2, pp. 584590, Mar. 2010. http://dx.doi.org/10.2514/1.47436

[63] D.W. Gim, K.T. Alfriend: *State Transition Matrix of Relative Motion for the Perturbed Noncircular Reference Orbit*, Journal of Guidance, Control, and Dynamics, vol. 26, no. 6, pp. 956971, Nov. 2003. http://dx.doi.org/10.2514/2.6924

[64] K.T. Alfriend, H. Yan: *Evaluation and Comparison of Relative Motion Theories*, Journal of Guidance, Control, and Dynamics, vol. 28, no. 2, pp. 254261, Mar. 2005. http://dx.doi.org/10.2514/1.6691

[65] J.A. Roberts, P.C.E. Roberts: *The Development of High Fidelity Linearized Models for Satellite Formation Flying Control*, Advances in the Astronautical Sciences, Vol. 119, Part 1, pp. 913–934, 2004.

[66] M. Sabu Sebastian, K.C. Unnikrishnan, S. Narayanan: *Viscoelastic properties of Kevlar®-29 fabric tape strength member*, Mechanics of Materials, vol. 40, no. 11, pp. 949960, Nov. 2008. http://dx.doi.org/10.1016/j.mechmat.2008.05.002

[67] Hughes, P.C.: *Spacecraft Attitude Dynamics*, Dover Publications, 2004.

[68] G. Genta: *Vibration Dynamics and Control*, Springer, 2009, DOI: 10.1007/978-0-387-79580-5.

[69] V.V. Beletsky, E.M. Levin: *Dynamics of space tether systems*, Advances in Astronautical Sciences, Volume 83, 1993.

[70] K.K. Mankala, S.K. Agrawal: *Dynamic Modeling and Simulation of Satellite Tethered Systems*, Journal of Vibration and Acoustics, vol. 127, no. 2, p. 144, 2005. http://dx.doi.org/10.1115/1.1891811

[71] M. Krupa, W. Poth, M. Schagerl, A. Steindl, W. Steiner, H. Troger, G. Wiedermann: *Modelling, Dynamics and Control of Tethered Satellite Systems*, Nonlinear Dyn, vol. 43, no. 12, pp. 7396, Jan. 2006. http://dx.doi.org/10.1007/s11071-006-0752-z

[72] M. Krupa, M. Schagerl, A. Steindl, P. Szmolyan, H.Troger: *Relative equilibria of tethered satellite systems and their stability for very stiff tethers*, Dynamical Systems, vol. 16, no. 3, pp. 253278, Sep. 2001. http://dx.doi.org/10.1080/14689360117072

[73] Y. Yan, A.K. Misra, N. Oshiro, T. Yamamoto: *Modeling of the Dynamics of N-Body Tethered Satellite Systems*, Asia-Pacific Vibration Conference, Kyongju, Korea, November 9-13, 1997.

[74] F. Dignath, W. Schiehlen: *Control of the Vibrations of a Tethered Satellite System*, Journal of Applied Mathematics and Mechanics, vol. 64, no. 5, pp. 715722, Jan. 2000. http://dx.doi.org/10.1016/s0021-8928(00)00100-3

[75] S.G. Tragesser: *Formation Flying with Tethered Spacecraft.* Astrodynamics Specialist Conference, Aug. 2000. http://dx.doi.org/10.2514/6.2000-4133

[76] S.G. Tragesser, A. Tuncay: *Orbital Design of Earth-Oriented Tethered Satellite Formations.* AIAA/AAS Astrodynamics Specialist Conference and Exhibit, Aug. 2002. http://dx.doi.org/10.2514/6.2002-4641

[77] A.P. French: *Vibrations and Waves*, The MIT Introductory Physics Series. The Massachusetts Institute of Technology, 1966.

[78] J. Peláez: *On the Dynamics of the Deployment of a Tether from an Orbiter - I. Basic Equations*, Acta Astronautica, vol. 36, no. 2, pp. 113122, Jul. 1995. http://dx.doi.org/10.1016/0094-5765(95)00045-2

[79] J. Peláez: *On the Dynamics of the Deployment of a Tether from an Orbiter - II. Exponential Deployment*, Acta Astronautica, vol. 36, no. 6, pp. 313335, Sep. 1995. http://dx.doi.org/10.1016/0094-5765(95)00117-4

[80] N.N. Smirnov, Yu.A. Demyanov, A.V. Zvyaguin, A.A. Malashin, A.A. Luzhin: *Dynamical simulation of tether in orbit deployment*, Acta Astronautica, vol. 67, no. 34, pp. 324332, Aug. 2010. http://dx.doi.org/10.1016/j.actaastro.2010.02.020

[81] A. Steindl, H. Troger: *Optimal Control of Deployment of a Tethered Subsatellite*, Nonlinear Dynamics 31: 257274, 2003.

[82] A. Steindl, W. Steiner, H. Troger: *Optimal Control of Retrieval of a Tethered Subsatellite*, IUTAM Symposium on Chaotic Dynamics and Control of Systems and Processes in Mechanics, pp. 441450, 2005. http://dx.doi.org/10.1007/1-4020-3268-4_41

[83] A.E. Bryson, Y.-C. Ho: *Applied Optimal Control: Optimization Estimation and Control*, Taylor & Francis, 1988.

[84] K. Nakaya, M. Iai, K. Omagari, H. Yabe, S. Matunaga: *Formation Deployment Control for Spinning Tethered Formation Flying -Simulations and Ground Experiments-*, AIAA Guidance, Navigation, and Control Conference and Exhibit, Aug. 2004. http://dx.doi.org/10.2514/6.2004-4896

[85] B.S. Yu, D.P. Jin: *Deployment and retrieval of tethered satellite system under J_2 perturbation and heating effect*, Acta Astronautica, vol. 67, no. 78, pp. 845853, Oct. 2010. http://dx.doi.org/10.1016/j.actaastro.2010.05.013

[86] J.L. Tang, G.X. Ren, W.D. Zhu, H. Ren: *Dynamics of variable-length tethers with application to tethered satellite deployment*, Communications in Nonlinear Science and Numerical Simulation, vol. 16, no. 8, pp. 34113424, Aug. 2011. http://dx.doi.org/10.1016/j.cnsns.2010.11.026

[87] P. M. Bainum, V. K. Kumar: *Optimal Control of the Shuttle–Tethered–Subsatellite System*, Acta Astronautica, vol. 7, no. 12, pp. 13331348, Dec. 1980. http://dx.doi.org/10.1016/0094-5765(80)90010-7

[88] A.K. Misra: *Dynamics and control of tethered satellite systems*, Acta Astronautica, vol. 63, no. 1112, pp. 11691177, Dec. 2008. http://dx.doi.org/10.1016/j.actaastro.2008.06.020

[89] A. Pizarro-Chong, A. K. Misra: *Dynamics of a Multi-Tethered Satellite Formation*, AIAA/AAS Astrodynamics Specialist Conference and Exhibit, Aug. 2004. http://dx.doi.org/10.2514/6.2004-5308

[90] P. Williams: *Dynamics and Control of Spinning Tethers for Rendezvous in Elliptic Orbits*, Journal of Vibration and Control, vol. 12, no. 7, pp. 737771, Jul. 2006. http://dx.doi.org/10.1177/1077546306065710

[91] P. Williams: *Libration Control of Tethered Satellites in Elliptical Orbits*, Journal of Spacecraft and Rockets, vol. 43, no. 2, pp. 476479, Mar. 2006. http://dx.doi.org/10.2514/1.17499

[92] H.A. Fujii, W. Ichiki: *Nonlinear Dynamics of the Tethered Subsatellite System in the Station Keeping Phase*, Journal of Guidance, Control, and Dynamics, vol. 20, no. 2, pp. 403406, Mar. 1997. http://dx.doi.org/10.2514/2.4057

[93] V. A. Zlatoustov, A. P. Markeev: *Stability of Planar Oscillations of a Satellite in an Elliptical Orbit*, Celestial Mechanics, vol. 7, no. 1, pp. 3145, Jan. 1973. http://dx.doi.org/10.1007/bf01243507

[94] A. Celletti, V. Sidorenko: *Some properties of the dumbbell satellite attitude dynamics*, Celest Mech Dyn Astr, vol. 101, no. 12, pp. 105126, Mar. 2008. http://dx.doi.org/10.1007/s10569-008-9122-0

[95] H.A. Fujii, W. Ichiki, S. Suda, T.R. Watanabe: *Chaos Analysis on Librational Control of Gravity-Gradient Satellite in Elliptic Orbit*, Journal of Guidance, Control, and Dynamics, vol. 23, no. 1, pp. 145146, Jan. 2000. http://dx.doi.org/10.2514/2.4500

[96] A. Burov, I. Kosenko: *Dumb–Bell of Variable Length in an Elliptic Orbit: Relative Equilibria, Periodicity, and Chaos*. Proceedings, 4th Chaotic Modelling and Simulation International Conference, 31 May - 3 June, 2011.

[97] A. Burov, I. Kosenko: *On planar oscillations of a body with a variable mass distribution in an elliptic orbit*. Proceedings of the Institution of Mechanical Engineers, Part C: Journal of Mechanical Engineering Science, vol. 225, no. 10, pp. 22882295, Sep. 2011. http://dx.doi.org/10.1177/0954406211404327

[98] D.P. Jin and H. Y. Hu: *Optimal Control of a Tethered Subsatellite of*

Three Degrees of Freedom, Nonlinear Dyn, vol. 46, no. 12, pp. 161178, Aug. 2006. http://dx.doi.org/10.1007/s11071-006-9021-4

[99] J.R. Sanmartin, E.C. Lorenzini, M. Martinez-Sanchez, *A Review of Electrodynamic Tethers for Space Applications*, 44th AIAA/ASME/SAE/ASEE Joint Propulsion Conference; Exhibit, Jul. 2008. http://dx.doi.org/10.2514/6.2008-4595

[100] J.R. Sanmartin, E.C. Lorenzini, M. Martinez-Sanchez: *Electrodynamic Tether Applications and Constraints*, Journal of Spacecraft and Rockets, vol. 47, no. 3, pp. 442456, May 2010. http://dx.doi.org/10.2514/1.45352

[101] M. Sanjurjo-Rivo and J. Pela'ez: *Energy Analysis of Bare Electrodynamic Tethers*, Journal of Propulsion and Power, vol. 27, no. 1, pp. 246256, Jan. 2011. http://dx.doi.org/10.2514/1.48168

[102] V.A. Chobotov and D.L. Mains: *Tether Satellite System Collision Study*, Acta Astronautica, vol. 44, no. 712, pp. 543551, Apr. 1999. http://dx.doi.org/10.1016/s0094-5765(99)00098-3

[103] I. Kim, H. Hirayama, T. Hanada: *Practical guidelines for electrodynamic tethers to survive from orbital debris impacts*, Advances in Space Research, vol. 45, no. 10, pp. 12921300, May 2010. http://dx.doi.org/10.1016/j.asr.2010.01.012

[104] G.L. Gittins, G.G. Swinerd, H.G. Lewis, D.N. Williams: *A study of debris impact collision probabilities to space tethers*, Advances in Space Research, vol. 34, no. 5, pp. 10801084, Jan. 2004. http://dx.doi.org/10.1016/j.asr.2003.01.013

[105] J. Pearson, E. Levin, J. Oldson, H. Wykes: *Lunar space elevators for cislunar space development*, NASA Research Subaward No.: 07605-003-034, 2005. http://www.niac.usra.edu/files/studies/final_report/1032Pearson.pdf

[106] DuPont™ Advanced Fiber Systems: *Kevlar® aramid fiber technical guide*, www.dupont.com

[107] M.M. Wallace, C. W. Bert: *Experimental determination of dynamic Young's modulus and damping of an aramid-fabric/polyester composite material*, Proc. Okla. Acad. Sci. 59:98-101, 1979.

[108] K.D. Godard, A. Kumar, B. Tan: *Nonlinear optimal control of tethered satellite systems using tether offset in the presence of tether failure*, Acta Astronautica, vol. 66, no. 910, pp. 14341448, May 2010. http:

//dx.doi.org/10.1016/j.actaastro.2009.10.037

[109] S.-J. Chung, J.-J. Slotine, D. W. Miller: *Nonlinear Model Reduction and Decentralized Control of Tethered Formation Flight*, Journal of Guidance, Control, and Dynamics, vol. 30, no. 2, pp. 390400, Mar. 2007. http://dx.doi.org/10.2514/1.21492

[110] J.A. Carroll, J.C. Olson: *Tethers for Small Satellite Applications*, AIAA/USU Small Satellite Conference in Logan, Utah, 1995.

[111] R. Orban: *Advances in space tether materials*, 3rd Tethers in Space/ Toward Flight International Conference, May 1989.

[112] D.D. Tomlin, G.C. Faile, K.B. Hayashida, C.L. Frost, C.Y. Wagner, M.L. Mitchell, J.A. Vaughn, and M.J. Galuska: *Space Tethers: Design Criteria*, NASA Technical Memorandum 108537, 1997.

[113] A.B. DeCou: *Tether Static Shape for Rotating Multimass, Multitether, Spacecraft for 'Triangle' Michelson Interferometer*, Journal of Guidance, Control and Dynamics, vol. 2, no. 2, pp. 273-275, March 1989. http://dx.doi.org/10.2514/3.20401

[114] A. Amour, A.K. Misra, V.J. Modi: *Equilibrium Configurations and Their Stability in Three-Dimensional Motion of Three-Body Tethered Systems*, International Astronautical Federation, IAF-01-A.4.07, 2001.

[115] D.A. Quinn, R.E. Farley: *Tethered Formation Configurations: Meeting the Scientific Objectives of Large Aperture and Interferometric Science*, AIAA Space 2001 Conference and Exposition, Aug. 2001. http://dx.doi.org/10.2514/6.2001-4770

[116] T. Williams, K. Moore: *Dynamics of Tethered Satellite Formations*, AAS 02-198, AAS/AIAA Spaceflight Mechanics Meeting, Jan. 2002.

[117] M. Sabatini, G.B. Palmerini, *Dynamics of a 3D Rotating Tethered Formation Flying Facing the Earth*, IEEE Aerospace Conference, 2007. http://dx.doi.org/10.1109/aero.2007.352671

[118] D. McKenzie, M. Cartmell, G. Radice, and M. Vasile. Space webs final report 05-4109a. Ariadna study 05-4109a, University of Glasgow and ESA, 2006. URL http://www.esa.int/gsp/ACT/doc/ARI/ARIStudyReport/ACT-RPT-MAD-ARI-05-4109b-SpaceWebs-Glasgow.pdf

[119] A.D. Guerman, G. Smirnov, P. Paglione, A. M. Vale Seabra: *Stationary Configurations of a Tetrahedral Tethered Satellite Formation*, Journal of Guidance, Control, and Dynamics, vol. 31, no. 2, pp. 424428, Mar. 2008.

http://dx.doi.org/10.2514/1.31979

[120] S.M. Yoo, S.Y. Park: *Determination of Initial Conditions for Tetrahedral Satellite Formation*, Journal of Astronomy and Space Sciences, vol. 28, no. 4, pp. 285290, Dec. 2011. http://dx.doi.org/10.5140/jass.2011.28.4.285

[121] G. Avanzini, M. Fedi: *Refined dynamical analysis of multi-tethered satellite formations*, Acta Astronautica, vol. 84, pp. 3648, Mar. 2013. http://dx.doi.org/10.1016/j.actaastro.2012.10.031

[122] V.V. Beletskii, V.V.: *Motion of an Artificial Satellite About its Center of Mass*, Israel Program for Scientific Translations, NASA-TT-F-429, TT-67-51366, 1966.

[123] M. Fedi, G. Avanzini, *Virtual Structure Formation Control for Tethered Satellite Formations*, 7th International Workshop on Satellite Constellations and Formation Flying, 2013

[124] P. Erichsen: *Performance Evaluation of Spacecraft Propulsion Systems in Relation to Mission Impulse Requirements*, Second European Spacecraft Propulsion Conference, Proceedings of the conference, 27-29 May 1997 in Noordwijk, The Netherlands. ESA SP-398.

[125] R. H. Frisbee: *Advanced Space Propulsion for the 21st Century*, Journal of Propulsion and Power, vol. 19, no. 6, pp. 11291154, Nov. 2003.

[126] Chobotov, V.A.: *Spacecraft Attitude Dynamics and Control*, Krieger Publishing Company, 1991.

[127] J. Gonzalez del Amo: *European Space Agency Activities in Electric Propulsion*, The 33st International Electric Propulsion Conference, The George Washington University, USA, 2013.

[128] T. Rupp, S. D'Amico, O. Montenbruck, E. Gill: *Autonomous Formation Flying at DLR's German Space Operations Center (GSOC)*, 58th International Astronautical Congress, 2007-09-24 - 2007-09-28, Hyderabad.

[129] A. Garcia-Rodriguez, et al: *GNSS in Space, Part 2: Formation Flying Radio Frequency Techniques and Technology*, Inside GNSS Jan./Feb. 2009, http://www.insidegnss.com/node/1123

[130] J.R. Wertz: *Spacecraft Attitude Determination and Control*, Kluwer Academic Publishers, 1990.

[131] M. J. Sidi: *Spacecraft Dynamics and Control. A Practical Engineering Approach*, Cambridge University Press, 1997.

[132] Scott R. Starin: *Attitude Determination and Control Systems*, NASA report. http://ntrs.nasa.gov/archive/nasa/casi.ntrs.nasa.gov/20110007876.pdf

[133] A. Pizarro-Chong: *Dynamics of multi-tethered satellite formations*, VDM, 2008.

[134] K.A. Vogel: *Dynamics and Control of Tethered Satellite Formations for the Purpose of Space-Based Remote Sensing*, Ph.D. Thesis, Air Force Institute of Technology, AFIT/DS/ENY/06-04, 2006.

[135] G. Avanzini, M. Fedi: *Effects of eccentricity of the reference orbit on Multi-Tethered Satellite Formations*, Acta Astronautica, vol. 94, no. 1, pp. 338350, Jan. 2014. http://dx.doi.org/10.1016/j.actaastro.2013.03.019

[136] G. Avanzini, M. Fedi: *Effects of J2 perturbations on multi-tethered satellite formations*. AAS 11-631, AAS/AIAA Astrodynamics Specialist Conference, 2011.

[137] K.T. Alfriend, S.R. Vadali, P. Gurfil, J. P. How, L. S. Breger: *Spacecraft Formation Flying. Dynamics, control and navigation*, Elsevier 2010.

[138] D.P. Scharf, F.Y. Hadaegh, S.R. Ploen: *A Survey of Spacecraft Formation Flying Guidance and Control (Part I): Guidance*, Proceedings of the 2003 American Control Conference, 2003. http://dx.doi.org/10.1109/acc.2003.1239845

[139] D.P. Scharf, F.Y. Hadaegh, S.R. Ploen: *A Survey of Spacecraft Formation Flying Guidance and Control (Part II): Control*, Proceedings of the American Control Conference, 2004.

[140] R. Bevilacqua, M. Romano, F. Curti: *Decoupled-natural-dynamics Model for the Relative Motion of two Spacecraft without and with J_2 Perturbation*, Nonlinear Dynamics and Systems Theory, 10 (1) 1120, 2010.

[141] H. Liang, J. Wang, Z. Sun *Robust decentralized coordinated attitude control of spacecraft formation*, Acta Astronautica, vol. 69, no. 56, pp. 280288, Sep. 2011. http://dx.doi.org/10.1016/j.actaastro.2011.03.018

[142] R. Pongvthithum, S.M. Veres, S.B. Gabriel, E. Rogers: *Universal adaptive control of satellite formation flying*, International Journal of Control, vol. 78, no. 1, pp. 4552, Jan. 2005. http://dx.doi.org/10.1080/00207170412331330887

[143] R. Kristiansen, P. J. Nicklasson: *Spacecraft formation flying: A review and new results on state feedback control*, Acta Astronautica, vol. 65, no. 1112, pp. 15371552, Dec. 2009. http://dx.doi.org/10.1016/j.actaastro.2009.04.014

[144] Y. Xu, N. Fitz-Coy, Rick Lind, A. Tatsch: *μ Control for Satellites Formation Flying*, J. Aerosp. Eng., vol. 20, no. 1, pp. 1021, Jan. 2007. http://dx.doi.org/10.1061/(asce)0893-1321(2007)20:1(10)

[145] J.T. Wen, K. Kreutz-Delgado: *The Attitude Control Problem*, IEEE Trans. Automat. Contr., vol. 36, no. 10, pp. 11481162, 1991. http://dx.doi.org/10.1109/9.90228

[146] Wie, B.: *Space Vehicle Dynamics and Control*, American Institute of Aeronautics and Astronautics, Inc., Reston, VA, 1998.

[147] G. Avanzini, G. de Matteis, V. Tarantini: *Control of an Orbiting Formation of Satellites Using the Virtual Structure Approach*, AAS 05-276, AAS/AIAA Astrodynamics Specialists Conference, August 7-11, 2005.

[148] Y. Kim, C. Ahn: *Point Targeting of Multisatellites via a Virtual Structure Formation Flight Scheme*, Journal of Guidance, Control, and Dynamics, vol. 32, no. 4, pp. 13301344, Jul. 2009. http://dx.doi.org/10.2514/1.39537

[149] S.-J. Chung, D. W. Miller: *Propellant-Free Control of Tethered Formation Flight, Part 1: Linear Control and Experimentation*, Journal of Guidance, Control, and Dynamics, vol. 31, no. 3, pp. 571584, May 2008. http://dx.doi.org/10.2514/1.32188

[150] S.-J. Chung, J.-J. Slotine, D. W. Miller: *Propellant-Free Control of Tethered Formation Flight, Part 2: Nonlinear Underactuated Control*, Journal of Guidance, Control, and Dynamics, vol. 31, no. 5, pp. 14371446, Sep. 2008. http://dx.doi.org/10.2514/1.32189

[151] S.-J. Chung, J.-J. Slotine, D. W. Miller: *New Control Strategies for Underactuated Tethered Formation Flight Spacecraft*, AIAA Guidance, Navigation and Control Conference and Exhibit, Aug. 2007. http://dx.doi.org/10.2514/6.2007-6858

[152] K. Nakaya, S. Matunaga: *On Attitude Maneuver of Spinning Tethered Formation Flying Based on Virtual Structure Method*, AIAA Guidance, Navigation, and Control Conference and Exhibit, Aug. 2005. http://dx.doi.org/10.2514/6.2005-6088

[153] Z. Qu, J. Dorsey: *Robust Tracking Control of Robots by a Linear Feedback Law*, IEEE Trans. Automat. Contr., vol. 36, no. 9, pp. 10811084, 1991. http://dx.doi.org/10.1109/9.83543

[154] Siciliano, B., Khatib, O., *Springer Handbook of Robotics*, Springer, 2008.

[155] D.S. Bernstein, S.P. Bhat: *Lyapunov Stability, Semistability, and Asymptotic Stability of Matrix Second-Order Systems*, Proceedings of 1994 American Control Conference - ACC 94, 1994. http://dx.doi.org/10.1109/acc.1994.752501

[156] J.-J. Slotine, W. Li: *Applied Nonlinear Control*, Englewood Cliffs, NJ: Prentice-Hall, 1991.

[157] Haddad, W.M., Chellaboina, V.: *Nonlinear Dynamical Systems and Control. A Lyapunov-Based Approach*, Princeton University Press, 2008.

[158] J.J. Slotine, W. Li: *On the Adaptive Control of Robot Manipulators*, The International Journal of Robotics Research, vol. 6, no. 3, pp. 4959, Sep. 1987. http://dx.doi.org/10.1177/027836498700600303

[159] P. Tomei: *Adaptive PD controller for robot manipulators*, IEEE Transactions on Robotics and Automation, vol. 7, no. 4, pp. 565570, 1991. http://dx.doi.org/10.1109/70.86088

[160] R. Kelly: *PD control with desired gravity compensation of robot manipulators: A review*, The International Journal of Robotics Research, vol. 16, no. 5, pp. 660672, Oct. 1997. http://dx.doi.org/10.1177/027836499701600505

[161] A. Loria, E. Lefeber, H. Nijmeijer: *Global Asymptotic Stability of Robot Manipulators with Linear PID and PI2D Control*, SACTA, pp. 138-149, 2000.

[162] J.A. Ramirez, I. Cervantes, R. Kelly: *PID regulation of robot manipulators: Stability and Performance*, Systems and Control Letters, vol. 41, no. 2, pp. 7383, Oct. 2000. http://dx.doi.org/10.1016/s0167-6911(00)00038-4

[163] J.T. Wen, S. Murphy: *PID control for robot manipulators*, CIRSSE Document 54, Rensselaer Polytechnic Institute, May 1990.

[164] Y. Choi, W.K. Chung: *PID Trajectory Tracking Control for Mechanical Systems*, Lecture Notes in Control and Information Sciences, 2004. http://dx.doi.org/10.1007/b10906

[165] H.A. Fujii, T. Watanabe, P. M. Trivailo: *Wave-absorbing control of*

transverse vibration of Tether Systems, The Journal of the Astronautical Sciences, Vol. 51, No. 3, pp. 249-259, July-September 2003.

[166] P. Williams: *Optimal Deployment and Offset Control for a Spinning Flexible Tethered Formation*, AIAA Guidance, Navigation, and Control Conference and Exhibit, Aug. 2006. `http://dx.doi.org/10.2514/6.2006-6041`

[167] S.J. Chung and D.W. Miller: *Nonlinear Control and Synchronization of Multiple Lagrangian Systems with Application to Tethered Formation Flight Spacecraft*, Ph.D. Thesis, Massachusetts Institute of Technology, 2007.

[168] A.B. DeCou: *Attitude and Tether Vibration Control in Spinning Tethered Triangles for Orbiting Interferometry*, The Journal of the Astronautical Sciences, Vol. 41, No. 3, July-September 1993, pp. 373-398.